REDOX-ACTIVE CARBON-BASED ELECTRODES FOR HIGH-PERFORMANCE ELECTROCHEMICAL ENERGY STORAGE DEVICES

A Dissertation
Presented to
The Academic Faculty

by

Tianyuan Liu

In Partial Fulfillment
of the Requirements for the Degree
Doctor of Philosophy in the
Georgia W. Woodruff School of Mechanical Engineering

Georgia Institute of Technology
May 2018

REDOX-ACTIVE CARBON-BASED ELECTRODES FOR HIGH-PERFORMANCE ELECTROCHEMICAL ENERGY STORAGE DEVICES

Approved by:

Dr. Seung Woo Lee, Advisor
School of Mechanical Engineering
Georgia Institute of Technology

Dr. Seung Soon Jang
School of Materials Science and Engineering
Georgia Institute of Technology

Dr. Hailong Chen
School of Mechanical Engineering
Georgia Institute of Technology

Dr. Thomas Fuller
School of Chemical & Biomolecular Engineering
Georgia Institute of Technology

Dr. Peter J. Hesketh
School of Mechanical Engineering
Georgia Institute of Technology

Date Approved: Nov-27-2017

To my family.

ACKNOWLEDGEMENTS

I wish to thank my advisor, Professor Seung Woo Lee, for his guidance and encouragement during pursuing this degree. I'm lucky to be one of the first graduate students in this dynamic and growing group. I would appreciate Prof. Lee's endless support on my research, he always encourages the students to pursuit their research ideas, and treats them as independent researchers. I truly appreciate my committee members, Prof. Seung Soon Jang, Prof. Hailong Chen, Prof. Peter J. Hesketh, and Prof. Thomas Fuller for constructive and insightful comments on my research.

I would also thank my collaborators, Prof. Ki Chul Kim, Prof. Seung Soon Jang for fruitful discussions and collaborations on understanding electrochemical properties of redox-active carbon materials and organic molecules. Prof. Suguru Noda, Prof. Zhongming Chen for their wonderful submillimeter long few-walled carbon nanotubes which has been extensively in my research. Prof. Satish Kumar, Dr. Amir A Bakhtiary Davijani, Dr. Kishor Gupta for their high-quality carbon nanotube films and high surface area carbon materials, which helps me to obtained more valuable results. Prof. Shuo Chen, and Ms. Jingying Sun for their help in transmission electron microscope characterization. I would like to thank all former and current group members in Lee's group whom I learned lot from and enjoyed working with. Dr. Reza Kavian, Dr. Jinho Park, Mr. Byeongyong Lee, Mr. Jong Ha, Mr. Michael Lee, Mr. Siyao Cai, and Mr. Dong Yeeb Shin.

Financial support of this research was provided by Prof. Lee's startup fund from the Georgia Institute of Technology, Samsung Advanced Institute of Technology

(SAIT)'s Global Research Outreach (GRO) Program, Georgia Tech Research Institute on IRAD.

Lastly, I would like to thank my family who sacrifice their time, and support me with their love and encouragement in all my pursuits.

TABLE OF CONTENTS

LIST OF TABLES

LIST OF FIGURES

LIST OF SYMBOLS AND ABBREVIATIONS

GO	Graphene oxide
EC	Electrochemical capacitor
EES	Electrochemical energy storage
EC	Electrochemical capacitor
AC	Activated carbon
FWNT	Few-walled carbon nanotube
CNT	Carbon nanotube
MWNT	Multi-walled carbon nanotubes
GA	Graphene aerogel
PDA	Polydopamine
$LiPF_6$	Lithium hexafluorophosphate
EC	Ethylene carbonate
DMC	Dimethyl carbonate
SEM	Scanning electron microscope
TEM	Transmission electron microscope
XPS	X-ray photoelectron spectroscopy
XRD	X-ray diffraction
FTIR	Fourier-transform infrared spectroscopy
CV	Cyclic voltammetry
EIS	Electrochemical impedance spectroscopy
AFM	Atomic force microscope

EDX	Energy-dispersive X-ray spectroscopy
UV-Vis	Ultraviolet–visible spectroscopy
EDLC	Electrical double layer capacitor
DFT	Density functional theory
TGA	Thermogravimetric analysis

SUMMARY

The fast development of electric vehicles and portable electronics has been urging the development of high-performance electrochemical energy storage devices with long cycle life and made from low-cost and sustainable materials. Electrochemical capacitors (ECs) and Li-ion batteries (LIBs) are the most widely studied electrochemical energy storage devices during the past few decades. However, since the different energy storage mechanism in ECs and LIBs, they exhibited different performance in terms of energy density and power density. Generally, LIBs exhibit high energy density but low power density owing to the bulk intercalation process. On the contrary, ECs exhibit high power density but low energy density which is limited by the surface charge storage mechanism. To bridge the performance between LIB and ECs, Li-ion capacitors (LICs) have been developed by utilizing a battery-type anode paired with a supercapacitor-type cathode, LICs can combine the advantages from both types of devices and provide high energy and high power simultaneously.

Activated carbon, which has high electrical conductivity and high surface area, has been the most widely used cathode materials, however, the available capacities have been limited within 38-71 mAh/g which significantly limits the energy density of LICs. Thus, the first part of my research focused on the development of high density carbon-based cathodes with enhanced energy storage capability for high energy LICs (for both gravimetric and volumetric performance). To achieve this target, we first investigate the role of oxygen functional groups on graphene for additional Li-ion storage by DFT calculation. Our experimental results also confirm that surface redox-active oxygen

functional groups were introduced on nanocarbon materials, such as graphene and carbon nanotubes. We develop a simple two-step compression and vacuum-drying process for preparing compact graphene films from graphene hydrogels, which show a capacity up to 160 mAh/g and 91.5 Ah/L as capacitive cathodes in Li-ion batteries. Because of the trade-off between redox-active oxygen functional groups and electrical conductivity of reduced graphene oxide, we introduce redox-active organic molecules on the surface of reduced graphene oxide by the π-π interaction. In addition, the redox-active organic molecules are also able to reduce the GO more effectively. The functionalized graphene films deliver a capacity of 165 mAh/g.

Another issue of LIBs is that the electrode materials are mainly from transitional metal elements (Ni, Co, Mn) which are non-sustainable mineral resources and also not environmental-friendly. Organic materials, especially organic carbonyl molecules, which can be directly prepared from natural biomass, have always been considered as promising candidates as sustainable electrodes. In the second part of this thesis, I develop a hydrothermal carbonization process that converts glucose, the most common biomass into redox-active carbonaceous cathodes for Li-ion batteries. These cathodes delivered a capacity of ~210 mAh/g.

Our recent collaboration investigated the Li binding thermodynamics and redox properties of several anthraquinone derivatives. However, since only two carbonyl groups are available for Li ion storage in each molecule, these molecules only show theoretical capacities less than 250 mAh/g. In addition, these small organic molecules are easily dissolved in the organic electrolytes, which significantly limits their cycling stability. Thus, in the final part of my thesis, I investigate the electrochemical properties of

spontaneously polymerized dopamine since its oxidation state, 5,6- indolequinone has similar quinone structure. We fabricate a free-standing electrode by using few-walled carbon nanotubes as a template for the growth of polydopamine. The redox properties of the self-polymerized dopamine are studied by both theoretical and experimental methods. These films show promising performance as organic cathode materials for both Li- and Na-ion batteries. Furthermore, we use graphene oxide as a template and an oxidant for the controlled growth of polydopamine sheet. The higher surface area of graphene oxide is critical for conformal coating of polydopamine on reduced graphene oxide. Compact polydopamine-graphene films are obtained by compressing the 3D-structured aerogels and these films showed enhanced performance in both Li- and Na-ion batteries.

In summary, this dissertation discusses the strategies for enhancing the gravimetric and volumetric performance of capacitive cathode materials for use in hybrid capacitors. Sustainable options for preparing high-performance electrode materials are also discussed by using glucose as an example. What's more, new guidelines for further enhancing the performance are also discussed.

CHAPTER 1. INTRODUCTION

1.1 Motivation

Electrochemical energy storage systems have attracted considerable attention over the past few decades for energy storage, this is because of their short charge/discharge time, high energy storage efficiency, long cycle life, and ease of integration into renewable energy sources.[1, 2] Among these systems, electrochemical capacitors (ECs) and rechargeable batteries are the most widely studied electrochemical energy storage (EES) devices.[1, 3] The ECs and rechargeable batteries have similar structures, which both consist of two electrodes (positive vs. negative or cathode vs anode), a porous polymer film that serves as the separator, which physically separates these two electrodes, and electrolyte. However, the charge storage mechanisms in both devices are different.[4]

Charge is mostly stored on/near the surface of electrodes in ECs, however, ECs can be further divided into two subgroups, which are electrical double layer capacitors (EDLCs) and pseudocapacitors. In EDLCs, charge is mainly stored on the surface of the electrode, during the charge/discharge process, the ions physically absorb or desorb from the surface of the electrodes (**Figure 1.1**a). Thus, the performance of the EDLCs depends on the surface area, pore size, and electrolyte ions.[5-7] High surface area carbon materials, such as activated carbon (ACs),[8-10] carbon nanotubes,[11, 12] and graphene[13-18], have been widely studied as electrode materials in EDLCs. In contrast to EDLCs, pseudocapacitors store charges through faradic processes, which involve fast and reversible surface redox reactions between the electrolyte ions and active materials.

Thus, the surface chemistry of the electrode materials plays a critical role in the performance of the pseudocapacitors. The common active materials include metal oxides, such as manganese oxide,[19, 20] ruthenium oxide[21-23] or conducting polymers such as polyaniline,[24-27] polypyrrole.[22, 28, 29]

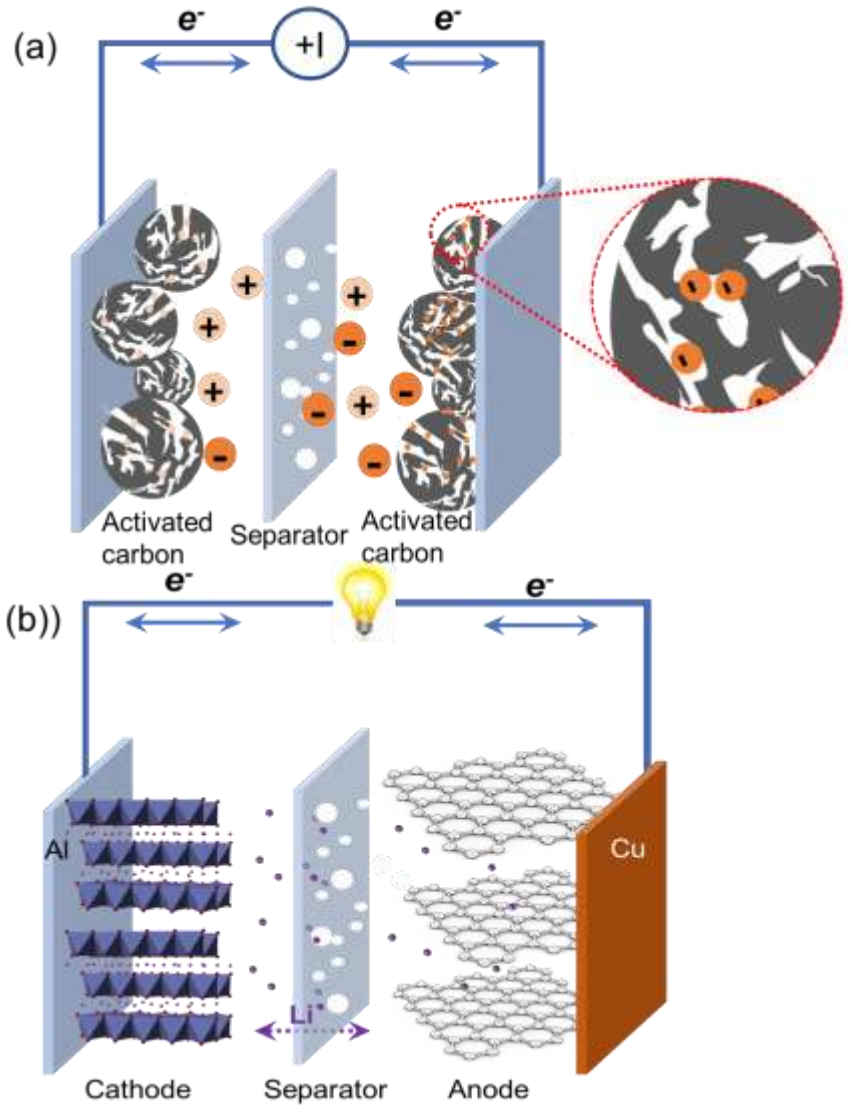

Figure 1.1 Schematic of charging and discharging process in (a) ECs and (b) Li-ion batteries

Comparing to ECs, charges are stored in rechargeable batteries, such as Li-ion batteries, through a bulk process, where Li ions are intercalated/deintercalated from the active materials during the charge/discharge process (**Figure 1.1b**). Thus, the particle size, crystal structure and surface chemistry will be crucial for the performance of the electrode materials. Taking graphite as an example, during the charging process, Li ions will be continuously intercalated between the graphene layers at specific voltages (~ 0.1 V vs. Li), and forming fully lithiated graphite, LiC_6, contributing a theoretical capacity of 372 mAh/g. Based on the reduction potential towards Li, the active materials can be divided into cathode and anodes. Lithium transition metal oxide ($LiCoO_2$, $Li_{1+x}(Ni_{0.33}Co_{0.33}Mn_{0.33})_{1-x}O_2$, $LiNi_{0.8}Co_{0.15}Al_{0.05}O_2$) [30-33] or phosphate materials ($LiFePO_4$)[34, 35] have been the widely studied as the cathode materials, which give specific capacities of 150-300 mAh/g in the high voltage region between 3.5- 4.5 V vs. Li. On the other hand, graphite has been the most widely used anode materials owing to its lower intercalation potential (0.1 V vs. Li) and low cost. However, for achieving higher energy density, other anode materials such as Si,[36, 37] Ge,[38] that can provide much higher capacity are also being actively investigated. Commercial products that use graphite with a small amount of Si as the anode are already available on market.

However, owing to different energy storage mechanisms in ECs and Li-ion batteries, there is a tradeoff between the energy and power densities of these two devices.[39, 40] ECs exhibit high power density because of the surface driven process but suffer from low energy density. State-of-the-art ECs deliver a specific energy of 4-5 Wh/kg.[41] On the other hand, recharge batteries, such as Li-ion batteries (LIB), deliver high energy but suffer from the low power performance that is limited by Li-ions

diffusion in the bulk materials. Ragone plot (**Figure 1.2**) is usually used for evaluating the performance in terms of energy density and power density either based on the mass or the volume of the devices.[4, 42]

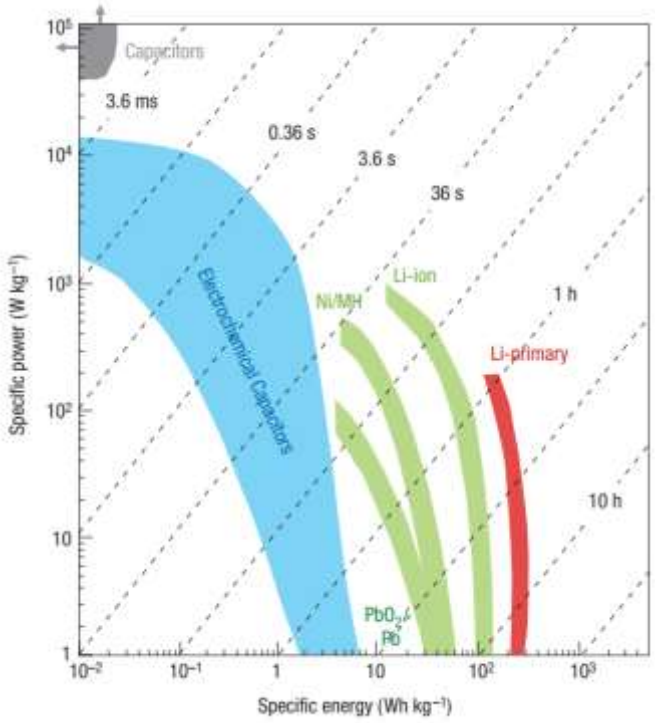

Figure 1.2 A Ragone plot showing the specific power against specific energy for various electrical energy storage devices (Reproduced from Ref #39 copyright (2008), Rights Managed by Nature Publishing Group)

1.2 Li-ion capacitors

Tremendous efforts have been devoted to achieving high-energy and high-power simultaneously in either ECs or batteries. For ECs, enhancing the energy can be achieved by increasing the working voltage window by switching from the aqueous electrolyte into the non-aqueous electrolyte or ionic liquids.[43, 44] For Li-ion batteries, high power density can be achieved through optimizing the structure and particle size of the electrode materials.[33, 45, 46] To further combine the advantages of both devices, scientists have

invented a hybrid capacitor that combines the charge storage mechanisms of ECs and Li-ion batteries.[47-49] In the hybrid capacitor, the capacitive electrode from ECs is working as a cathode, and an anode from Li-ion batteries is working as an intercalation-type anode. The electrolyte used in the hybrid capacitor is the same as that in Li-ion batteries. Thus, the hybrid capacitor can also be called as Li-ion capacitors (**Figure 1.3**). [39, 48, 49]

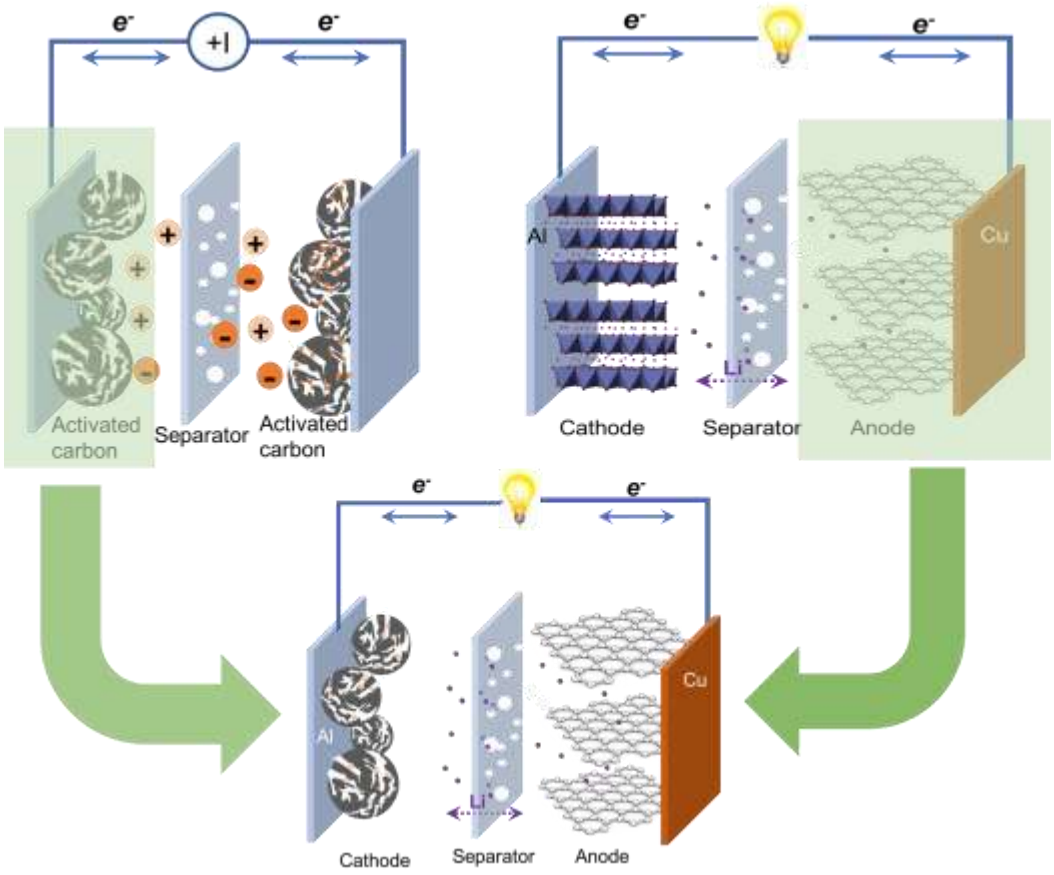

Figure 1.3 The schematic of Li-ion capacitor

In this respect, there have been extensive studies based on this type of hybrid capacitor trying to achieve both battery-level energy density and EC-level power density. In these studies, graphite[50-53] and Li titanium oxide ($Li_4Ti_5O_{12}$)[54-56] have been the

most widely investigated anode materials. For further increasing the energy density, other anode materials are being actively investigated. Recently, M. Cai *et al.* incorporate Si as the anode materials in Li-ion capacitor, which shows a theoretical capacity of 4200 mAh/g. During the charge process, anions (PF_6^-) are absorbed on the surface of the capacitive cathode, while Li^+ inserted into Si.[47] However, the poor performance of the hybrid capacitors is critically limited by the low capacity of capacitive cathodes. Activated carbon (AC) has been the dominant capacitive cathode in hybrid capacitors owing to its good electrical conductivity and high surface area. However, since only electrical double layer capacitance is available in ACs, their capacity is mostly limited between 38-71 mAh/g in the voltage range 3-4.5 V,[57] which significantly limits the energy density of the practical devices. Besides structure optimization, heteroatoms doping (such as B or N) has been one effective method in enhancing the performance of ACs. Recently, Lee *et al* showed the oxygen functional groups on carbon materials (CNTs, and graphene) are redox active towards Li at a voltage ~3.2 V vs. Li.[58, 59] Thus, two charge storage mechanisms, electrical double layer capacitance and pseudocapacitance, are both available in these redox-active carbon electrodes, which opens up new opportunities for design high-performance cathode materials for Li-ion capacitors. In line with this approach, various carbon-based cathode materials have been developed, Lee *et al* used layer-by-layer method developed functionalized multi-walled carbon nanotubes (**Figure 1.4a and b**),[58] carbon nanotube/graphene (**Figure 1.4c and d**),[60] and carbon nanotube/polyaniline electrodes (**Figure 1.4e and f**).[61] Other rapid methods such as spray layer-by-layer[62] and vacuum filtration methods[63] are also used to develop high-performance carbon-based cathodes. The state of the art

performance of the carbon-based cathodes lies in the range of 90-150 mAh/g. Although progress has been made over the past few years, a lack of fundamental understanding of the redox-reactions between oxygen functional groups and Li-ions limits further development of better carbon-based cathode materials.

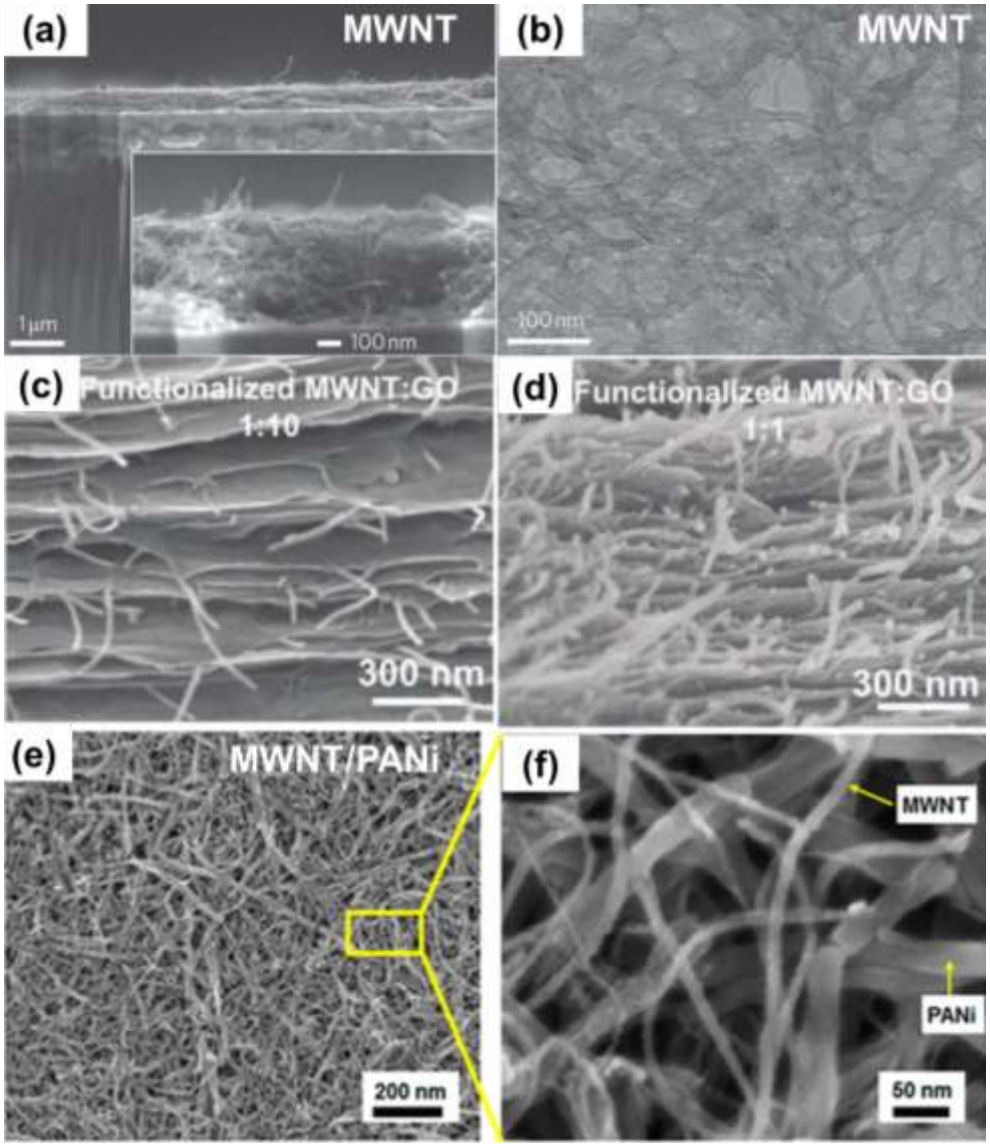

Figure 1.4 Scanning electron microscope images of various carbon-based cathode materials, (a, b) Layer-by-layer multi-walled carbon nanotube (MWNT) films. Adapted with permission from Ref #58. Copyright (2010) Nature Publishing Group. (c, d) MWNT/GO films. Adapted with permission from Ref #60. Copyright (2012) WILEY-VCH Verlag GmbH & Co. KGaA, Weinheim. (e, f) the composite films

consist of PANi and MWNTs. Adapted with permission from Ref #61. Copyright (2014) American Chemical Society.

1.3 Renewable electrode materials

Transition metals such as Co, Mn, or Ni, are critical in commercial rechargeable batteries, but one pitfall of these elements is that they are not renewable, and heavily depends on the limited natural mineral resources. As the demands for batteries grow continuously the sustainable issue of these mineral elements is becoming more and more important. Although efforts have been devoted to recycling the mineral elements in the used batteries, the potential environmental issues should also be considered. In addition, in line with the renewable, clean energy, such as wind, solar, it is highly desirable to investigate the more sustainable or 'greener' electrode materials for future electrochemical energy storage (**Figure 1.5**). [64-66] A growing trend in the scientific community is trying to obtain high-performance electrode materials from earth-abundant biomass.

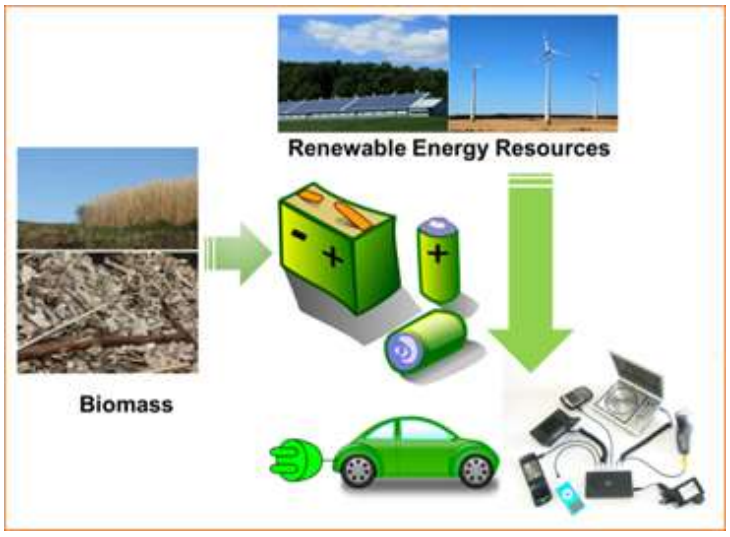

Figure 1.5 Biomass derived 'green' batteries that connect renewable energy resources with end-user applications.

Biomass is cheap and renewable and has received considerable attention over the past few decades. Several methods have been developed to convert this biomass into various types of carbon materials for electrochemical energy storage application. Direct carbonization and hydrothermal carbonization are the most frequently reported methods, scientists have successfully prepared electrode materials from various biomass materials, such as chicken eggshell membranes,[67] peanuts shells,[68] and banana peels.[69] Mitlin *et al.* have demonstrated that by selecting different parts of peanut shells both high-performance cathode and anode materials can be obtained simultaneously.[68] They used the peanut inner part as the precursor for the anode materials due to the homogenous structure composed of lignin, while the outer shell is used for preparing the capacitive cathode materials owing to more heterogeneous but nanoscale periodicity. By coupling the intercalation anode and capacitive cathode, a high-energy Na-ion capacitor has been built. However, as mentioned, these cathode materials are still EDLC-mechanism limited, thus the available capacity will be very limited, other methods which can incorporate redox-active functional groups are highly desirable.

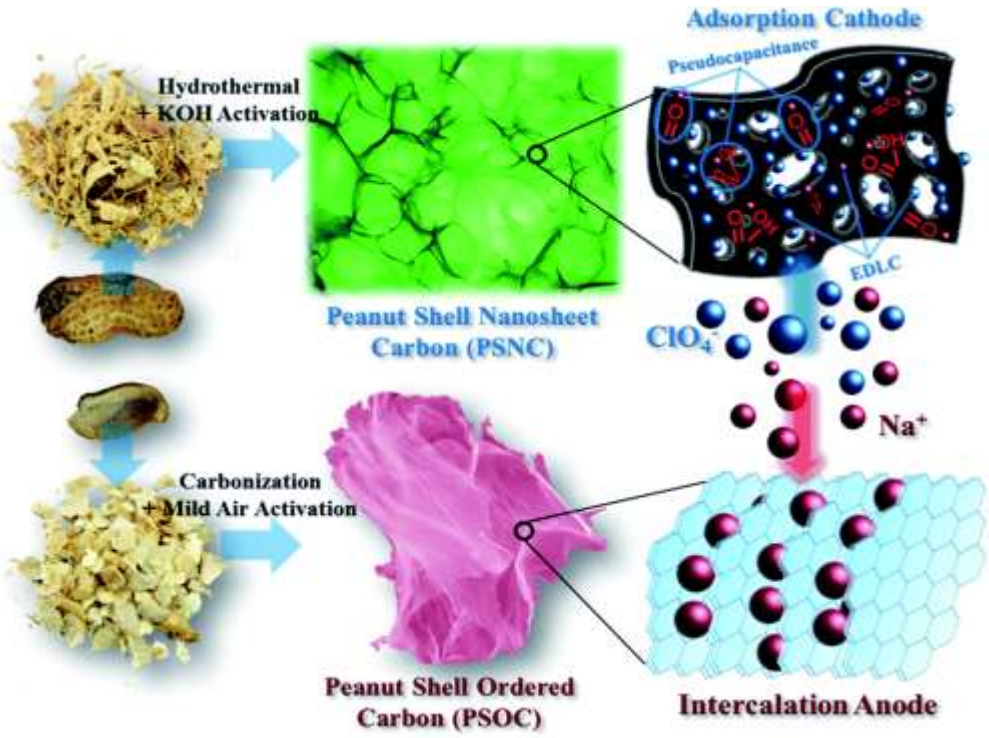

Figure 1.6 Material synthesis process employed for each of the electrodes and the relevant cathode/anode charge storage mechanisms in the hybrid capacitor. Reproduced with permission from Ref #68. Copyright (2014) Royal Society of Chemistry.

1.4 Organic electrode materials

Besides carbon materials, organic materials are also one of the promising products that we can obtain from biomass. Organic materials have been intensively investigated since the invention of Li-ion batteries, this is due to their low cost, high theoretical capacity, structural diversity, and environmental friendliness.[65, 70-73] Over the past few decades, different organic electrode materials have been developed, such as organosulfur compounds,[74, 75] organic free radical compounds,[76, 77] organic carbonyl compounds,[78-83] and conducting polymers. Carbonyl compounds are one of the earliest investigated organic electrode materials.[78-83] The charge storage mechanism in carbonyl based on compounds can be explained by the reversible reactions

between carbonyl groups and Li ions (**Figure 1.7**). Moreover, recently several groups have shown these carbonyl-based compounds can also be used in Na- or Mg-ion batteries following a similar mechanism.

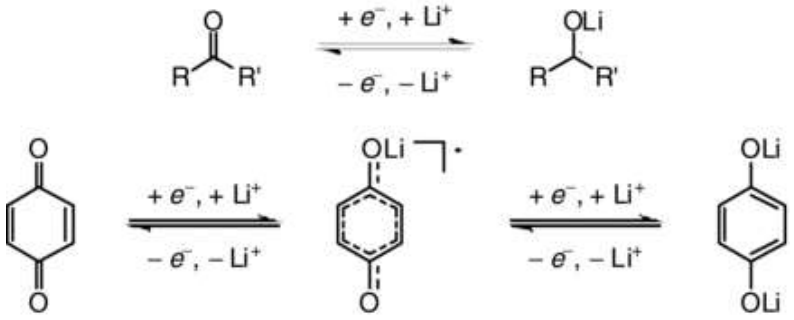

Figure 1.7 Charge storage mechanism for reversible reduction of general carbonyl compounds (up) and quinone (down) in Li-ion batteries. Reproduced with permission from Ref #73. Copyright (2012) WILEY-VCH Verlag GmbH & Co. KGaA, Weinheim

However, most of these small organic molecules are soluble in the organic electrolyte, which results in low cycling stability and low coulombic efficiency. Tremendous efforts have been devoted to enhancing the cycling stability of these organic materials. Polymerization has been the most widely investigated method through which the soluble small molecules are polymerized into insoluble polymers or oligomers. Song et al. have successfully synthesized lithium salt of poly(2,5-dihydroxy-p-benzoquinonyl sulfide),[84] poly (benzoquinonyl sulfide),[85] and poly(anthraquinonyl sulfide)[86] *via* the polycondensation reactions between aromatic halide and sodium (lithium) sulfide (**Figure 1.8a**), showing significantly enhanced cycling stabilities. However, during this process, the linkage groups, such as -S-, decrease the theoretical capacity of the final polymers. Thus, Song *et al.* improved the polymerization process and synthesized poly(1,4-anthraquinone) and poly(1,5-anthraquinone) through an organometallic

dehalogenation polycondensation method (**Figure 1.8b**).[87] Considering the complicated polymerization process, several other simple methods have been proposed, such as immobilization of molecules on the surface of carbon materials,[88] or using Li-ion-selective membrane as the separator,[89] which also alleviates the dissolution issue of these organic active materials. Another issue limiting the wide application of organic electrode materials is their poor electrical conductivity, which significantly limits their rate performance. A growing trend, which attempts to coat the organic active materials on the surface of highly conductive carbon nanomaterials, has received considerable attention. Wang *et al.* successfully coated the poly(anthraquinonyl sulfide) and polyimide on the surface of graphene sheets showing a significantly enhanced rate performance up to 100C (**Figure 1.9a and b**).[90] Wei *et al*, used flexible single-walled carbon nanotube films as the substrates for the growth of polyimide and fabricated flexible composite films which showed enhanced rate performance. [91, 92]

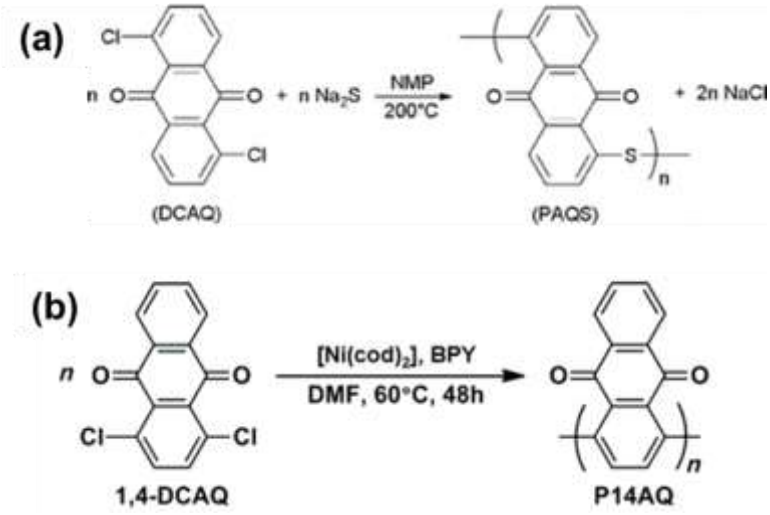

Figure 1.8 Synthetic route of (a) poly(anthraquinonyl sulfide). Adapted with permission from Ref #86. Copyright (2008) Royal Society of Chemistry, and (b)

poly(1,4-anthraquinone). Adapted with permission from Ref #85. Copyright (2015) WILEY-VCH Verlag GmbH & Co. KGaA, Weinheim

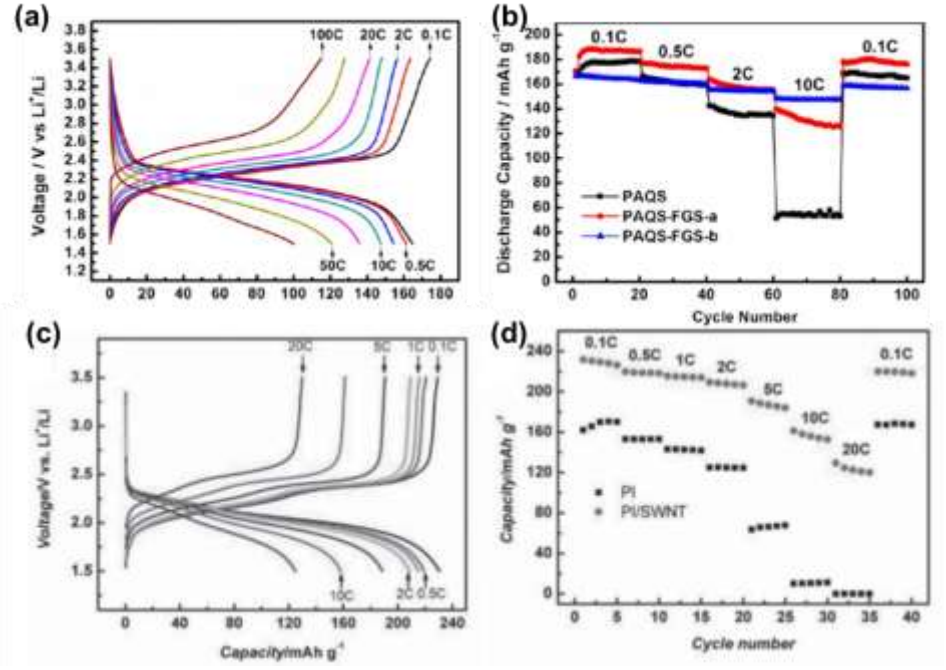

Figure 1.9 (a) Galvanostatic charge/discharge profiles of PAQS-FGS-b, (b) Rate performance of pristine poly(anthraquinonyl sulfide), and poly(anthraquinonyl sulfide)/graphene composites. Adapted with permission from Ref #90. Copyright (2012) American Chemical Society (c) Galvanostatic charge/discharge profiles of polyimide/SWNT, (d) Rate performance of pristine polyimide and polyimide/SWNT at different current rates. Adapted with permission from Ref #92. Copyright (2014) WILEY-VCH Verlag GmbH & Co. KGaA, Weinheim

1.5 Chapter Organization

In **Chapter 2**, the reduced graphene oxide is used as a cathode material for lithium-ion energy storage. Firstly, the redox reactions between surface oxygen functional groups on reduced graphene oxide and Li-ions are confirmed by both density functional theory (DFT) calculations and electrochemical measurements at a high voltage of ~3 V vs. Li. The DFT results reveal the carbonyl and epoxide groups are the main contributor to these redox reactions. In addition, a two-step compression process is

developed for fabricating highly compact reduced graphene oxide films from reduced graphene hydrogels. These films show advantages in high Li-ion energy storage within a confined mass and volume with a density of ~0.64 g/cm^3, showing a capacity of 160 mAh/g and 91.5 Ah/L as capacitive cathodes in Li-ion batteries, which indicating these films as promising positive electrodes for Li-ion batteries.

In **Chapter 3**, tetrahydroxyl-1,4-benzoquinone (THQ) is used as both chemical reductant for efficiently reducing graphene oxide at low temperature and redox-active molecules for functionalization of reduced graphene oxide. By controlling the loading amount of THQ molecules, the oxygen ratio in the final graphene hydrogels can be easily tuned. The electrochemical performance of the electrode is correlated with surface oxygen chemistry. By optimizing the loading amount of THQ, we show that the functionalized graphene electrodes exhibit high capacities of ~165 mA h/g in Li cells and ~120 mA h/g in Na cells, opening a new opportunity to further improve the performance of these carbon-based cathode materials

In **Chapter 4**, recent results in biomass materials derived carbonaceous electrode materials for Li-ion batteries are discussed. The earth-abundant glucose is converted into redox-active carbon spheres through a hydrothermal carbonization process. The electrochemical measurements show that these carbon spheres (CS) exhibit a specific capacity of ~210 mAh/g_{CS}, with high redox potentials in the voltage range of 2.2–3.7 V *vs.* Li. Few walled carbon nanotubes are used as the internal current collectors for fabricating free-standing films that can be directly used as cathodes in Li-ion batteries. These films deliver high specific capacities, up to ~155 mAh/g based on the total mass of

electrodes. I believe this method opens up a green and sustainable process for designing promising cathode materials for lithium-ion batteries or capacitors.

Chapter 5 covers the research related with organic/polymer-based electrode materials, which also mainly consist of carbon and oxygen, but show advantages in high theoretical capacity and low cost. Dopamine can be easily self-polymerized as a versatile coating material on any object. In this study, the redox properties of dopamine are studied by both density functional theory (DFT) calculations and electrochemical measurements, revealing the multiple redox reactions between self-polymerized dopamine and electrolyte ions in the high voltage region from 2.5 to 4.1 V *vs.* Li. By coating polydopamine on the outer surface of few-walled carbon nanotube, free-standing and flexible hybrid films are fabricated by a simple vacuum filtration process. These films exhibit high specific capacities of ~133 mA h g^{-1} in Li-cells and ~109 mA h g^{-1} in Na-cells based on the total mass of electrodes. Furthermore, the capacity contribution from polydopamine is estimated by using the rule of mixture, polydopamine itself can deliver high gravimetric capacities of ~235 mAh/g in Li-cells and ~213 mAh/g in Na-cells.

In **Chapter 6**, the polydopamine-based electrode materials are further optimized. In **Chapter 5**, dopamine is oxidized by the dissolved oxygen in the aqueous solution, which proves to be a low efficiency polymerization process. In this chapter, graphene oxide is used as both an oxidant and template for high efficient conformal coating of polydopamine on the surface of reduced graphene oxide. Highly compact films are fabricated by compressing the polydopamine coated graphene aerogels and directly used as cathodes in both Li- and Na-ion cells. The compact films deliver high capacities of ~230 mAh/g in Li cells and ~211 mAh/g in Na cells based on the total mass of electrodes.

In **Chapter 7**, a summary and suggestions for future technical work are provided.

CHAPTER 2. HIGH-DENSITY LITHIUM-ION ENERGY STORAGE UTILIZING THE SURFACE REDOX REACTIONS IN FOLDED GRAPHENE FILMS

2.1 Introduction

The ever increasing demand for the portable electronic devices and electric vehicles has been urging the development of low-cost, sustainable, and high-performance energy storage devices, having both high energy and power density along with stable cycling performance.[1, 93, 94] Recently, graphene based energy storage devices, including electrochemical capacitors (ECs)[14, 18, 95-100] and Li-ion batteries,[90, 101-104] have been intenstively explored owing to its unique physical and chemical properties, such as high electrical conductivity and high surface area.[105-108] In addition, the scalable synthetic route of graphene from GO, which can be simply prepared from graphite by the modified Hummer's method,[109, 110] has accelerated the development of graphene based electrode materials. To maximize the electrochemically active surface area as well as facilitate electrolyte ion diffusion, nanostructured 3D graphene electrodes have been assembled for advanced EC applications using various fabrication methods, including chemical vapor deposition,[111] laser-scribing,[98] self-

assembly,[15, 112, 113] freeze-casting[114] and the template method.[96] Although these 3D graphene nanostructured electrodes have significantly increased energy and power density per unit mass of the electrode, they generally have low packing densities due to their well-developed open pores, limiting the volumetric energy density. The open pores within the 3D graphene electrodes are flooded with electrolytes, eventually leading to a low gravimetric and volumetric performance in a real device, when the weight of electrolyte is considered.[42] Thus, recent efforts on graphene electrodes have been focused on increasing the packing density using various fabrication methods, including electrolyte mediated densification of films[16] and evaporation-induced drying of 3D graphene assembly,[13, 99] which can significantly enhance the volumetric capacitance for EC applications.

These carbon based ECs, which store charge by a surface adsorption process of electrolyte ions, are classfied as EDLCs. These EDLCs can deliver high power density owing to their rapid charge storage mechanism. However, their energy density is significantly limited compared to that of rechargeable batteries based on redox (Faradaic) reactions of electrode materials. Recent studies have shown that oxygen functionalized nanocarbons, including CNTs and reduced GOs, can enhance the energy density of the carbon electrodes by employing the surface redox reactions beween oxygen groups and Li ions.[58-60] Since these surface redox reactions are centered at high potential regions of ~3 V vs. Li, these functionalized carbon electrodes have been employed as positive electrodes for high-power Li-ion batteries or Li-ion capacitors.[58, 62, 63, 115, 116] However, the clear charge storage mechanism of these functionalized nanocarbons remains unanswered since various oxygen functional groups, such as carbonyl, epoxide,

hydroxyl, and carboxylic acid, may play different roles for the redox reactions with Li ions. Thus, understanding different roles of the various oxygen functional groups is crucial for identifying specific oxygen chemistries with high redox potentials.

In this study, we demonstrated a simple synthesis of reduced GO electrodes, which can deliver both high gravimetric and volumetric energy density with exceptional cycling stability in Li-cells, by the effective utilization of surface redox reactions of oxygen functional groups. Additive-free, free-standing, high-density, redox-active graphene electrodes were fabricated by compressing and subsequent vacuum-drying process of the hydrothermally reduced graphene hydrogel. The fabricated graphene electrodes displayed a folded micro-structure due to the anisotropic capillary force during the vacuum-drying process of the compressed film, which can increase their density up to ~0.64 g/cm^3. In addition, the surface oxygen chemistry and corresponding redox reactions were controlled by the hydrothermal reduction temperature. The folded graphene film (*f*-GF) electrodes delivered both high gravimetric and volumetric capacities up to ~160 mAh/g and 91.5 Ah/L, respectively. When *f*-GFs were employed as positive electrodes with Li metal negative electrodes, they exhibited a gravimetric energy density up to ~419 Wh/kg and a volumetric energy density up to ~239 Wh/L. In addition, a high gravimetric capacity of ~160 mAh/g was maintained over 50,000 cycles with a coulombic efficiency close to ~100%. More importantly, we demonstrated for the first time a correlation between the redox potential of various oxygen functional groups on the graphene with their local oxygen chemistries, using First-Principles DFT modeling. Based on the DFT calculation, we revealed that surface carbonyl and epoxide groups are responsible for high-potential surface reactions in the range of 2~3 V vs. Li.

2.2 Experimental

Sample preparation: Folded graphene film electrodes: GO was synthesized by the modified Hummer's method[110] (the detailed process can be found in previous works[60, 95]). The 3D Graphene hydrogel was prepared using the hydrothermal reduction method based on a previous report.[117] 1 mg/mL of GO dispersion was sonicated for 1 h by a bath sonicator (Branson, Bransonic). Next, the GO dispersion was sealed in a Teflon-lined autoclave and was maintained at high temperatures (130~230 °C) for 6 h. After a waiting period, the autoclave was naturally cooled down to room temperature, and the assembled graphene hydrogel was taken out with a tweezer. To prepare a pressed graphene film, a small piece of graphene hydrogel was cut and pressed into a film by 5 MPa for 15 s. The pressed films were dried in vacuum oven overnight at 70 °C, yielding the fabricated folded graphene films (*f*-GFs). The thickness of the final film was controlled in the range of 30-50 μm. The mass loading of the *f*-GF-130 °C and *f*-GF-180 °C were 1.7 mg/cm^2 and 2.2 mg/cm^2, respectively. ***3D-graphene electrodes*:** Graphene hydrogel assembly was dried using a freeze-dryer at -84 ^{o}C (FreeZone Plus 2.5 Liter Cascade Benchtop Freeze Dry System) for 24 h to maintain the 3D structure. The dried electrode was pressed into a film gently by hand in order to improve the electrical contact between the electrode and the current collector. The density of the electrode was ~0.17 g/cm^3. ***GO-film electrodes*:** GO-film electrodes were prepared by a vacuum-filtration process on a filtration membrane with 0.1 μm pore size and 47 mm diameter (PC, Whatman).[115] The thickness of the GO-film electrodes was ~10 μm after the drying process.

Characterization: The microstructure and morphology of the electrode were investigated using a SEM (Hitachi SU8010, operated at 3 kV). The elemental analysis of the electrodes was charcterized by XPS (Thermal Scientific K-alpha XPS instrument), and the high-resolution C1s peaks were fitted by the XPSPEAKS 4.1. XRD patterns were measured by XPert Pro Alpha-1 using Cu K-α1 X-rays.

Electrochemical measurements: The *f*-GFs were used as the positive electrodes in Swagelok-type electrochemical cells, pieces of Li foils were used as the negative electrodes. Two pieces of Celgard 2500 separators were placed between the negative and positive electrodes. The electrolyte was 1 M $LiPF_6$ in a mixture of EC and DMC (3:7 volume ratio, BASF). The cells were assembled in an Argon-filled glovebox (MBraun O_2<0.1 ppm; H_2O<0.1 ppm). The electrochemical performance of the Li-cells was measured by Bio-Logic VMP3 potentiostat/galvanostat in the voltage range of 1.5-4.5 V vs. Li at room temperature. The cells were charged or discharged at different galvanostatic current densities ranging from 0.05 to 50 A/g, and at the end of the charging/discharging process, the cell voltage was held constant for 30 min at either 4.5 or 1.5 V vs. Li, respectively. The Li cells were tested by an accelerated galvanostatic cycling method, that is, the cells were charged/discharged at 0.1 A/g for one cycle, and every 99 cycles at 10 A/g, up to 10,000 cycles. Cell voltage holding stage was also applied for 30 min at 1.5 V or 4.5 V vs. Li prior to low-rate charge or discharge, respectively. For cycle numbers between 10,000 and 50,000, 499 accelerated cycles were performed at every slower charge/discharge cycle, while other prarameters were kept the same within the first 10,000 cycles.

Specific energy densities (E) and specific power densities (P) in the Ragone plot were evaluated by using the below equations.[118] Only positive electrode weight was considered in the specific energy and power density calculations.

$$E = \int_0^{\tau} V(t) i dt \quad (1)$$

Where V is the voltage of the cell, τ is the total discharge time when the gravimetric current density is *i*.

$$P = \frac{E}{\tau} \quad (2)$$

Where τ is the total discharge time at a given gravimetric current density.

Redox potential calculations: All of the calculations were performed by using the Jaguar software with a 6-31G+(d,p) basis set.[119] Both the PBE0 and PWB6K levels of theory were chosen to compute the optimized geometries of the pristine graphene and the oxygen functional groups on the graphene. The vibrational frequency calculations, with the same levels of theory and basis set, were further computed to evaluate the Gibbs free energies at 298 K in the gas phase. The solvation free energy calculations were computed using Poisson-Boltman implicit solvation model to approximate the solvation contributions to the free energies. A dielectric constant of 16.14, which reliably describes the polarity of the solvent in our systems, was used for the solvation free energy calculations.

A pristine graphene sheet consisting of 54 carbon atoms and 18 terminal hydrogen atoms was prepared for the calculations. Various GO sheets were prepared separately by incorporating the oxygen functional groups (*i.e.*, carbonyl, epoxide, hydroxyl, and carboyxlic acid), either on the center or at the edge of the pristine graphene sheet to mimic the experimentally observed oxide environment.[106, 107] The effect of the oxygen functional group density on the redox potentials was considered by incorporating two identical oxygen functional groups on the graphene. The thermodynamic cycle which was used to predict the redox potentials of the pristine graphene and the oxygen functional groups on the graphene is described elsewhere.[120, 121] The redox potential (ΔE^{red}) of an active electrode material in solution with respect to a Li/Li^+ reference electrode can be predicted by Equation 3 as,

$$\Delta E^{red} = \frac{-\Delta G^{soln}}{nF} - 1.44V \quad (3)$$

where, ΔG^{soln} is the difference in the Gibbs free energy in solution during the reduction, *n* is the number of electrons transferred, and *F* is the Faraday constant. The constant, 1.44 V, indicates the redox potential of the Li/Li^+ reference electrode. The HOMO-LUMO energy levels of the active electrode materials were also computed to rationalize the predicted redox potentials.

2.3 Results and Discussions

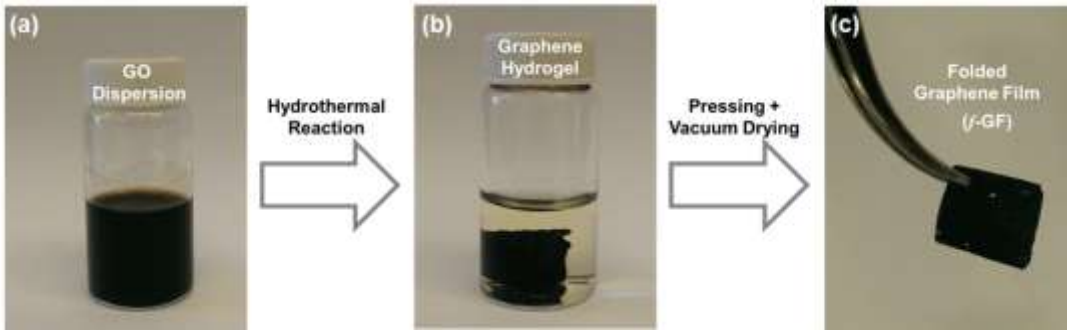

Figure 2.1 (a) The fabrication process of the folded graphene films from the dispersion of GO in water (1 mg/mL) via hydrothermal reaction at 180 °C for 6 h (*f*-GF-180 °C) and subsequent compressing and vacuum drying process at 70 °C.

Graphene hydrogel was obtained from the dispersion of GO in water (1 mg/mL) *via* a hydrothermal reduction process at 180 °C for 6 h (**Figure 2.1a, b**).[117] The reduction process of GO was induced by superheated water in hydrothermal condition, where the generated H^+ ions from the superheated water can reduce the oxygen functional groups on the GO.[122] As the GO sheets lose the oxygen functional groups, they tend to interact with each other through the combination of hydrophobic and π-π interactions.[113, 117] If the concentration of GO is high enough (typically higher than 1 mg/mL), the 3D structured graphene hydrogel can be assembled without using any chemical reducing agents.[123, 124] Since the most widely used reducing agents, such as hydrazine[125, 126] and hydroiodic acid (HI)[127], are toxic, the hydrothermal reduction process can represent a green reduction route to fabricate 3D reduced GO assembly.[117, 122]

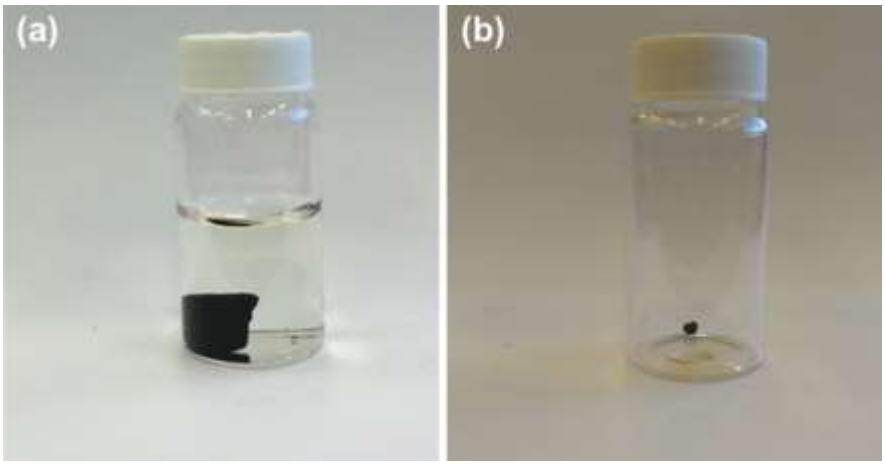

Figure 2.2 Digital images of (a) the as prepared graphene hydrogel from the dispersion of GO in water (1 mg/mL) *via* hydrothermal reaction at 180 °C for 6 h and (b) the directly vacuum dried graphene hydrogel at 70 °C overnight without the pressing process.

Since the assembled reduced GO hydrogel usually consists of over 90% water, the hydrogel needs to be fully dried for non-aqueous electrolyte based energy storage applications. However, if the hydrogel is directly dried using the conventional vacuum-drying process at high temperatures, the hydrogel would shrink into a small aggregate by capillary compressible forces during the evaporation of the water within the pores. **Figure 2.2** shows the small aggregate after the vacuum-drying process at 70 ^{0}C overnight, at which point it is too brittle for assembly as an electrode in the Li-cells. To preserve the 3D structure of the graphene assembly, freeze drying or critical point drying methods are generally used.[18, 100, 112, 124, 128] The freeze-dried 3D graphene assembly has a hierarchical porous structure with the pore sizes of up to tens of micrometers (**Figure 2.3a**), with a very low packing density (~0.02 g/cm^3).[99] Although the hierarchical porous structure of the 3D graphene assembly is beneficial for fast diffusion of electrolytes—for electrochemical energy storage—the low density of the electrode significantly decreases its volumetric energy density.[13, 16, 42] In addition,

the large pore volume in the 3D graphene assembly consumes a large amount of electrolyte, decreasing the gravimetric performance of real devices taking the weight of the electrolyte into account.[42]

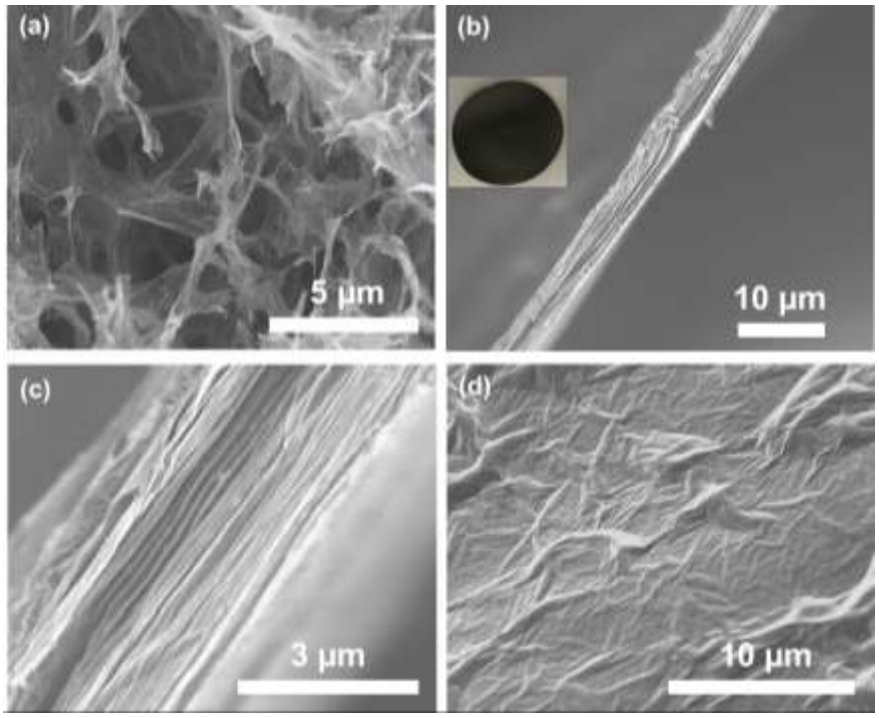

Figure 2.3 SEM images of (a) the 3D-graphene obtained by freeze-drying process of the graphene hydrogel. (b, c) cross-sectional view and (d) top-view SEM images of the pristine GO-film obtained by a vacuum-filtration process. The digital image of the GO-film is shown as an inset in (b).

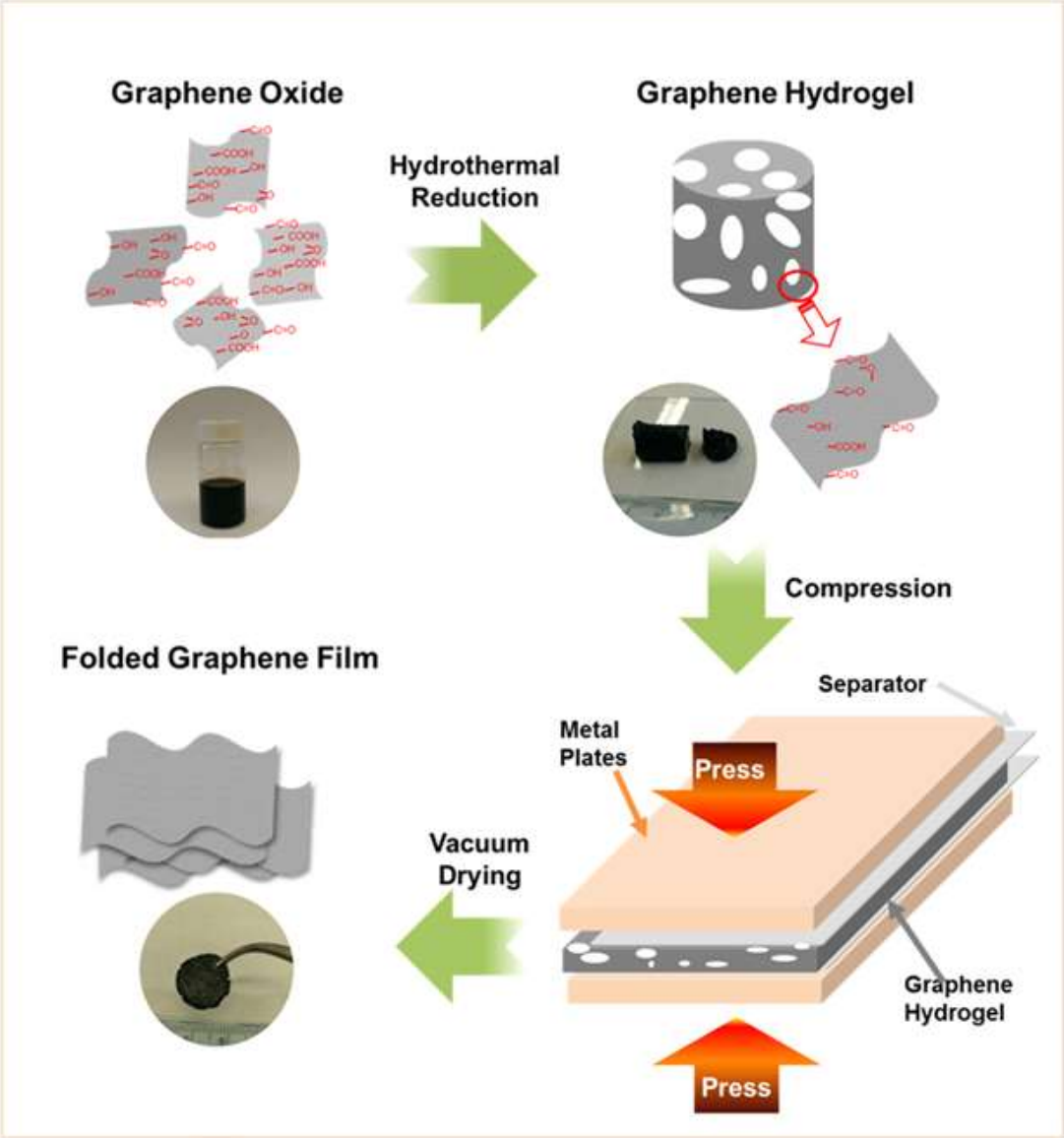

Figure 2.4 The schematic procedure for the preparation of the folded graphene film (*f*-GF) from the dispersion of GO in water. Graphene hydrogel was assembled from the GO dispersion via a hydrothermal reduction process, and a piece of the graphene hydrogel was cut and pressed between two separators. The pressed graphene hydrogel was dried in the vacuum oven at 70 ºC overnight, obtaining the *f*-GF electrode. The ~260 μm thick *f*-GF film was obtained after a compression and vacuum drying process of a ~1 cm thick graphene hydrogel. The ratio of the film thickness changes before and after the compression and vacuum drying process is about 38:1.

To increase the packing density as well as preserve pore interconnectivity of the graphene electrode, we developed a simple two-step electrode fabrication process based

on compression and a subsequent vacuum drying process, resulting in free-standing, high-density, folded graphene films (*f*-GFs) (**Figure 2.4**). This process was inspired by the drying process of 2D graphene films, in which, great shrinkage exists mainly in the vertical direction, with small shrinkage in the lateral direction.[129] A piece of graphene hydrogel was cut and pressed into a thin film between two pieces of separator material, and subsequently dried in vacuum oven at 70 ^{0}C overnight. After the drying process, a free-standing *f*-GF was obtained, and the thickness of the film controlled in a range of 30-50 μm (**Figure 2.1c**). The density of the *f*-GFs was in the range of 0.44-0.64 g/cm^3, which is significantly higher than that of the freeze-dried 3D graphene assembly at ~0.02 g/cm^3, but lower than that of the GO-films obtained by a vacuum-filtration process at ~1.4 g/cm^3.[99]

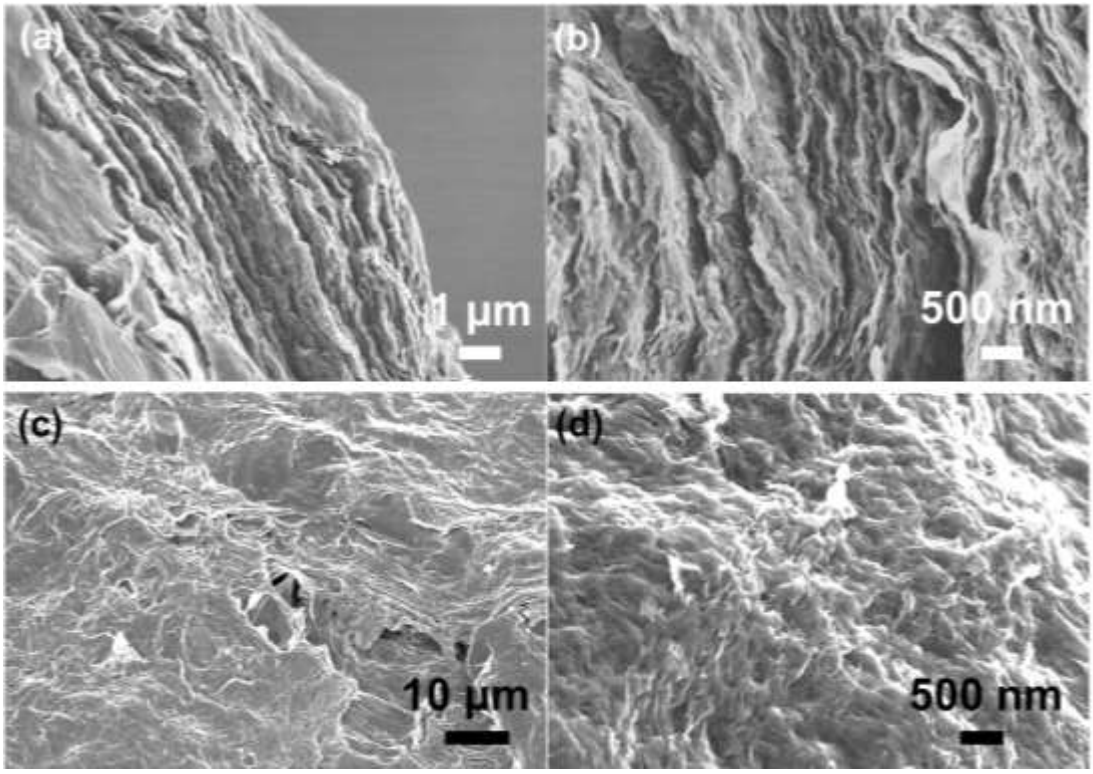

Figure 2.5 SEM (a, b) cross-section view and (c, d) top view images of the folded graphene film (*f*-GF-180 °C).

The microstructure of the *f*-GFs was investigated by SEM analysis (**Figure 2.5**). The *f*-GFs have a laterally developed pore structure between the corrugated reduced GO sheets (SEM cross-section images, **Figure 2.5a, b**). The scale of the horizontally developed pores of the *f*-GF is much smaller compared to the hierarchically developed micro-pores of the freeze-dried 3D-graphene assembly (**Figure 2.3a**), but lager than that of the compactly packed GO-films (**Figure 2.3b-c**). In addition, the surface morphology of the *f*-GFs show a rougher structure-characterized by sporadic vertical holes throughout the graphene sheets (SEM top-view images, **Figure 2.5c-d**)-in contrast to the much flatter surface of the GO-films obtained via the vacuum-filtration process **Figure 2.3d**). The structural characteristic of the *f*-GFs can be attributed to the anisotropic compression applied during the fabrication process. Since the graphene hydrogel was compressed before the drying process, most of the capillary force existed in the vertical direction. This anisotropic compression can drive the horizontally aligned graphene layers closer, while the vertically aligned graphene layers are folded between those that are horizontally aligned, resulting in a horizontally developed yet vertically interconnected porous structure within the *f*-GFs. The high packing density of the resulting *f*-GFs can yield high volumetric performances of the electrodes, whereas the interconnected porous structure can still support fast ion diffusion for electrochemical charge storage.

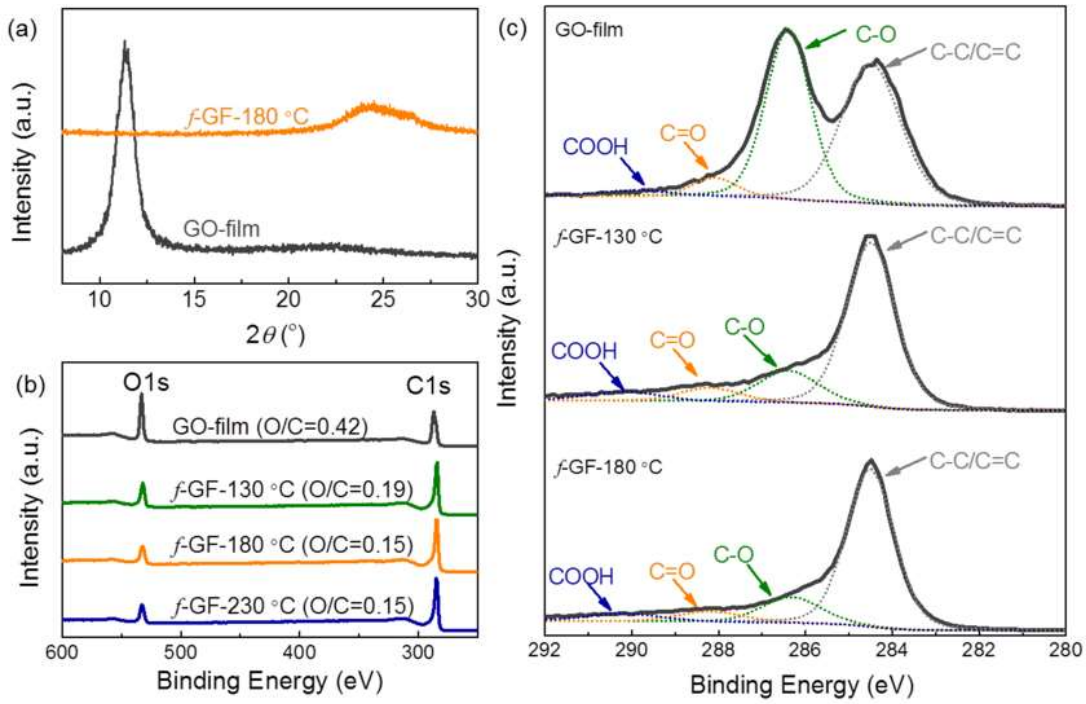

Figure 2.6 (a) XRD spectra of the GO-film and the *f*-GF-180 °C. (b) XPS wide scan survey of the GO-film and the folded graphene films (*f*-GF) obtained at different hydrothermal reaction temperatures. (c) High-resolution XPS C1s spectra of the GO-film (top), *f*-GF-130 °C (center), and *f*-GF-180 °C (bottom).

The XRD pattern of the GO film displayed a sharp peak at 2θ = 11.10° with an interlayer distance of 7.96 Å, which is usually observed in layered GO films,[127, 130] indicative of strong ordering in the thickness direction (**Figure 2.6a**). On the other hand, the XRD pattern of the *f*-GFs that was obtained at 180 °C (*f*-GF-180 °C) showed a much broader peak around 25°, which corresponds to an interlayer distance of 3.56 Å (**Figure 2.6a**). This broader peak with a decreased interlayer distance can be attributed to the less ordered porous structure, given by the compactly packed reduced graphene sheets.

The reduction process of GO during the hydrothermal reaction was confirmed by XPS measurements (**Figure 2.6b, c**). The atomic ratios of oxygen to carbon (O/C) of the GO-film and *f*-GFs obtained at different hydrothermal reaction temperatures were

compared using XPS wide scan survey (**Figure 2.6b**). The O/C ratios significantly decreased from 0.42 for the GO-film to 0.19 for *f*-GF prepared by hydrothermal reaction at 130 °C (*f*-GF-130 °C), and further decreased to 0.15 for *f*-GF obtained at higher reaction temperatures (both *f*-GF-180 °C and *f*-GF-230 °C), which confirmed an effective reduction process of GO during the hydrothermal reduction process. The detailed surface chemistry of the GO-film and *f*-GFs was investigated using high-resolution XPS C1s spectra (**Figure 2.6c**). The C1s spectra can be fitted into four different peaks: the peak centered at 284.5 eV for sp^2-hybridized graphitic carbon (C-C/C=C), 286.4 ± 0.1 eV for hydroxyl or epoxide groups (C-O), 288.2 ± 0.1 eV for carbonyl group (C=O), and 290.2 ± 0.1 eV for carboxylic group (COOH), respectively.[107, 127] Comparison of the C1s spectra of the GO-film and the *f*-GF-130 °C clearly shows a significant reduction of hydroxyls and epoxide groups (C-O) and a partial decrease of carbonyl and carboxylic groups (C=O and COOH) with concomitant recovery of the conjugated carbon (C-C/C=C) during the reduction process. Consistent with the trend of the O/C ratio, oxygen functional groups further decreased for the *f*-GF-180 °C obtained with a higher reduction temperature of 180 °C.

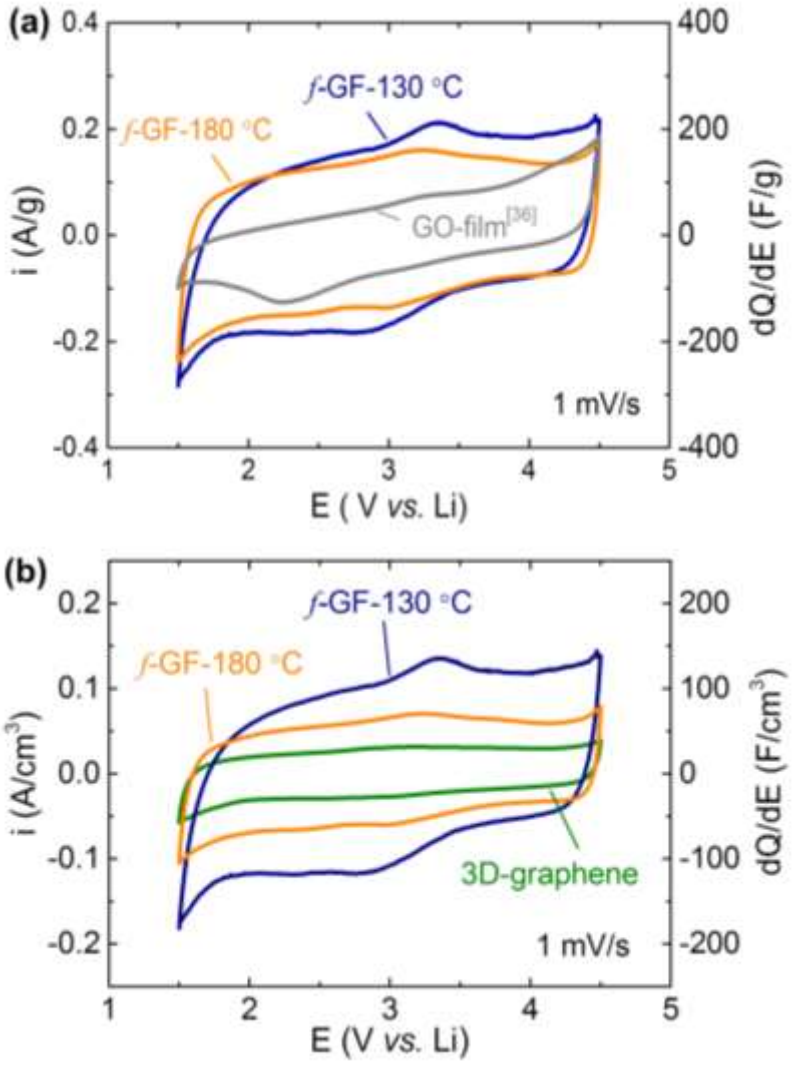

Figure 2.7 CV scans based on (a) gravimetric and (b) volumetric current for different electrodes at 1 mV/s between 1.5 to 4.5 vs. Li in 1 M $LiPF_6$ in a mixture of EC and DMC (3:7 volume ratio).

Charge storage characteristics of the *f*-GF electrodes were evaluated using CV scans in the Li-cells (**Figure 2.7a and b**). The *f*-GF electrodes exhibited much higher gravimetric currents than that of the GO-film prepared through a vacuum-filtration process. Despite its high O/C ratio of 0.42, the GO-film showed smaller current density with weak redox peaks due to the limitations of electron or ion transport through the film. The transport resistance of the GO-film can be attributed to the low electronic

conductivity[115] and limited accessibility of electrolyte ion into the inner space of the layered GO sheets (**Figure 2.3b-c**). On the other hand, the *f*-GF-130 °C electrode showed a significant increase in gravimetric current with strong redox peaks owing to the recovery of electronic conductivity during the reduction process, and the increased electrochemically active surface within the interconnected porous structure (**Figure 2.5a-d**), which can effectively support the redox reactions between the oxygen functional groups and Li ions.[60] The *f*-GF-180 °C electrode showed a slightly decreased gravimetric current compared to that of the *f*-GF-130 °C, indicating a reduction in redox-active oxygen functional groups during the higher temperature reduction process.

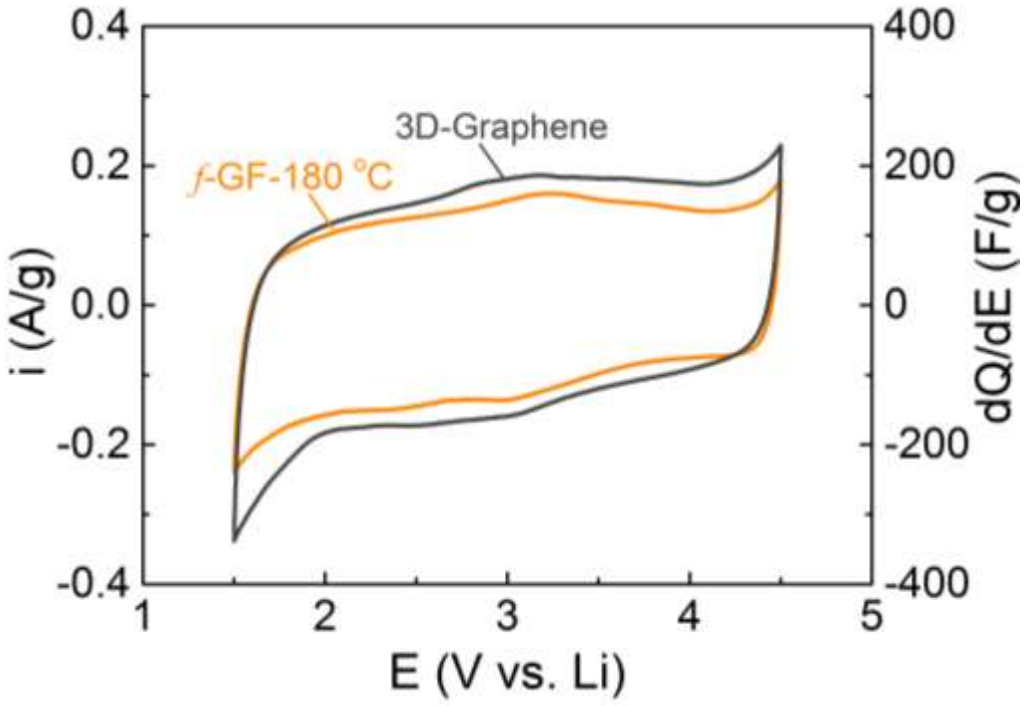

Figure 2.8 Comparison of the steady-state CV scans of the *f*-GF-180 °C and the freeze-dried 3D-graphene electrodes. CV scans were obtained at 1 mV/s between 1.5 to 4.5 vs. Li in 1 M $LiPF_6$ in a mixture of EC and DMC (3:7 volume ratio).

In addition, galvanostatic and volumetric currents of the *f*-GF electrodes were compared with the freeze-dried 3D graphene assembly (3D-graphene, **Figure 2.8**). The 3D-graphene electrode was gently pressed into a film with a density of 0.17 g/cm^3 in order to improve the electrical contact between the electrode and the current collector. Comparing with the freeze-dried 3D graphene, the *f*-GF electrode retained ~80% of the gravimetric capacitance (**Figure 2.8**), indicating that only ~20% of the electrochemical active surface area was decreased during the two-step compression and vacuum drying process. However, the *f*-GF electrodes showed a much higher volumetric current than the 3D-graphene electrode, owing to their high packing density of 0.44~0.64 g/cm^3. The *f*-GF-130 °C electrode exhibited the highest volumetric current because of the higher packing density of 0.64 g/cm^3 and the atomic O/C ratio of 0.19 compared to those (packing density=0.44 g/cm^3, O/C=0.15) of the *f*-GF-180 °C.

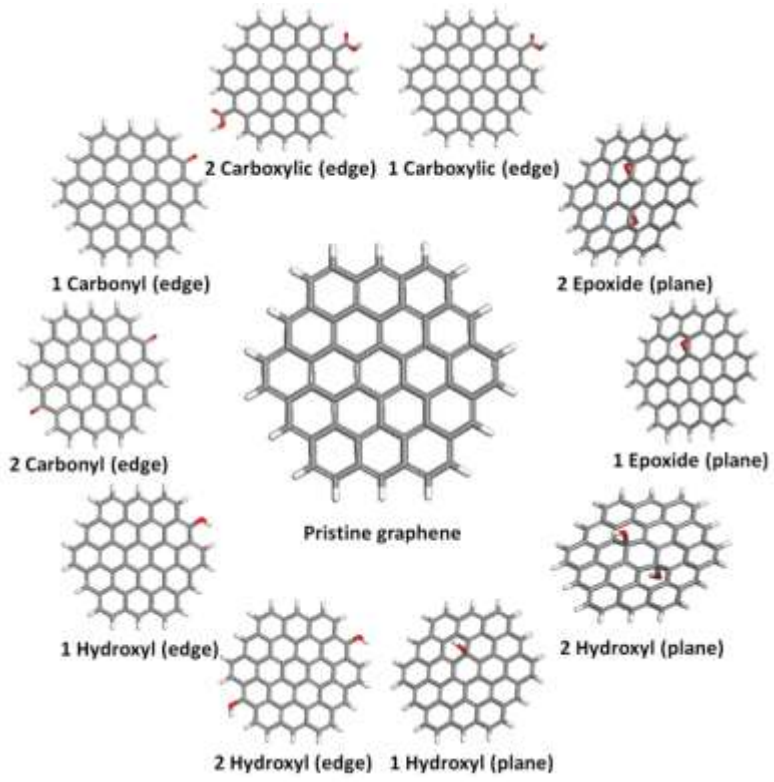

Figure 2.9 The chemical structures of four pairs of the feasible oxygen functional group cases incorporated either on the plane or edge of a pristine graphene. Either one or two identical oxygen functional groups were incorporated for each case. The grey, white, and red colors represent carbon, hydrogen, and oxygen, respectively.

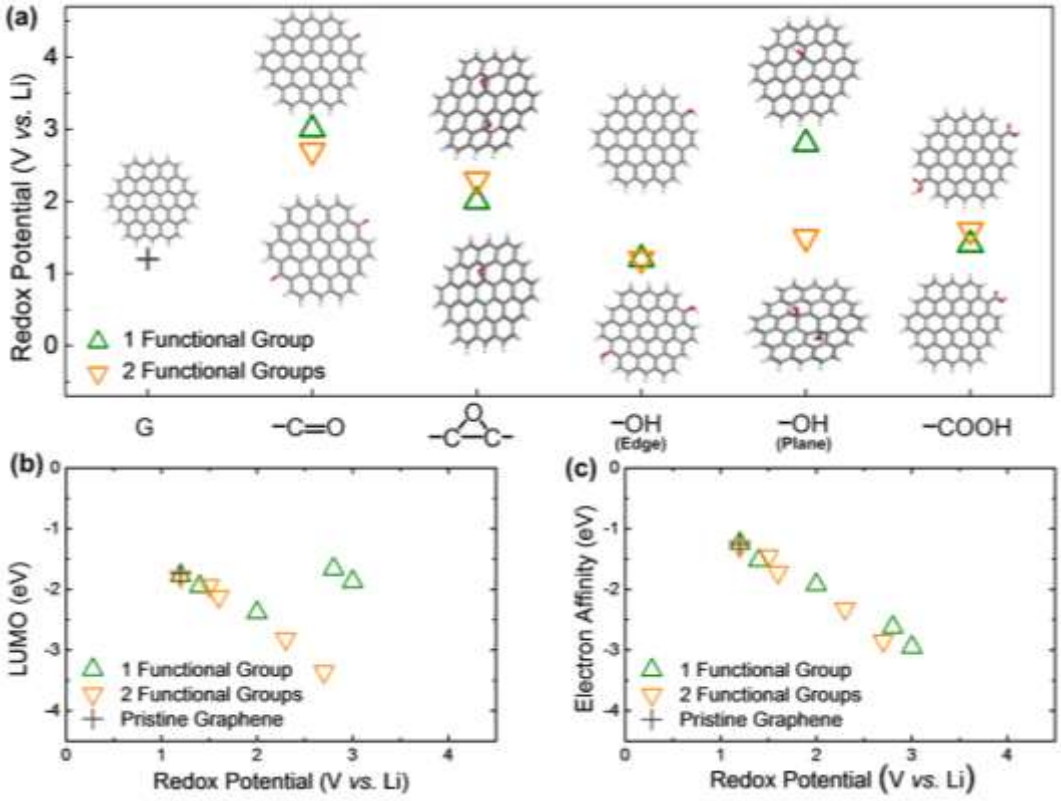

Figure 2.10 (a) The calculated redox potentials for graphene and oxygen functional groups using PWB6K. One (green) and two (orange) functional groups were considered for each functional group to consider the effect of oxygen percentage on the redox potential. The correlation between the calculated redox potentials and the electronic properties, (b) LUMO energy levels and (c) electron affinities, of graphene and oxygen functional groups.

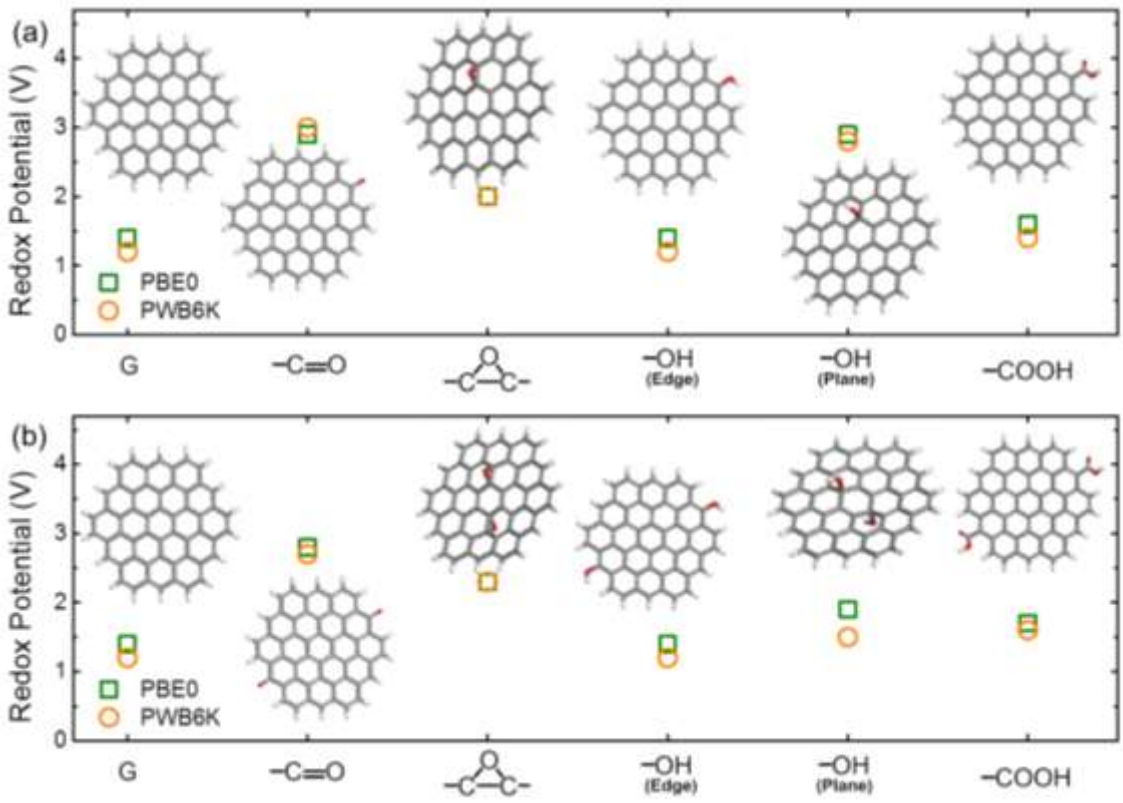

Figure 2.11 The redox potentials for different oxygen functional groups were calculated using two DFT methods (PBE0, green and PWB6K, orange). (a) One or (b) two functional groups were considered for each oxygen functional groups in order to show the effect of oxygen percentage on the redox potential.

Table 2.1 The DFT-calculated redox potentials (in V), highest occupied molecular orbital (HOMO) (in eV), lowest unoccupied molecular orbital (LUMO) (in eV), and electron affinity (EA) (in eV) for the five pairs of feasible oxygen functional group cases on the graphene shown in Figure 2.9 with pristine graphene as a reference. (EA: The DFT-calculated total energy difference at 0K between anion and neutral cases). One or two identical oxygen functional groups were incorporated for each case. Two different levels of theory (PBE0 and PWB6K) were used for the calculations.

Oxygen functional group	PBE0				PWB6K			
	Redox potential (V)	HOMO (eV)	LUMO (eV)	EA (eV)	Redox potential (V)	HOMO (eV)	LUMO (eV)	EA (eV)
1 Carbonyl (edge)	2.9	-5.02	-2.44	-2.96	3.0	-5.44	-1.87	-2.95
2 Carbonyl (edge)	2.8	-5.63	-3.81	-2.95	2.7	-6.05	-3.36	-2.85
1 Epoxide (plane)	2.0	-5.10	-2.86	-2.04	2.0	-5.48	-2.38	-1.92
2 Epoxide (plane)	2.3	-4.90	-3.21	-2.36	2.3	-5.21	-2.82	-2.32
1 Hydroxyl (edge)	1.4	-5.24	-2.31	-1.46	1.2	-5.69	-1.77	-1.24
2 Hydroxyl (edge)	1.4	-5.11	-2.32	-1.49	1.2	-5.57	-1.79	-1.29
1 Hydroxyl (plane)	2.9	-4.78	-2.26	-2.68	2.8	-5.16	-1.66	-2.62
2 Hydroxyl (plane)	1.9	-5.47	-2.57	-1.71	1.5	-5.99	-1.94	-1.45
1 Carboxylic (edge)	1.6	-5.47	-2.51	-1.72	1.4	-5.92	-1.95	-1.52
2 Carboxylic (edge)	1.7	-5.56	-2.68	-1.94	1.6	-6.01	-2.12	-1.72
Pristine graphene	1.4	-5.38	-2.31	-1.45	1.2	-5.82	-1.74	-1.25

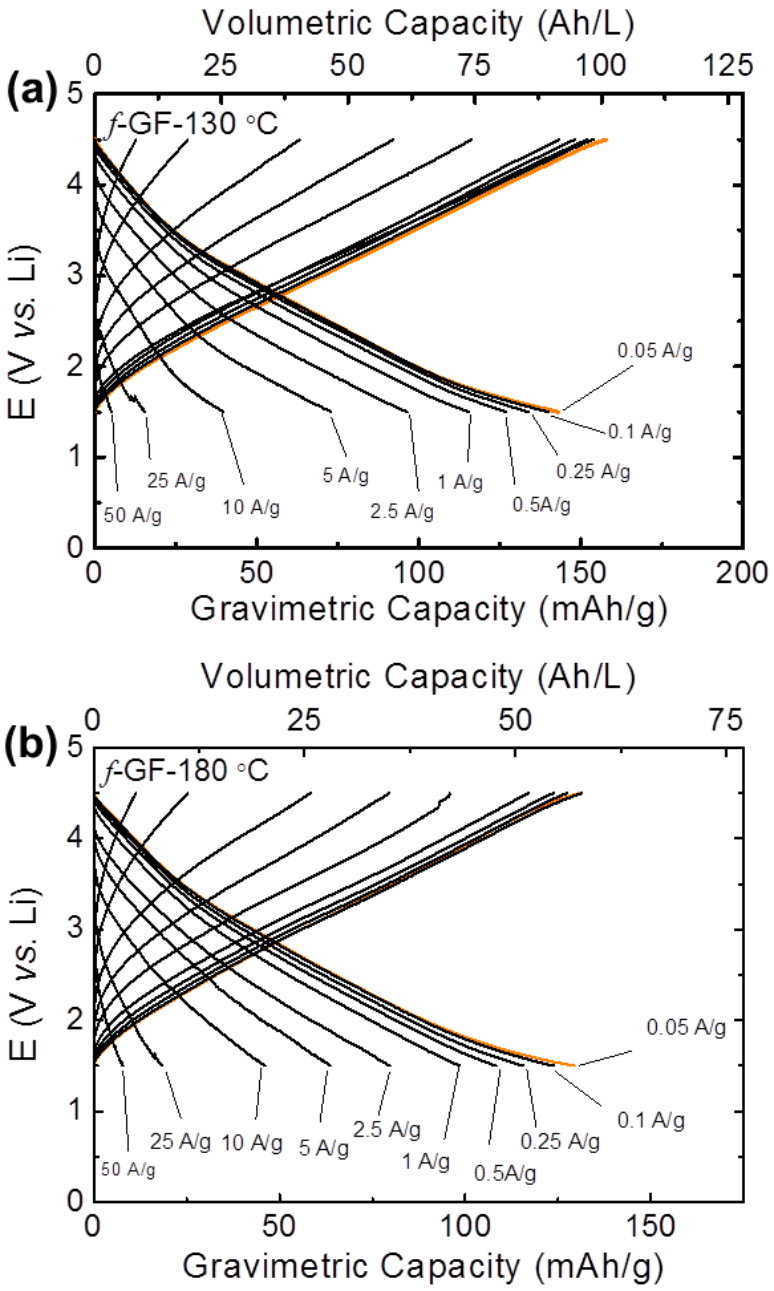

Figure 2.12 (a) Rate dependent galvanostatic charge and discharge curves for the *f*-GF-130 °C electrode with a thickness of 26 µm and (b) the *f*-GF-180 °C electrode with a thickness of 51 µm. The cell was tested between 1.5 and 4.5 V vs. Li and gravimetric current density was controlled from 0.05 to 50 A/g.

Previous studies[58-60, 62, 63, 115, 131] hypothesized that surface carbonyl groups (C=O) on nanocarbons can react reversibly with Li ion, which is supported by the redox reaction mechanism between organic carbonyl compounds and Li ions.[73, 86,

132-135] However, it is unclear how the oxygen chemistry and the amount of the oxygen functional groups can affect the redox reactions on graphene. To answer these questions, DFT calculations were employed to investigate the redox potentials of the available oxygen functional groups on graphene (**Figure 2.9**). The calculations were performed with two different DFT methods (PBE0 and PWB6K) for pristine graphene, and its derivatives with carbonyl, epoxide, hydroxyl or carboxyl acid groups on the edge or plane. To consider the effect of the density of oxygen functional groups on the redox potentials, placing two identical oxygen functional groups on graphene was also considered in addition to one oxygen function group cases (**Figure 2.9**, **Figure 2.10a**, and **Table 2.1**). It is interesting to note that the redox potentials predicted by two different DFT methods were very similar, and the deviations were less than 0.2 V for most cases (**Figure 2.11, Table 2.1**). Graphene itself as well as carboxylic, and hydroxyl groups on the edge showed low redox potentials in the range of 1.2 -1.6 V vs. Li (**Figure 2.10a**), indicating that their contributions are negligible in the CV scans (**Figure 2.7a, b**), with a voltage window between 1.5 - 4.5 V vs. Li. One hydroxyl group on the plane showed a high redox potential of 2.8 V vs. Li, but two hydroxyl groups exhibited significantly decreased potential to 1.5 V vs. Li (**Figure 2.10a, Table 2.1**), corresponding to the lower limit of the operation voltage window of the CV scans. This suggests that increasing the density of hydroxyl groups on the graphene plane may decrease the overall redox potentials of the electrode. On the other hand, carbonyl and epoxide groups showed higher and stable redox potentials in the range of 2.0 - 3.0 V vs. Li, indicating that they are the major redox-active functional groups for the broad redox peaks around 3 V vs. Li in CV scans. Highest-occupied molecular orbital (HOMO), lowest-unoccupied

molecular orbital (LUMO) energy levels and electron affinity of each system were calculated to investigate their correlations with the redox potential. Previous studies have employed LUMO energy levels to explain different redox behaviors of various carbonyl containing molecules.[136, 137] However, the LUMO energy levels of various oxygen functional groups on the graphene were not well correlated to the calculated redox potentials (**Figure 2.10b, Table 2.1**), which is mainly due to the structural difference between the neutral and anionic states of the calculated models. In contrast, the calculated electron affinities were found to have a strong correlation with the calculated redox potential (**Figure 2.10c, Table 2.1**).

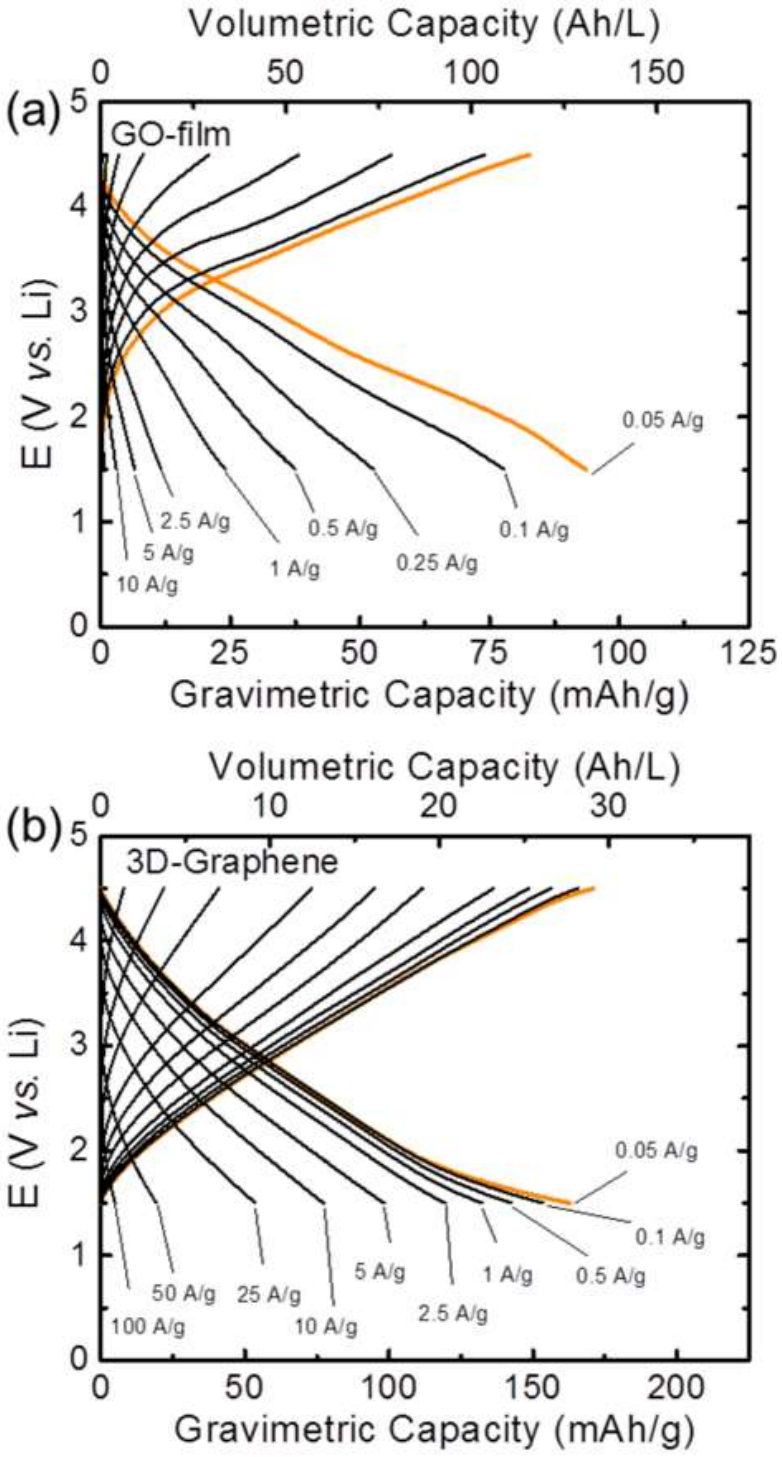

Figure 2.13 The rate-dependent galvanostatic charge and discharge profiles of (a) the GO-film with a thickness of 10 μm (the data is modified from reference 5), and (b) the 3D-graphene electrode. The cell was tested between 1.5 to 4.5 V *vs.* Li and gravimetric current changed from 0.05 to 50 A/g.

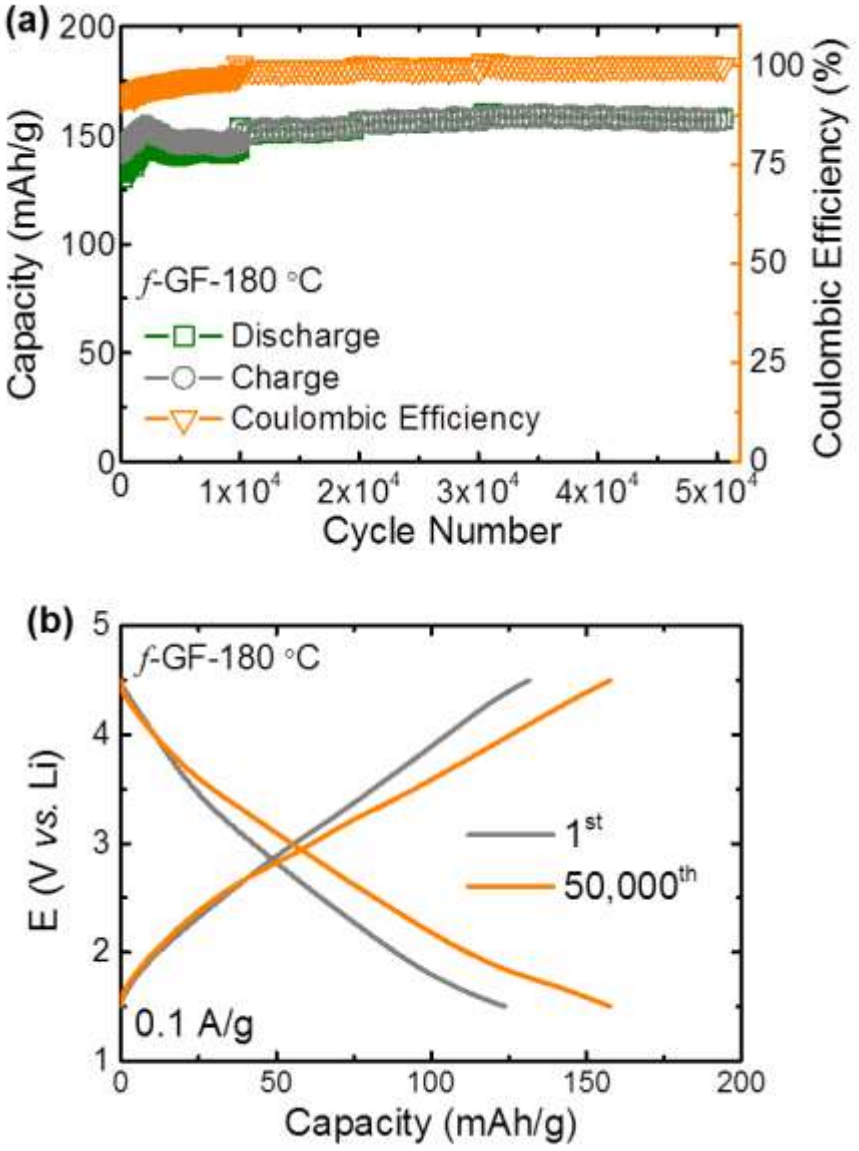

Figure 2.14 (a) Cycling performance of the *f*-GF-180 °C electrode tested galvanostatically up to 50,000 cycles. The data points indicate gravimetric change and discharge capacities obtained at a slow rate of 0.1 A/g and its coulombic efficiency. The cell was cycled at an accelerated rate of 10 A/g between the slow rate (0.1 A/g) measurements. (b) Charge and discharge profile comparison between the first and the 50,000th cycle of the *f*-GF-180 °C electrode.

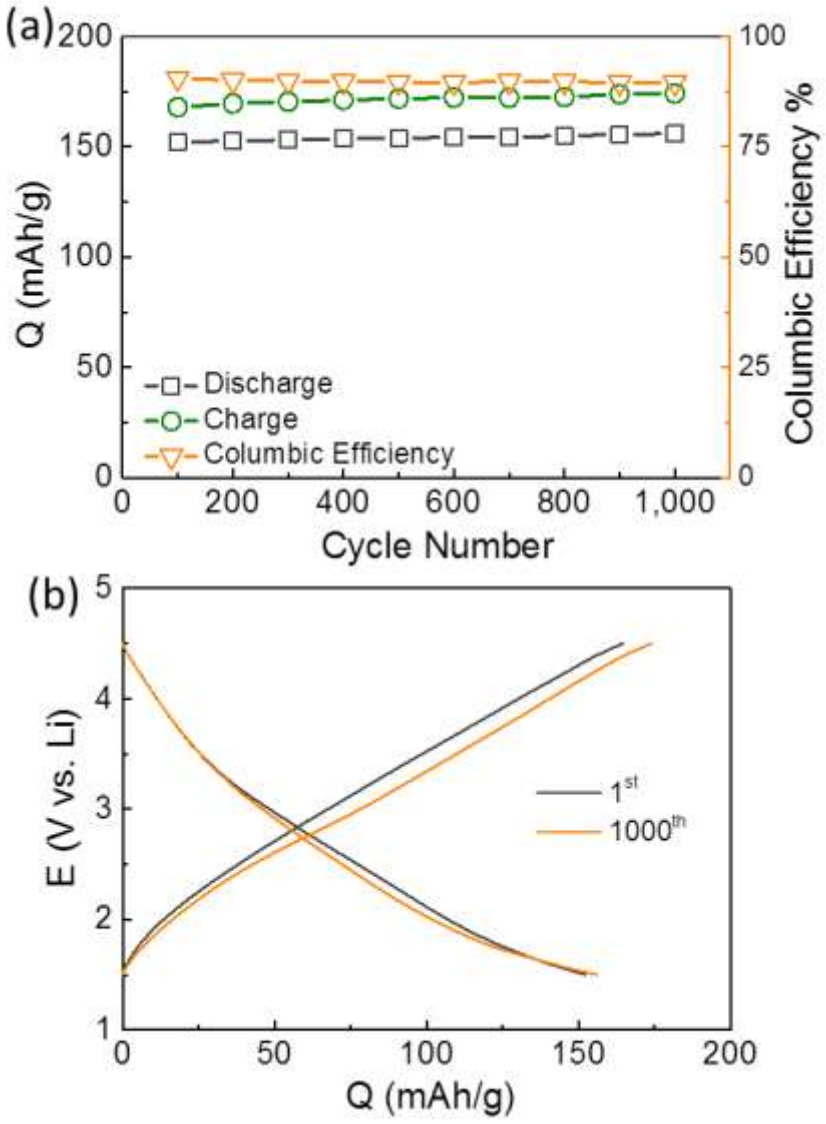

Figure 2.15 (a) Cycling performance of the *f*-GF-130 °C electrode tested galvanostatically up to 1,000 cycles. The data points indicate gravimetric change and discharge capacities obtained at a slow rate of 0.1 A/g and its coulombic efficiency. The cell was cycled at an accelerated rate of 10 A/g between the slow rate (0.1 A/g) measurements. (b) Charge and discharge profile comparison between the first and the 1,000th cycle of the *f*-GF-130 °C electrode.

Li-ion storage performance of the *f*-GF electrodes was evaluated using rate dependent galvanostatic charge and discharge tests (**Figure 2.12a, b**). It is interesting to note the sloped charge and discharge profiles of the *f*-GF electrodes. These sloped charge

and discharge characteristics can be attributed to the coupling of different charge storage mechanisms: double-layer capacitance and the surface redox reactions between various surface functional groups and Li ions at different potentials.[58, 60, 63] In this study, DFT calculations further confirm that various oxygen functional groups on the graphene have different redox potentials depending on their local oxygen chemistries, resulting in sloped characteristics of the *f*-GF electrodes**.** The *f*-GF-130 °C electrode exhibited a high gravimetric capacity of ~143 mAh/g at 0.05 A/g (**Figure 2.12a**), which is higher than ~94 mAh/g of the GO-film electrode (**Figure 2.13a**)[115] and ~130 mAh/g of the *f*-GF-180 °C (**Figure 2.12b**). In addition, the *f*-GF-130 °C electrode delivered a high volumetric capaicty of 91.5 Ah/L (**Figure 2.12a**). Moreover, the *f*-GF electrodes showed excellent cycling performance (**Figure 2.14a** and **Figure 2.15**). The *f*-GF electrodes were accelerated cycled at 10 A/g and the capacities were measured at a slow rate of 0.1 A/g. The *f*-GF-130 °C electrode showed stable cycling stability up to 1,000 cycles with a negligible change of the voltage profiles in the first and 1,000 cycles (**Figure 2.15**). Interestingly, the capacity of the *f*-GF-180 °C electrode was found to progressively increase up to 2,000 cycles, presumably due to the gradual diffusion of the electrolyte into more of the inner-space of the electrodes. The cell was left open circuit for ~2 weeks after the 10,000 cycles, and then cycling was continued up to 50,000 cycles. The coulombic efficiencies of the electrode were also gradually improved during cycling, which approached values close to 100% (**Figure 2.14a**). The voltage profile comparison between the first and 50,000th cycle showed that the capacity of the *f*-GF-180 °C electrode increased ~30 mAh/g after cycling, resulting in a higher capacity of ~160 mAh/g (**Figure 2.14b**). This capacity is almost the same value as the 3D-graphene

electrode obtained by the freeze-drying method, indicating the highly accessible active surface area in the folded structure of the *f*-GF electrodes. These high gravimetric capacities and exceptional cycling stabilities show superior performance of the *f*-GFs electrodes, in comparison to other organic based positive electrode materials for Li ion storage applications.[71]

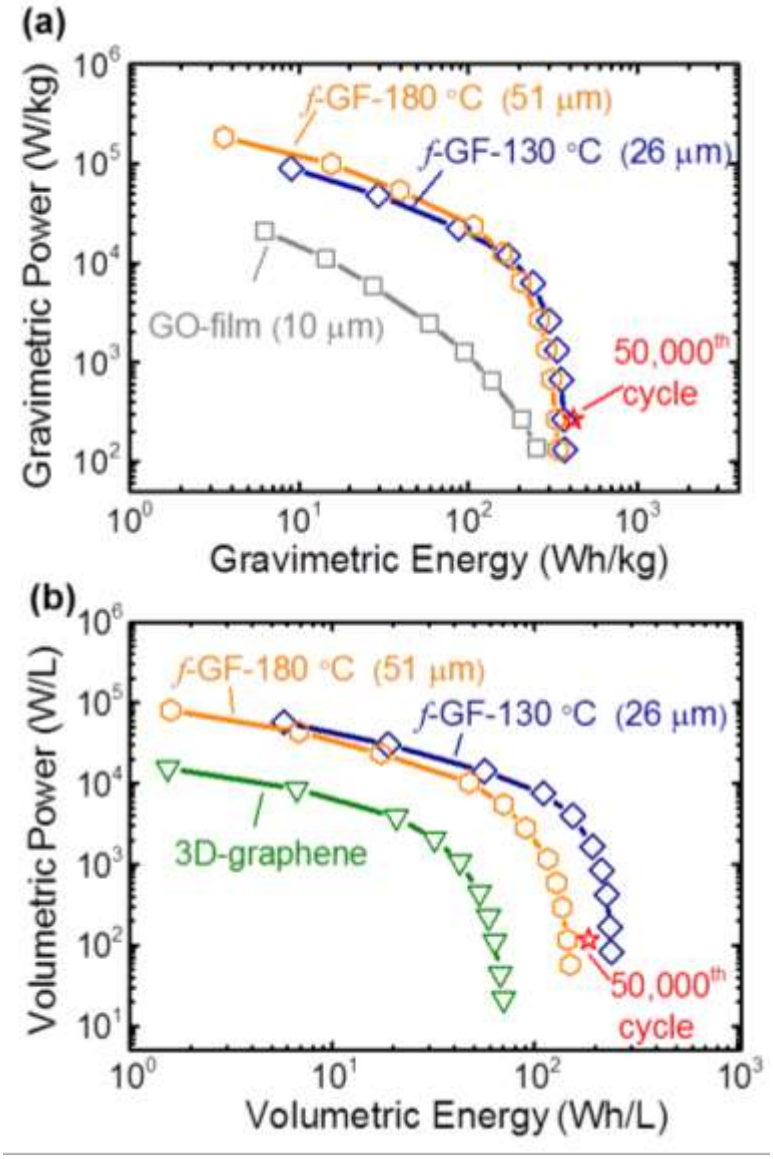

Figure 2.16 (a) Ragone plot comparing gravimetric energy and power performances of the GO-film and *f*-GF electrodes. (b) Ragone plot comparing volumetric energy

and power performance of the *f*-GF and 3D reduced graphene electrode (3D-graphene) obtained from a freeze-drying process of the graphene hydrogel.

Gravimetric and volumetric energy and power characteristics of the *f*-GF electrodes were assessed by Ragone plots (**Figure 2.16a, b**) based on galvanostatic charge and discharge tests (**Figure 2.12a, b** and **Figure 2.13**). At a low power density of ~130 W/$kg_{electrode}$, the *f*-GF electrodes exhibited energy densities of ~340 Wh/$kg_{electrode}$ for the *f*-GF-180 °C and of ~370 Wh/$kg_{electrode}$ for *f*-GF-130 °C, while the GO-film only delivered ~250 Wh/$kg_{electrode}$. Interestingly, the energy density for *f*-GF-180 °C after 50, 000 cycles increased to ~419 Wh/$kg_{electrode}$ at a power density of 266 W/$kg_{electrode}$ (the star-shaped point in **Figure 2.16a**). This energy density (~419 Wh/$kg_{electrode}$) attainable by the *f*-GF electrodes is higher than those of the oxidized CNT, oxidized CNT/graphene composite, and reduced GO film electrodes assembled by vacuum-filtration process (300~350 Wh/$kg_{electrode}$),[60, 63, 116] and is close to that of 3 μm thick thin-film CNT electrodes (~422 Wh/$kg_{electrode}$).[58] At a higher power density of ~10 kW/$kg_{electrode}$, the difference in the attainable energy density between the GO-film (~16 Wh/$kg_{electrode}$) and the *f*-GF electrodes (180~200 Wh/$kg_{electrode}$) became more significant. The improved power density of the *f*-GF electrodes when compared to the GO-film can be attributed to the significantly improved electrical conductivity[117] and the favorable porous structure for fast ion diffusion.[96, 138] In addition, at a lower power density range (less than 100 W/L), the *f*-GF electrodes showed high volumetric energy density—239 Wh/L for the *f*-GF-130 °C—which is ~3.4 times higher than that (70.3 Wh/L) of the 3D-graphene electrode obtained from the freeze-drying method (**Figure 2.16b**).

2.4 Conclusions

In summary, we have assembled free-standing, high-packing density, and redox-active graphene electrodes from the dispersion of GO in water by a simple compressing and vacuum-drying process of the hydrothermally reduced graphene hydrogels. The assembled graphene electrodes have high packing densities of up to ~0.64 g/cm^3 with the folded micro-structure. The surface oxygen chemistry of the electrodes was controlled by the hydrothermal reduction temperatures, and correlated with the redox reaction with Li ions. DFT calculations were used to determine the role of different oxygen functional groups in the electrodes, revealing that carbonyl and epoxide groups are the dominating contributors to the high potential redox reactions. When employed as positive electrodes in Li-cells, the *f*-GF electrodes showed excellent gravimetric and volumetric performance, delivering both high gravimetric energy of ~419 Wh/kg$_{electrode}$ and high volumetric energy of ~239 Wh/L. More importantly, the *f*-GF electrodes showed an exceptional cycling stability, retaining a gravimetric capacity of ~160 mAh/g after 50,000 cycles. The results provide significant insights on the Li ion storage mechanisms of the oxygen functional groups on the reduced GO electrodes, and the effective utilization method to maximize their performance within the confined mass and volume for Li-ion battery or hybrid capacitor applications.

CHAPTER 3. SELF-ASSEMBLED, REDOX-ACTIVE GRAPHENE ELECTRODES FOR HIGH-PERFORMANCE ENERGY STORAGE DEVICES

3.1 Introduction

Nanocarbons, such as CNT and graphene, have become rising electrode materials for electrochemical energy storage devices, such as ECs and rechargeable batteries.[105, 108, 139-143] This is owing to their superior physicochemical properties, including high surface area, high electrical conductivity, high mechanical strength, and chemical stability.[144, 145] In particular, the scalable and low-cost synthesis methods of graphene materials from GO using solution-based processes open up a new opportunity to develop large-scale graphene based electrodes.[110, 146]

Graphene based electrodes have been intensively studied for EDLCs,[96, 147-149] one type of ECs, which store charge by electrolyte ion adsorption (double layer capacitance) on high surface area conductive carbon materials.[39] However, graphene sheets can be readily restacked via the strong π-π interaction during the electrode fabrication and subsequent drying process, eventually decreasing the available surface

area for electrochemical reactions. Accordingly, research efforts have been focused on preventing the restacking of graphene sheets, which can maximize electrochemically active surface area, by KOH activation,[149] laser-scribing,[98] and hydrothermal reaction.[117] Although these graphene-based EDLCs represent state-of-the-art high-power energy storage devices, their energy density utilizing double layer capacitance is significantly lower than that of Li-ion batteries employing intercalation reaction mechanism in the bulk of active materials.

A promising approach to increase the energy density of carbon based electrodes is incorporating heterogeneous atoms into the electrodes, such as nitrogen or oxygen[150-153] which have pseudocapacitive (surface redox) reactions. Recently, reversible surface redox reactions between Li ions and the oxygen functional groups on the nanocarbons, including CNT and graphene, have been observed at a high redox potential of ~3.2 V vs. Li.[58-60] Based on these surface redox reactions, oxygen group functionalized carbon materials have been employed as positive electrodes in Li-cells, providing both high energy and power density with stable cycling stability.[63, 95] The electrochemical performance of these functionalized carbon electrodes strongly depends on their physical and chemical structures. Binder free 3D porous nanostructured electrodes showed enhanced electrochemical performance than that of the composite electrodes including polymer binder owing to increased electrochemically active surface area.[58] The thickness of the electrodes is also an important factor, as it was previously shown that thicker functionalized CNT electrodes exhibited lower energy and power density compared to those of thin-film CNT electrodes due to increased electronic and ionic resistance. [58, 62] In addition, oxidized CNT and CNT/graphene composite electrodes

showed that surface oxygen chemistry can greatly influence the electrochemical performance.[60, 63] Therefore, the assembly of 3D nanostructured electrodes with a fine tuning of surface oxygen chemistry as well as controlled physical properties is a crucial design factor in developing high-performance pseudocapacitive carbon electrodes.

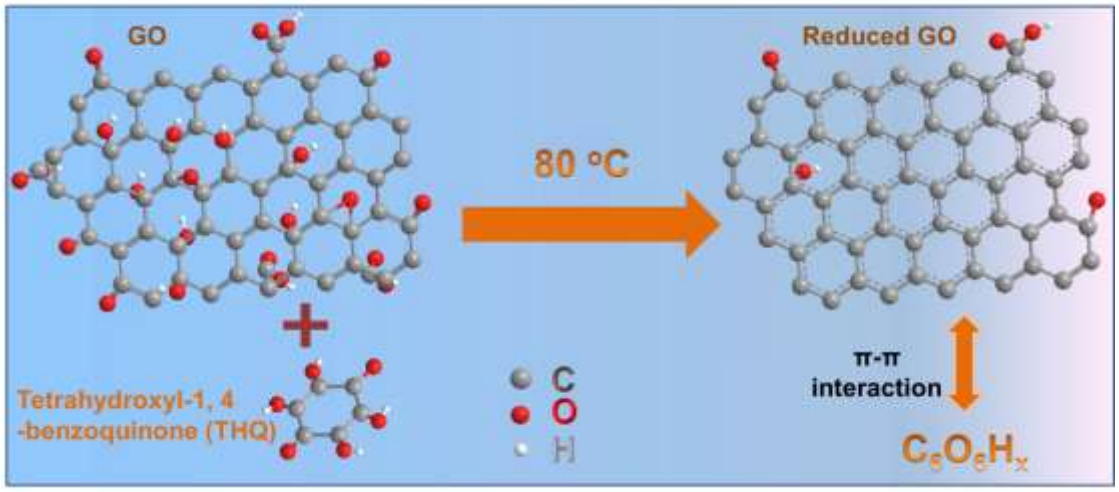

Scheme 3.1 The reduction and functionalization mechanism of GO by tetrahydroxyl-1,4-benzoquinone (THQ). The mixture of GO and THQ in water was heat- treated at 80 ^{0}C, during which H^+ released from THQ can reduce the oxygen functional groups on the surface of the GO. The remaining THQ and oxidized THQ ($C_6O_6H_x$) can adsorb on the surface of the reduced GO by π-π interaction, forming functionalized graphene.

In this study, we present a simple synthetic route to assemble 3D nanostructured graphene electrode and simultaneously introduce redox-active oxygen functional groups on the surface of the electrode using tetraydroxy-1,4-benzquinone (THQ) as both the reducing and functionalization agent (**Scheme 3.1**). THQ exhibits a strong reducing ability, enabling the fast self-assembly of 3D functionalized graphene from the dispersion of GO in water at a low temperature of ~80 ^{0}C under atmospheric pressure without any disturbance. In addition, the surface oxygen chemistry of the graphene electrodes can be manipulated by simply controlling the concentration ratio of THQ to GO in water. We

correlate the surface oxygen chemistry with gravimetric capacity of the electrodes assembled at different THQ concentrations, confirming the introduction of the surface redox reactions by THQ into the electrodes. In addition, we reveal that the microstructure of the functionalized graphene electrodes consists of 3D interconnected graphene sheets with hierarchically developed pores, using SEM. The 3D functionalized graphene electrodes can be employed as positive electrodes in both Li- and Na-cells, storing Li up to a gravimetric capacity of ~165 mAh/g and Na up to ~120 mAh/g due to the surface redox reactions between oxygen functional groups and cations. The energy and power density of the functionalized graphene electrodes have been evaluated in both Li-cells and Na-cells using current density dependent galvanostatic charge and discharge test, showing high energy density up to ~410 $Wh/kg_{electrode}$ and power density over ~100 $kW/kg_{electrode}$ with excellent cycling stability up to 10,000 cycles. As THQ can be produced in high yield from renewable *myo*-inositol, a kind of natural compounds which widely exists in plants,[154-156] the simple THQ based assembly process opens a new pathway to synthesize large-scale, high-performance positive electrodes for both Li- and Na-ion batteries.

3.2 Experimental

Functionalized Graphene Electrode Preparation: GO was prepared by a modified Hummer's method.[109, 110] Detailed synthesis procedure of GO can be found in previous reports.[23,] [95] 10 mL of GO dispersion (1 mg/mL) in deionized water was mixed with tetrahydroxy-1,4-benzquinone (THQ, Sigma-Aldrich, 99% purity) at different concentration ratios (GO:THQ=1:1, 1:2, and 1:4) and the mixture was stirred for 1 hr. Then, the mixture was sealed in a glass vial and was heated at 80 ^{0}C for 3 hr under

atmospheric pressure without any disturbance. The self-assembled functionalized graphene hydrogel was observed in the glass vial after 3 hr.

After cooling the mixture for ~1 hr, the assembled graphene hydrogel was taken out from the vial with a tweezer and was washed with D.I. water (Milli-Q, 18.2 MΩ) several times to remove the weakly adsorbed molecules. Next, it was freeze-dried at -84 ^{0}C (FreeZone Plus 2.5 Liter Cascade Benchtop Freeze Dry System) for 24 hr to remove water within its pores. For electrochemical tests, a small part of the functionalized graphene was cut from the freeze-dried sample and pressed into a film. The thickness of the functionalized graphene film electrodes was controlled to be around 100 μm.

GO Electrode Preparation: GO film was obtained by the vacuum-filtration process. 10 mL of GO solution (1 mg/mL) was vacuum filtrated using a filtration membrane with 0.1 μm pore size and 47 mm diameter (PC, Whatman). After the drying process, the thickness of the prepared GO film electrodes was around 10 μm.

Characterization: The microstructure of the functionalized graphene electrodes was characterized by the SEM (Hitachi SU8010 operated at 10 kV). The surface chemistry analysis of the electrodes was carried by the XPS (Thermal Scientific K-alpha XPS instrument), and the peaks were fitted by the XPSPEAKS 4.1.

Electrochemical Measurement: Electrochemical measurements were performed by a Bio-logic VMP3 potentiostat/galvanostat. Two-electrode Swagelok type cells were used for the Li-cell and Na-cell tests. The Li-cells were assembled with a functionalized graphene positive electrode, a lithium foil negative electrode, two pieces of Celgard 2500 separators, and 1 M $LiPF_6$ in EC and DMC (3:7 volume ratio) electrolyte (BASF

Novolyte) inside an Argon-filled glovebox (MBraun O_2<0.1 ppm; H_2O<0.1 ppm). The Li-cells were tested in the voltage range of 1.5-4.5 V vs. Li. For charge and discharge test, the current density was controlled from 0.05 to 100 A/g. At the end of the charge or discharge process, the cells were kept at 4.5 or 1.5 V for 30 minutes, respectively. The cycling test was carried by an accelerated galvanostatic cycling method. Charge and discharge profiles were measured at 0.1 A/g once every 100 cycles up to 1,000 cycles and once every 500 cycles between 1,001 to 10,000 cycles, after voltage holding process for 30 minutes. Within these slow rate measurements at 0.1 A/g, the Li-cells were cycled at an accelerated rate of 10 A/g.

The Na-cells were composed of a functionalized graphene positive electrode, a thin Na foil (Sigma Aldrich) negative electrode, one piece of glass fibre film (VWR International) separator, and 1 M $NaPF_6$ (Alfa Aesar) in ethylene carbonate (EC): dimethyl carbonate (DMC) (3:7 volume ratio) electrolyte (BASF Novolyte). The Na-cells were tested in the voltage range from 1.3 to 4.2 V vs. Na. For the galvanostatic charge and discharge test, the current rate was controlled from 0.05 to 25 A/g. At the end of the charge or discharge process, the cells were kept at 4.2 or 1.3 V for 30 minutes respectively.

3.3 Results and Discussions

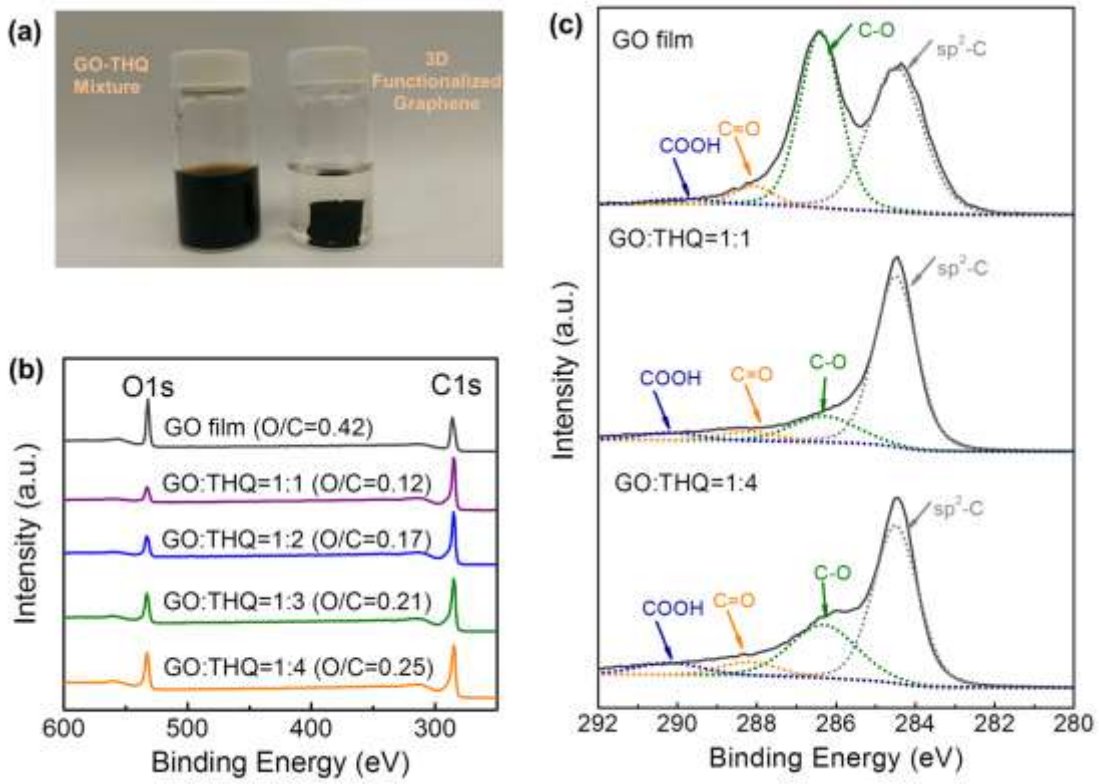

Figure 3.1 (a) Digital images of the mixture of GO (1 mg/mL) and tetrahydroxyl-1,4-benzoquinone (THQ, 3 mg/mL) in water (left), and the assembled functionalized graphene hydrogel (right). (b) XPS wide scan survey of the GO film and the functionalized graphene electrodes. (c) XPS C1s spectra of the GO film (top) and the functionalized graphene electrodes obtained from mixtures of GO and THQ with different concentration ratios (GO:THQ=1:1, (middle), and GO:THQ=1:4, (bottom)).

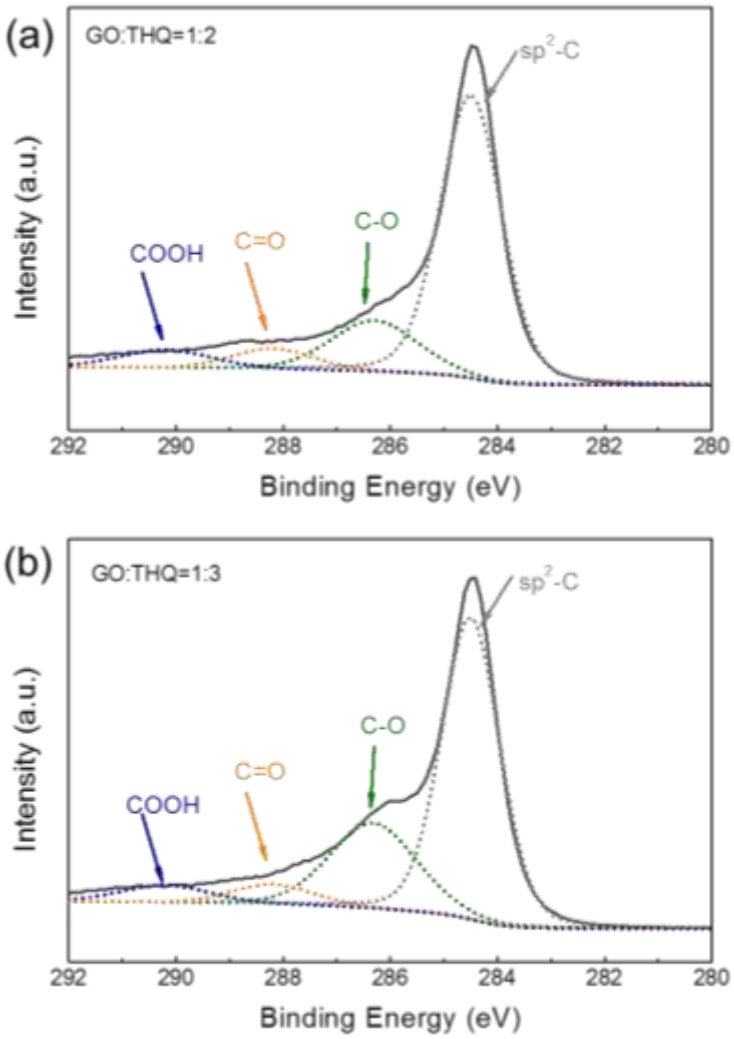

Figure 3.2 XPS C1s spectra of the functionalized graphene electrodes obtained from the mixtures GO and THQ with different concentration ratios, (a) GO:THQ=1:2 and (b) GO:THQ= 1:3.

Functionalized graphene hydrogel was self-assembled by heating a mixture of GO (1 mg/mL) and THQ (1-4 mg/mL) in deionized water at 80 ^{0}C for 3 hr under atmospheric pressure without any disturbance (**Figure 3.1a**). The hydroxyl groups in THQ can generate H^+ ions in water, and the released H^+ ions react with the oxygen functional groups, such as hydroxyls, epoxide and carbonyl groups, on the GO surface, enabling the deoxygenation (reduction) of the GO.[122] The reduced graphene sheets have

hydrophobic properties, and therefore they tend to interact with each other through the hydrophobic and π-π interaction.[15, 113, 117] When the concentration of the GO is high enough (>1 mg/mL), the reduced graphene sheets can self-assemble into a 3D structure (**Figure 3.1a**). Functionalized graphene electrode was prepared by removing water within the graphene hydrogel using a freeze-dryer.

The surface oxygen chemistry of the functionalized graphene electrodes was determined by XPS analysis (**Figure 3.1b, c** and **Figure 3.2**). XPS wide scan survey peaks revealed that the functionalized graphene electrode prepared from a mixture of GO and THQ with a 1:1 concentration ratio (GO:THQ=1:1) had a significantly reduced atomic ratio of oxygen to carbon (O/C=0.12) compared to that of a pristine GO film (O/C=0.42) (**Figure 3.1b**), indicating that THQ is an efficient reducing agent. High resolution C1s spectra of the electrodes were fitted with sp^2-hybridized graphitic carbon peak (284.5 eV) and oxygenated carbon groups (C–O: hydroxyl or epoxide group peak at 286.4±0.1 eV, C=O: carbonyl group peak at 288.2±0.1 eV, and COOH: carboxylic group peak at 290.2±0.1 eV).[127] C1s spectra of the functionalized graphene electrode (GO:THQ=1:1) had a significantly reduced hydroxyl or epoxide (C–O) peak and partially decreased carbonyl (C=O) peak relative to sp^2-hybridized carbon (sp^2-C) peak compared to those of the GO film, showing the recovery of a conjugated carbon structure during the reduction process (**Figure 3.1c**). In addition, the O/C ratio of the functionalized graphene electrodes was found to increase from 0.12 to 0.25 as the concentration of THQ increased from GO:THQ=1:1 to 1:4 (**Figure 3.1b**). This trend is supported by high resolution C1s spectra, which showed the increased intensities of both C-O and C=O in the functionalized graphene electrodes as the THQ concentration increased (**Figure 3.1c** and

Figure 3.2). We postulate that excess THQ ($C_6O_6H_4$) or oxidized THQ ($C_6O_6H_x$)[157, 158] molecules can adsorb on the reduced graphene sheets via π–π interaction,[15, 159-161] incorporating oxygen functional groups in the electrodes prepared with high THQ concentration.

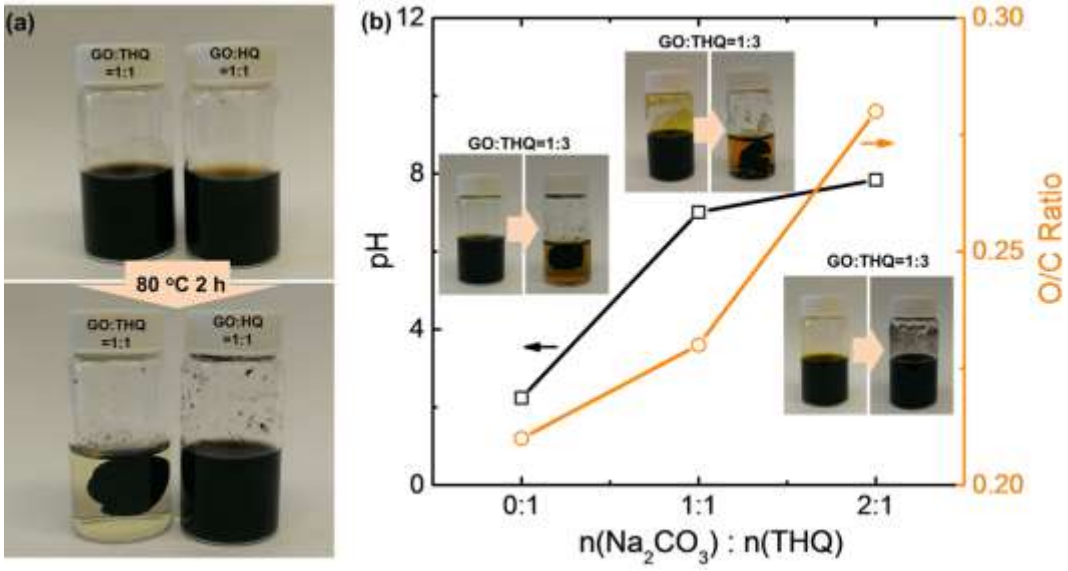

Figure 3.3 (a) Digital images of the mixture of GO (1 mg/mL) and THQ (1 mg/mL) (GO:THQ=1:1, top left), and the mixture of GO (1 mg/mL) and hydroquinone (HQ, 1 mg/mL) (GO-HQ (1:1), top right) in water. After heat-treatment at 80 ^{0}C for 2 h, a graphene hydrogel was formed in the mixture of GO and THQ (bottom left), while no obvious change was observed for the mixture of GO and HQ (bottom right). (b) The pH of the mixtures of GO and THQ (GO:THQ=1:3) on the left y-axis and the atomic ratio of oxygen to carbon (O/C) of the reaction products in the mixture after heat-treatment at 80 ^{0}C for 3 h on the right y-axis as a function of the molar ratio of Na_2CO_3 and THQ in water.

Previous work has shown that hydroquinone ($C_6O_6H_4$, HQ) has a similar reduction and functionalization mechanism, which can contribute to assembling 3D graphene hydrogels from the dispersion of GO.[15, 113, 162] **Figure 3.3** compares the reducing ability of THQ and HQ for the self-assembly process of reduced GO in water. Functionalized graphene hydrogel was assembled when the mixture of GO (1 mg/mL)

and THQ (1 mg/mL) was kept at 80 ^{0}C for 2 hr, while no obvious change was observed for the mixture of GO (1 mg/mL) and HQ (1 mg/mL), indicative of stronger reducing power of THQ than HQ (**Figure 3.3**). The aggregation of GO (1mg/mL) was even initiated with THQ (2mg/mL) at a lower temperature of 50 ^{0}C (**Figure 3.4**). THQ can release H^+ ions from four hydroxyl groups in aqueous solution, forming anions such as $C_6H_2O_6^{2-}$ and $C_6O_6^{4-}$.[157] The ionization constants of THQ for releasing the first two H^+ are pK_1=4.8 and pK_2=6.8 in aqueous solution,[157] which are much lower than pK_1=9.9 of HQ.[163] Accordingly, the mixture of GO and THQ showed lower pH (2.82) than that of the mixture of GO and HQ (3.38), indicating more H^+ exist in the THQ solution. Furthermore, the adsorbed THQ or oxidized THQ ($C_6O_6H_x$) on the graphene sheets have four more oxygen donor atoms compared to HQ or benzoquinone (the final oxidization state of HQ), which can adopt more oxidation and reduction states for surface redox reactions.

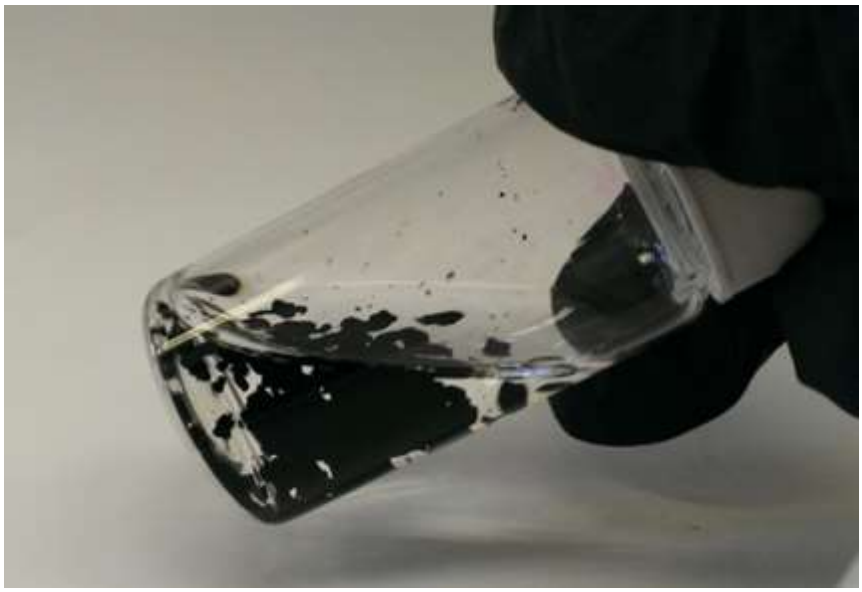

Figure 3.4 A digital image of the aggregates of reduced GO in a mixture of GO (1 mg/mL) and tetrahydroxyl-1,4-benzoquinone (THQ) (2 mg/mL) in deionized (DI) water at 50 ^{o}C after 3 h without stirring condition.

The reduction and self-assembly process in the mixture of GO and THQ showed a strong pH dependence. Na_2CO_3 was used to tune the pH of the solution with the fixed concentration ratio of GO and THQ at 1:3. The initial pH of the solution was 2.24, and the pH increased with the increased Na_2CO_3 concentration relative to THQ (pH 7.01 for 1:1 molar ratio and pH 7.84 for 2:1 molar ratio of Na_2CO_3 and THQ) (**Figure 3.3b**). After heat-treatment at 80 ^{0}C for 3 hr, stable graphene hydrogel was assembled in the solution without Na_2CO_3 (pH 2.24), whereas meta-stable hydrogel was formed in the solution with 1:1 molar ratio of Na_2CO_3 and THQ (pH 7.01). Even gentle shake of the glass vial could tear the assembled meta-stable hydrogel. In the high pH solution with 2:1 molar ratio of Na_2CO_3 and THQ (pH 7.84), no graphene hydrogel was observed and the GO dispersion was stable for several weeks. This pH dependent assembly behaviour can be explained by the reduction trend of GO. The O/C ratios of the products (the self-assembled graphene or the dispersed GO) after the reduction process with THQ gradually increased with the higher concentration of Na_2CO_3 relative to THQ, showing that high pH condition can depress the reduction of GO (**Figure 3.3b**). Accordingly, at high pH condition, GO still can preserve the hydrophilic characteristic, preventing the self-assembly process via the hydrophobic and π-π interaction.

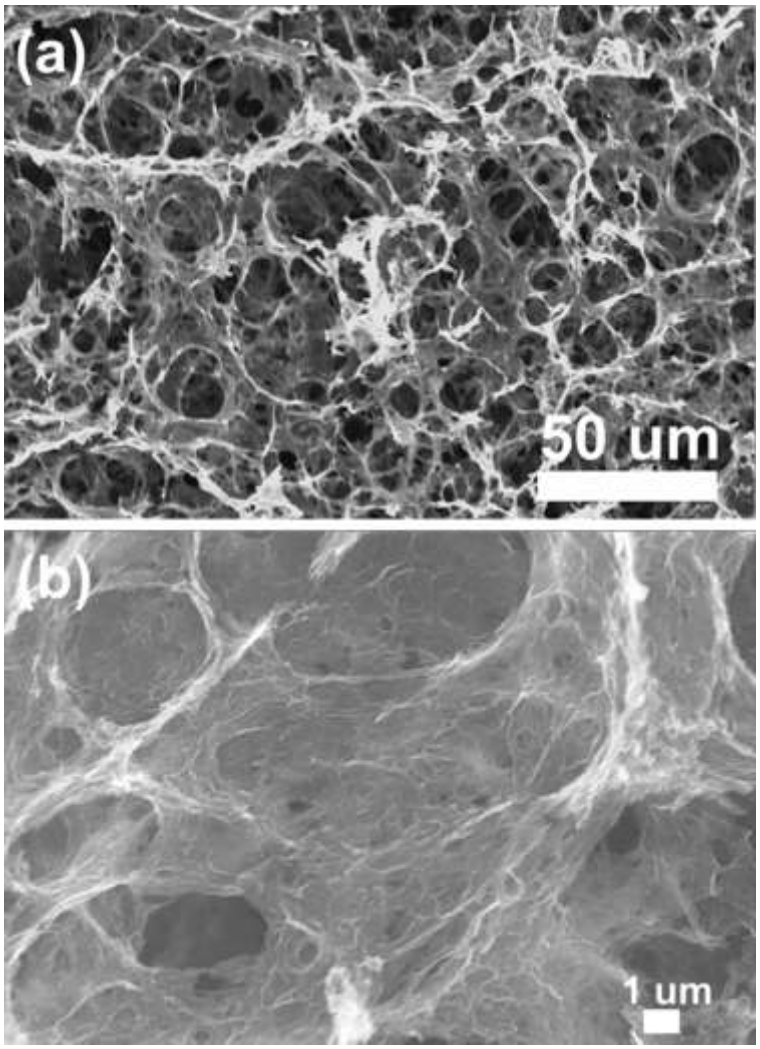

Figure 3.5 (a) Low-magnification and (b) high-magnification SEM images of the 3D functionalized graphene obtained from the mixture of GO and THQ (GO:THQ=1:3).

The microstructure of the 3D functionalized graphene electrodes was characterized by a SEM. The electrodes showed 3D interconnected conductive network structure assembled by the partial stacking of the graphene sheets (**Figure 3.5**). The hierarchical porous structure was observed with the pore size ranging from tens of nanometers to tens of micrometers (**Figure 3.5**), which can facilitate ionic transport and increase electrochemically accessible surface areas. Thus, this 3D porous microstructure

can provide continuous electronic and ionic transport pathways within the electrode, supporting fast surface redox reactions on the oxygen functional groups.

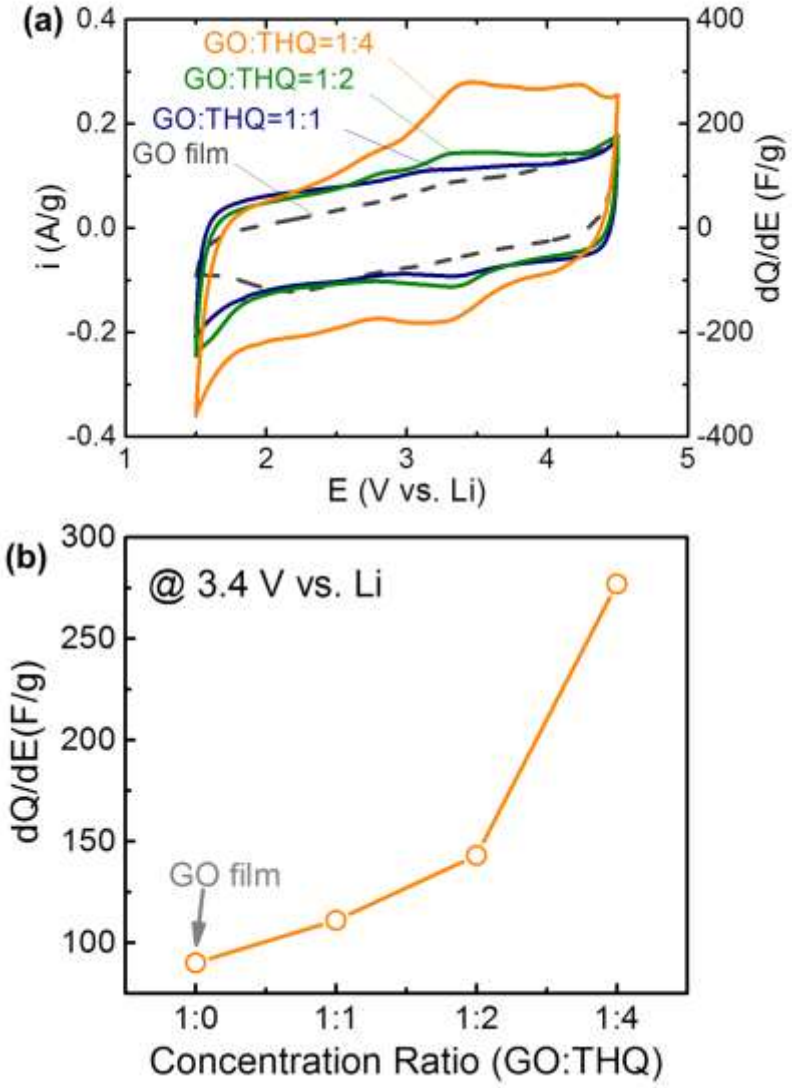

Figure 3.6 (a) Comparison of the steady-state CV scans of the GO film and functionalized graphene electrodes with different concentration ratios of GO and THQ in Li-cells, in 1 M $LiPF_6$ in a mixture of EC and DMC (3:7 volume ratio). The voltage window of the CV was 1.5 - 4.5 V vs. Li at a scan rate of 1 mV/s. (b) Instantaneous specific capacitance of the electrodes at 3.4 V vs. Li as a function of the concentration ratio of GO and THQ.

The introduction of redox-active oxygen functional groups of THQ into the graphene electrodes can be confirmed by investigating surface redox reactions using CV. **Figure 3.6a** shows the stead-state CV scans of the electrodes in Li-cells as a function of the concentration ratio of GO and THQ in the solution. The graphene electrode prepared from the 1:1 concentration ratio of GO and THQ (GO:THQ=1:1) showed a small redox peak around ~3.2 V vs. Li (**Figure 3.6a**) on top of double layer capacitance, which is similar to that found for previously reported oxidized CNT and CNT/graphene composite electrodes (**Figure 3.6a**).[58-60] The surface redox current and redox potential region were found to increase gradually as the concentration of THQ increased (**Figure 3.6a**). The functionalized graphene electrode prepared from the 1:4 concentration ratio of GO and THQ (GO:THQ=1:4) showed the enhanced redox current from several redox peaks in a broad range of 2.5-4.3 V vs. Li, which can be attributed to the multiple redox reactions of the adsorbed THQ or oxidized THQ ($C_6O_6H_x$). In contrast, the CV scan of the GO electrode prepared by vacuum filtration exhibited smaller current density with negligible redox peaks compared to those of the graphene electrodes. To estimate the introduced redox-active oxygen functional groups from THQ into the electrodes, the instantaneous capacitances at 3.4 V vs. Li were plotted as a function of the concentration ratio of GO and THQ (**Figure 3.6b**). The instantaneous capacitance gradually increased with higher THQ concentration from ~90 F/g of GO up to 277 F/g of the graphene electrode (GO:THQ=1:4), confirming the role of THQ for introducing redox-active oxygen functionality into the electrodes.

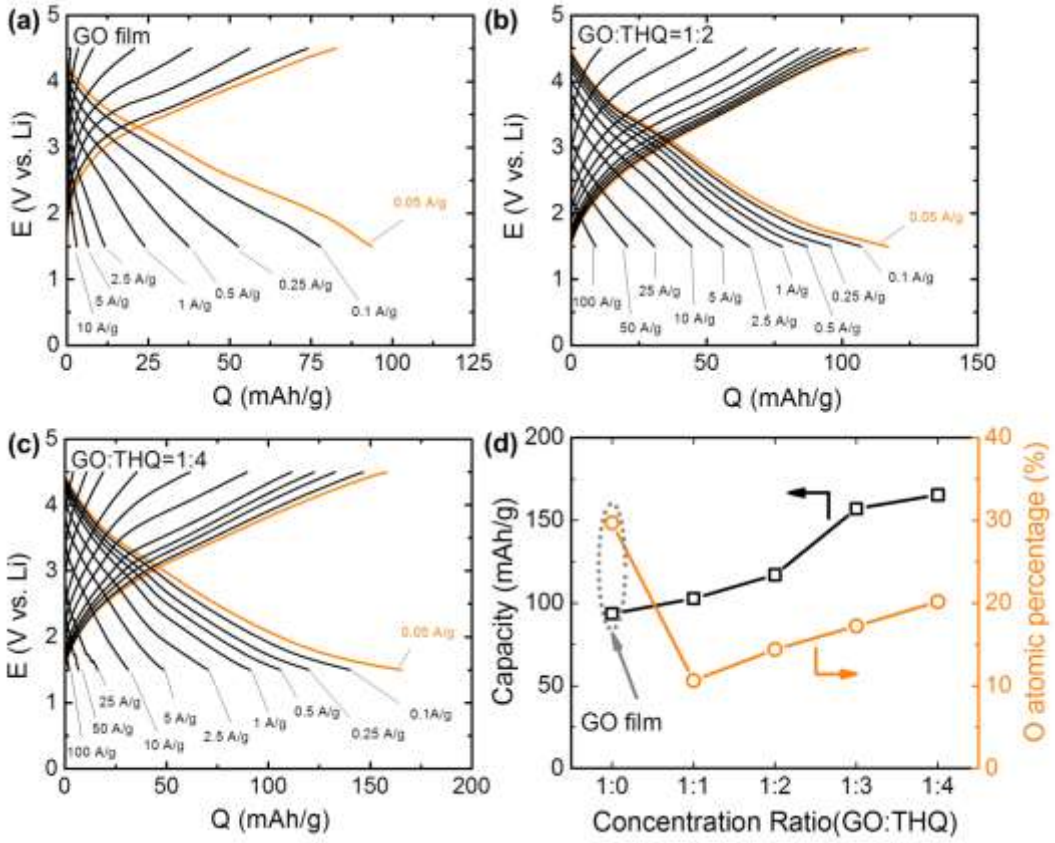

Figure 3.7 Current density dependent galvanostatic charge and discharge curves of (a) the GO film electrode prepared by the vacuum-filtration process and the functionalized graphene electrodes assembled at different concentration ratios of GO and THQ, (b) GO:THQ=1:2 (c) GO:THQ=1:4 in the voltage range between 1.5-4.5 V vs. Li. Before each discharge and charge process, the cells were held at a constant voltage of 4.5 or 1.5 V vs. Li, respectively, for 30 minutes, and the gravimetric current density were controlled from 0.05 to 100 A/g. (d) Gravimetric capacity and oxygen atomic percentages of the electrodes as a function of the concentration ratio of GO and THQ. GO:THQ=1:0 indicates the GO film. The thicknesses of the electrodes were ~10 µm for the GO electrodes, ~113 µm for GO:THQ=1:2, and ~107 µm for GO:THQ=1:4.

Galvanostatic charge and discharge tests of the electrodes in Li-cells revealed that the capacities at a slow rate of 0.05 A/g increased with increasing THQ concentration (**Figure 3.7** and **Figure 3.8**). The capacity of the GO electrode assembled by vacuum-filtration process was ~94 mAh/g, while the capacities of the functionalized graphene electrodes progressively increased from ~102 mAh/g for GO:THQ=1:1, to ~117 mAh/g

for GO:THQ=1:2, to 165 mAh/g for GO:THQ=1:4 (**Figure 3.7**, **Figure 3.8a**). The functionalized graphene electrodes also showed significantly improved rate capability compared to that of the GO film. The capacity of the GO film at 1 A/g was ~25 mAh/g (27% of the capacity at 0.05 A/g) (**Figure 3.7a**), whereas the capacities of the functionalized graphene electrodes at 1A/g were 78 mAh/g for GO:THQ=1:2 (66.5% of the capacity at 0.05 A/g) and 91 mAh/g for GO:THQ=1:4 (55% of the capacity at 0.05 A/g), respectively (**Figure 3.7b** and **c**). It should be noted that the thicknesses of the functionalized graphene electrodes (~100 μm) were 1 order of magnitude higher than that of the GO film (~10 μm). The significantly enhanced rate capability of the functionalized graphene electrodes can be attributed to their favourable chemical and physical structure, which can facilitate electronic and ionic transportation to support fast electrochemical reactions. The functionalized graphene electrodes have higher electrical conductivity than that of GO film (**Figure 3.9**) owing to the recovery of a conjugated sp^2 structure. In addition, the 3D hierarchical pore structure (**Figure 3.5**) of the functionalized graphene electrodes can provide faster ion diffusion pathway and larger electrochemically accessible surface area compared to those of GO films having the 2D layered structure.[130]

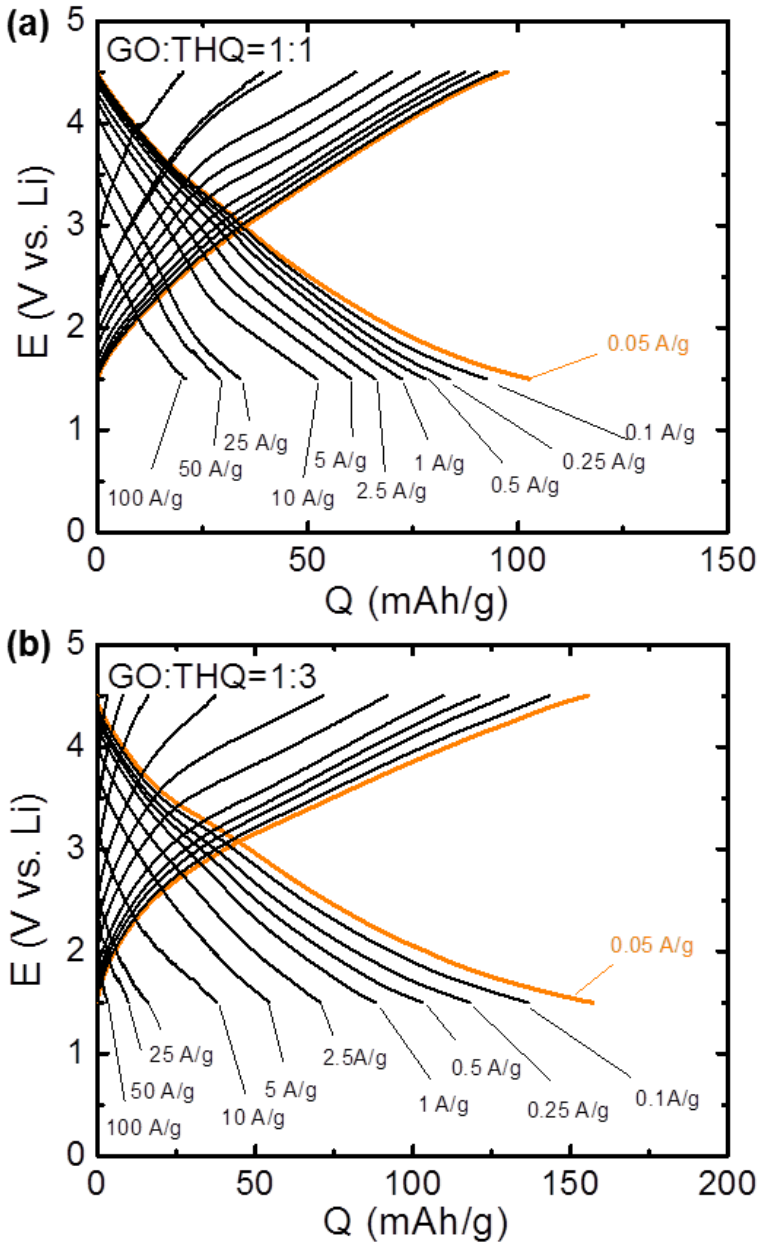

Figure 3.8 Current density dependent galvanostatic charge and discharge curves of the functionalized graphene electrodes assembled at different concentration ratios of GO and THQ, (a) GO:THQ=1:1 and (b) GO:THQ=1:3 in the voltage range between 1.5-4.5 V vs. Li. Before each discharge and charge process, the cells were held at a constant voltage of 4.5 or 1.5 V vs. Li, respectively, for 30 minutes, and the gravimetric current density controlled from 0.05 to 100 A/g.

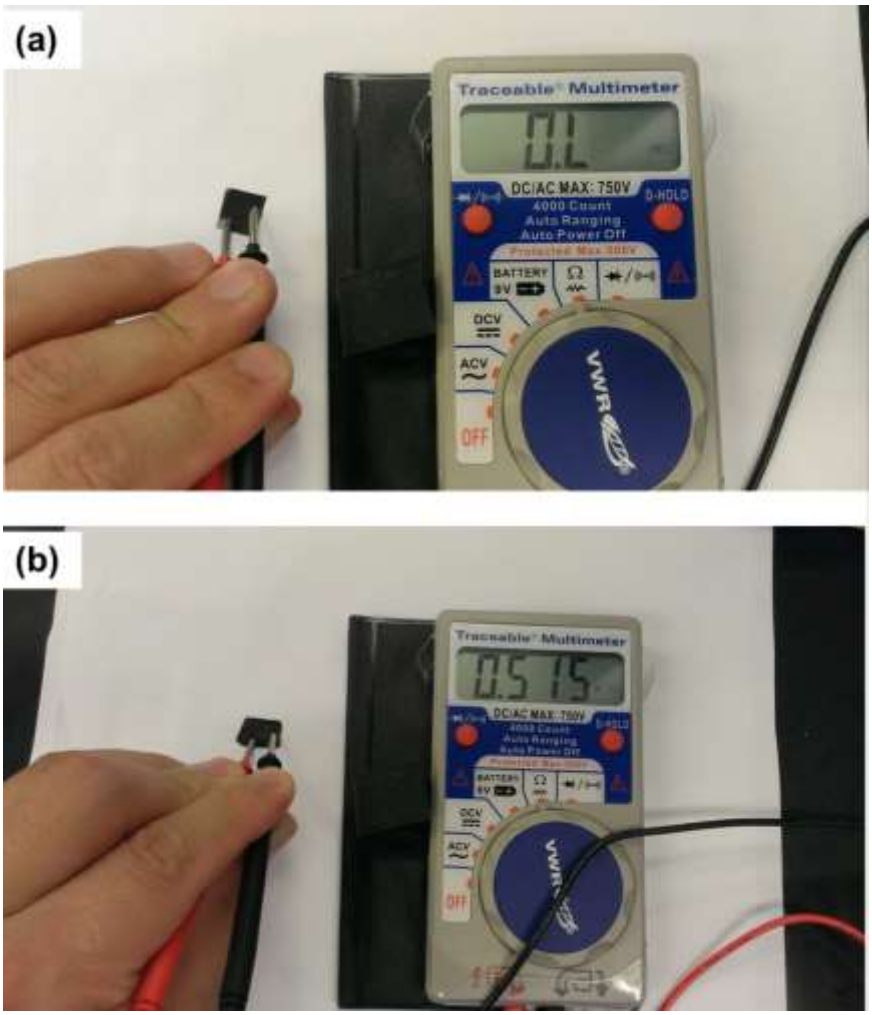

Figure 3.9 The electrical resistance measurements of (a) the GO film prepared by vacuum-filtration process and (b) the pressed 3D functionalized graphene electrode prepared at GO:THQ=1:2 condition.

The gravimetric capacities of the electrodes were plotted with their oxygen atomic percentage (**Figure 3.7d**). The functionalized graphene electrodes showed a strong correlation between the oxygen percentage and the gravimetric capacity, while the GO electrode showed the highest oxygen percentage (29.7%), but the lowest capacity (~94 mAh/g) compared to those of the graphene electrodes. This comparison indicates that THQ can replace electrochemically inactive oxygen groups on the surface of GO with redox-active oxygen functional groups on the surface of the reduced graphene via the

reduction and concomitant functionalization process. It is interesting to note that the ~100 μm thick 3D functionalized graphene electrodes showed higher capacity (~165 mAh/g) than those (120~135 mAh/g) of 10~20 μm thick oxidized CNT or 4 μm thick CNT/graphene composite electrodes having similar oxygen percentages (15~17%).[60, 63] Since the oxygen functional groups of the oxidized CNT or CNT/graphene composite electrodes were incorporated into the electrode by chemical oxidation process using strong acids,[60, 63] such an increase of the capacity for the functionalized graphene electrodes can be attributed to the enhanced redox-active oxygen functionality introduced by external THQ molecules.

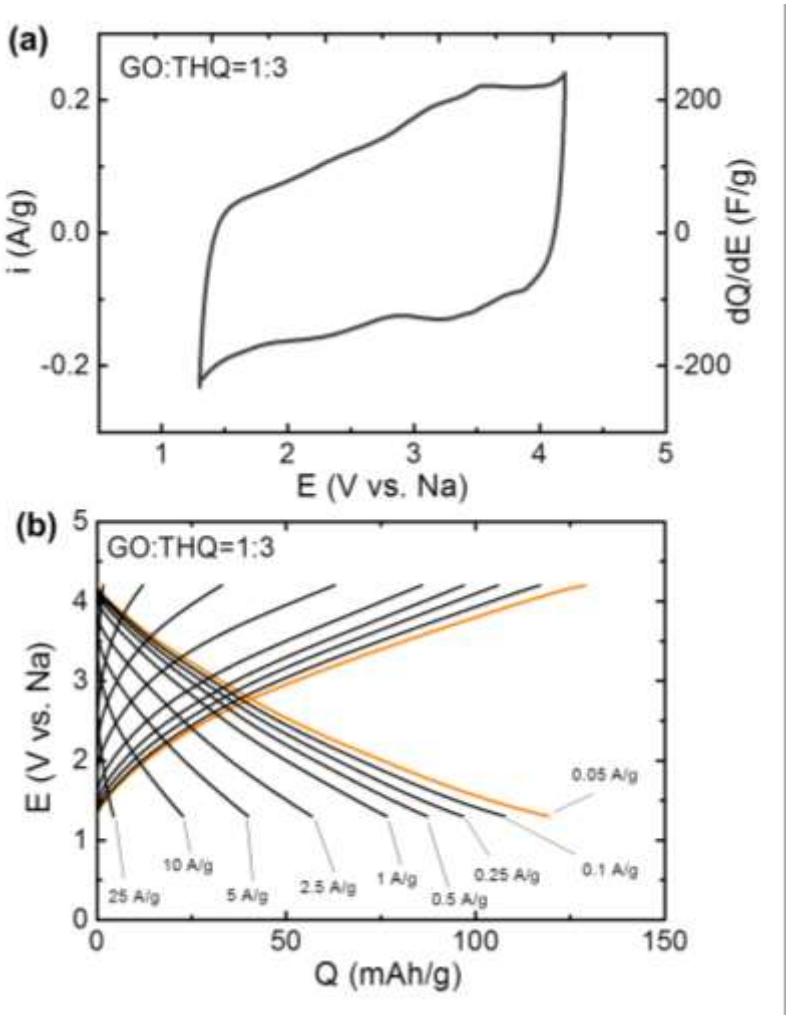

Figure 3.10 (a) The steady-state CV scan of the functionalized graphene electrode (GO:THQ= 1:3) in a Na-cell in the voltage range between 1.3 and 4.2 V vs. Na at a scan rate of 1 mV/s in 1M $NaPF_6$ in a mixture of EC and DMC (volume ratio 3:7). (b) Current density dependent charge and discharge curves for the graphene electrode (GO:THQ=1:3). The current density was controlled from 0.05 to 25 A/g in a voltage window of 1.3-4.2 V vs. Na. Before each discharge and charge process, the cells were held at a constant voltage of 4.2 or 1.3 V vs. Na for 30 minutes, respectively. The thickness of the electrode was ~225 μm for GO:THQ=1:3.

Recently, oxidized carbon foam electrodes have shown the surface redox reactions between oxygen functional groups and Na ions, in a similar way with Li, showing that functionalized carbon materials can also be utilized as positive electrodes for Na-ion batteries.[164] Electrochemical performance of the functionalized graphene electrodes was also evaluated in Na-cells. The CV scan of the graphene electrode (GO:THQ=1:3) showed redox peaks in a broad potential range of 2 ~ 4.2 V vs. Na that are ascribed to the surface redox reactions between oxygen functional groups introduced by THQ and Na ions (**Figure 3.10a**). It is worth to point out that the surface redox reactions on the functionalized graphene electrodes are mainly centered at higher potential region from 3 to 4.2 V vs. Na, which is significantly higher that (2~3 V vs. Na) of the oxidized carbon foam electrodes,[164] which may be attributed to the different chemical structures of oxygen functional groups in the graphene and carbon foam electrodes. The gravimetric capacity of the electrode (GO:THQ=1:3) was ~120 mAh/g at a slow rate of 0.05 A/g and ~76.5 mAh/g at 1 A/g (64% of the capacity at 0.05 A/g) in a Na-cell, showing comparable gravimetric capacity as well as rate capability to those measured in Li-cells (**Figure 3.10b**).

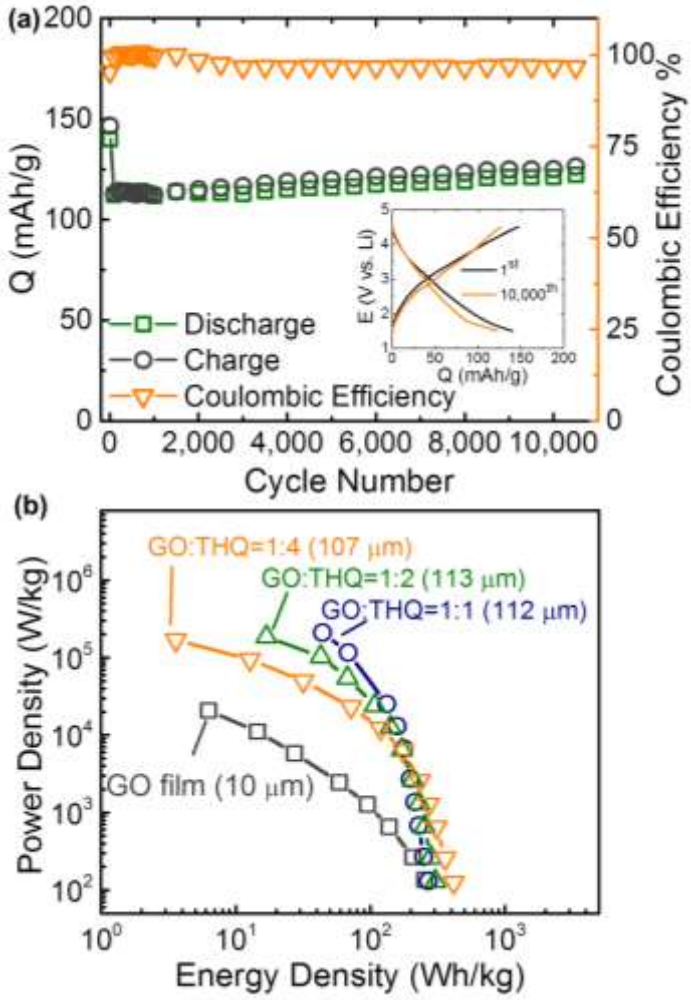

Figure 3.11 (a) Gravimetric charge and discharge capacities of the functionalized graphene electrode (GO:THQ=1:4) and its columbic efficiency as a function of cycle number up to 10,000 cycles. Charge and discharge capacities were measured at 0.1 A/g, once every 100 cycles up to 1,000 cycles and once every 500 cycles between 1,001 to 10,000 cycles, after voltage holding process for 30 minutes. Within these measurements at 0.1 A/g, the Li-cells were cycled at an accelerated rate of 10 A/g. The figure inset compares the charge and discharge curves for the first and the 10,000th cycle at 0.1 A/g. (b) Ragone plot comparing gravimetric energy and power density of the electrodes, which was calculated from galvanostatic data in Figure 3.7a-c and Figure 3.8a. Only the weight of positive electrode was considered for the calculation of the gravimetric energy and power density.

The functionalized graphene electrodes showed excellent cycling stability in Li-cells (**Figure 3.11a**). Galvanostatic charge and discharge cycle test showed that after

10,000 cycles, the capacity at 0.1 A/g retained 122 mAh/g which was 87.4% of the initial capacity, and the coulombic efficiency was maintained at 96.7~100% during the cycling test (**Figure 3.11a**). The energy and power characteristics of the electrodes in Li-cells were evaluated by a Ragone plot (**Figure 3.11b**) based on the galvanostatic charge and discharge tests (**Figure 3.7** and **Figure 3.8**). At a low power density of ~130 $W/kg_{electrode}$, the GO electrodes exhibited an energy density of ~254 $Wh/kg_{electrode}$ and the functionalized graphene electrodes showed progressively increased energy density with the THQ concentration: ~270 $Wh/kg_{electrode}$ for GO:THQ=1:1, ~304 $Wh/kg_{electrode}$ for GO:THQ=1:2, and ~416 $Wh/kg_{electrode}$ for GO:THQ=1:4. The maximum energy density (~416 $Wh/kg_{electrode}$) attainable at the functionalized graphene electrodes is higher than those of the oxidized CNT, oxidized CNT/graphene composite, and reduced GO film electrodes assembled by vacuum-filtration process (300~350 $Wh/kg_{electrode}$),[60, 63, 116] and approaches close to that of 3 μm thick thin-film CNT electrodes (~422 $Wh/kg_{electrode}$).[58] At a higher power density of ~10 $kW/kg_{electrode}$, the difference in the attainable energy density between the GO electrode (~16 $Wh/kg_{electrode}$) and the functionalized graphene electrodes (140~170 $Wh/kg_{electrode}$) became more significant. This energy and power characteristic of the 100 μm thick functionalized graphene electrodes is comparable to that of the 20 μm thick oxidized CNT electrode. It is interesting to note that, at an extremely high power density of ~100 $kW/kg_{electrode}$, the energy density trend of the functionalized graphene electrode becomes reversed with the THQ concentration: ~80 $Wh/kg_{electrode}$ for GO:THQ=1:1, ~40 $Wh/kg_{electrode}$ for GO:THQ=1:2, and ~12 $Wh/kg_{electrode}$ for GO:THQ=1:4. We postulate that the introduced surface redox reactions by THQ may give rise to the charge transfer resistance,

decreasing the attainable energy of the electrodes at an extremely fast discharge condition. It should be mentioned that the functionalized graphene electrode (GO:THQ=1:3) also delivered a high energy density of 292 $Wh/kg_{electrode}$ at a low power region (~120 $W/kg_{electrode}$) and maintained a significant energy density of 100 $Wh/kg_{electrode}$ at a high power region (~10 $kW/kg_{electrode}$) in Na-cells, showing promise for Na-ion batteries (**Figure 3.12**).

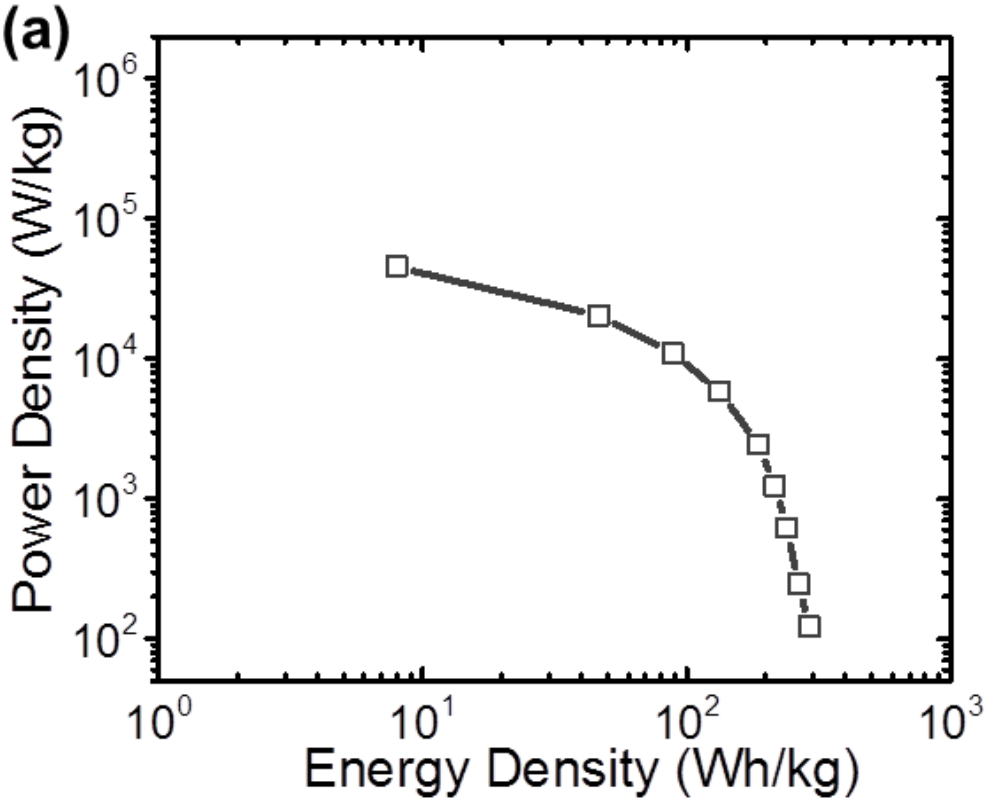

Figure 3.12 (a) Ragone plot for the functionalized graphene electrode (GO:THQ=1:3) in a Na-cell, which was calculated from galvanostatic data in Figure 3.10b. Only the positive electrode weight was considered for the calculation of the gravimetric energy and power density. The thickness of the electrode was ~225 µm.

3.4 Conclusions

In summary, we have assembled 3D functionalized graphene electrodes from the dispersion of GO in water at a low temperature of ~80 ^{0}C within a short period of time of ~3 hr under atmospheric condition using THQ as both the reducing and redox-active functionalization agent. THQ replaced electrochemically inactive oxygen groups on the surface of GO with redox-active oxygen functional groups on the surface of graphene during the reduction and functionalization process. The surface oxygen chemistry of the graphene electrodes and corresponding surface redox reactions can be controlled by the concentration of THQ relative to GO. 3D functionalized graphene electrodes delivered high gravimetric capacities of ~165 mAh/g in Li-cells and ~120 mAh/g in Na-cells with high redox potentials, which can be employed as positive electrodes for both Li- and Na-ion batteries. Owing to the 3D hierarchical porous structure and the enhanced surface redox reactions introduced by THQ, the functionalized graphene showed high energy density (up to ~410 $Wh/kg_{electrode}$) and high power density (over ~100 $kW/kg_{electrode}$), while maintaining cycling stability up to 10,000 cycles. The 3D functionalized graphene electrodes assembled by a simple aqueous process, provide a new opportunity to develop low-cost, large-scale, and high-performance positive electrodes for both Li- and Na-ion batteries.

CHAPTER 4. BIOMASS-DERIVED CARBONACEOUS POSITIVE ELECTRODES FOR SUSTAINABLE LITHIUM-ION STORAGE

Reproduced from Tianyuan Liu, Reza Kavian, Zhongming Chen, Samuel S. Cruz, Suguru Noda and Seung Woo Lee, *Biomass-derived carbonaceous positive electrodes for sustainable lithium-ion storage.* Nanoscale, 2016. **8**(6): 3671-3677. with permission from the Royal Society of Chemistry.

4.1 Introduction

Replacing fossil fuels with various types of clean and renewable energy sources is vital in order to effectuate the world's sustainable development.[165] However, inconstant and location dependent natures of renewable energy sources, such as wind or solar, require the integration with electrical energy storage systems for improving reliability.[1, 2] Electrochemical energy storage systems, including rechargeable lithium-ion batteries and electrochemical capacitors (ECs), take possession of several advantages for effective renewable energy storage, such as compact size, long cycle life, high efficiency, short charge/discharge time and pollution free operation.[1, 166] Despite these merits, high cost of electrode materials, such as transition metal oxides, limits their market penetration for large-scale energy storage applications.[1, 167] Thus, it is critical to develop low-cost, sustainable, and high-performance electrode materials to support

electrochemical energy storage devices in line with the green and renewable energy sources.[64, 71, 94]

Redox-active organic electrode materials derived from low-cost and sustainable sources has attracted extensive attention to replace transition metal based electrodes.[71, 137] In particular, organic carbonyl molecules showed high capacities (up to 580 mAh/g for $Li_xC_6O_6$),[65] by employing the reversible redox reaction between carbonyl group and lithium ion.[137] However, dissolution of these organic molecules into organic electrolytes during cycling limits their cycling stability within few hundred cycles.[83, 86, 132, 168] In addition, the insulating nature of organic molecules requires mixing with a large amount of conductive carbons during the electrode fabrication process to support electrical conductivity.[72, 82, 84, 137] Alternative approach to resolve these challenges is to incorporate redox-active oxygen functional groups on conductive carbon matrix, such as carbon nanotube or graphene, via surface oxidation process.[58, 60, 63, 169, 170] In addition, these functionalized carbon materials can be fabricated as free-standing electrodes. Free-standing carbon electrodes are free of metal current collector, which can improve electrochemical performance of practical devices.[63] Free-standing Oxidized carbon nanotube or reduced GO electrodes show enhanced rate capability as well as cycling stability over 1,000 cycles owing to the covalent-bonded oxygen functional groups on the conductive carbon matrix.[169, 170].

Biomass is renewable, cheap, and is the most abundant carbon source for synthesizing sustainable functional carbon materials.[171-173] Among various conversion methods, a hydrothermal carbonization (HTC) process has shown promising outcome in converting biomass to various functional carbon materials utilizing its unique

advantages, including environmentally benign process, relatively low reaction temperature, and versatile morphology control of carbon products.[171] Recent studies synthesized carbon spheres from carbohydrates, such as glucose, sucrose, or cellulose, via the HTC process, which can be used as catalyst support[174] or active electrode materials for electrochemical double layer capacitor (EDLC) applications.[175, 176] However, redox-active properties of these carbon spheres have not been explored intensively. If comprehensively studied and rationally utilized, these properties can open up new possibilities to develop renewable electrode materials for lithium-ion batteries or lithium-ion capacitors.

In this study, for the first time, we demonstrate that carbon sphere products from glucose via a HTC process have redox-active properties with lithium ions, which enables those carbon spheres as active electrode components for lithium-ion batteries or capacitors. We assembled free-standing composite electrodes by mixing the carbon spheres with sub-millimeter long few-walled carbon nanotubes (FWNTs)[177, 178] using vacuum-filtration process. In addition, we showed that a microwave treatment can improve connectivity between the carbon spheres and FWNTs. After the microwave process, the composite electrode exhibits a high capacity of ~155 $mAh/g_{electrode}$ with significantly enhanced rate capability compared to that before the microwave treatment. Moreover, the electrode shows an excellent cycling stability up to 10,000 cycles. Considering the redox-active carbon spheres are prepared from earth-abundant biomass via scalable HTC process, this approach guides a promising green route to develop sustainable organic electrodes for large-scale energy storage devices.

4.2 Experimental

Sample preparation: Carbon sphere synthesis. 3 mg/mL of D-(+)-Glucose (Sigma Aldrich) was dissolved in DI-water by sonication for 30 min. The mixture was sealed in a Teflon-lined autoclave and maintained at 200 °C for 18 h for a hydrothermal carbonization (HTC) process, forming carbon spheres. The autoclave was naturally cooled down to room temperature as the HTC process finished. ***FWNT.*** FWNTs were synthesized by chemical vapor deposition method according to previous papers.[177, 178] The FWNTs were dispersed in a mixture of ethanol and DI-water (1:1 volume ratio) by short sonication. Pristine FWNT films were prepared by vacuum- filtration process. ***Composite film fabrication.*** The aqueous dispersion of carbon spheres was mixed with different amounts of FWNTs by short sonication for ~10 min. Composite films were fabricated via vacuum-filtration process of the mixture. The films were dried in a vacuum oven at 70 ^{o}C overnight. Microwave treatment was carried out for 30 s at a power of 1250 W under Ar protection using a commercial microwave (Panasonic).

Characterization: The microstructures of the films were characterized using a SEM (Hitachi SU8010, operated at 5 kV). The Raman spectra were collected by Thermo Nicolet Almega XR Dispersive Raman Spectrometer using a 488-nm wavelength laser. XPS (Thermal Scientific K-alpha XPS instrument) was employed to analyze the chemical composition of the films. High-resolution C1s peaks were fitted using XPSPEAKS 4.1 software. Electrical conductivities of the films were measured by a standard four-point probe configuration (Signatone).

Electrochemical measurements: Swagelok cells were assembled in an Argon filled glovebox (MBraun). The carbon (FWNT or composite) films and pieces of Li foil were used as the positive and negative electrodes, respectively. The negative and positive

electrodes were separated by two pieces of Celgard 2500 separators. 1M $LiPF_6$ in a mixture of EC and DMC (3:7 volume ratio, BASF) was used as an electrolyte. The electrochemical characteristics of the carbon films were evaluated using Bio-Logic VMP3 potentiostat/galvanostat at room temperature. The voltage window was kept at 1.5-4.5 V vs. Li for cyclic voltammetry and galvanostatic charge/discharge tests. Current densities were controlled from 0.05 to 100 A/g during the galvanostatic tests. At the end of each charging or discharging process, a voltage holding was applied for 30 min at either 4.5 V or 1.5 V vs. Li. The cycling stability of the carbon electrodes were tested via an accelerated cycling method up to 10 000 cycles based on a previous report.[170] Loading density of the positive electrodes was in the range of 0.9 ~ 3 mg/cm^2.

4.3 Results and Discussions

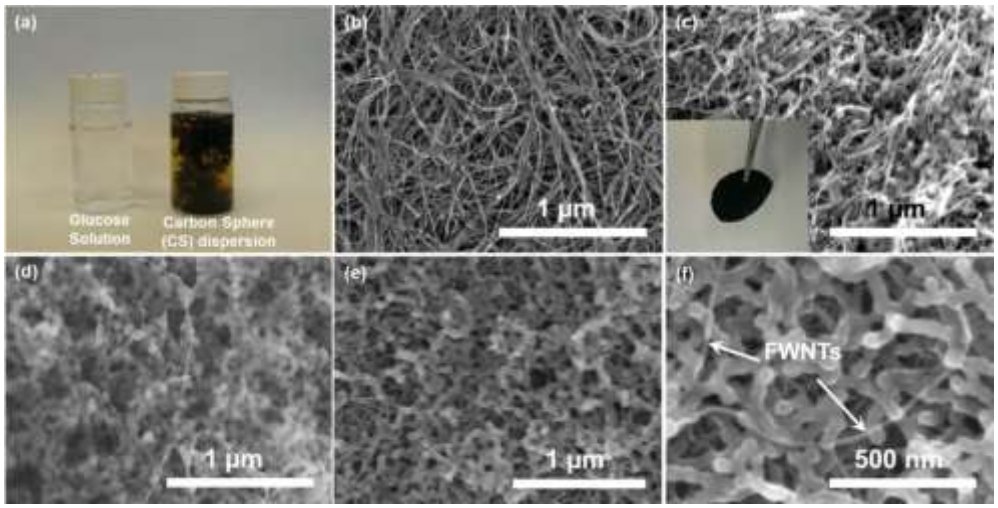

Figure 4.1 (a) Digital images of the glucose aqueous solution (3 mg/mL, left) and collidial dispersion of synthesized carbon spheres (CSs) after the hydrothermal carbonization (HTC) process (right). SEM images of (b) the pristine few-walled carbon nanotube (FWNT) film and composite films consisting of (c) 40 wt% of CSs (CS-0.4), (d) 68 wt% of CSs (CS-0.68). The digital image of the composite film (CS-0.4) fabricated by vacuum-filtration process is shown in the inset (c). (e) Low- and (f) high-magnification SEM images of the composite film (CS-0.68) after the microwave process at 1250 W for 30 s in Ar.

Table 4.1 Densities and electrical conductivities of the pristine FWNT and composite films.

Sample	Density (g/cm^3)	Electrical Conductivity (Scm^2/g)
FWNT	0.24	209.2
FWNT-MW	0.20	183
CS-0.4	0.37	93
CS-0.4-MW	0.34	93.8
CS-0.68	0.41	64.4
CS-0.68-MW	0.35	75.7

The carbon spheres were prepared from an aqueous solution of glucose (3 mg/mL) via a HTC process at 200 ^oC for 18 h, during which the transparent glucose solution was transformed into a brownish colloidal dispersion (**Figure 4.1a**). The HTC process consists of complex chemical transformation cascades, including dehydration, condensation, polymerization and aromatization reactions, which results in the formation of carbon-rich organic compounds (carbon spheres).[171, 179-181] The sizes of synthesized carbon spheres are mainly in the range of 60 - 100 nm as shown in **Figure 4.2c**. Free-standing composite films were fabricated via filtering the aqueous mixture of carbon spheres and FWNTs, where sub-millimeter long FWNTs were employed as a conductive agent (**Figure 4.1c inset**). Pristine FWNT films were also prepared via vacuum-filtration process for comparison. The FWNT films exhibited intertwined network structure with a high electrical conductivity of ~209 Scm^2/g (**Figure 4.1b** and **Table 4.1**). The density of a composite film with 40 wt% of carbon spheres (CS-0.4) increased to 0.37 g/cm^3 from 0.24 g/cm^3 of the pristine FWNT, whereas electrical conductivity of the composite films decreased to ~93 Scm^2/g (**Table 4.1**). Incorporating

more carbon spheres into the composite electrode to 68 wt% (CS-0.68) further increased the density to 0.41 g/cm^3 and decreased the electrical conductivity to ~64.4 Scm^2/g (**Table 4.1**). Most of the carbon spheres were attached on the surface FWNTs in the composite film with a lower loading (CS-0.4) (**Figure 4.1c**), while considerable amount of the carbon spheres was separated from FWNTs in the film with a higher loading (CS-0.68) (**Figure 4.1d**, **Figure 4.2b**). Irradiating microwave to nanocarbon materials has been widely used as a rapid heat treatment method.[149, 182, 183] After a microwave process for 30 s under Ar environment, the carbon spheres in the film (CS-0.68) were 'glued' together forming peanut-shaped nanorod structures, creating a dense network structure which was well threaded by FWNTs (**Figure 4.1e** and **f**, CS-0.68-MW). During the microwave treatment, FWNTs in the composite films strongly absorbed the microwave and act as an internal heat source which can be heated up to up to 2000 ^{o}C.[184-186] Therefore, we postulated that the heated FWNTs enable the reconstruction of the interface between CSs and FWNTs, giving rise to the fusion of CSs and FWNTs. The electrical conductivity of the film after the microwave process (CS-0.68-MW) was found to increase to ~75.7 Scm^2/g, owing to the improved connectivity between CSs and FWNTs during the process.

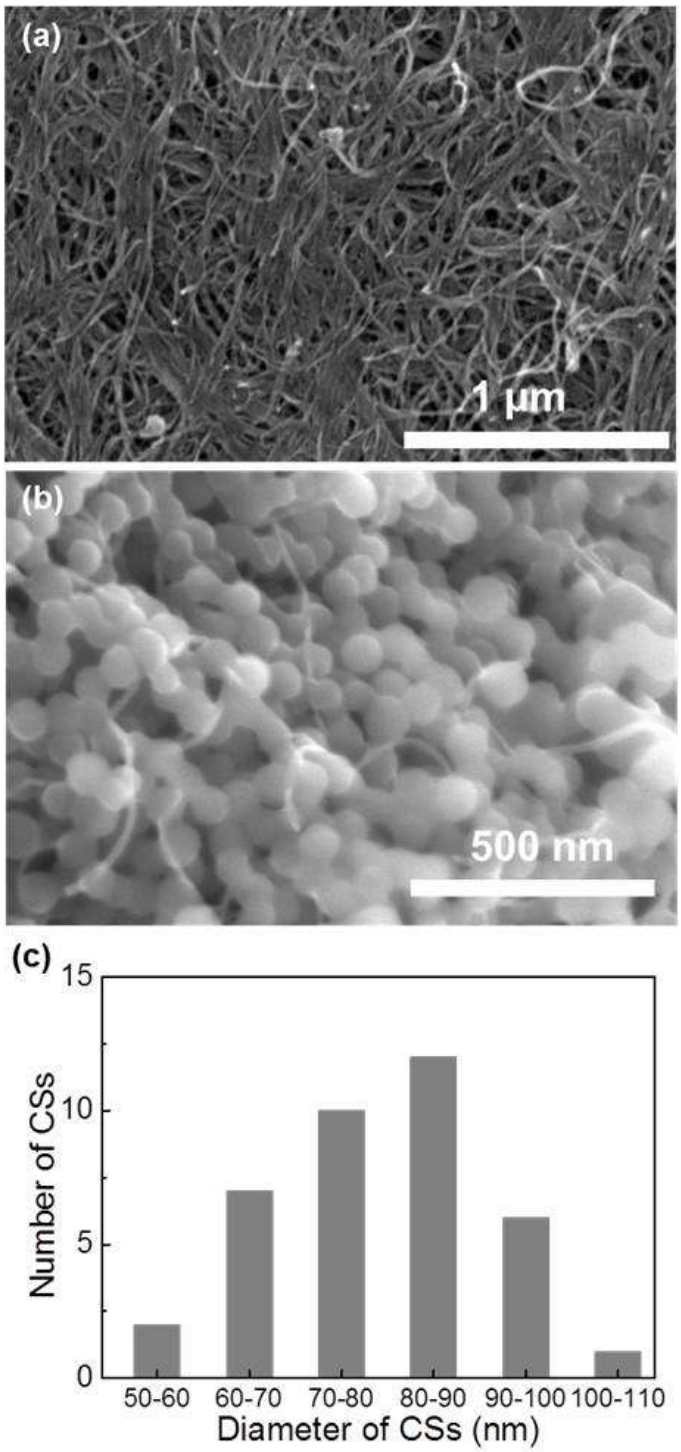

Figure 4.2 SEM images of (a) the pristine few-walled carbon nanotube (FWNT) film after the microwave process and (b) the composite film including 68 wt% of carbon spheres (CS-0.68). (c) A histogram of the diameter of the carbon spheres, which was analyzed by SEM. The average diameter is 79.9±11.9 nm by counting 38 carbon spheres.

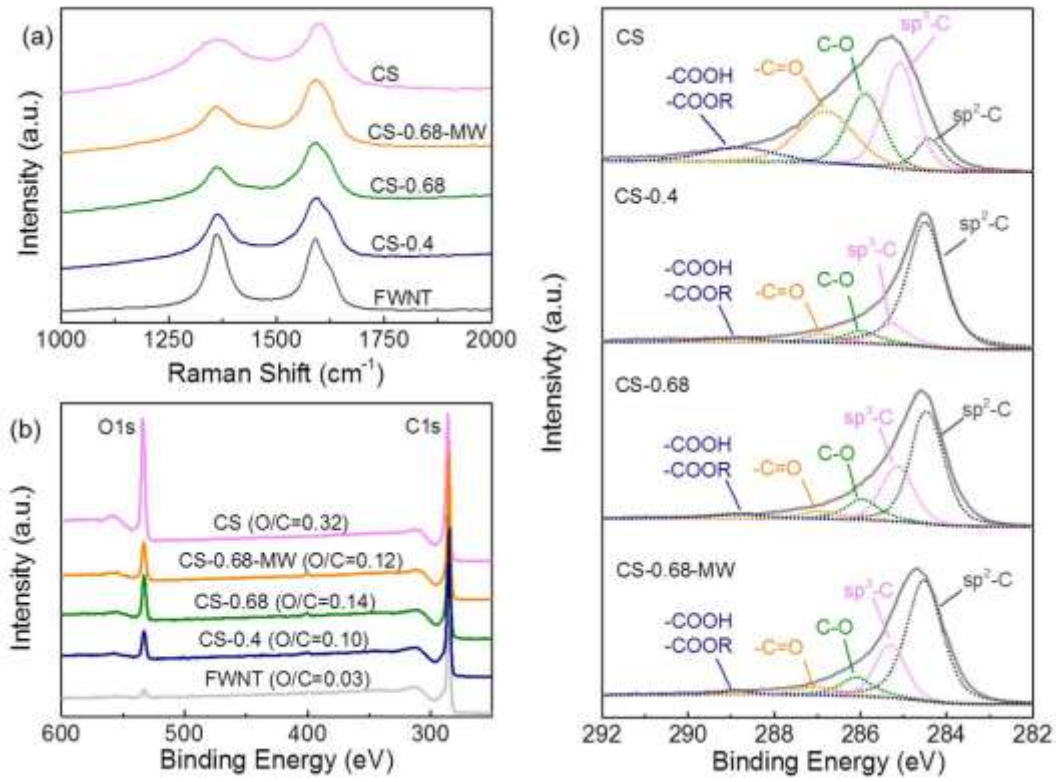

Figure 4.3 (a) Raman spectra, (b) X-ray photoelectron spectroscopy (XPS) wide scan survey of as-synthesized carbon sphere (CS), pristine FWNT, and composite films at different loadings of CSs. (c) The high resolution C1s spectra of the CS and composite films.

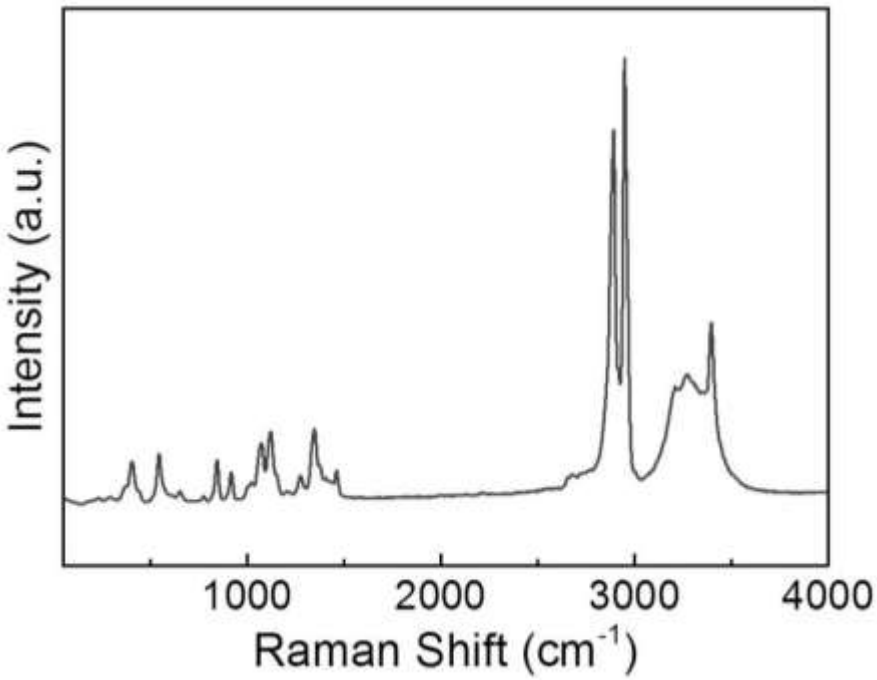

Figure 4.4 Raman spectrum of glucose in the range of 50-4000 cm^{-1}. A broad plateau between 3100 and 3500 cm^{-1} is associated with bonded hydroxyl groups, while superimposed three sharp peaks above 3200 cm^{-1} are ascribed to non-hydrogen-bonded hydroxyl groups.[187] Two sharp peaks between 2800 and 3000 cm^{-1} can be assigned to C-H symmetric and asymmetric stretching. A complex series of sharp peaks below 1200 cm^{-1} are due to the vibration of the C-O, C-C, and C-O-H groups.

Chemical structure of the carbon spheres was investigated by Raman spectroscopy and XPS. The Raman spectrum of the carbon spheres exhibited two broad overlapping bands at ~1350 cm^{-1} (D mode) and ~1580 cm^{-1} (G mode) (**Figure 4.3a**), which are completely different from that of glucose (**Figure 4.4**). Rather, these two peaks resemble the characteristics of carbon materials [188-190] that includes sp^2 hybridized carbon atoms in benzene or condensed benzene structures.[190] The pristine FWNT film displayed much sharper peaks, and the spectrum of the composite films showed blended characteristics between the carbon sphere and FWNT (**Figure 4.3a**, **Figure 4.5a**). Chemical elements analysis of the carbon sphere and composite films was conducted by XPS (**Figure 4.3b**, **Figure 4.5b**). As-synthesized carbon spheres showed significant oxygen content with an atomic ratio of oxygen to carbon (O/C ratio) of 0.32. According to the LaMer model, hydrothermally synthesized carbon spheres have a core-shell type structure consisting of highly dehydrated hydrophobic core and oxygen-rich hydrophilic shell.[171, 179] Thus, the high O/C ratio of the carbon spheres can be attributed to a large number of oxygen functional groups on the surface.[172] On the other hand, pristine FWNT film exhibited negligible oxygen content with an O/C ratio of 0.03, which was probably due to the adsorbed oxygen or introduced defects during the dispersion process. The O/C ratios of the composite films were found to increase from 0.10 to 0.14 as the loading of the carbon sphere increased from 40 wt% (CS-0.4) to 68 wt% (CS-0.68) (**Figure 4.3b**). Detailed chemical structures of the composite films were further analyzed

by fitting the high resolution C1s peaks (**Figure 4.3c**).[58] The main peak at 284.5 eV was attributed to sp^2 hybridized graphitic carbon,[58] and binding energy for sp^3 hybridized diamond-like carbon shifted to a higher binding energy at 285.2±0.1 eV. C1s spectra of the carbon sphere exhibited dominant sp^3 hybridized carbon peak with minor sp^2 hybridized graphitic carbon peak, while the FWNT film showed major sp^2 carbon peak with minor sp^3 carbon peak (**Figure 4.5c**). In addition, various oxygen functional groups, including hydroxyl/phenolic (C-O centered at 286.0±0.1 eV), carbonyl (C=O centered at 286.9±0.1 eV), and carboxylic/carboxylate (COOH/COOR, centered at 288.9±0.1 eV),[63] were found for the carbon sphere, which is consistent with LaMer model. Therefore, the ratio of sp^3 peak to sp^2 peak and the amount of oxygen functional groups progressively increased with higher loading of the carbon spheres in the composite films (**Figure 4.3c**). After the microwave process, the O/C ratios of the composite films were found to slightly decrease from 0.10 to 0.08 for CS-0.4 and from 0.14 to 0.12 for CS-0.68 (**Figure 4.3b**, **Figure 4.5b**) presumably due to further carbonization of CSs. Fourier transform infrared (FTIR) spectroscopy comparison of the composite films before (CS-0.68) and after (CS-0.68-MW) the microwave treatment showed significant decrease of peaks in the range of 1000-1300 cm^{-1}, which correspond to the C-OH stretching and OH bending vibrations,[179] further confirming the carbonization process of the carbon spheres (**Figure 4.6**).

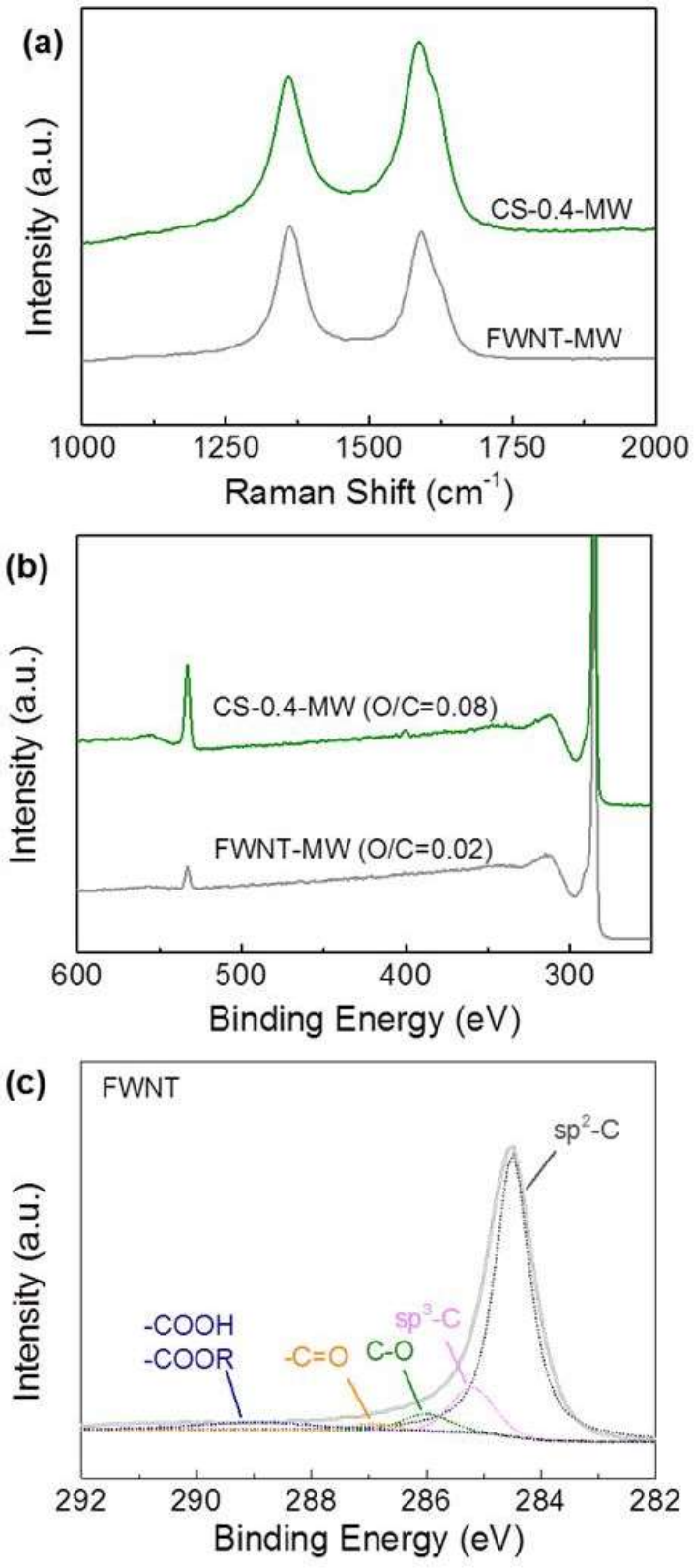
(a)
Intensity (a.u.)
CS-0.4-MW
FWNT-MW
1000
1250
1500
1750
2000
Raman Shift (cm-1)
(b)
Intensity (a.u.)
CS-0.4-MW (O/C=0.08)
FWNT-MW (O/C=0.02)
600
500
400
300
Binding Energy (eV)
(c)
FWNT
sp2-C
sp3-C
-COOH
-COOR
-C=O
C-O
Intensity (a.u.)
292
290
288
286
284
282
Binding Energy (eV)

Figure 4.5 (a) Raman spectra, (b) XPS wide scan survey of the microwave processed FWNT film and the CS-0.4-MW. (c) High resolution C1s spectra of pristine FWNTs.

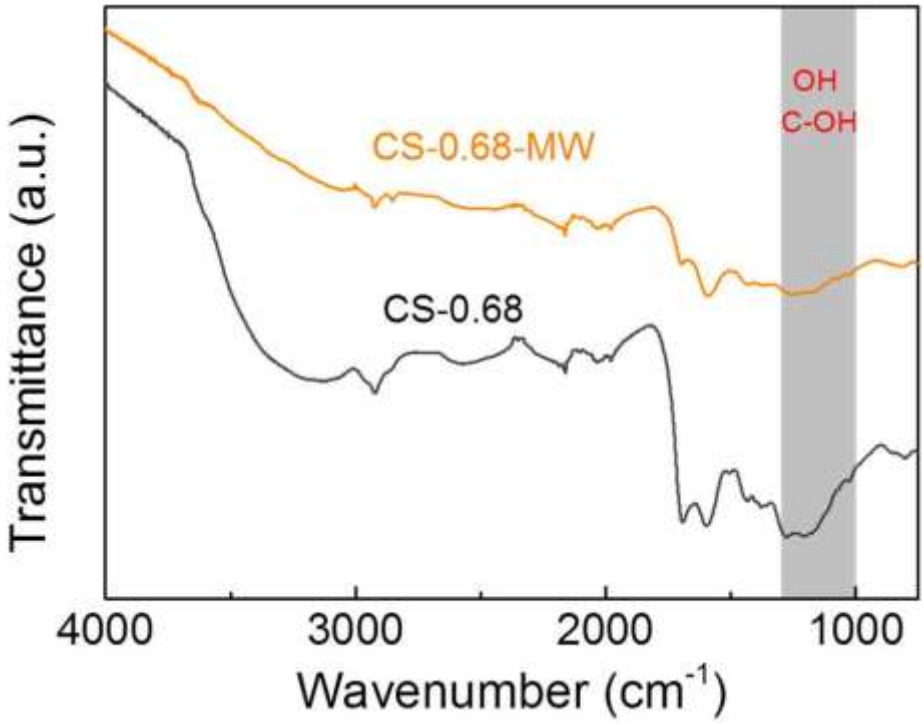

Figure 4.6 (a) FTIR spectroscopy comparison of the composite films before (CS-0.68) and after (CS-0.68-MW) microwave process.

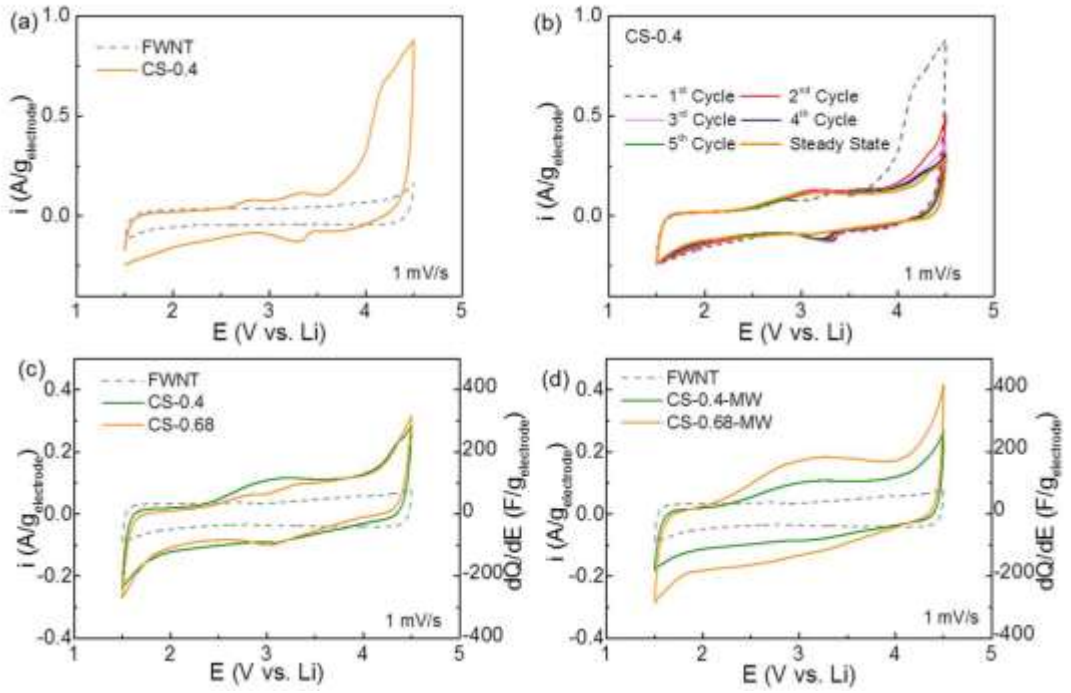

Figure 4.7 CV scan comparisons of the FWNT and composite electrodes at 1 mV/s in lithium cells with 1M $LiPF_6$ in a mixture of EC and DMC (3:7 volume ratio). (a) Comparison of initial CV scans of the pristine FWNT electrode and CS-0.4. (b) CV scans of the CS-0.4 as a function of cycle number. Comparisons of steady-state CV scans for different composite electrodes (c) before and (d) after microwave process. CV scans of the pristine FWNT electrodes were utilized as guidelines. The weight of the total positive electrode (carbon spheres + FWNTs) was considered in the current density calculation.

Cyclic voltammetry (CV) measurements were conducted to investigate the charge storage characteristics of the carbon spheres in lithium cells. The first CV scan of the pristine FWNT electrode displayed a rectangular shape (**Figure 4.7a**) and subsequent potential cycling showed negligible difference (**Figure 4.8a**), indicative of charge storage based on double-layer capacitance. In contrast, the first CV scan of the composite electrodes including the carbon spheres exhibited oxidation current with an onset potential of ~2.5 V vs. Li and a strong oxidation wave at an onset potential of ~3.7 V vs. Li (**Figure 4.7a** and **Figure 4.8b-d**). The strong oxidation wave may be attributed to the

anodic polymerization of aromatic hydrocarbons.[166, 191-194] Upon subsequent potential cycling, the anodic oxidation current gradually decreased and finally arrived at steady-state, which is accompanied by the formation of a broad redox peak in voltage range of 2.2 - 3.7 V vs. Li (**Figure 4.7b**). The remaining redox peak of the composite electrodes can be ascribed to the surface redox reactions between oxygen functional groups on the carbon spheres and lithium ions. Comparison of steady-state CV scans showed that the composite electrodes have higher gravimetric current densities compared to that of pristine FWNT owing to the additional surface redox reactions on top of double layer capacitance (**Figure 4.7c**). Interestingly, there was a little difference in CV scans between the CS-0.4 and CS-0.68 (**Figure 4.7c**). We postulate that a significant amount of carbon spheres was not effectively utilized in the composite film with high loading (68 wt%), since many carbon spheres were separated from conductive FWNT matrix (**Figure 4.1d**). Comparison of steady-state CV scans after the microwave process displayed a significant increase in current for the CS-0.68-MW (**Figure 4.9a**), resulting in higher gravimetric current density compared to that of the CS-0.4-MW (**Figure 4.7d**). Moreover, the CS-0.68-MW retained its redox behavior at a high scan rate of 100 mV/s (**Figure 4.9b**). Such enhanced charge storage performance after the microwave treatment can be attributed to the increased redox-active surface as well as electrical conductivity on the connected carbon nanorod structure that was well threaded by conductive FWNTs (**Figure 4.1e** and **f**).

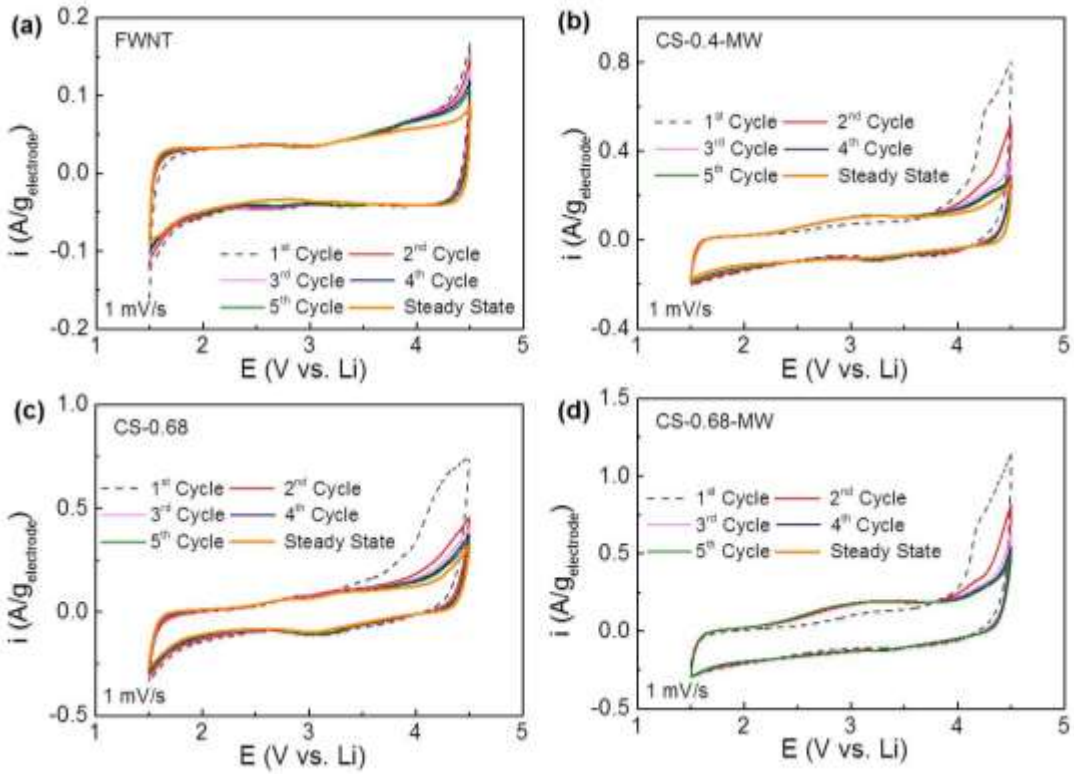

Figure 4.8 CV scans of (a) the pristine FWNTs electrode, (b) CS-0.4-MW, (c) CS-0.68, and (d) CS-0.68-MW as a function of cycle number.

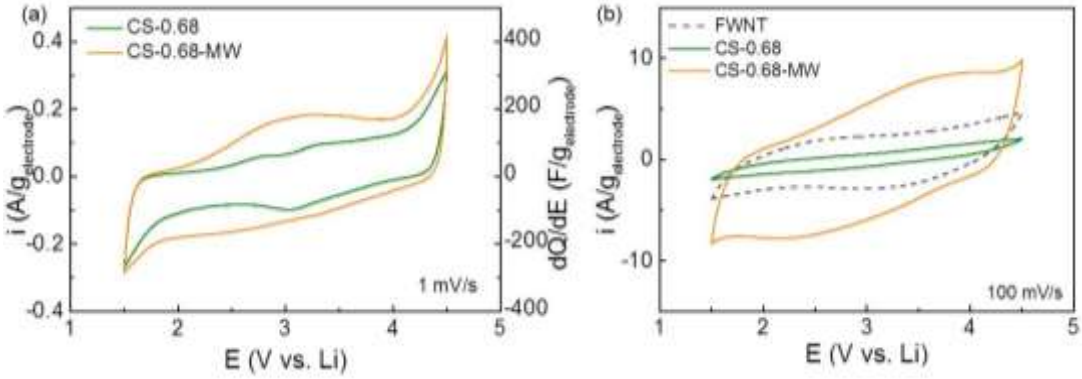

Figure 4.9 Comparison of steady state CV scans before (CS-0.68, olive) and after (CS-0.68-MW, orange) microwave process at (a) 1 mV/s and (b) 100 mV/s. A CV scan of the FWNT electrode was compared as control in (b).

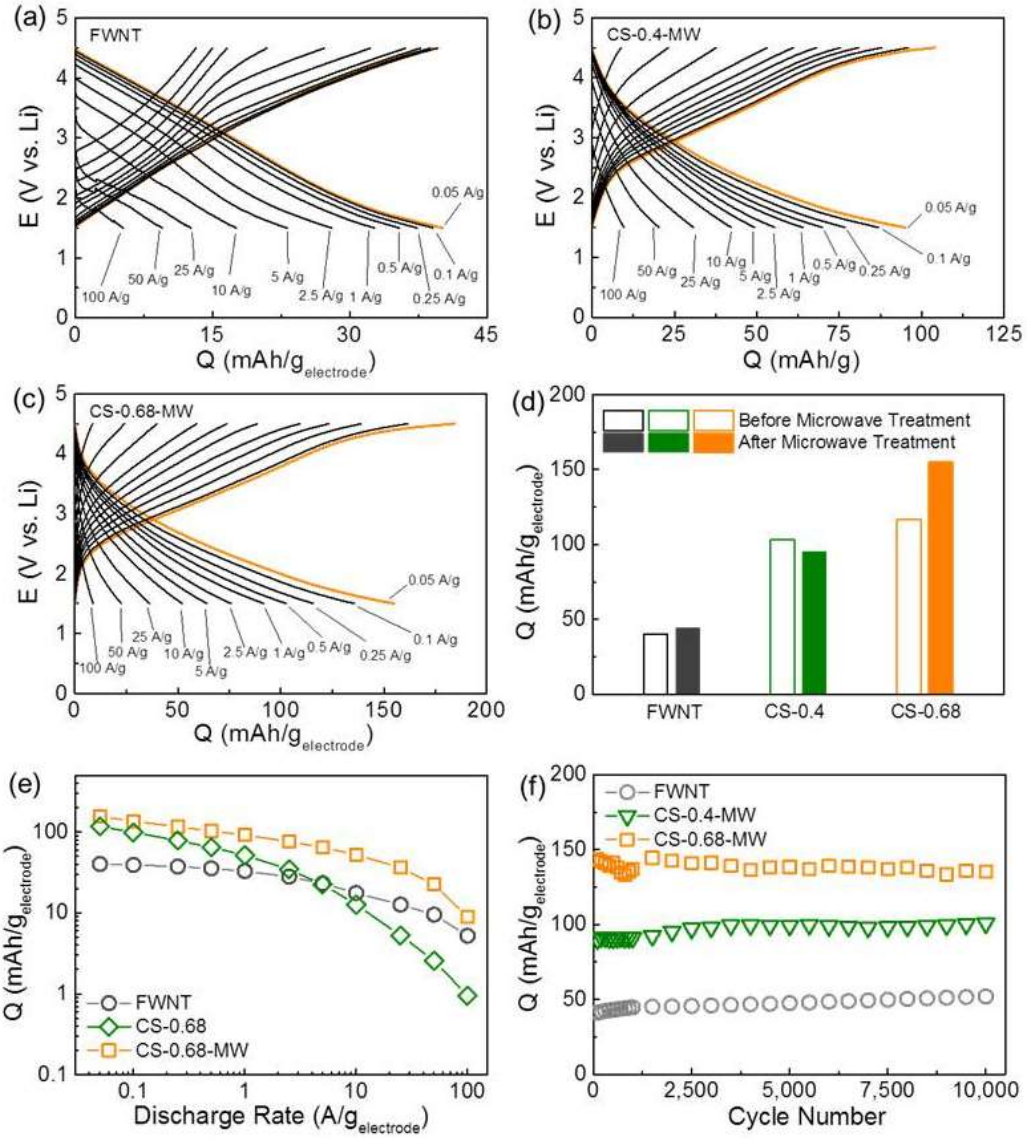

Figure 4.10 Rate-dependent galvanostatic charge and discharge curves of (a) the pristine FWNT electrode, (b) CS-0.4-MW, and (c) CS-0.68-MW in lithium cells. (d) Discharge capacity comparisons of the FWNT and composite electrodes at 0.05 A/g before and after microwave treatments. (e) Specific capacity comparison of the FWNT, CS-0.68 and CS-0.68-MW as a function of discharge current densities. (e) Specific capacities of the FWNT, CS-0.4-MW and CS-0.68-MW as a function of cycle number up to 10,000 cycles using an accelerating cycling method.[170] Data points indicate specific discharge capacities of the electrodes measured at a slow rate of 0.1 A/g. Between each slow measurement, the cells were cycled at high current density of 10 A/g.

Charge storage performance of the electrodes was further evaluated using rate-dependent galvanostatic charge and discharge tests (**Figure 4.10a-c** and **Figure 4.11**).

The pristine FWNT electrode delivered a low specific capacity of ~40 mAh/$g_{electrode}$ at 0.05 A/g, while the capacities of the composite electrodes were significantly increased to ~103 mAh/$g_{electrode}$ for CS-0.4 and ~117 mAh/$g_{electrode}$ for CS-0.68 (**Figure 4.10d**). After the microwave treatment, the FWNT and CS-0.4 showed negligible changes of their capacities, whereas the CS-0.68 exhibited considerable increase of capacity from ~117 to ~155 mAh/$g_{electrode}$ owing to the improved utilization of the carbon spheres for charge storage (**Figure 4.10d**). This capacity is higher than those of previous reported carbon based electrodes (38~135 mAh/g)[54, 60, 63, 116, 195] and comparable to those of recently reported redox-active graphene electrodes (~160 mAh/g).[169] Based on the rule of mixture, specific capacity of the carbon spheres in the CS-0.68-MW was estimated to be ~210 mAh/$g_{carbon\ sphere}$, which is higher than those of previous reported redox-active polyimides[90, 196, 197] and carbonyl compounds.[88, 137] Microwave treatment also significantly improved the rate capability of the composite electrode (CS-0.68). The capacities of the CS-0.68 were compared before and after microwave treatment as a function of discharge rate (**Figure 4.10e**). Rate dependent capacity curve of the CS-0.68-MW was almost parallel with that of the pristine FWNT electrode, while the curve of the CS-0.68 dropped rapidly when the current densities were higher than 1 A/g (**Figure 4.10e**). The CS-0.68-MW retained ~59% of the capacity when the current density increased from 0.05 to 1 A/g, and ~15% at an extremely high current density of 50 A/g. The significant enhancement in both capacity and rate performance after the microwave process can be attributed to the transformation of isolated carbon spheres into connected peanut-shaped nanorods penetrated by FWNTs (**Figure 4.1e** and **f**), which facilitates

electronic transportation from FWNT network to redox-active sites on the carbon spheres.

It should be noted that the composite electrodes have sloped charge and discharge profiles. Our recent DFT calculation study on similar redox reactions of the reduced GO showed that various oxygen functional groups on the GO have different redox potentials depending on their oxygen chemistry as well as local chemical environments [169]. Thus, the sloped profiles of the composite electrode can be attributed to overlap of double-layer capacitance and the redox reactions of various oxygen functional groups on the carbon spheres.

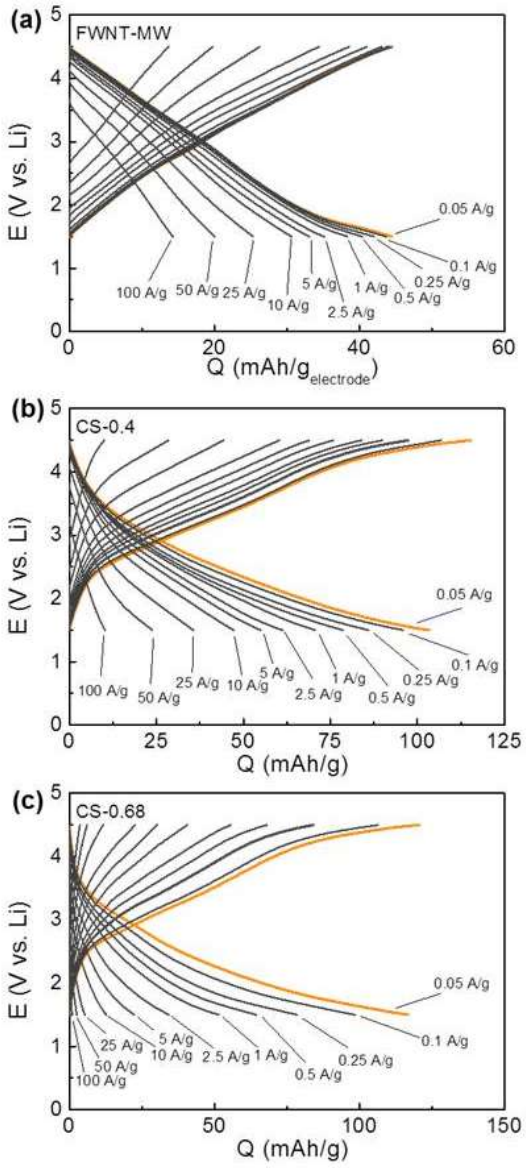

Figure 4.11 Rate-dependent galvanostatic charge and discharge curves for (a) the microwave processed FWNT film (FWNT-MW), (b) CS-0.4, and (c) CS-0.68 in lithium cells.

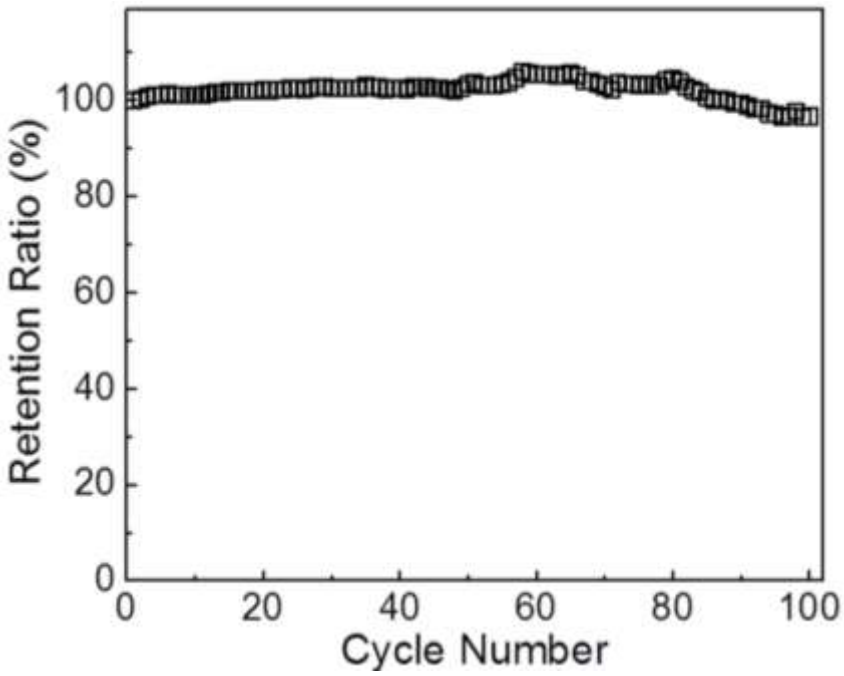

Figure 4.12 Cycling stability of CS-0.68-MW at a current density of 0.1 A/g up to 100 cycles.

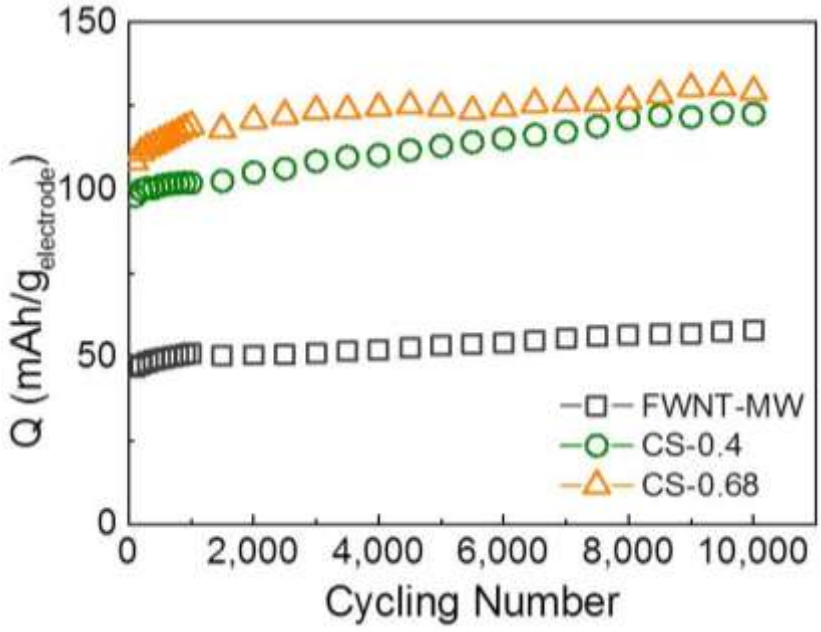

Figure 4.13 Specific capacities of the FWNT-MW, CS-0.4 and CS-0.68 as a function of cycle number up to 10,000 cycles using an accelerating cycling method. Data points indicate specific discharge capacities of the films measured at a slow rate of 0.1 A/g. Between each slow measurement, the cells were cycled at high current density of 10 A/g.

Cycling stability of the electrodes was evaluated at 0.1 A/g up to for 100 cycles (**Figure 4.12**), which showed no obvious capacity fading. In order to evaluate the long term stability of the electrodes, an accelerated cycling method, was also conducted according to our previous works.[169, 170] Specific capacities displayed in **Figure 4.10** were measured at a slow current density of 0.1 A/g, while the cells were accelerated at a high current density of 10 A/g between each measurement. The pristine FWNT and composite electrodes exhibited a negligible capacity decrease up to 10,000 cycles (**Figure 4.10f, Figure 4.13**). The excellent cycling stability of the composite electrodes, which is superior than most of the organic electrode materials,[72, 81, 82, 84, 86, 88, 137, 168] can be attributed to the covalently bonded redox-active oxygen functional groups on the carbon spheres.

4.4 Conclusions

In summary, redox-active carbon spheres were synthesized from the glucose aqueous solution via the HTC process. The free-standing composite electrodes were fabricated by mixing the carbon spheres with sub-millimeter long FWNTs using vacuum-filtration process. The composite electrodes exhibited broad redox peaks in voltage range of 2.2 - 3.7 V vs. Li and delivered high specific capacities up to ~155 $mAh/g_{electrode}$ in lithium cells. In addition, these electrodes maintained their high capacity up to 10,000 cycles. Moreover, we demonstrated that microwave treatment can improve the utilization of carbon spheres for effective charge storage. The simple HTC conversion process from earth-abundant biomass source to redox-active electrode material enables the development of high-performance lithium-ion storage systems, which can provide a sustainable solution towards clean and renewable energy storage.

CHAPTER 5. SELF-POLYMERIZED DOPAMINE AS AN ORGANIC CATHODE FOR LI- AND NA-ION BATTERIES

Reproduced from Tianyuan Liu, Ki Chul Kim, Byeongyong Lee, Zhongming Chen, Suguru Noda, Seung Soon Jang and Seung Woo Lee *Self-polymerized dopamine as an organic cathode for Li- and Na-ion batteries.* Energy & Environmental Science, 2017. **10**(1): 205-215 with permission from the Royal Society of Chemistry.

5.1 Introduction

Organic electrode materials have been intensively investigated to replace conventional transitional metal based inorganic cathodes for rechargeable batteries.[66, 71] This is because of their potential advantages, including high theoretical capacity, environmental friendliness, and use of low cost and earth-abundant resources, which is ideal for large-scale electrical energy storage applications, such as grid load-leveling, renewable energy storage, and electric vehicles.[64, 66, 71] The past few decades have witnessed the development of various organic electrode materials, such as conductive polymers,[198, 199] organosulfur compounds,[74, 75] organic free-radical compounds,[76, 77] and organic carbonyl compounds.[78-80, 86, 137, 168, 200] Despite their high theoretical capacities, the development of organic cathodes has been hindered by two factors, which significantly limits their practical applications. First, most of the organic molecules are highly soluble in organic electrolytes, which results in low cycling

stability. The second shortcoming is their poor electrical conductivity limiting the rate-performance of the electrodes.

A promising strategy to overcome these issues is to polymerize redox-active molecules onto conductive carbon substrates.[90, 92, 166] In this nanocomposite structure, the linkage of molecules by covalent bond prevents the dissolution of molecules, while conductive carbon network supports fast redox reactions in the polymer. Utilizing this strategy, Song *et. al* synthesized poly (anthraquinonyl sulfide) and polyimide on graphene flakes, demonstrating significantly enhanced rate performances of the composite electrodes as organic cathodes in Li-cells.[90] However, most of the reported polymerization processes of carbonyl compounds are complicated and usually introduce inactive linkers.[86, 90] In addition, the electrochemical performance of the composite electrodes significantly depends on the morphology of the polymer coatings on the substrate.[92] This indicates that there is an optimized interface structure between polymer coating and conductive substrate that can maximize the electrochemical performance of the composite electrodes. Thus, identifying a simple and versatile polymerization process that enables the strong adhesion of redox-active carbonyl compounds on the surface of conductive substrates is highly desirable.

With a similar molecular structure to adhesive proteins in mussel, dopamine can be oxidized and self-polymerized into polydopamine in alkaline aqueous solutions, generating adhesive polymer coatings on various types of substrates.[201-205] After a series of cyclisation and oxidation reactions in alkaline environment, it is proposed that the dopamine can be oxidized into 5,6-indolequinone before the polymerization (Scheme 5.1).[206] We noticed that 5,6-indolequinone has a similar molecular structure with

benzoquinone and naphthoquinone which have two redox-active quinone groups that can store Li- or Na-ions.[207-209] Thus, if the polymerized form of 5,6-indolequinone or other dopamine intermediates have redox-active properties with Li- or Na-ions, this polydopamine can be a promising carbonyl-based cathode for rechargeable batteries (Scheme 5.1). However, the redox properties of polydopamine with Li- or Na-ions remain unclear. Here, we investigate the electrochemical properties of polydopamine by both computational and experimental methods. Density functional theory (DFT) calculations show the multiple redox reactions of the polydopamine with electrolyte ions at high voltage region of 2.5~4.1 V vs. Li, which is also confirmed by cyclic voltammetry measurements. To maximize its electrochemical performance, we fabricate flexible, free-standing hybrid films via spontaneous coating process of polydopamine on few-walled carbon nanotubes (FWNTs) and continuous vacuum-filtration method. Hybrid electrodes consisting of polydopamine-coated FWNTs exhibit enhanced rate-performance and excellent cycling stability owing to the unique combination of the redox-active polydopamine and superior electrical conductivity of FWNTs.

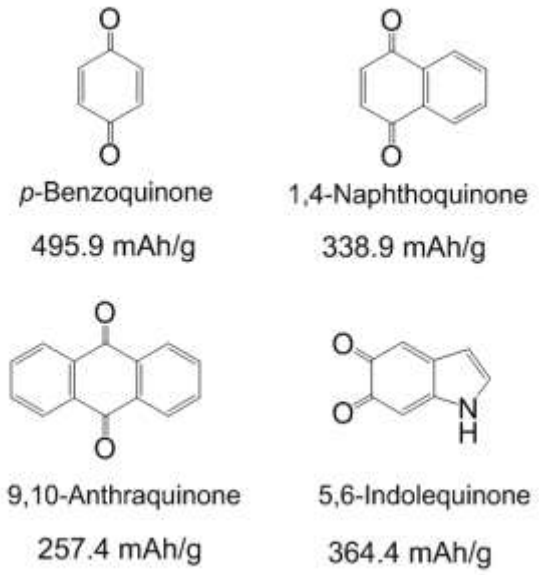

Scheme 5.1 Molecular structures and corresponding theoretical capacity of p-benzoquinone, 1,4-naphthoquinone, 9,10-anthraquinone and 5,6-indolequinone. The theoretical capacities are calculated based on the redox reactions of carbonyl groups in the molecules.

5.2 Experimental

DFT Calculations*:* All the calculations to compute the redox potentials of molecules were performed by the Jaguar software with the PBE0 level of theory and 6-31G+(d,p) basis set.[210],[211] First of all, we geometrically optimized the 5,6-dihydroxyindole and 5,6-indolequinone monomers and their oligomers such as dimer and trimer. The vibrational frequency calculations with the same level of theory and basis set were further performed to compute the Gibbs free energies at 298 K in the vacuum. The solvation free energy calculations were finally performed using Poisson-Boltzman implicit solvation model to evaluate the contribution of the solvation free energies to the free energies. In

the solvation free energy calculations, a dielectric constant of 16.14 was used to reliably describe the polarity of the solvent mixture in our systems.

The thermodynamic cycle, which was used to predict the redox potentials of the molecules, is described elsewhere.[212] The redox potential (ΔE^{red}) of a molecule within the solvent mixture with respect to a Li/Li$^+$ reference electrode can be predicted by

$$\Delta E^{red} = \frac{-\Delta G^{soln}}{nF} - 1.44V$$

where ΔG^{soln} is the difference in the Gibbs free energy in solution during the reduction, *n* is the number of electrons transferred, and *F* is the Faraday constant. The constant 1.44 V indicates the redox potentials of the Li/Li$^+$ reference electrode. The computed redox potentials of the molecules are listed in **Table 5.1**. The electronic properties such as the highest occupied molecular orbital (HOMO) and lowest unoccupied molecular orbital (LUMO) energy levels of the molecules were also computed to investigate the correlations with their redox potentials.

Sample preparation: Few-walled carbon nanotubes (FWNTs) (6–10 nm diameter, 0.4 mm length, 99 wt% purity, triple-walled on average) were synthesized by CVD method in a single fluidized bed reactor.[177, 178] Dopamine (Sigma-Aldrich) and FWNTs were mixed at different mass ratio (*i.e.* 1:1, 2:1, 4:1 and 8:1) in 1.2 mg/mL 2-amino-2-hydroxymethylpropane-1,3-diol (Tris, Aldrich) aqueous solution. The solutions were stirred for 6 ~ 18 h, then, were vacuum filtered using a filtration membrane with 0.1 μm pore size. After drying at 70 ^{o}C under vacuum overnight, a piece of free-standing hybrid film was obtained. Pristine FWNT films were obtained by vacuum filtering the aqueous

dispersion of FWNTs. Pristine PDA particles were also prepared by the similar process by stirring dopamine in weak alakline soltuion (pH=8.5) for 6 h without adding FWNTs.

Characterization: The microstructures and morphologies of pristine FWNT films and various hybrid films were characterized by a SEM (Hitachi SU8010, operated at 10 kV). The EDX mapping was performed using Hitachi SU8230 equipped with an EDX detector (Oxford Instruments) at 10 kV. XPS (Thermal Scientific K-alpha XPS instrument) was employed to analyze the chemical composition. The high-resolution C 1s, N 1s and O 1s peaks were fitted by the software XPSPEAKS 4.1. Electrical conductivities of various FWNT films were measured by a standard four-point probe configuration (Signatone). The UV-vis spectroscopy was conducted by sonicating a small piece of the composite film in water for 1 h, the supernatant was used for UV-vis measurement. In comparison, fresh dopamine aqueous solution was prepared just before UV-vis measurement to avoid the possible oxidation.

Electrochemical Measurements*:* Swagelok-type cells were used for the electrochemical measurements. For Li-cell tests, 1 M $LiPF_6$ in a mixture of EC and DMC (3:7, volume ratio, BASF) was used as an electrolyte and two pieces of Celgard 2500 as separators. The voltage window for Li-ion batteries was controlled in the range of 1.5-4.5 V vs. Li. For Na-cell tests, 1 M $NaPF_6$ in EC/DMC (3:7, volume ratio, BASF) was used as electrolyte, and a piece of glass fiber (VWR International) was used as separator. The Na-cells were tested in the voltage range from 1.3 to 4.2 V vs. Na. All of the cells were assembled in an Argon filled glovebox (MBraun, $O_2 < 0.1$ ppm and $H_2O < 0.1$ ppm). The thickness of the hybrid films is 97 μm for PDA 39 wt%, and 54 μm for PDA 53 wt%. Current densities were controlled from 0.05 to 50 A/g during the galvanostatic tests and

at the end of each charging or discharging process, the voltage was held for 30 min at either 4.5 V or 1.5 V vs. Li (4.2 V or 1.3 V vs. Na). The conventional cycling test was conducted by repeatedly charging and discharging the cell at 0.25 A/g for 100 cycles. The cycling test with potentiostatic holding was held at 4.5 V or 1.5 vs. Li (4.2 V or 1.3 V vs. Na) for 5 min at the end of charge/discharge process. The accelerated cycling test was conducted following our previous reports.[213] Briefly, the charge or discharge capacity was obtained from a low current density of 0.1 A/g and at the end of each charge or discharge process, the cell was held at 4.5 or 1.5 V vs. Li for 30 min. Between each data point, the cell was cycled at a high current density of 10 A/g for 99 cyces (1-1,000th cycle) or 499 cycles (1,100th-10,000th cycle).

***Self-discharge course and the ex-situ XPS measuremen*t**: The hybrid electrodes were charged or discharged to target voltage at 0.1 A/g and held at costant voltage (4.5, 3.5, 1.5 V vs. Li) for 60 min. After hold process, the cell was rested at open-circuit condition for ~18 h and the voltage was recorded with time. After the voltage of the cell was stabalized for ~18 h, the cell was dissembled and the electrode was washed with DMC for several times, and vacuum dried at 70 ^{o}C for overnight before the XPS measurement.

5.3 Results and discussion

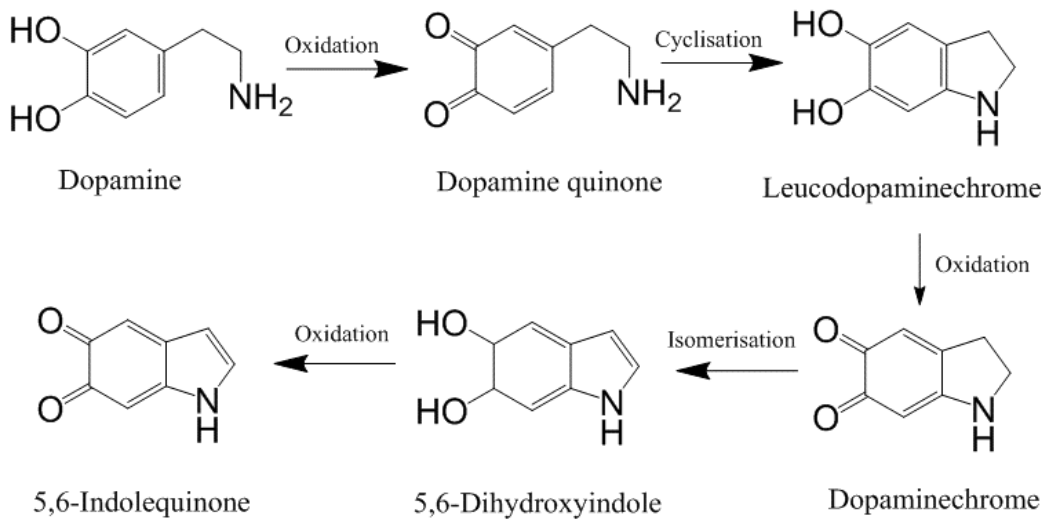

Scheme 5.2 Contemporary reaction mechanism of polydopamine from dopamine including various intermediate species, which is modified from the previous study.[214]

In this study, the first principle DFT method was employed with the *PBE0*[215, 216] and standard 6-31+G(d,p) basis set[210] via Jaguar.[211] We investigated the redox-potentials of monomers, and corresponding oligomers such as dimers and trimers based on two most reported structural units in polydopamine,[217-219] namely, 5,6-indolequinone and 5,6-dihydroxyindole in **Scheme 5.2**. The calculated redox potentials are shown in **Figure 5.1a**. 5,6-indolequinone with carbonyl groups showed a high redox potential of 2.83 V vs. Li, while 5,6-dihydroxyindole including hydroxyl groups had a very low redox potential of -0.26 V vs. Li (**Table 5.1**). This indicates that the only 5,6-indolequinone with a high redox potential can be employed as the cathode material for rechargeable batteries. The high redox potential of 5,6-indolequinone is consistent with our previous findings of redox-active carbonyl groups on reduced GO[169] and quinone derivatives.[207] It is also interesting to note that the redox potentials for both structural units are not significantly dependent on the degree of the polymerization: the oligomers

containing quinone showed slightly increased redox-potential to 2.93-2.94 V vs. Li, whereas those of oligomers containing hydroxyl groups increased to 0.11-0.27 V vs. Li. Previous studies employed the lowest unoccupied molecular orbital (LUMO) energy levels to explain different redox behaviors of various organic molecules.[137, 169, 207] We find that the redox potentials calculated in this study also show linear correlations not only with the LUMO energy levels but also with the electron affinity (EA) and the gap between highest occupied molecular orbital (HOMO) and LUMO (HOMO-LUMO) (**Figure 5.1b-d**). This infers that redox-active molecules with more negative EA and LUMO energy levels would have higher redox potentials due to the preferentially reductive nature of the molecules. In addition, we considered the existence of secondary amine (R−NH−R) in the molecules, which can contribute additional charge capacity to polydopamine through the p-type doping/de-doping process with anions (**Scheme 5.3**). To confirm this contribution, we computed the redox potentials of the molecules binding with the anion (PF_6^-). The DFT calculation showed that the doping/de-doping process of anions (PF_6^-) occurred at 4.03 and 4.41 V vs. Li for 5,6-dihydroxyindole and 5,6-indolequinone monomers, respectively. These redox potentials decreased to 3.73-3.82 and 3.95-3.97 V vs. Li for corresponding dimers and trimers, respectively (**Table 5.2**). Thus, these computation results predict multiple redox reactions of the polydopamine with electrolyte ions in the broad voltage range of 2.5 ~ 4.1 V vs. Li.

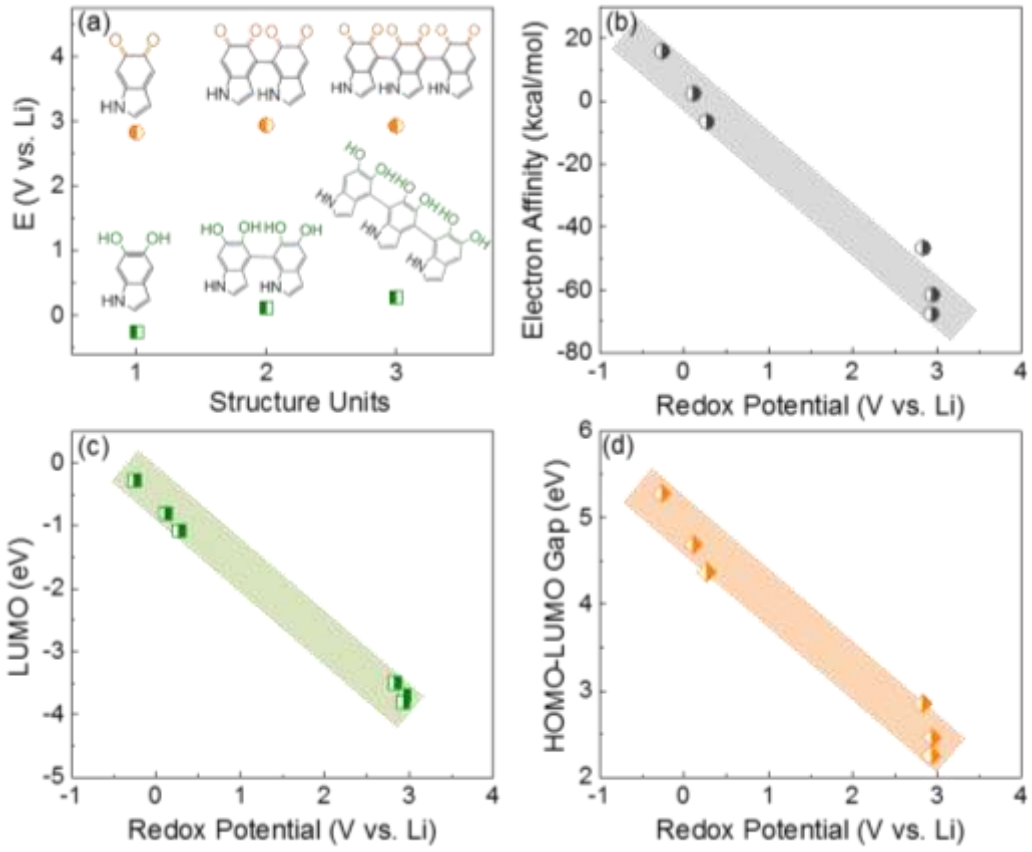

Figure 5.1 (a) The calculated redox potentials of 5,6-dihydroxyindole and 5,6-indolequinone monomers and their oligomers (dimers and trimers). The correlations of the redox potentials of the molecules in (a) with their electronic properties, namely (b) EA, (c) LUMO, and (d) HOMO-LUMO gap.

Table 5.1 The calculated redox potentials of 5,6-dihydroxyindole and 5,6-indolequinone monomers and their oligomers illustrated in Figure 5.1.

Molecule		Redox potential (V *vs.* Li/Li^+)
5,6-dihydroxyindole	Monomer	-0.26
	Dimer	0.11
	Trimer	0.27
5,6-indolequinone	Monomer	2.83
	Dimer	2.94
	Trimer	2.93

Table 5.2 The calculated redox potentials of 5,6-dihydroxyindole and 5,6-indolequinone monomers and their oligomers associated with the doping and de-doping process of anions.

Molecules		Calculated Redox Potential (V)	Electron affinity (kcal/mol)	HOMO (eV)	LUMO (eV)	HOMO-LUMO Gap (eV)
5,6-dihydroxyindole	Monomer	4.03	-100.9	-7.72	-3.85	3.87
	Dimer	3.82	-92.8	-6.27	-3.59	2.68
	Trimer	3.73	-91.9	-6.11	-3.55	2.56
5,6-indolequinone	Monomer	4.41	-114.2	-8.75	-5.76	2.99
	Dimer	3.97	-104.1	-7.32	-5.2	2.12
	Trimer	3.95	-106.0	-6.98	-5.10	1.88

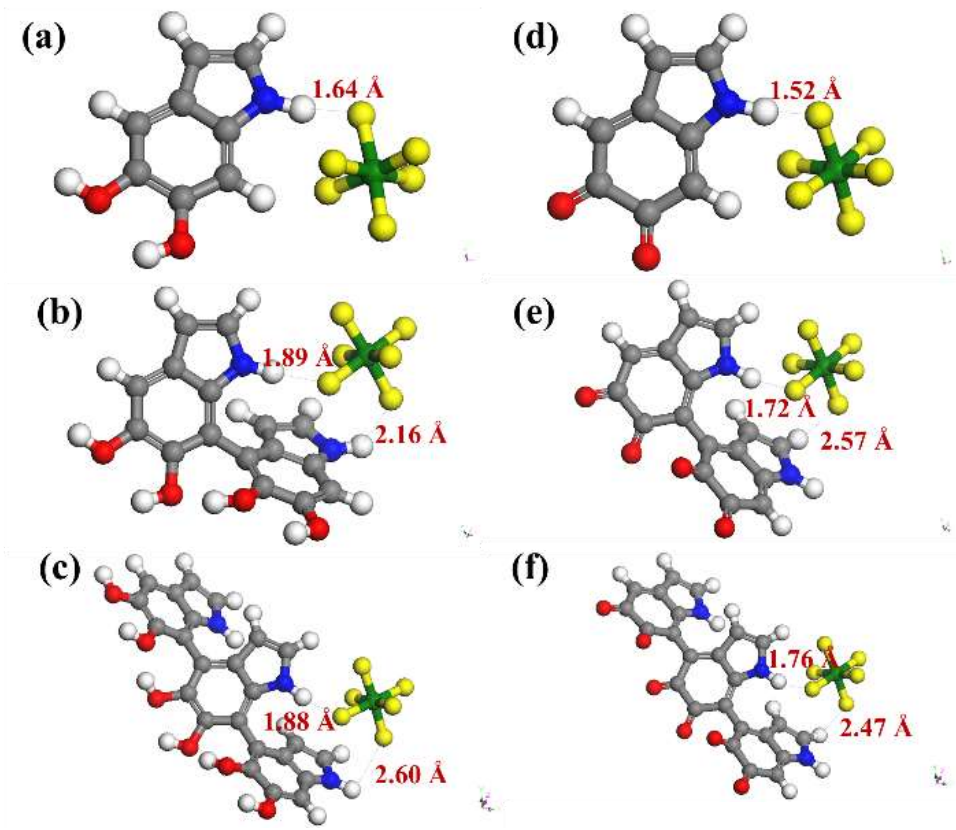

Scheme 5.3 Geometrically optimized structures for the monomers and oligomers of 5,6-dihydroxylindole and 5,6-indolequinone with PF_6^-. The shortest distances of P-H in Å are shown in red. Gray, white, blue, red, green, and yellow in color depict carbon, hydrogen, nitrogen, oxygen, phosphorus, and fluorine, respectively.

Because most organic electrode materials have poor electrical conductivity, they require a mixing process with a large amount of conductive additive to activate the redox reactions. In this study, we employed sub-millimeter long FWNT, which was synthesized by fluidized-bed chemical vapor deposition method, as a conductive substrate owing to its high electrical conductivity and high aspect ratio.[177, 178] We coated polydopamine on the surface of FWNTs through the self-polymerization process of dopamine in weak alkaline solutions (**Scheme 5.4**a). Dopamine and FWNTs were mixed at different concentration ratios (*i.e.* FWNT/dopamine = 1:1, 1:2, 1:4, and 1:8) in 2-amino-2-hydroxymethylpropane-1,3-diol (Tris) aqueous solution (1.2 mg/mL, pH=8.5). The

mixtures were stirred at room temperature for 6~18 h, during which polydopamine was coated on the surface of FWNTs. Flexible and free-standing films were assembled via vacuum-filtering the aqueous mixture (**Scheme 5.4b**). The loading amount of polydopamine within the hybrid films can be controlled by the concentration ratio and stirring time of the aqueous mixture. The hybrid films were labeled with the concentration ratios of FWNT and dopamine in the aqueous mixtures (i.e. PDA-X indicates the film prepared from the concentration ratio of FWNT/dopamine = 1:X, where X = 1, 2, 4 and 8). We estimated the weight percentage of polydopamine in hybrid films by measuring the mass difference between the used FWNTs and hybrid films. As the concentration of dopamine increased, the weight percentage of polydopamine progressively increased (**Figure 5.2a**), whereas their yield percentage from monomer to polymer gradually decreased (**Figure 5.2b**). It is interesting to note that increasing stirring time can increase both weight percentage and yield of polydopamine, indicating that the effective polymerization process takes place under stirring condition (**Figure 5.2a, b**). After stirring the mixture for 18 h, a maximum loading of 65.6 wt% was achieved for PDA-8, while a maximum yield of 65.5% was obtained for PDA-1. In addition, the normalized electrical conductivity decreased from 209 Scm^2/g for the pristine FWNT film to 20 Scm^2/g for PDA-8 (65.6 wt%) owing to the insulating nature of polydopamine coating on the surface of FWNTs (**Figure 5.2c**).

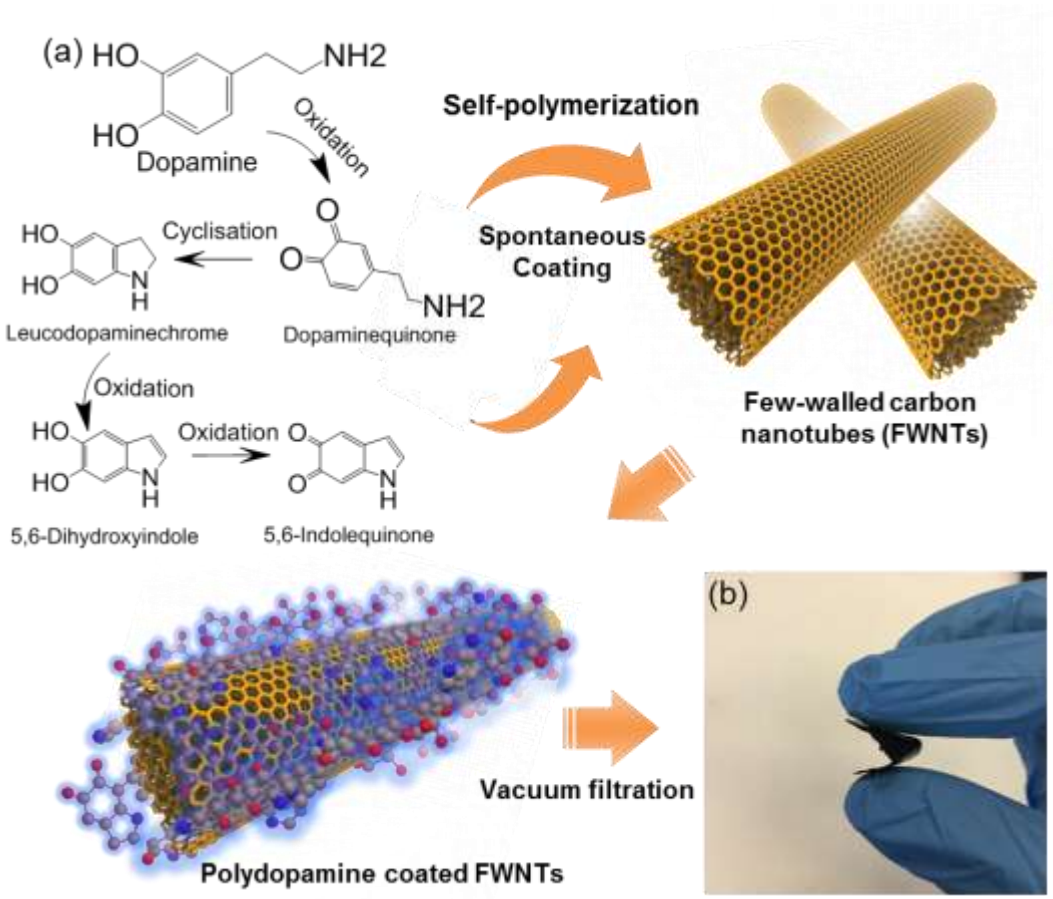

Scheme 5.4 (a) Oxidative self-polymerization reactions of dopamine in weak aqueous solution and continuous coating process of polydopamine on the surface of few-walled carbon nanotubes (FWNTs). (b) Digital image of a flexible hybrid film consisting of polydopamine coated FWNTs.

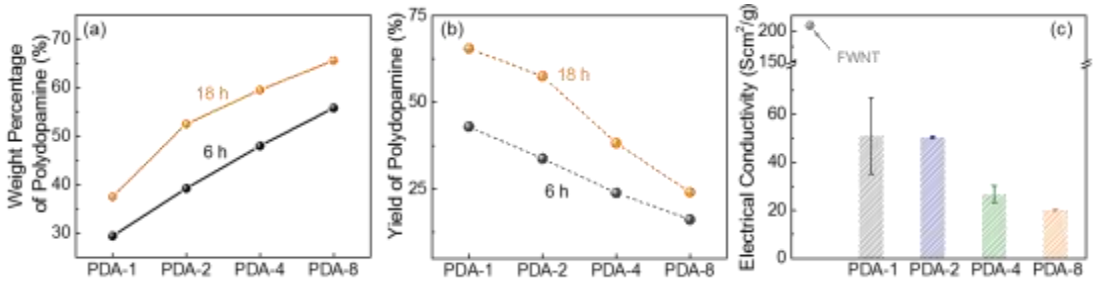

Figure 5.2 (a) Weight percentage and (b) yield of polydopamine in the hybrid films as a function of the concentration of dopamine and stirring time. (c) Normalized electrical conductivities of hybrid films as a function of the concentration of dopamine (18 h stirring).

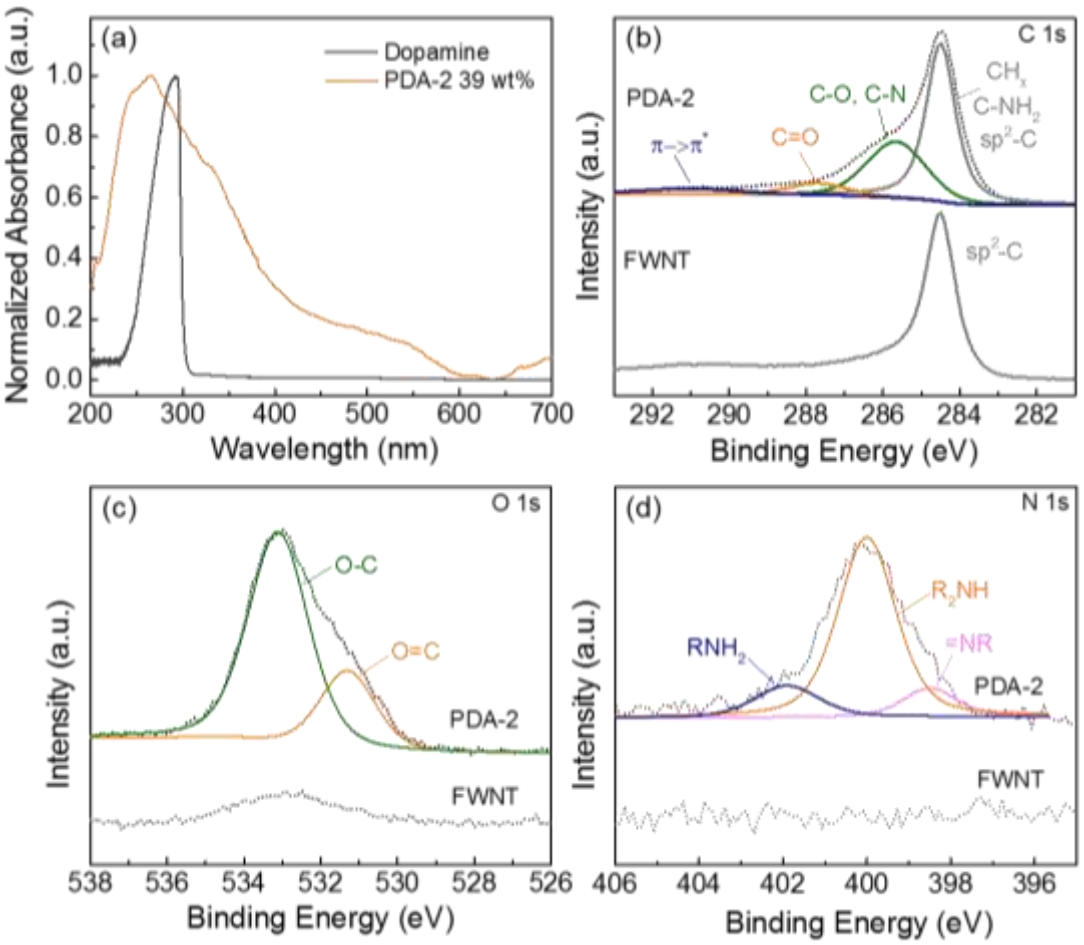

Figure 5.3 UV-vis spectra of aqueous solutions of pristine dopamine and hybrid film (PDA-2, 6 h stirring, 39 wt%). High-resolution XPS (d) C 1s, (e) O 1s, and (f) N 1s spectra of the pristine FWNT and hybrid film (PDA-2, 18 h stirring, 53 wt%).

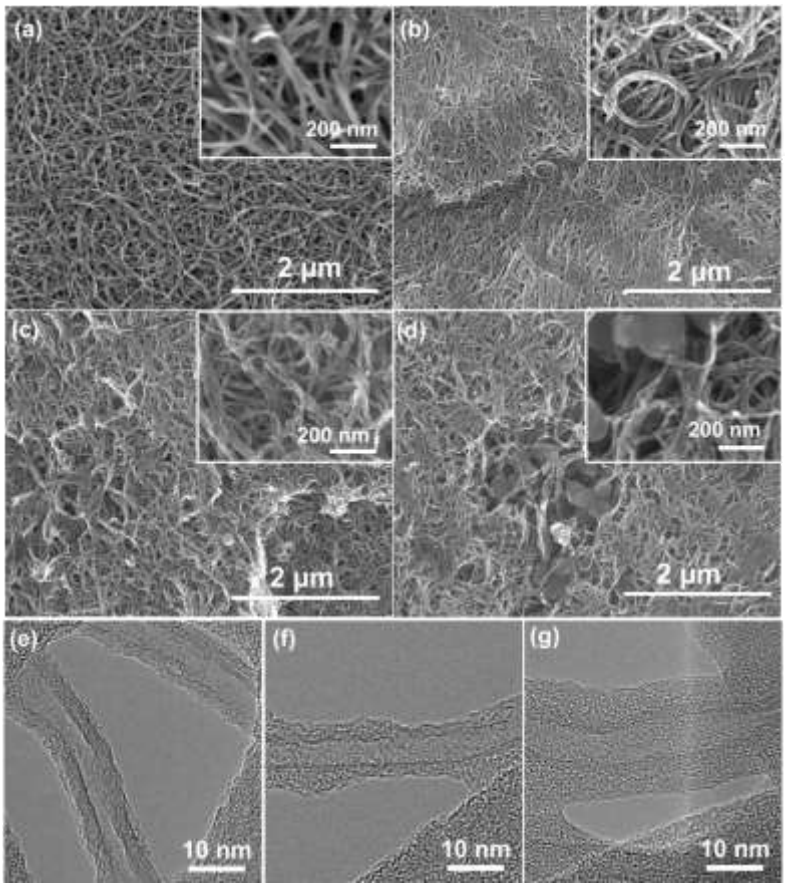

Figure 5.4 SEM images of (a) the pristine FWNT and hybrid films: (b) PDA-2 (53 wt%), (c) PDA-4 (59.5 wt%), and (d) PDA-8 (65.6 wt%). High resolution transmission electron microscopy (TEM) images of (e) pristine FWNT and hybrid films: (f) PDA-2 (39 wt%) and (g) PDA-2 (53 wt%).

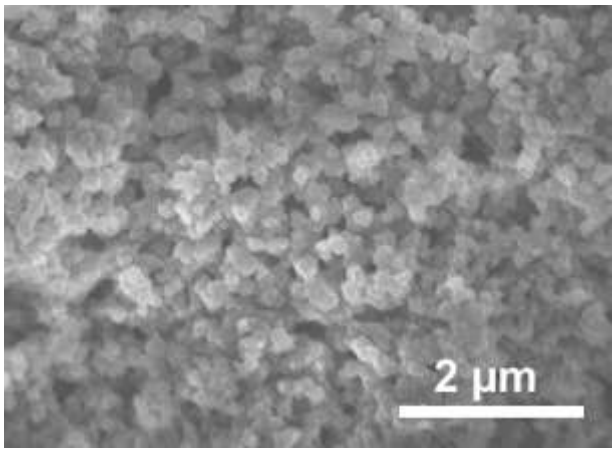

Figure 5.5 SEM image of as prepared PDA particles. The PDA particles were prepared by directly stirring dopamine solution in weak alkaline solution (pH=8.5) for 6 h without using FWNTs as a template.

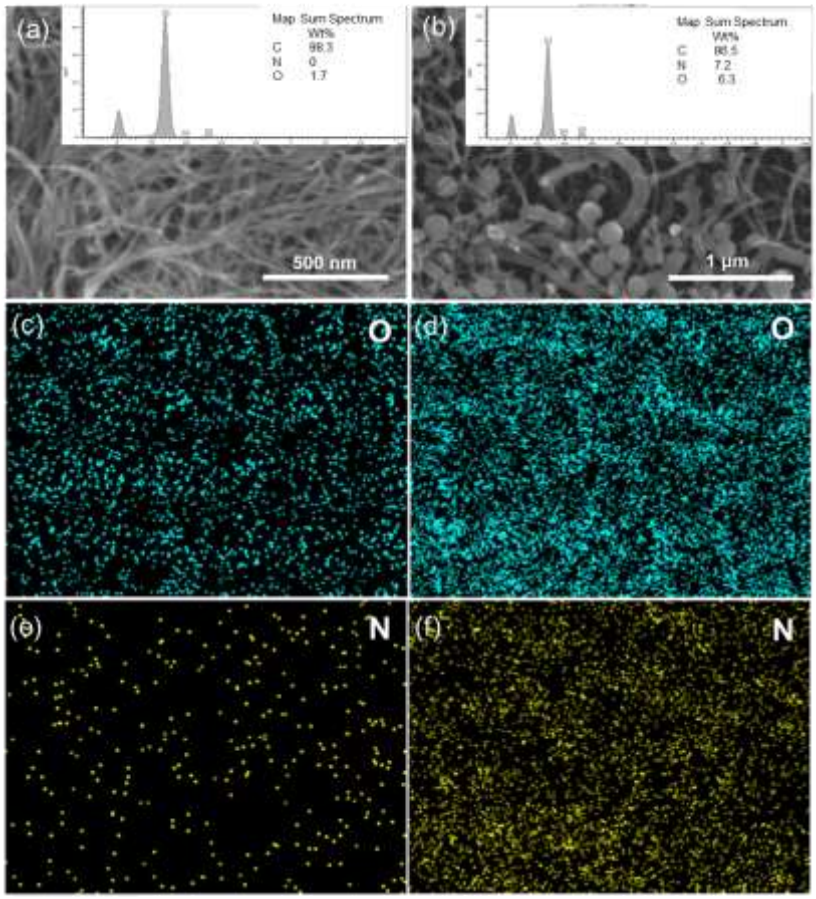

Figure 5.6 SEM images of (a) pristine FWNT film and (b) hybrid film (PDA-2, 53%) and corresponding EDX elemental mapping of (c, d) oxygen and (e, f) nitrogen.

The formation of quinone groups in the polydopamine was investigated by the UV-vis spectra (**Figure 5.3a)**. Compared with the spectrum of pristine dopamine, the hybrid film (PDA-2, 6 h stirring, 39 wt%) displayed an intensive absorption band at ~266 cm^{-1} due to the π-plasmon absorption of carbon nanotubes[220] and a shoulder absorption peak ~350 nm that is ascribed to the formation of the quinone.[217] Detailed surface chemistry of the hybrid film (PDA-2, 18 h stirring, 53 wt%) was further analyzed by XPS (**Figure 5.3b-d**). High-resolution C 1s spectrum of the pristine FWNTs was dominated by the sp^2-hybridzed carbon peak, while the hybrid film displayed broadened spectrum towards higher binding energy owing to the introduced polydopamine coating on the

FWNTs (**Figure 5.3b**). The C 1s spectrum of the hybrid film can be fitted into four peaks at 284.5±0.1 eV for CH_x/C-NH_2 and sp^2-hybridized carbon, 285.6±0.1 eV for C-O/C-N, 287.7±0.1 eV for C=O and 290.9±0.3 eV for the $\pi \rightarrow \pi^*$ transition satellite for aromatic carbon species.[214, 221] The O 1s spectrum of the hybrid film were fitted with two main peaks, the peak centered at 533.1±0.2 eV for O-C and 531.2±0.1 eV for O=C,[214, 221] where the percentage of carbonyl species (quinone group) is 26%. In addition, the N 1s spectrum of the hybrid film was revealed three peaks at 401.9±0.1 for primary amine ($R-NH_2$), 399.9±0.1 eV for secondary amine (R−NH−R), and 398.5±0.1 eV for tertiary/aromatic (=N−R) amine functional groups.[214, 221] The primary amine peak comes from dopamine, the secondary amine peak is associated with polydopamine or oxidized intermediates, and the tertiary/aromatic peak is ascribed to tautomers of the 5,6-dihydroxyindole and 5,6-indolequinone (**Scheme 5.4a**).[214] A recent study proposed that the polydopamine consists of the combination of covalent polymerization of 5,6-indolequinone and non-covalent self-assembly of dopamine and its intermediates.[222] Therefore, the coexistence of the different amine groups in the hybrid film is consistent with the proposed structural model of polydopamine.[222]

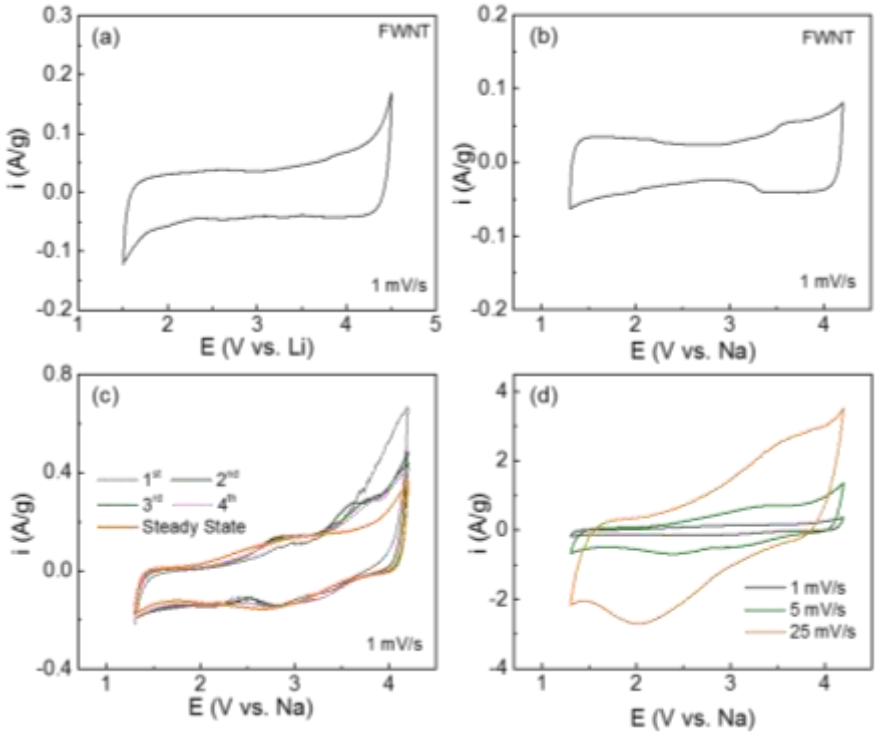

Figure 5.7 CV scans of the pristine FWNT electrodes 1 mV/s in (a) Li and (b) Na-cells. (c) The first four CV scans and (d) Rate-dependent CV scans of the hybrid electrode (PDA-2, 39 wt%).

The pristine FWNT and hybrid films both exhibited 3D interpenetrating network structures consisting of FWNTs (**Figure 5.4a**) or polydopamine coated FWNTs in the SEM images (**Figure 5.4b-d**). In addition, when the concentrations of dopamine are high, randomly distributed polydopamine spheres with diameters of ~200 nm were also observed within the hybrid films (**Figure 5.4c** and **d**). These polydopamine spheres were synthesized via self-nucleation reactions in aqueous solution as the concentration of dopamine increases.[223] These polydopamine spheres were also observed from the homogeneous polymerization process of dopamine without FWNTs (Figure 5.5). We further conducted the elemental mapping of oxygen and nitrogen on pristine FWNT and hybrid films by EDX. Despite the observation of the polydopamine particles within the

selected area for the EDX mapping, the hybrid film exhibited homogenous distribution of oxygen and nitrogen with higher density compared to those of the pristine FWNT film, confirming the successful coating of polydopamine on FWNTs (**Figure 5.6**). The conformal coating of amorphous polydopamine on the surface of FWNTs was further confirmed by high-resolution TEM images. Pristine FWNTs exhibited slightly roughened outer wall owing to the introduced defects during the growth process (**Figure 5.4**). Synthesized polydopamine formed irregular coating on the surface of FWNT for the hybrid film with a low loading amount of the polymer (39 wt%) (**Figure 5.4f**). This coating became more uniform with a thickness of ~5 nm as the loading of polydopamine increased to 53 wt% (**Figure 5.4g**).

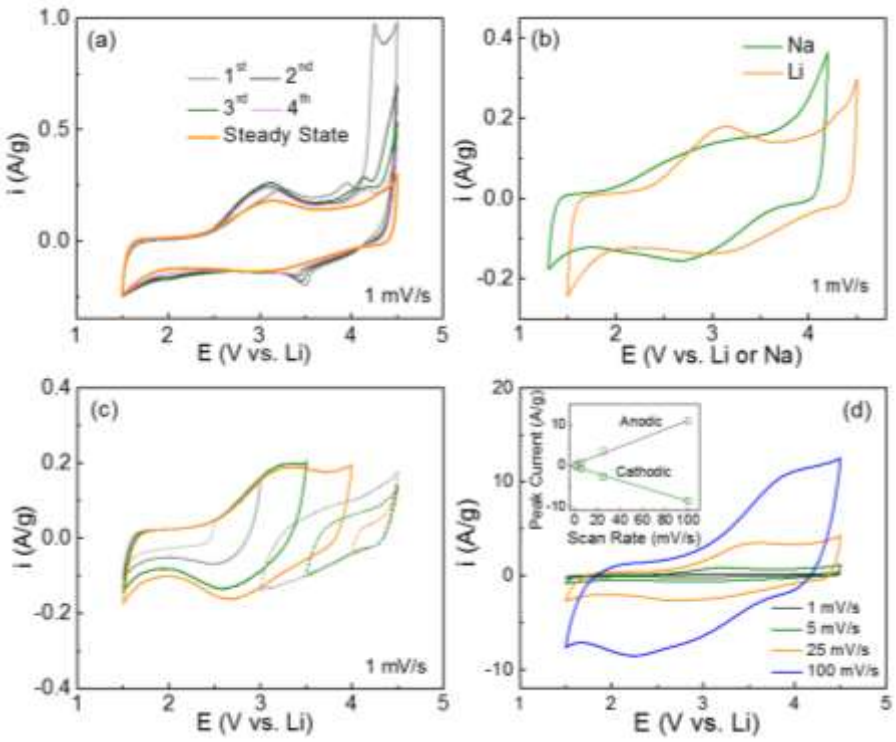

Figure 5.8 CV measurement of the hybrid electrode (PDA-2, 39 wt%) in Li- and Na-cells. (a) The first four CV scans at 1 mV/s in a Li-cell. (b) Comparison of steady-state CV scans in Li- and Na-cells. (c) Potential-dependent and (d) rate-dependent CV scans in Li-cells. Peak current of the electrode as a function of a scan rate is shown in 3d inset. The voltage window of the CV scans in Li-cells was 1.5 – 4.5 V vs.

Li in 1 M $LiPF_6$ in a mixture of EC and DMC (3:7 volume ratio) and the voltage window in Na-cells was 1.3 – 4.2 V vs. Na in 1 M $NaPF_6$ in a mixture of EC and DMC (3:7 volume ratio).

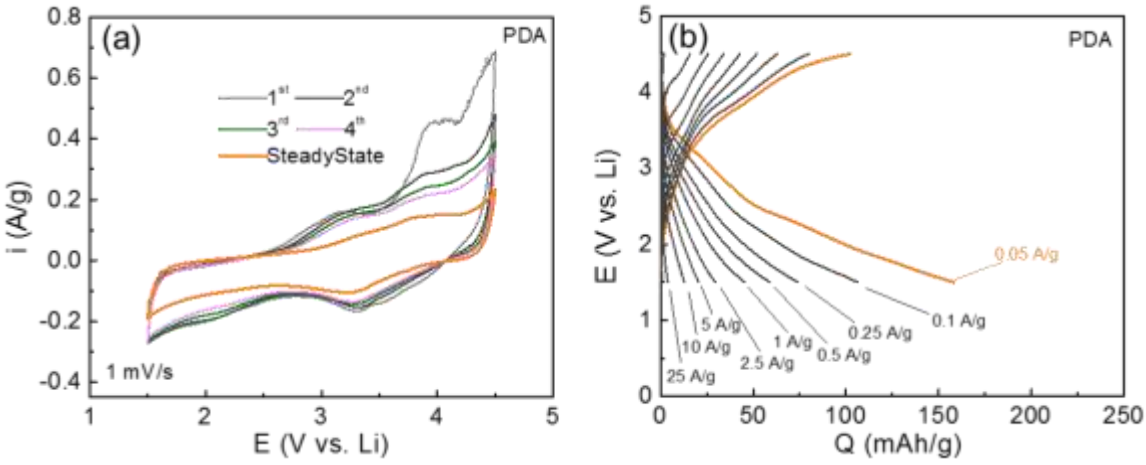

Figure 5.9 (a) CV measurement of pristine PDA and (b) rate-dependent galvanostatic charge-discharge profiles of the pristine PDA in Li-cells.

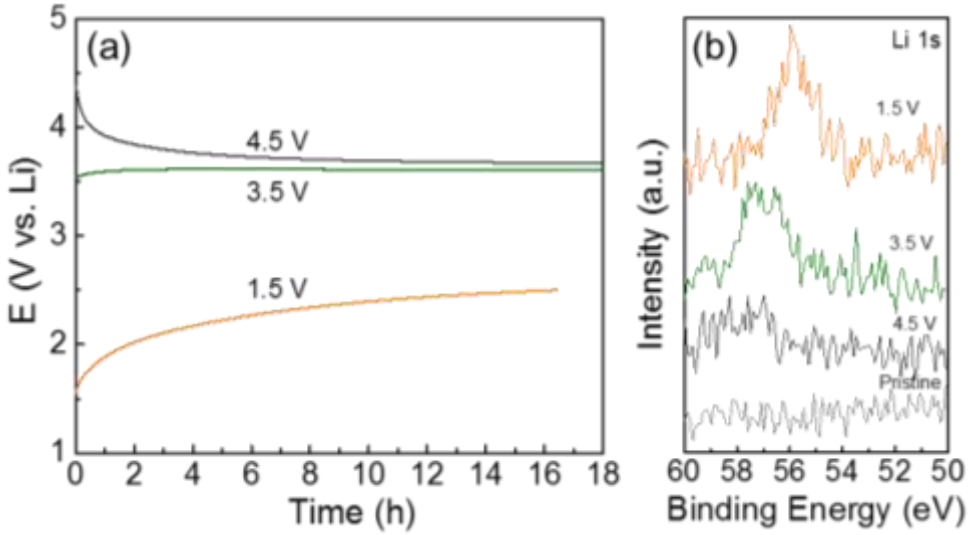

Figure 5.10 (a) The self-discharge course of the hybrid films after holding at different voltages. (b) XPS Li 1s spectra of the hybrid films (PDA-2, 53wt%) after the hold at different voltage and continuous self-discharge test.

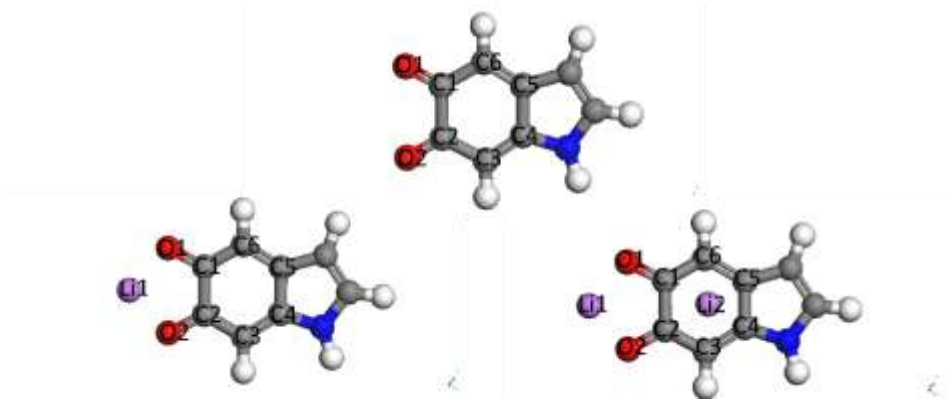

Figure 5.11 Change in the structure (PBE0 functional) as a function of the Li atoms binding with 5,6-indolequinone monomer.

Table 5.3 Change in the bonding distance and charge distribution (PBE0 functional) as a function of the Li atoms binding with 5,6-indolequinone monomer.

Bond Type	Distance (Å)			Atom	Charge		
	Without Li	With 1Li	With 2Li		Without Li	With 1Li	With 2Li
Li1-O1	-	1.81	1.79	Li1	-	0.51	0.46
Li1-O2	-	1.81	1.80	Li2	-	-	0.08
Li2-C1	-	-	2.31	O1	-0.37	-0.52	-0.58
O1-C1	1.22	1.28	1.30	O2	-0.39	-0.52	-0.59
O2-C2	1.22	1.28	1.29	C1	0.26	0.29	0.34
C1-C2	1.57	1.50	1.50	C2	0.25	0.31	0.38
C2-C3	1.46	1.41	1.41	C3	-0.26	-0.32	-0.34
C3-C4	1.36	1.38	1.42	C4	0.25	0.22	0.32
C4-C5	1.48	1.45	1.42	C5	-0.02	-0.07	0.01
C5-C6	1.36	1.39	1.43	C6	-0.23	-0.27	-0.30
C6-C1	1.46	1.41	1.41				

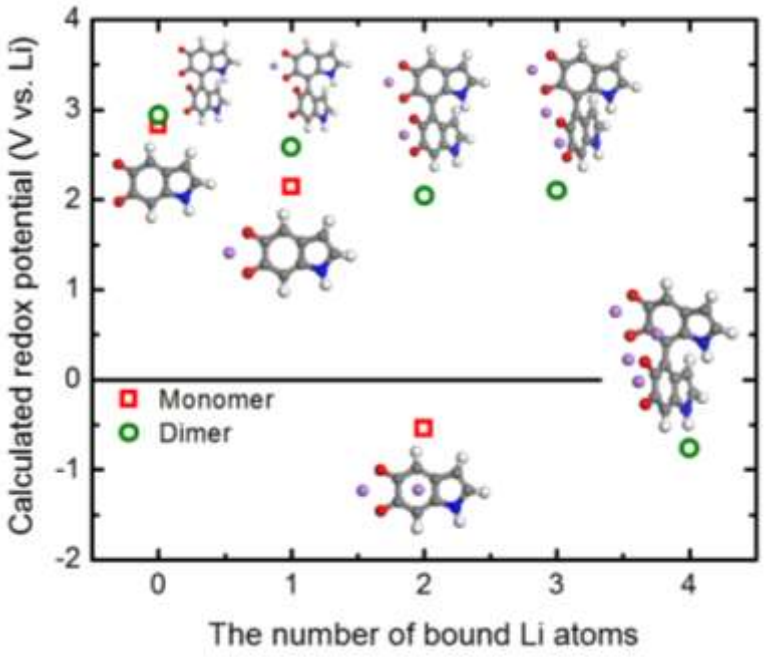

Figure 5.12 Change in the redox potentials (PBE0 functional) as a function of the Li atoms binding with 5,6-indolequinone monomer and dimer.

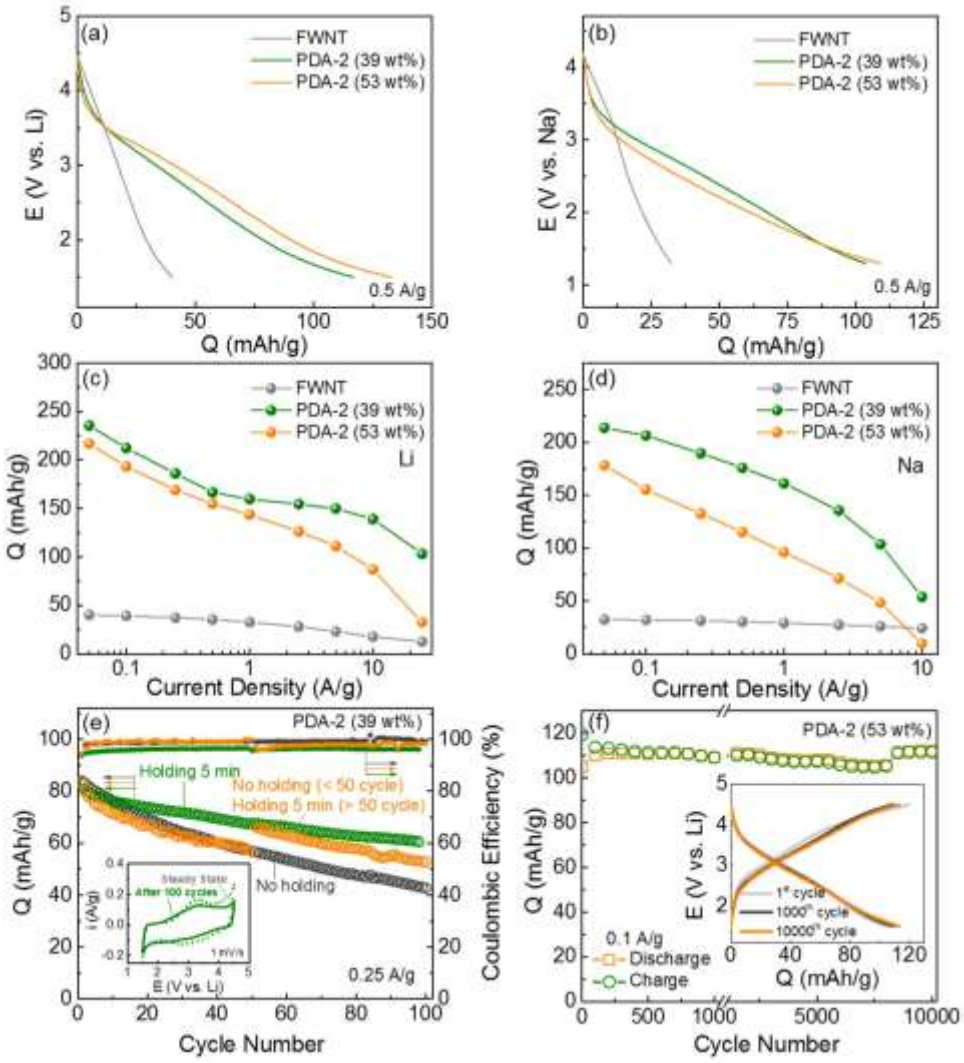

Figure 5.13 Comparison of discharge profiles of the pristine FWNT (grey) and hybrid electrodes (PDA-2, 39 wt% (olive) and 53 wt% (orange)) at 0.05 A/g in (a) Li- and (b) Na-cells. Gravimetric discharge capacities of polydopamine as a function of discharge rate in (c) Li- and (d) Na-cells. Gravimetric capacities of the polydopamine were calculated based on the rule of mixtures. (e) Cycling stabilities of the hybrid electrodes (PDA-2, 39 wt%) and their Coulombic efficiencies. The cells were cycled at 0.25 A/g up to 100 cycles with three different methods: dark grey circle for continuous cycles without any potentiostatic holding process, olive circle for cycles including a short 5 min potentiostatic holding at 4.5 or 1.5 V vs. Li at the end of each charge and discharge cycle, and orange circle for initial 50 cycles without holding and subsequent 50 cycles with the 5 min potentiostatic holding. Inset is the comparison of CV scans of PDA-2 (39 wt%) at the initial cycle and 100th cycle at 1 mV/s. (f) Gravimetric charge and discharge capacities of the hybrid electrode (PDA-2, 53 wt%) as a function of cycle number up to 10,000 cycles using an accelerating cycling method.[213] Figure 5.13f inset compares the charge and

discharge curves of the 1st and 1000th and 10,000th cycles. The capacities were measured based on the total weight of the hybrid electrodes.

Redox-active properties of the polydopamine were investigated by CV measurements in both Li- and Na-cells. The free-standing hybrid films with mass loading of 1-3 mg/cm^2 were directly used as cathodes against Li or Na metal anodes. The CV scans of pristine FWNT films were also measured as references, showing characteristic box-like shapes owing to their electrical double-layer capacitance charge storage mechanism (**Figure 5.7a** and **b**).[63, 166, 213] The first forward scan of the hybrid electrode exhibited a wide oxidation peak with an onset potential of ~2.5 V vs. Li that is ascribed to the interactions between quinone groups in polydopamine and Li-ions. The oxidation peak position of ~3.3 V vs. Li is similar with that of benzoquinone (~3.1 V vs. Li)[207] (**Figure 5.8a**). The second oxidation peak at ~3.9 V vs. Li is associated with the *p*-doping process of anions (PF_6^-) into the polymer chain or nitrogen atoms, which is also consistent with the DFT calculation results (**Table 5.2**).[72, 224] A strong oxidation wave with an onset potential of ~4 V vs. Li can be attributed to further anodic polymerization of intermediates within the polydopamine film.[29] Upon subsequent CV cycling, the anodic polymerization current progressively disappeared and the broad redox peaks centered at ~3.1 V vs. Li approached stable current values (**Figure 5.8a** and **b**), this redox potential is very consistent with those calculated by DFT method (2.83-2.93 V vs. Li) (**Figure 5.1a**). The pristine polydopamine electrode, which was prepared from polydopamine spheres, exhibited similar redox characteristic in a Li-cell (**Figure 5.9a**). Similar to the results in Li-cells, the hybrid electrode displayed steady-state redox peaks centered at ~2.8 V vs. Na after the anodic polymerization process in Na-cells (**Figure 5.7c** and **Figure 5.8b**). These high redox potentials suggest that polydopamine is an ideal

candidate for organic cathodes for both Li- and Na-ion batteries. The charge storage characteristics of the polydopamine were further analyzed by the potential-dependent CV measurements in Li-cells (**Figure 5.8c**). At a low voltage range of 1.5 - 2.5 V vs. Li, the CV scan showed a box-like shape, indicative of double layer capacitance from FWNTs. In contrast, the redox peaks were gradually developed as the voltage increased from 2.5 to 4 V vs. Li, which clearly revealed the redox reactions between quinone groups and Li ions. In addition, the backward CV scans from 4.5 V to 3.5 V showed the gradual increase of currents, which can be attributed to the p-doping process of anions into the polymer chain or nitrogen atoms.[72, 224] Moreover, rate-dependent CV scans in both Li- and Na-cells maintained the redox features at higher scan rates (100 mV/s for Li-cells and 25 mV/s for Na-cells) owing to the fast surface redox reactions (**Figure 5.8d** and **Figure 5.7d**). The linear relationship between the peak current and scan-rate indicates a surface-controlled redox process of polydopamine within the hybrid films (**Figure 5.8d inset**).

To further understand the redox reactions between quinone groups in polydopamine and Li ions, we conducted ex-situ XPS measurements of the hybrid electrode (PDA-2, 53 wt%) after the constant potential holding and continuous self-discharge process in Li-cells. The voltage drift of the hybrid electrode was measured at open circuit for ~18 h after holding the cell at a target voltage for 60 min (**Figure 5.10a**). The open circuit potential of the hybrid electrode is ~3.2 V vs. Li. After voltage hold process at 4.5 V vs. Li, the open-circuit voltage gradually dropped to ~3.6 V vs. Li during the rest process owing to parasitic leakage current.[131] In contrast, after hold process at 1.5 V vs. Li, the voltage progressively recovered to ~2.5 V vs. Li with time. The

electrode also showed almost constant voltage behavior after hold at 3.5 V vs. Li, which is close to the open circuit potential of the as-assembled electrode. After self-discharge test, we washed the electrodes in DMC and then measured XPS Li 1s spectrum to compare the remaining Li ions on the polydopamine (**Figure 5.10b**). The hybrid electrode that was held at 1.5 V vs. Li showed strong Li 1s peak owing the adsorbed Li ions on quinone groups in the polydopamine after discharge process. The Li 1s peak intensity was found to decrease with increasing hold voltage, indicating the desorption process of Li ions on the quinone groups during the charge process. This potential dependent Li adsorption and desorption behavior further supports the reversible redox reactions between quinone groups in the polydopamine and Li ions.

We further employed the DFT method to structurally characterize the redox reactions between quinone groups in polydopamine and Li ions in molecular levels. The changes in the structural and electronic properties derived by the Li binding to the monomer constituting the polydopamine are depicted in **Figure 5.11**. The first Li ion positioned between the two carbonyls loses its electrons to the neighboring oxygen atoms, exhibiting the charge of +0.52. The charge transfer between Li and O subsequently affects the bonding characteristics of the carbonyls, partially losing their double bond nature. The second Li ion adsorbed on top of the aromatic ring in the molecule provides additional charge transfer with the neighboring oxygen atoms. This ultimately leads to the further change in the bonding characteristics of the carbonyls, forming in the C-O-Li bonds (**Table 5.3**). **Figure 5.12** shows how the redox potentials for the 5,6-indolequinone monomer and dimer consisting of the polydopamine are changed with the number of bound Li ions during the discharge process. As expected, the

redox potentials are gradually reduced as the number of the bound Li ions increases. They become negative after binding with two and four Li ions, respectively, losing their cathodic activities.

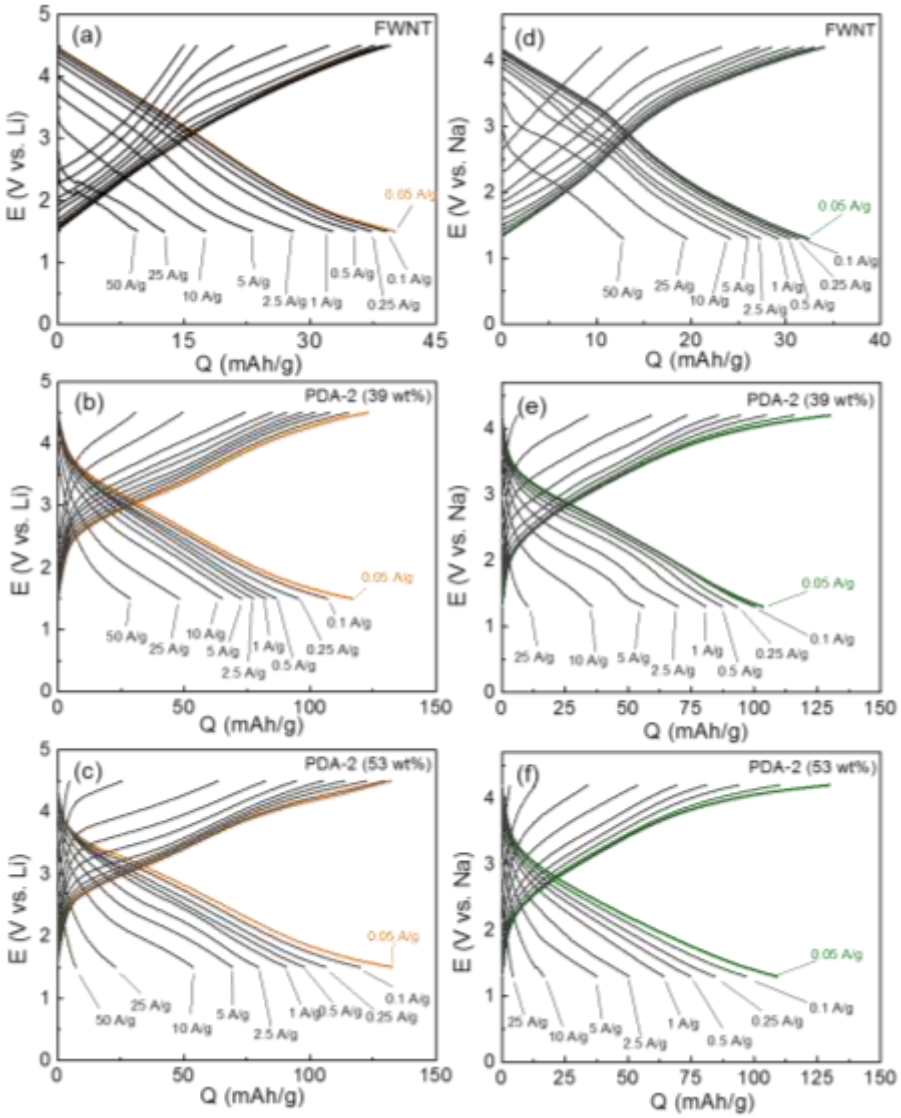

Figure 5.14 Rate-dependent galvanostatic charge-discharge profiles of the pristine FWNT electrodes in (a) Li- and (d) Na-cells. Rate-dependent galvanostatic charge-discharge profiles of the hybrid electrodes (PDA-2) in Li-cells (b for 39 wt% and c for 53wt%) and Na-cells (e for 39 wt% and f for 53wt%).

Galvanostatic charge and discharge tests were conducted in both Li- and Na-cells for evaluating the charge storage capabilities of the hybrid electrodes. We compared the discharge profiles of the pristine FWNT and hybrid electrodes in Li- and Na-cells (**Figure 5.13a** and **b**). The pristine FWNT electrodes showed small gravimetric capacities of ~40 mAh/g in a Li-cell[63, 166, 213] and ~32 mAh/g in a Na-cell, while the hybrid electrodes (PDA-2, 39 wt%) delivered significantly enhanced capacities of ~117 mAh/g and ~103 mAh/g in Li- and Na-cells, respectively. It is interesting to note that the hybrid electrodes have sloped discharge profiles, which can be attributed to the combination of double-layer capacitance and multiple redox reactions. As the loading of polydopamine increased from 39 to 53 wt%, the gravimetric capacities of the hybrid films slightly increased to ~133 mAh/g in a Li-cell and ~109 mAh/g in a Na-cell. To understand intrinsic charge storage capability of polydopamine, we calculated the rate-dependent gravimetric capacities of polydopamine in the hybrid electrodes based on the rule of mixtures in Li- and Na-cells (**Figure 5.13c, d** and **Figure 5.14**). At a slow discharge rate of 0.05 A/g, the polydopamine in the hybrid electrode with lower loading (PDA-2, 39 wt%) delivered higher capacities of ~235 mAh/g in a Li-cell and ~213 mAh/g in a Na-cell compared to those of the polydopamine with higher loading (PDA-2, 53 wt%) (~217 mAh/g in a Li-cell and ~178 mAh/g in a Na-cell). In addition, the pristine PDA electrode, which was prepared from polydopamine spheres, delivered a discharge capacity of 158 mAh/g and a charge capacity of 102 mAh/g at a current density of 0.05 A/g (**Figure 5.9b**). The lower discharge capacity and the difference between the charge and discharge capacities of the pristine PDA electrode may be attributed to the electrical and ionic resistance through the large polydopamine particles. The capacity of polydopamine in the

hybrid electrodes is comparable or even higher than most of the reported carbonyl-based compounds.[82, 84, 86, 90, 92] Over higher current densities, the polydopamine with lower loading (39 wt%) showed overall enhanced rate-performance compared to that of the polydopamine with higher loading (53 wt%). At a high current density of ~10 A/g, the polydopamine with lower loading (39 wt%) exhibited high capacities of ~139 mAh/g in a Li-cell and 54 mAh/g in a Na-cell, whereas the polydopamine with higher loading (53 wt%) delivered decreased capacities of ~87 mAh/g and ~10 mAh/g in Li- and Na-cells, respectively. These differences indicate that a portion of the polydopamine is not effectively utilized as the loading amount increases. Such decreased charge storage performance of the polydopamine with high loading may be attributed to the polydopamine spheres that were separated from the conductive FWNT network (**Figure 5.4**), resulting in poor utilization of their redox activities. Relatively low capacity (121-129 mAh/g) and poor rate-performance of the hybrid electrodes prepared with the higher concentration of dopamine (PDA-4 and 8) (further confirm this trend (**Figure 5.15c, d**). **Figure 5.16** compares the Nyquist plots for the hybrid electrodes (PDA-1, 2, 4, 8, 18 h stirring). A single semicircle in the high-to-medium frequency region and an inclined line at low frequency give information about a charge-transfer resistance R_{ct} and a mass-transfer process, respectively. Higher R_{ct} (2051-2370 Ω) of the PDA-4 and PDA-8 compared to those of the PDA-1 and PDA-2 electrodes (1336 Ω) further indicates the significantly low charge transfer resistance within the PDA-4 and PDA-8 electrodes including separated polydopamine spheres. These results suggest that the conformal coating of polydopamine on the conductive substrate is a crucial design factor for maximizing the performance of the hybrid electrodes.

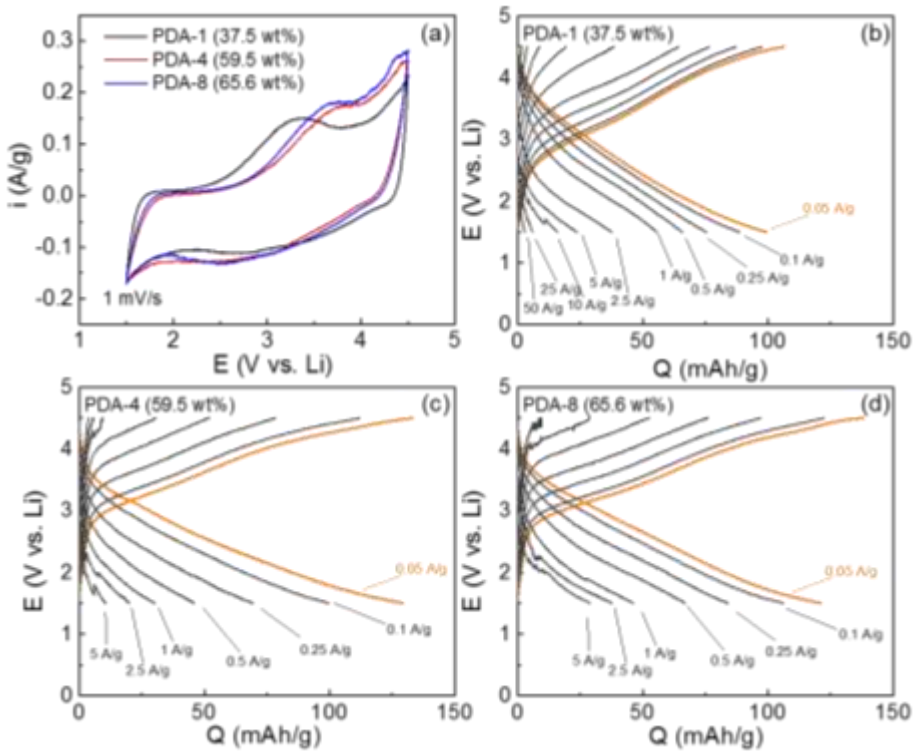

Figure 5.15 (a) CV measurement of the hybrid electrodes (PDA-1, 4, 8, 18 h stirring) in Li-cells. Rate-dependent galvanostatic charge-discharge profiles of the hybrid electrodes in Li-cells for (b) PDA-1, 37.5 wt%, (c) PDA-4, 59.5 wt%, (d) PDA-8, 65.6 wt%.

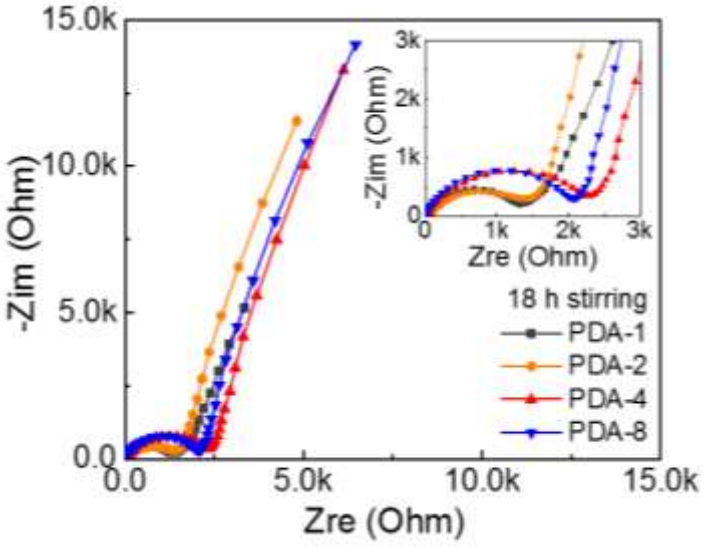

Figure 5.16 Nyquist plots of the hybrid electrodes (PDA-1,2,4, and 8) in fresh Li-cells from 200 kHz to 100 mHz at room temperature. The inset shows the magnified plot for the high frequency region.

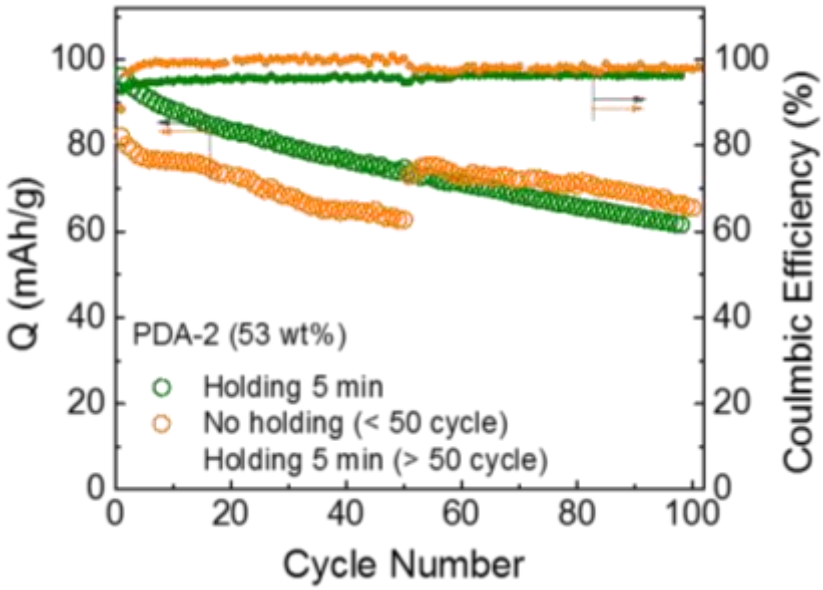

Figure 5.17 Cycling stabilities of the hybrid electrodes (PDA-2, 53 wt%) and their Coulombic efficiencies. The cells were cycled at 0.25 A/g up to 100 cycles.

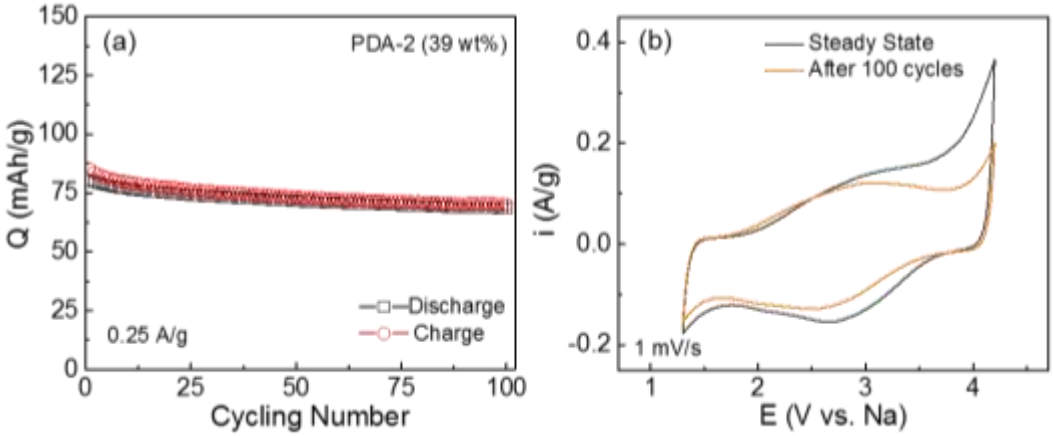

Figure 5.18 (a) Cycling stabilities of the hybrid electrode (PDA-2, 39 wt%) in a Na-cell. The cell was cycled at 0.25 A/g up to 100 cycles. (b) The comparison of CV scans at the initial cycle and after 100 cycles at 1 mV/s.

The cycling stabilities of the hybrid electrodes were evaluated by repeatedly charging and discharging the cells at a constant current density of 0.25 A/g (**Figure 5.13e, Figure 5.17,** and **Figure 5.18**). Different cycling test conditions were applied to the same electrode (PDA-2, 39 wt%). The electrode under repeated charge/discharge

cycles without any potentiostatic holding process exhibited a rapid capacity fading, retaining 50% of the initial capacity after 100 cycles. On the other hand, when a short potentiostatic holding for 5 min at 4.5 or 1.5 V vs. Li was applied at the end of each charge and discharge cycle, capacity retention is significantly improved, maintaining 78% of the initial capacity. Comparison of the CV scans before and after the cycling test (**Figure 5.13e** inset, PDA-2, 39 wt%) indicates that the loss of capacity was attributed to the decrease of the redox peaks. The control experiment is also conducted in which no potentiostatic holding was applied for the first 50 cycles, and a 5 min potentiostatic holding was applied for the subsequent 50 cycles. The capacity gradually decreased during the first 50 cycles, while the capacity immediately recovered once the potential holding was applied. It is interesting to note that this recovered capacity was similar to that of the cycling test with the continuous 5 min potentiostatic holding test. A similar result was also observed for the electrode with higher polydopamine loading (PDA-2, 53 wt%, **Figure 5.17**). This suggests that the gradual capacity loss during cycling is owing to the kinetic limitation of the redox reactions within polydopamine film rather than the dissolution of the molecules. We also evaluated the cycling stability of this electrode via an accelerated cycling where the cell was cycled at a high current density of 10 A/g and then the capacity was measured at a slow current density of 0.1 A/g after 30 min holding[213] (**Figure 5.13f**). The accelerated cycling test revealed negligible capacity fade up to 10,000 cycles, indicating most of the capacity of the hybrid electrode is recoverable after 30 min holding. To further confirm the stability of polydopamine in organic electrolyte, the stability and dissolution test were conducted following the method from the previous study.[208] A piece of the fresh hybrid electrode including

51.4 wt% of polydopamine was dipped into the electrolyte solvent, a mixture of ethylene carbonate (EC) and dimethyl carbonate (DMC). Although the electrode was kept for more than 12 h, no color change of the solvent was observed (**Figure 5.19a**). In addition, there was no mass change after completely drying the dipped electrode, indicating that synthesized polydopamine is stable in the electrolyte. Solubility tests of the hybrid electrodes at either fully charged or discharge state also showed no color changes even after keeping the electrodes in the electrolyte over 12 h (**Figure 5.19b**), indicating that polydopamine are also insoluble in the electrolyte at the charged or discharged states. These results further confirm that the self-polymerization process can prevent the dissolution of dopamine molecules, which is a common shortcoming of the most organic electrode materials.

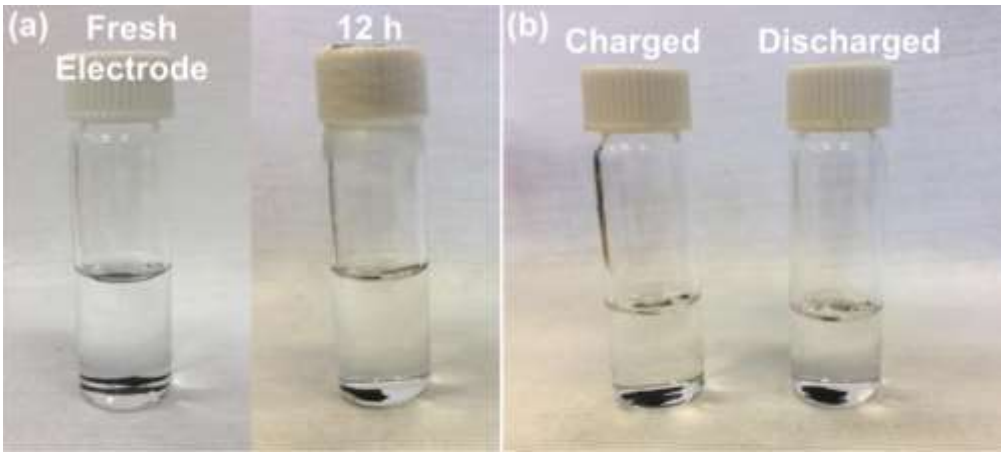

Figure 5.19 Dissolution tests of (a) fresh hybrid electrode and (b) charged (left) and discharged (right) electrode.

5.4 Conclusions

In conclusion, we have demonstrated that polydopamine can be utilized as high-performance organic cathode materials for rechargeable Li- and Na-ion batteries.

Dopamine was self-polymerized on the surface of FWNTs in alkaline aqueous solutions during which the loading of polydopamine can be simply controlled by the mixing time and concentration of dopamine. The free-standing and flexible hybrid films were assembled via a vacuum filtration method, which were employed as cathodes in both Li- and Na-cells. Polydopamine within the hybrid films exhibited multiple redox reactions with both electrolyte ions in the high voltage region of 2.5 ~ 4.1 V vs. Li, which were consistent with DFT computation results. The hybrid electrodes exhibited gravimetric capacities of ~133 mAh/g in Li-cells and ~109 mAh/g in Na-cells through double layer capacitance and multiple redox-reactions. We further revealed that the polydopamine itself in the hybrid electrodes can store high capacities of ~235 mAh/g in Li-cells and ~213 mAh/g in Na-cells. Moreover, the hybrid electrodes showed high rate-performance with excellent cycling stability. Combined with its advantage of simple polymerization process, the introduced polydopamine based electrodes can be an ideal candidate for developing high-performance organic batteries.

CHAPTER 6. POLYDOPAMINE FUNCTIONALIZED 3D GRAPHENE FOR HIGH-CAPACITY LI- AND NA-ION STORAGE

6.1 Introduction

Carbon materials have been dominantly used as electrodes for high-power electrochemical energy storage devices, especially for electrochemical capacitors (also called supercapacitors), because of their large surface area and high electrical conductivity.[71, 225-227] High surface area activated carbon (AC) has been mainly employed as an electrode material for commercial supercapacitors.[225-227] On the other hand, recently introduced graphene has been rapidly expanding its application range to electrochemical energy storage devices by taking advantage of its excellent physicochemical properties, such as high surface area, excellent electrical conductivity.[108, 142, 147, 228] However, an important challenge of graphene electrodes is that the graphene sheets are readily restacked and aggregated due to strong π–π interaction during the electrode fabrication, reducing the electrochemically active area.[229-231] Recent studies have shown that GO sheets dispersed in an aqueous solution can be reduced and subsequently self-assembled to 3D hydrogels under hydrothermal conditions,[117, 169] which can effectively prevent restacking. The 3D graphene hydrogels have been actively explored as electrode materials for supercapacitors and rechargeable batteries due to their unique advantages, including simple and mild synthesis condition, scalability, high electrical conductivity, and

interconnected porous structure.[17, 24, 117, 170, 232-234] Despite these advantages, the energy density of 3D graphene-based supercapacitors is considerably lower than that of rechargeable batteries.[16, 233] This is an intrinsic limitation of the surface-limited double layer capacitance charge storage mechanism of carbon-based supercapacitors over the faradaic (redox) reaction based batteries.[4] Therefore, research efforts have been focused on increasing the energy density of the electrodes by introducing redox-active conducting polymers[17, 24, 235] or metal oxides,[234, 236] into the 3D graphene hydrogels.

Recently, organic carbonyl compounds have been attracting considerable attention as active electrode materials for 'greener' rechargeable batteries due to their environmental benignity, sustainability, and high energy density.[64, 66, 71, 73, 78, 80, 82] For example, Chen *et al*. showed that the oxocarbon salt ($Li_2C_6O_6$) can deliver a high capacity of 580 mAh/g based on the multiple redox reactions between carbonyl groups and Li-ions.[65] Despite their high capacity, carbonyl-based electrodes have two critical limitations: poor cycling stability due to the dissolution of the carbonyl-based compounds into the electrolytes and low rate-performance due to their insulating natures. The researchers, therefore, have attempted to immobilize the carbonyl compounds on the conductive substrate by polymerization[90-92, 197] or covalent attachment[88, 237] to enhance both cycling stability and rate-performance. In line with this approach, researchers also have introduced carbonyl oxygen functional groups on the conductive carbon substrates, including carbon nanotube (CNT) and graphene, through the surface oxidation process.[169, 170, 213, 238-240]

Polydopamine, a functional coating material, also contains the redox-active carbonyl (quinone) functional groups, which can be applied for charge storage applications.[170, 239-241] Dopamine, a catechol structure with one amine group, can be self-polymerized with oxygen as the oxidant in alkaline environment, forming adhesive polydopamine coatings on almost any type of substrate.[203, 214, 217, 218, 222] Although the exact structure of polydopamine is still controversial due to the complex oxidation process involving various intermediates, the several proposed models include the 5,6-dihydroxyindole and 5,6-indolequinone as the major components of the polydopamine.[218, 222] Recent studies have shown that polydopamine can be employed as a promising electrode material for both Li- and Na-ion batteries.[200, 241, 242] In particular, we first revealed that polydopamine has multiple redox reactions at the high voltage region of 2.5 ~ 4 V vs. Li or Na, which can be used as positive electrodes for both Li- and Na-ion batteries.[241] The polydopamine and CNT composite electrodes were fabricated by coating polydopamine on CNTs through the self-polymerization process of dopamine under a simple stirring condition.[241] However, the polydopamine coating process on CNTs tends to produce polydopamine particle byproducts because of the self-nucleation reaction when the concentration of dopamine is high.[223, 241] In addition, due to the large portion of the CNTs, the overall electrode capacity was limited to ~133 mAh/g in Li-cells and ~109 mAh/g in Na-cells.[241] Thus, it is highly desirable to develop a novel synthesis method that can effectively utilize the redox reactions of polydopamine.

Here, we introduce a high-capacity functionalized graphene electrode for enhanced Li- and Na-ion storage. We incorporate polydopamine within a 3D reduced GO

assembly through a simple hydrothermal reaction. We show that the GO can assist the polymerization of dopamine due to its oxidizing nature and provide a large surface area substrate for the deposition of polydopamine, allowing a uniform polymer coating on the surface of 3D assembled rGO. We fabricate high-density and self-standing films by pressing the polydopamine functionalized graphene assembly. The fabricated films were further heat-treated to correlate chemical changes with their charge storage performances. The polydopamine functionalized graphene electrodes exhibit multiple redox reactions with electrolyte ions when used as positive electrodes in Li- or Na-ion batteries, giving rise to high capacities of ~230 mAh/g in Li-cells and ~ 211 mAh/g in Na-cells. The electrodes also show exceptional cycling stability and rate-performance, suggesting high-performance organic electrode materials for Li- and Na-ion batteries or hybrid capacitors.

6.2 Experimental

Sample preparation. GO was synthesized from graphite (Bay Carbon Inc.) by the modified Hummer's method.[109, 110] GO was mixed with dopamine hydrochloride (Sigma Aldrich) at the same concentration of 2 mg/mL by sonication for 1 h. The mixture was then sealed in a Teflon-lined autoclave, and the hydrothermal reaction was carried out at 180 °C for 6 h. The graphene-polydopamine composite (GD) hydrogel was formed after the hydrothermal reaction and was picked up by tweezers and washed several times with DI water. The hydrogel was by freeze-dried at -84 °C (FreeZone Plus 2.5 Liter Cascade Benchtop Freeze Dry System) for 24 h to obtain GD aerogel. The GD-200 and GD-650 were prepared by thermally treating the GD aerogel at 200 °C and 650 °C for 2 h, respectively. Graphene aerogel (GA) was also prepared from the GO solution by a

similar hydrothermal reaction without dopamine hydrochloride. For electrochemical measurements, the GD aerogels were cut and compressed into high-density films.

Characterizations. The microstructure and morphology were investigated using a SEM equipped with EDX (Hitachi SU8230, operated at 5 kV) and TEM (Hitachi HT7700, operated at 120 kV). The elemental analysis of the electrodes was characterized by XPS (Thermal Scientific K-alpha XPS instrument), and the high-resolution C 1s, O 1s, and N1s peaks were fitted by the XPSPEAKS 4.1. TGA was carried out by Q600 TGA/DSC in the temperature range of 50-700°C under air and nitrogen environment with a ramping rate of 5 °C min^{-1}.

Electrochemical measurements. Electrochemical measurements were conducted in two-electrode Swagelok-type cells. The Li- and Na-cells were operated using a piece of the various polydopamine functionalized graphene films as positive electrodes and a piece of Li or Na foil as negative electrodes. Two pieces of Celgard 2500 or glass fiber membrane (Whatman) were employed as separators in Li- and Na-cells. 1 M $LiPF_6$ or $NaPF_6$ in a mixture of EC and DMC (3:7 v/v, BASF) were used as the electrolyte for Li- or Na-cells, respectively. The operation voltage windows of Li- and Na-cells were 1.5 – 4.5 V vs. Li and 1.3 – 4.2 V vs. Na, respectively. Current densities were controlled from 0.05 to 25 A/g for Li-cells and 0.05 to 10 A/g Na-cells during the galvanostatic tests. At each end of charge and discharge, the voltage was held for 30 min at either 4.5 V or 1.5V vs. Li (4.2 V or 1.3 V vs. Na). The cycling stabilities of the electrodes were tested via an accelerated cycling method based on previous reports.[169, 170, 213, 240, 241] The accelerated cycling consists of the charge/discharge capacity measurements at 0.1 A/g and the high current density cycling at 20 A/g. Between each charge and discharge capacity

measurement at 0.1 A/g, the electrodes were cycled at a 20 A/g for 99 cycles (up to 1500th cycle) or 499 cycles (1501th-7,000th cycle). Before charge or discharge capacity measurements at 0.1 A/g, the electrodes were held at 4.5 or 1.5 V vs. Li (4.2 or 1.3 V vs. Na in Na-cells) for 30 min.

6.3 Results and Discussion

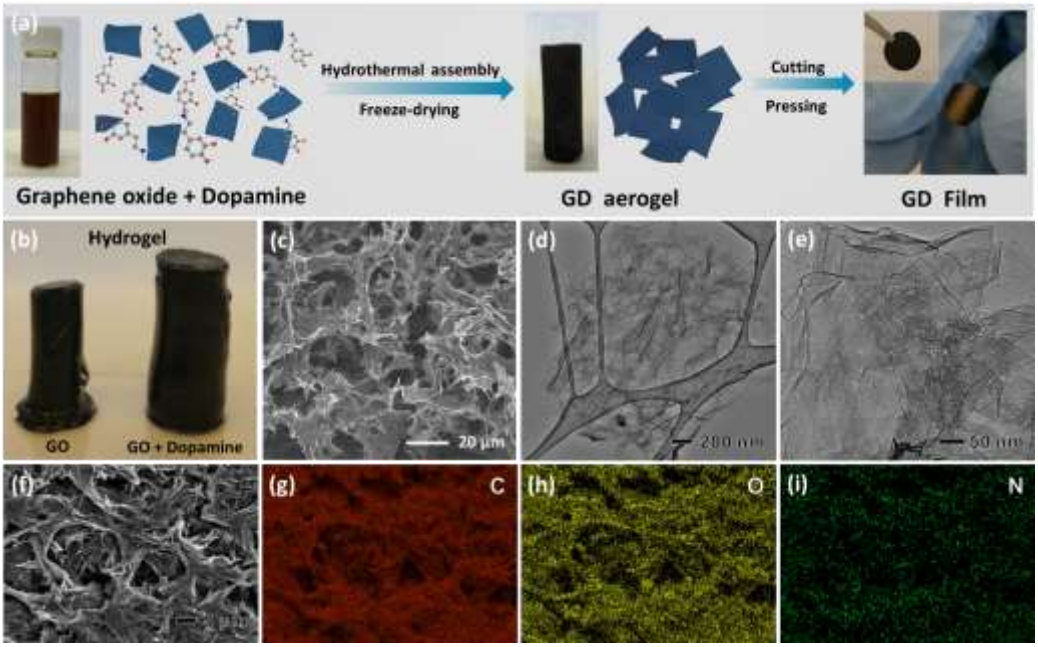

Figure 6.1 (a) Schematic preparation of a high-density and flexible graphene-polydopamine (GD) film. (b) Digital image of the graphene (left) and GD hydrogels (right). (c) SEM and (d and e) TEM image of the GD aerogel. (f) SEM and EDX elemental mapping of (g) carbon, (h) oxygen, and (i) nitrogen on the GD film.

Polydopamine functionalized graphene hydrogels were prepared by a simple hydrothermal reaction (**Figure 6.1a**). First, dopamine was uniformly mixed with the GO aqueous dispersion at the same concentration of 2 mg/mL by sonication for 1 h. The hydrothermal reaction was carried out on the mixture at 180 ^{o}C for 6 h, forming a 3D structured hydrogel. Under the hydrothermal condition, the H^{+} ions released from the superheated water can reduce the GO, and the rGO sheets can self-assemble into the

hydrogel through π-π and the hydrophobic interactions between the rGO layers.[117, 169, 232] The previous study has shown that the GO can act as a chemical oxidant for the polymerization of conducting polymers under a mild heating condition above 80 °C.[243] Therefore, we expect that dopamine is simultaneously polymerized on the rGO surface during the self-assembly process of the rGO sheets, resulting in a 3D graphene-dopamine composite (GD) hydrogel. It is interesting to note that the GD hydrogel has a larger volume than that of the graphene hydrogel prepared under the same condition without dopamine (**Figure 6.1b**). The previous study has shown that when pyrrole monomers are adsorbed to the GO surface via a π-π interaction or hydrogen bonding, the self-stacking process of rGO sheets can be effectively interrupted during the hydrothermal reaction, increasing the volume of the assembled hydrogel.[17] Therefore, the increased volume of the GD hydrogel can be attributed to the adsorption of the dopamine via π-π interaction and continuous formation of the polydopamine film on the surface of the rGO. The assembled hydrogel was freeze-dried to fabricate a GD aerogel (**Figure 6.1a**). The aerogel was cut and compressed into a high-density GD film with a density of ~0.75 g/cm^3, giving rise to flexible, self-standing electrodes. SEM images of the GD aerogel displayed a 3D porous interconnected network structure (**Figure 6.1c**). TEM images of the GD (**Figure 6.1d** and **e**) showed an assembly consisting of rougher layers compared to graphene aerogel (GA, **Figure 6.2, Figure 6.3**), indicating the deposition of the polydopamine on rGO surface. The vertically compressed GD films still exhibited a 3D interconnected porous structure, but the pore dimension was significantly reduced in the vertical direction (**Figure 6.1f** and **Figure 6.4**). To gain insight into the uniformity of the polydopamine coating on rGO surface, elemental mappings of carbon, oxygen, and

nitrogen on the GD film were conducted by EDX (**Figure 6.1f-i**). A homogenous distribution of each element was observed on the GD film, indicating the successful and uniform deposition of polydopamine with the 3D rGO assembly.

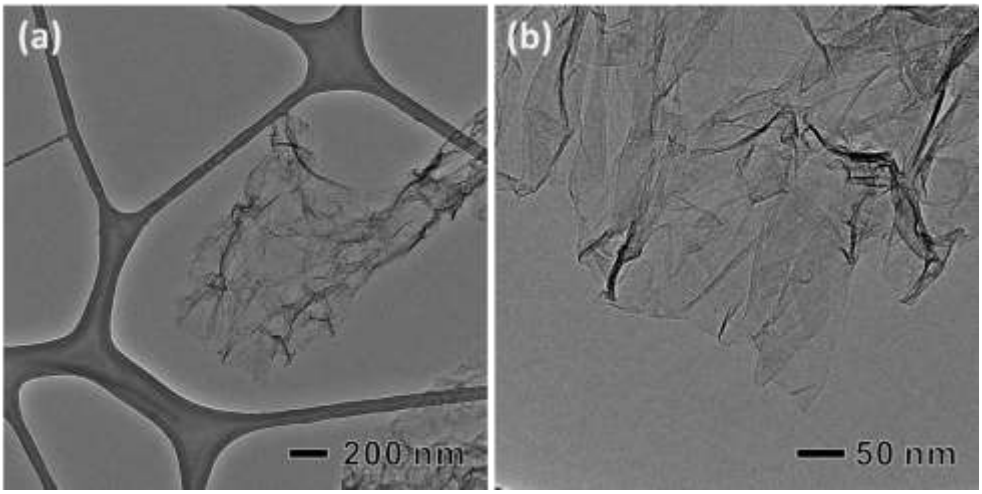

Figure 6.2 TEM images of a graphene aerogel (GA) at (a) low- and (b) high-magnification.

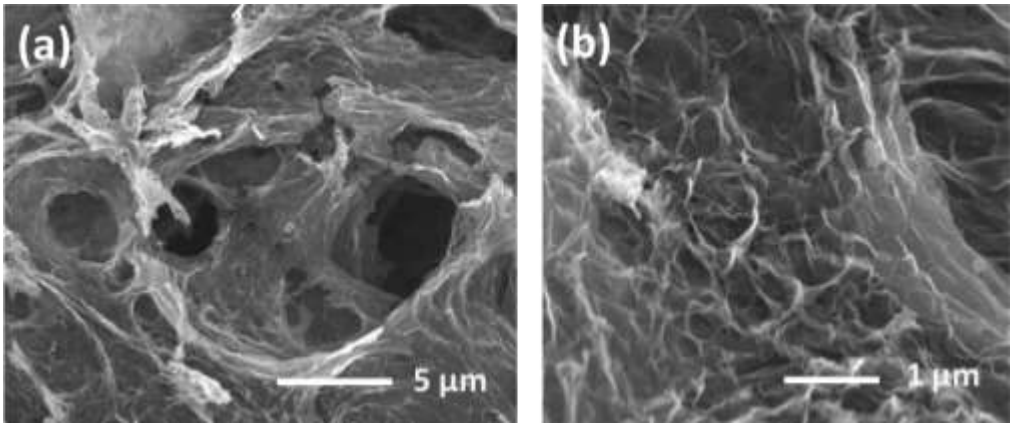

Figure 6.3 SEM images of a GD aerogel at (a) low- and (b) high-magnification.

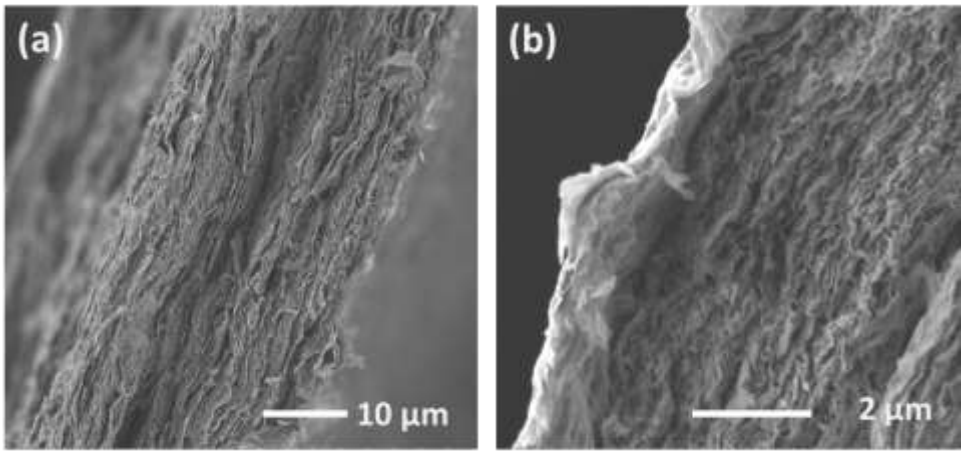

Figure 6.4 SEM images of a GD film in lateral view at (a) low- and (b) high-magnification, showing the densely-packed film.

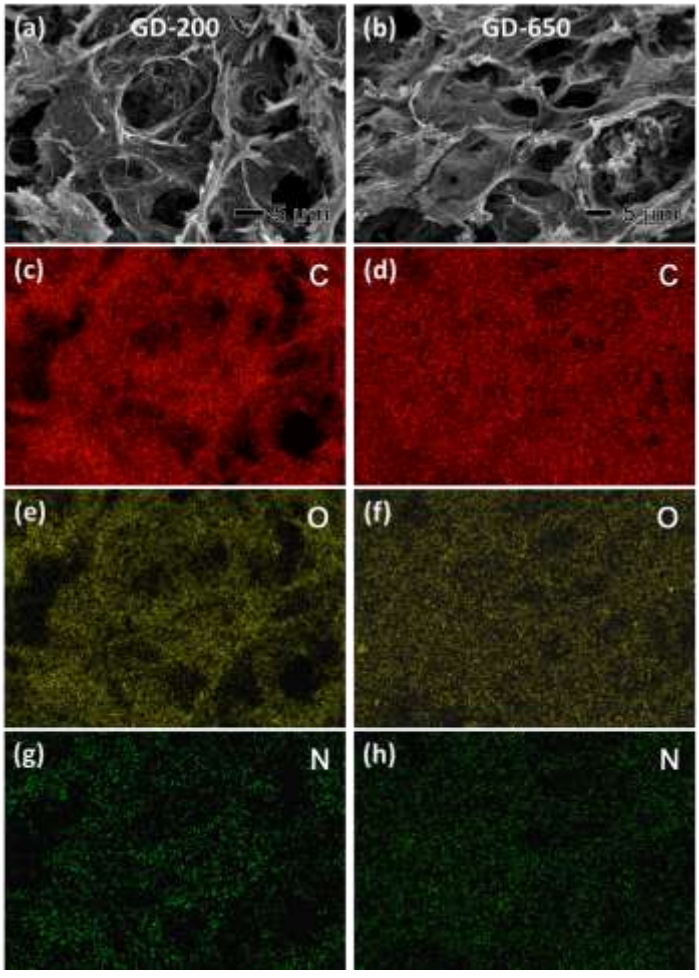

Figure 6.5 SEM images and energy-dispersive X-ray spectroscopy (EDX) mappings of the (a, c, e, g) GD-200 and (b, d, f, h) GD-650 films.

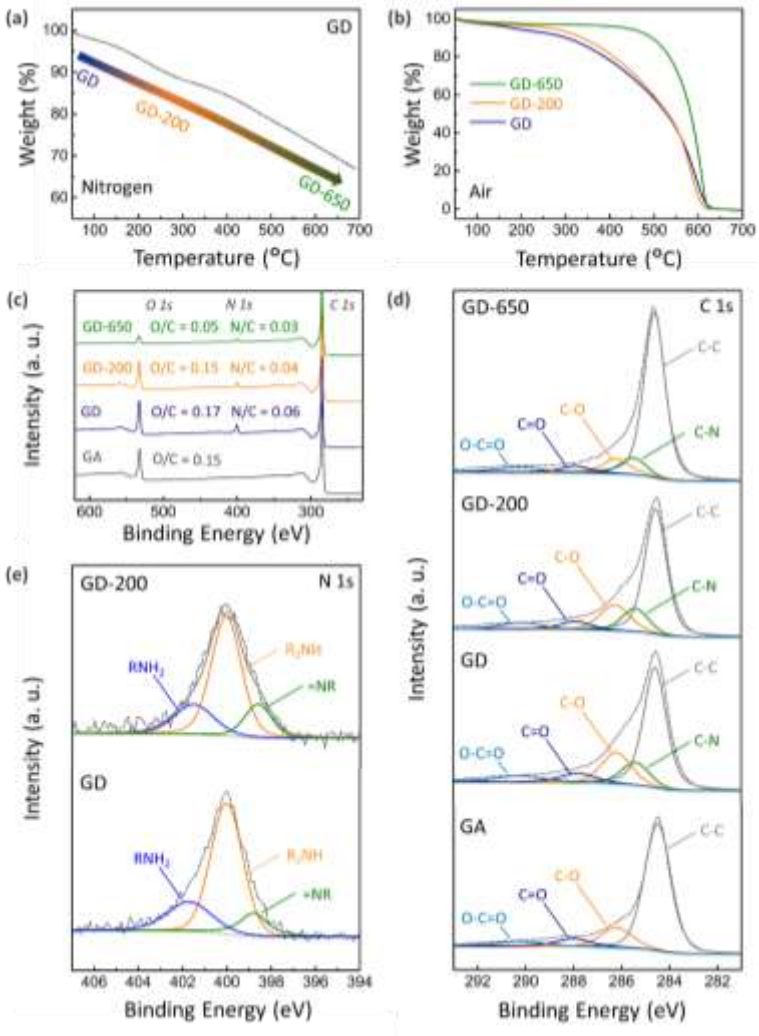

Figure 6.6 (a) TGA of the GD under nitrogen flow. (b) TGA of the GD, GD-200, and GD-650 under air flow. (c) XPS wide scan survey of the films with their O/C and N/C ratios. High-resolution XPS (d) C 1s and (e) N 1s spectra of the films

The fabricated films were further heat-treated to investigate chemical changes and corresponding charge storage performances. The GD aerogels were heat-treated at 200 ^{0}C (GD-200) and 650 ^{0}C (GD-650) under argon environment for 2h. After pressing, the densities of GD-200 (0.60 g/cm^3) and GD-650 (0.1 g/cm^3) films were lower than that of the GD (0.75 g/cm^3). The compressed GD-200 and GD-650 films also showed

interconnected 3D network structures with uniformly distributed nitrogen and oxygen in the SEM and EDX mapping (**Figure 6.5**). TGA of the GD was carried out under nitrogen at a flow rate of 50 mL min^{-1}, showing a gradual weight loss with increasing temperature (**Figure 6.6a**). During this gradual decay, weight losses of 7% and 31% were observed at 200 °C and 650 °C. The thermal stability of the films was compared by TGA under flowing air, showing the enhanced stability with higher preheating temperature from GD to GD-650 (**Figure 6.6b**). The enhanced stability of the GD-200 and GD-650 can be attributed to the preliminary removal of the oxygen and nitrogen functional groups during the heat-treatments under inert gas environment. The chemical composition and surface chemistry of the films were investigated by XPS. An atomic oxygen to carbon ratio (O/C) of 0.15 was observed for GA, and this ratio was increased to 0.17 for GD (**Figure 6.6c**). The GD film also showed an atomic nitrogen to carbon ratio (N/C) of 0.06 due to the incorporated polydopamine. The GD-200 film had slightly decreased O/C ratio of 0.15 and N/C ratio of 0.04, while the GD-650 showed more reduced O/C ratio of 0.05 and N/C ratio of 0.03 due to the thermal reduction of the rGO and carbonization of polydopamine.[205, 244] Detailed chemical states of the materials were analyzed by fitting the high-resolution C 1s, O1s and N1s spectra (**Figure 6.6d** and **e**, and **Figure 6.7**). The C 1s spectra were fitted by five characteristic peaks, including 284.6 ± 0.1 eV for CH_x and sp^2-hybridized carbon, 285.5 ± 0.1 eV for C–N, 286.4 ± 0.2 eV for C-O, 287.8 ± 0.2 eV for C=O, and 288.9 ± 0.2 eV for COOH.[245, 246] The C–N and C-O peaks were found gradually decreased from GD to GD-650 as the heat-treatment temperature increased, indicating the gradual removal of these functional groups during the heat-treatment. The O1s spectra were fitted by 533.1 ± 0.2 eV for O–C and 531.2 ±

0.1 eV for O=C and the percentage of carbonyl group (C=O) was calculated by comparing these two peaks (**Figure 6.7**).[214, 221] It is interesting to note that the GD film synthesized by hydrothermal reaction has a higher percentage of the carbonyl group (36%) compared to that of the self-polymerized dopamine on CNT (26%).[241] The N1s spectra was also fitted by assigning 401.7±0.1 to primary amine ($–NH_2$), 399.9±0.1 eV to secondary amine (–NH–), and 398.5±0.1 eV to tertiary/aromatic amine (–N=), respectively (**Figure 6.6e**).[214, 221] The existence of primary amine is due to the non-covalent self-assembly of dopamine,[222] while other amines are associated with the polydopamine and oxidized intermediates, including 5,6-dihydroxyindole and 5,6-indolequinone,[214, 241] further confirming the polymerization process under hydrothermal condition.

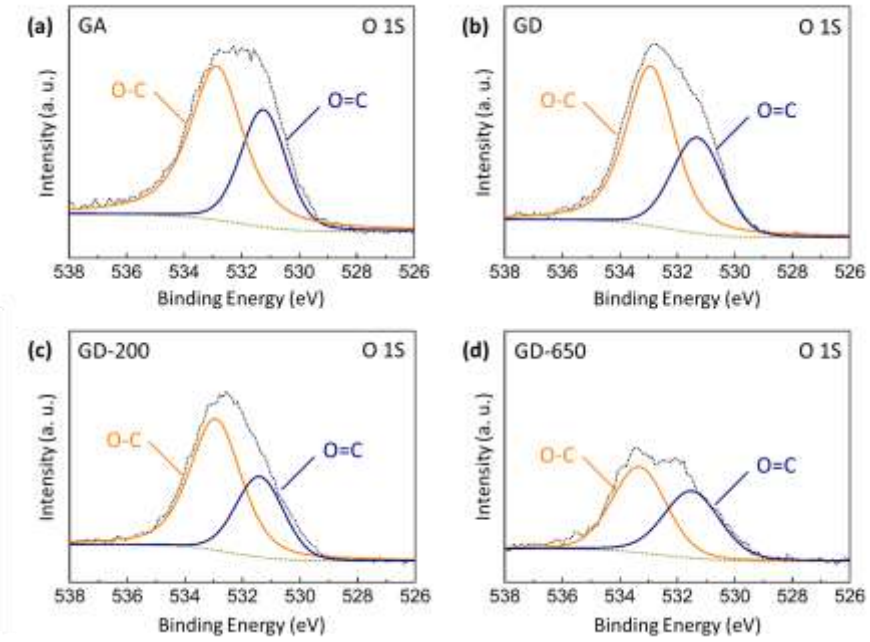

Figure 6.7 High-resolution O 1s spectra of the (a) graphene aerogel (GA), (b) GD, (c) GD-200 and (d) GD-650 films.

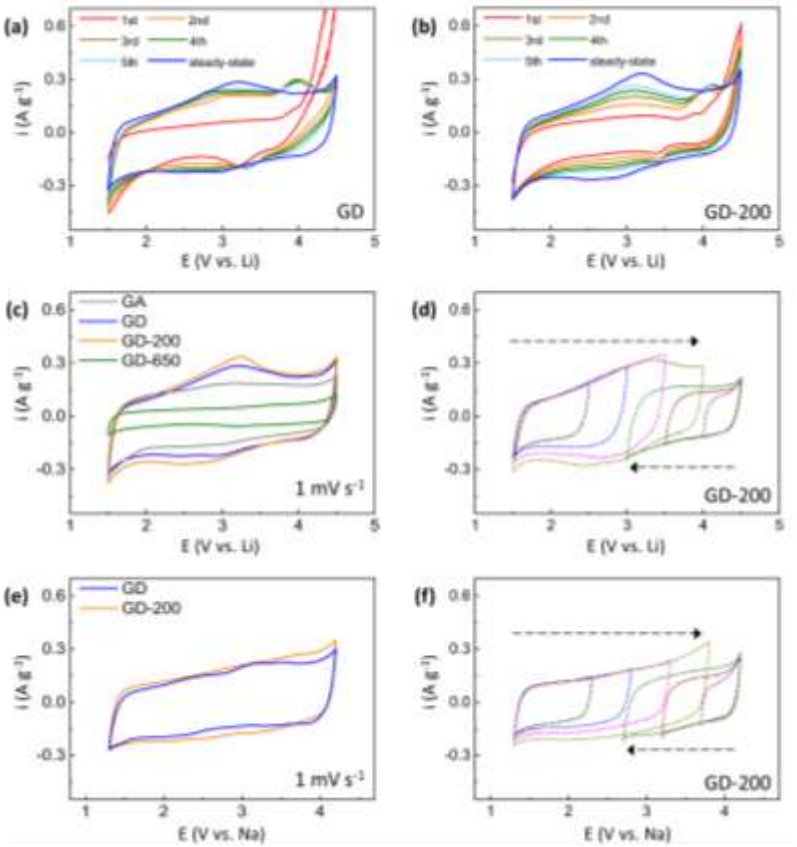

Figure 6.8 CV scans of the (a) GD and (b) GD-200 electrodes at 1 mV/s in Li-cells. (c) Comparisons of the steady-state CV scans of the GD, GD-200, GD-650 and GA electrodes in Li-cells. (d) Forward and backward potential-dependent CV scans of the GD-200 in Li-cells. (e) Comparisons of the steady-state CV scans of the GD and GD-200 electrodes in Na-cells. (f) Forward and backward potential-dependent CV scans of the GD-200 in Li-cells.

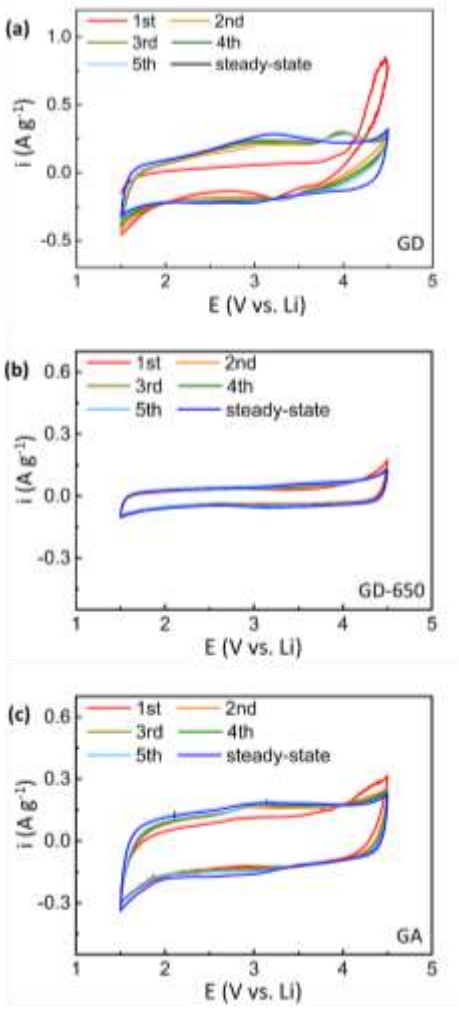

Figure 6.9 CV scans of the (a) GD, (b) GD-650 and (c) GA electrodes at 1 mV/s in Li-cells.

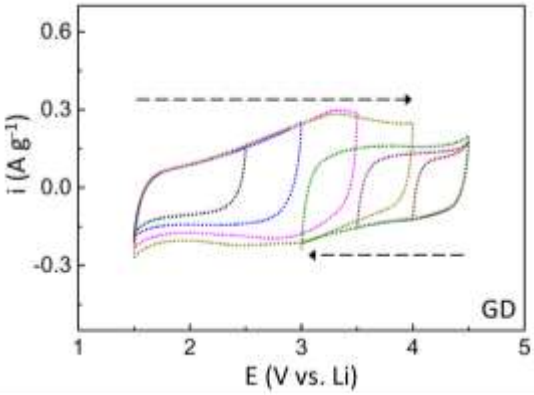

Figure 6.10 Forward and backward potential-dependent CV scans of the GD at 1 mV/s in Li-cells.

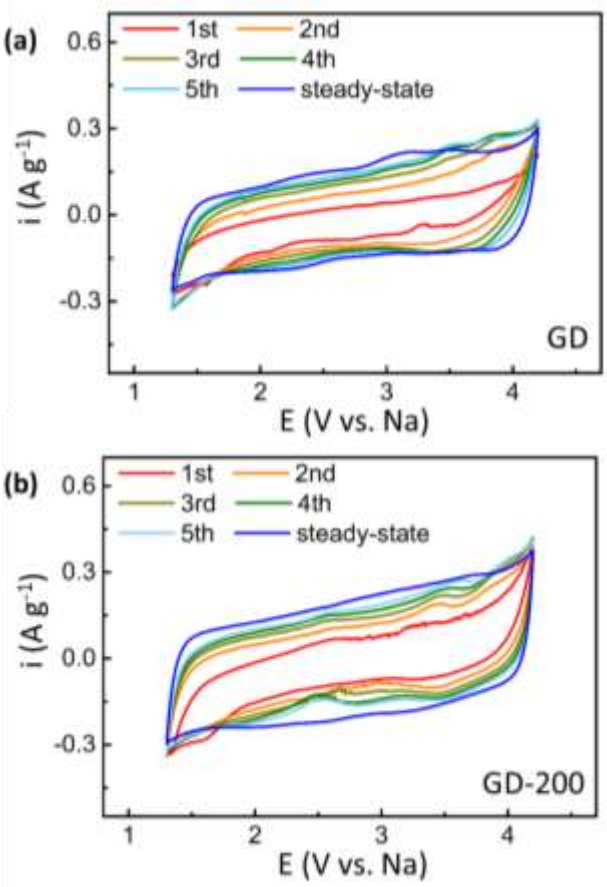

Figure 6.11 CV scans of the (a) GD and (b) GD-200 electrodes at 1 mV/s in Na-cells.

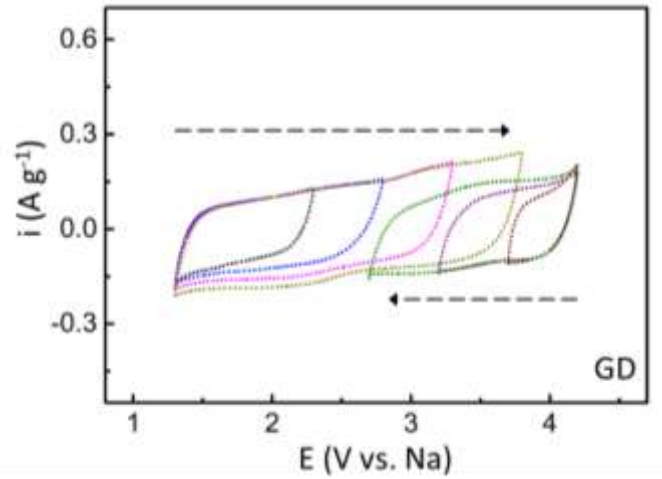

Figure 6.12 Forward and backward potential-dependent CV scans of the GD at 1 mV/s in Na-cells.

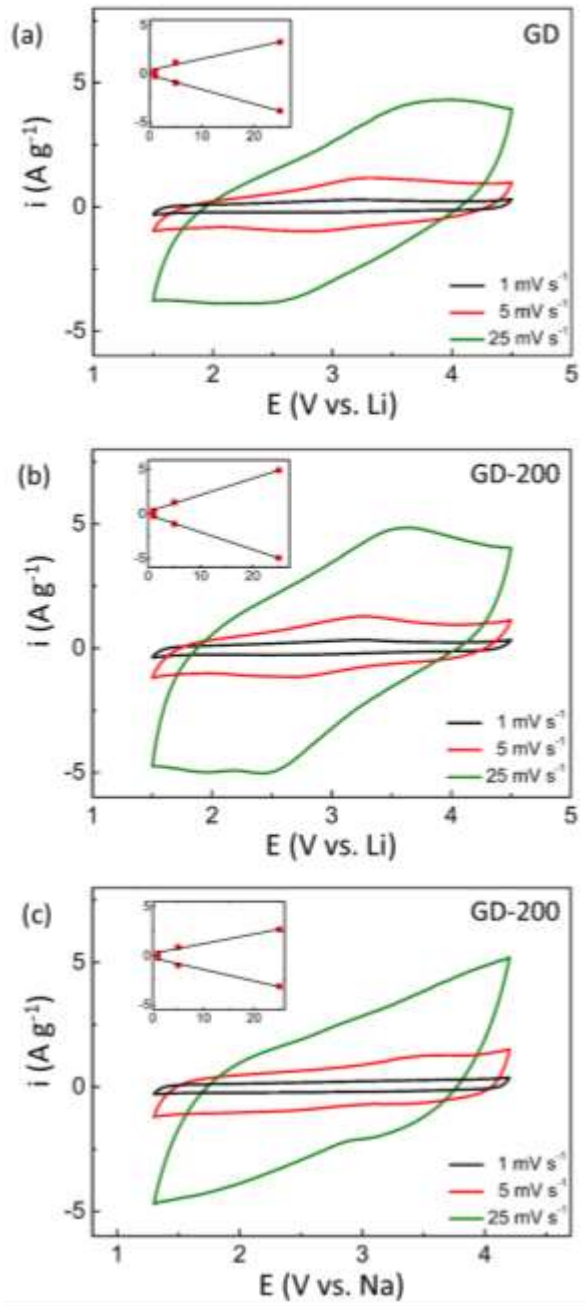

Figure 6.13 Rate-dependent CV scans of the (a) GD and GD-200 electrodes in Li-cells, and (c) GD-200 in a Na-cell. Insets show the anodic and cathodic currents as a function of scan rates.

The charge storage mechanism of the GD films was studied as positive electrodes against Li or Na metal foil negative electrodes by CV test. The initial CV scan of the GD electrode displayed a strong oxidation wave from ~4.1 V vs. Li due to the anodic

polymerization of the dopamine intermediate within the adsorbed polydopamine on the rGO (**Figure 6.8a** and **Figure 6.9a**).[241, 247] During sequential CV cycling, two distinct redox peaks were found at ~3.2 and ~4.0 vs. Li, and the second redox peak broadened at the steady state. The first sharp peak can be attributed the redox reactions between oxygen functional groups and Li ions, while the second broad peak is due to the PF_6^- anion insertion (p-doping) reaction into the polymer film.[224, 241] The GD-200 electrode exhibited the significantly reduced anodic wave in the high potential region, which may arise from the partial removal of functional groups that can participate in the anodic polymerization (**Figure 6.8b**). Upon CV cycling, two redox peaks were progressively developed and eventually one broad redox peak was observed at ~3.2 V vs. Li at the steady-state. The GD-650 showed the negligible anodic wave and redox peak, indicating a significant removal of the redox-active functional groups during the high-temperature heat-treatment (**Figure 6.9b**). The GA electrode displayed also a small redox peak around ~3 V vs. Li due to the redox reactions between the remaining oxygen functional groups and Li-ions (**Figure 6.9c**). Comparing the steady-state CV scans of the electrodes, both GD and GD-200 have the higher capacitances (~183 F/g for GD and ~202 F/g for GD-200) compared to that of GA (~147 F/g, **Figure 6.8c**). The significantly increased capacitances of the GD and GD-200 electrodes can be attributed to the multiple redox reactions of the introduced polydopamine in the voltage over ~2.5 V vs. Li. In contrast, the GD-650 exhibited the lowest capacitance of ~49 F/g mainly due to the removal of the redox-active functional groups. The potential-dependent CV tests were conducted for GD-200 and GD to gain further insight into its charge storage mechanism (**Figure 6.8d** and **Figure 6.10**). The gradual CV scans from a low voltage limit of 1.5 V

vs. Li to higher voltage ranges clearly visualized the development of the redox reaction with Li-ions (n-doping), while the CV scans from a high voltage limit of 4.5 vs. Li to lower voltage regions showed a small contribution of the p-doping mechanism. Upon CV cycling in Na-cells, both GD and GD-200 showed a gradual increase in current density over the entire voltage range of 1.3–4.2 V vs. Na (**Figure 6.11**). Despite its indistinct redox peaks compare to those in Li-cells, the GD-200 exhibited a high specific capacitance of ~174 F/g, which is higher than that of the GD (~150 F/g, **Figure 6.8e**). The enhanced capacitance of the GD-200 compared to the GD can be attributed to the partial removal of non-redox active oxygen and nitrogen functional groups during the heat treatment. The redox characteristic of the GD-200 can be more clearly observed by a potential-dependent CV test, demonstrating gradual evolutions of the redox reactions from continuously expanding CV scans (**Figure 6.8f** and **Figure 6.12**). Additionally, the rate-dependent CV tests for GD and GD-200 in both Li- and Na-cells showed that the current density of the main redox peak can be fitted almost linearly to the scan-rate, indicating that the redox reactions of the polydopamine are surface-controlled (**Figure 6.13**).[4]

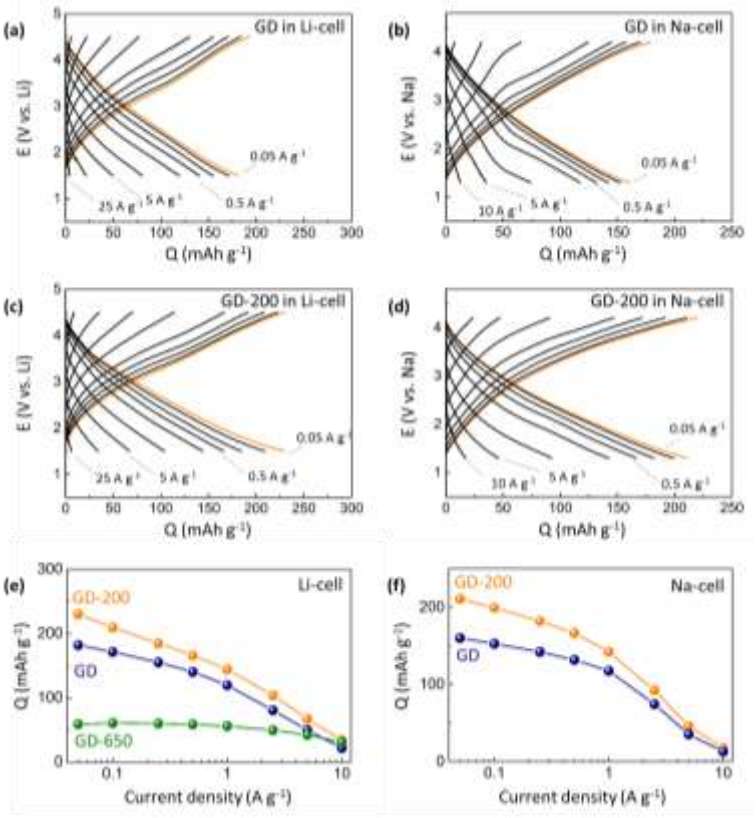

Figure 6.14 Galvanostatic charge-discharge profiles of the (a, b) GD and (c, d) GD-200 electrodes in Li-cells with a voltage window of 1.5-4.5 V vs. Li and Na-cells with a voltage window of 1.3-4.2 V vs. Na. Comparisons of galvanostatic discharge capacities of the electrodes in (e) Li-cells and (f) Na-cells.

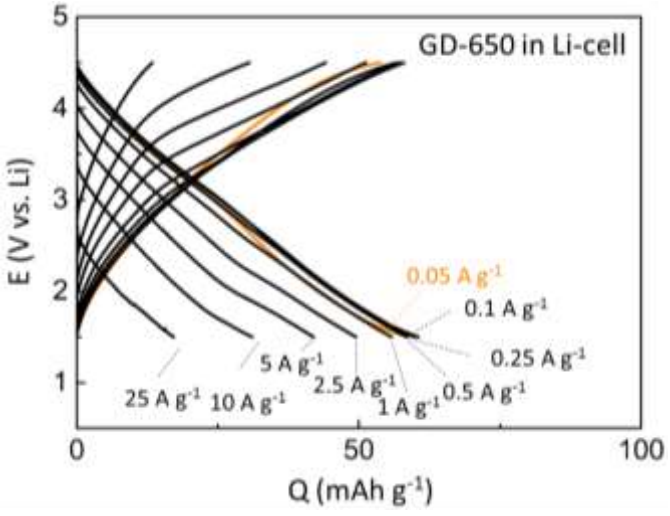

Figure 6.15 Rate-dependent galvanostatic charge/discharge profiles of the GD-650 electrode in a Li-cell.

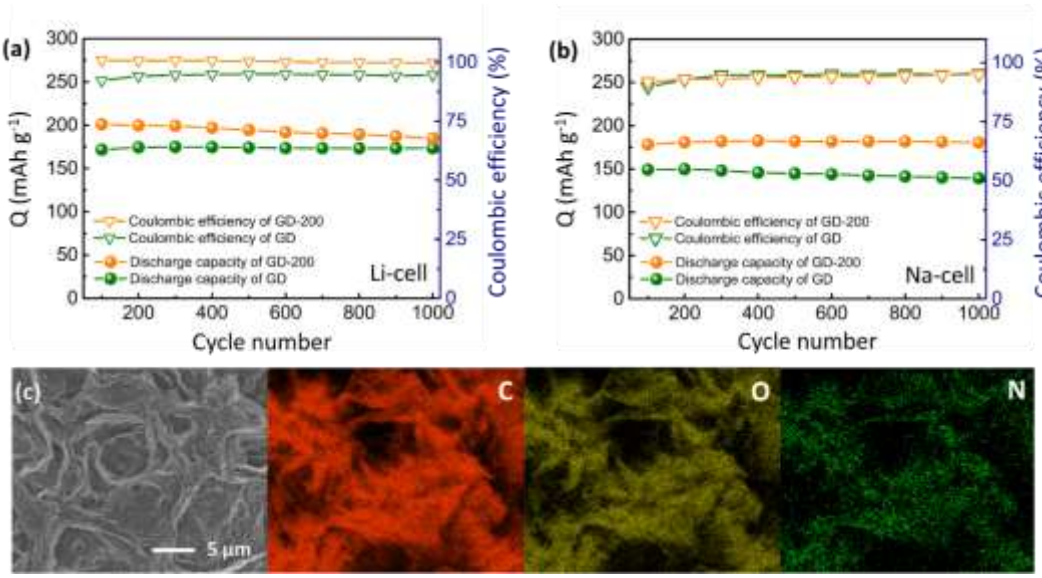

Figure 6.16 Gravimetric discharge capacities of the GD and GD-200 electrodes and their coulombic efficiencies in (a) Li- and (b) Na-cells as a function of cycle number. (c) SEM and EDX mapping of the GD-200 electrode after cycling. Between each charge and discharge capacity measurement at 0.1 A/g, the electrodes were cycled at 20 A/g for 99 cycles.

The steady-state charge storage capacities of the electrodes were evaluated by rate-dependent galvanostatic charge/discharge tests in both Li- and Na-cells (**Figure 6.14** and **Figure 6.15**). The GD and GD-200 displayed a small plateau around 3.2 V vs. Li that is ascribed to the main redox reaction between the oxygen functional groups and Li ions (**Figure 6.14a** and **c**). The overall sloped charge and discharge profiles can be attributed to the multiple redox reactions on top of double layer-capacitance.[169, 241] At a low current density of 0.05 A/g, the GD-200 electrode delivered the highest capacity of ~230 mAh/g compared to those of other electrodes (~163 mAh/g for GA, ~182 mAh/g for GD, and ~ 59 mAh/g for GD-650). This capacity (~230 mAh/g) is also significantly higher than that of the recently introduced polydopamine-coated CNT electrode (~133 mAh/g),[241] indicating a more effective utilization of the redox reactions from polydopamine within the 3D rGO assembly. The GD-200 maintained its high capacity of

~144 mAh/g at an increased current density of 1 A/g and ~ 67 mAh/g at a high current density of 5 A/g, outperforming GD and GD-650 (**Figure 6.14c**). Such high rate-performance should be attributed to the facilitated electron and ion transport through the 3D interconnected porous structure that supports fast surface redox reactions of polydopamine. The GD-200 also delivered a higher capacity of ~210 mAh/g that that of the GD (~160 mAh/g) at a 0.05 A/g in Na-cells. This capacity (~210 mAh/g) significantly exceeds those of the previously reported polydopamine-coated CNT (~109 mAh/g),[241] tetrahydroxyl-1,4-benzoquinone functionalized graphene aerogel (~120 mAh/g),[170] and oxygen functionalized carbon foams (~152 mAh/g).[164] The GD-200 also showed superior rate-performance relative to the GD in Na-cells (**Figure 6.14f**). The enhanced performance of the GD-200 compared to the GD can be attributed to the partial reduction of non-redox active functional groups. On the other hand, the remarkably decreased performance of the GD-650 is due to a significant reduction of redox-active functional groups. It is also worth to mention that the GD-200 and GA have the same O/C ratio of 0.15 (**Figure 6.6c**), but the GD-200 can deliver a significantly higher capacity (~230 mAh/g) than that of the GA (~163 mAh/g). These results suggest that controlling both the quantity and quality (type) of the functional groups is critical to achieve the maximum performance of the functionalized carbon electrode.

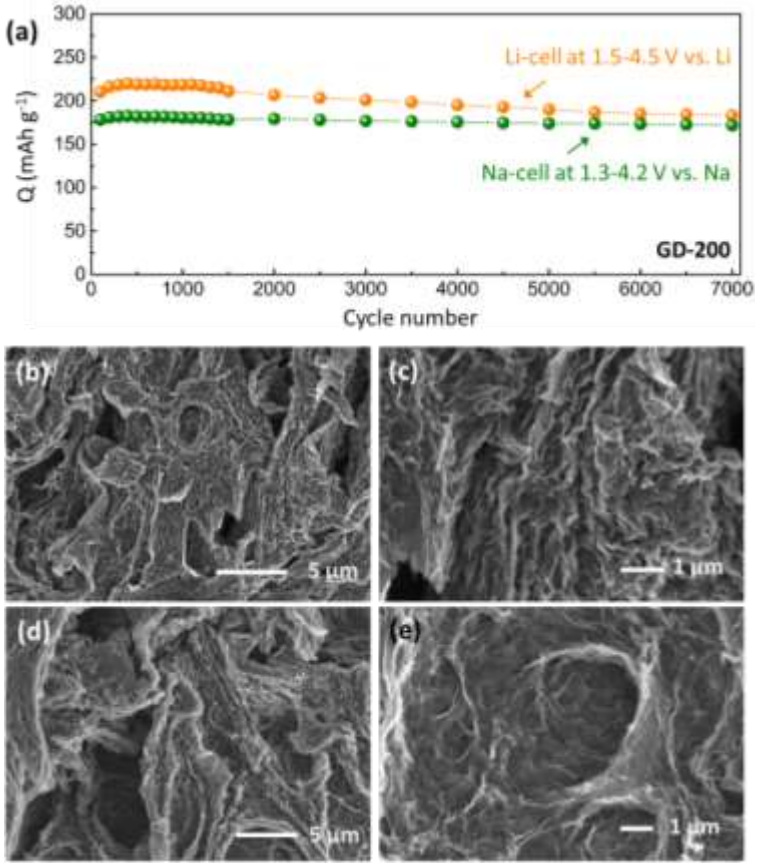

Figure 6.17 (a) Gravimetric discharge capacities of the GD-200 at 0.1 A/g as a function of cycle number up to 7,000 cycles in Li- and Na-cell via an accelerated cycling method. SEM images of the GD-200 after cycling in (b and c) Li-cell and (d and e) Na-cell. Between each charge and discharge capacity measurement at 0.1 A/g, the electrodes were cycled at 20 A/g for 99 cycles (up to 1500th cycle) or 499 cycles (1501th-7,000th cycle).

The cycling stability of the GD and GD-200 electrodes were evaluated by an accelerating cycling method in both Li- and Na-cells (**Figure 6.16a** and **b)**. The both electrodes showed the negligible decreases of their capacities over 1,000 cycles with high Columbic efficiencies over ~99% in Li-cells and ~95% in Na-cells. The extended cycling stability tests of the GD-200 electrodes were also conducted up to 7,000 cycles to investigate their structural changes after the cycling test (**Figure 6.17**). The SEM with EDX mapping showed that the GD-200 electrode maintained the interconnected 3D

network structure with the uniform distribution of nitrogen and oxygen atoms after the cycling process, further confirming its exceptional cycling stability (**Figure 6.16c**). This excellent cycling stability should be attributed to the polymerization process of dopamine and the strong adhesive property of the polydopamine coating on the rGO surface, which can effectively prevent the dissolution of active molecules.

6.4 Conclusions

We have fabricated a new organic electrode, polydopamine functionalized 3D graphene assembly, through a simple and scalable hydrothermal reaction. This polydopamine functionalized graphene electrode delivered high capacities of ~230 mAh/g in Li-cells and ~211 mAh/g in Na-cells in the high voltage regions utilizing the multiple redox reactions of polydopamine, suggesting high-capacity positive electrodes for both Li- and Na-ion storage. This electrode also showed excellent rate-performance due to its unique 3D structure that can support fast surface redox reactions of polydopamine. Furthermore, the polymerization process of dopamine during the hydrothermal reaction and the strong adhesive property of polydopamine can prevent the dissolution of active molecules, enabling exceptional cycling stability. Thus, the high-performance polydopamine functionalized graphene electrode opens a variety of opportunities up for electrochemical energy storage applications, including Li- and Na-ion batteries or hybrid-capacitors.

CHAPTER 7. CONCLUSION AND OUTLOOK

7.1 General Conclusions

In this thesis, we studied the energy storage mechanism in the redox-active carbon-based cathodes. Using reduced GO as an example, the interaction between oxygen functional groups and Li-ions were investigated by both theoretical and experimental methods. The redox active oxygen species were determined as carbonyl and epoxide groups. Electrochemical measurements showed that the reduced GO films delivered a capacity of 160 mAh/g (91.5 Ah/L) in Li-cells, the high capacity resulted from the contribution from both EDLC and Faradic capacitance. To further enhance the gravimetric capacity of redox-active graphene-based cathodes, we successfully incorporated redox-active molecules on the surface of reduced GO. The incorporated molecules could reduce and functionalize the GO simultaneously, resulting in functional graphene electrodes with an enhanced capacity of 165 mAh/g.

The second part of this thesis focused on developing high-performance carbon-based electrodes from renewable and low-cost biomass. Using glucose as an example, we successfully converted glucose into redox-active carbon materials through a hydrothermal carbonization process. The redox-active carbon materials delivered a capacity of ~210 mAh/g, owing to the existence of abundant oxygen functional groups. We also continuously optimized the carbon materials by modifying their morphologies. Adding a small amount of GO during the hydrothermal carbonization process of glucose, we obtained carbon sheets instead of carbon spheres, which would facilitate the electrical

connections. The utilization of GO served as a template as well as facilitated the carbonization of glucose.

In the last part of this thesis, we showed our research on organic electrode materials. Dopamine, which can be simply self-polymerized in weakly alkaline solution, was identified as promising cathode materials in both Li- and Na-ion batteries. DFT and electrochemical measurements were used to investigate the energy storage mechanism in polydopamine. Our results showed that polydopamine had multiple redox reactions with electrolyte ions (both cations and anions). Our electrochemical measurements showed that polydopamine could deliver high capacities of ~235 mAh/g in Li-cells and ~213 mAh/g in Na-cells, respectively. However, the self-polymerization process had a shortcoming of low efficiency, polydopamine particles couldn't be avoided at a high concentration of dopamine which resulted in the low usage of active materials and poor rate capability. To solve this issue, we used GO as an oxidant and developed a high-efficient hydrothermal polymerization process for dopamine. During the hydrothermal polymerization process, dopamine would reduce GO, while polydopamine would uniformly grow on the surface of the reduced GO. A compact polydopamine-graphene film (0.75 g/cm^3) could be easily obtained after compressing the freeze-dried 3D structured polydopamine-graphene composite. This compact film delivered high capacities of 230 mAh/g in Li-cells and 211 mAh/g in Na-cells based on the total mass of the electrodes.

7.2 Future and Challenges

The research in this thesis showed the promise of further enhancing the capacity of carbon-based cathode materials for hybrid capacitors (or Li-ion capacitors) by introducing additional oxygen functional groups. However, there are still several issues should be investigated or improved. Firstly, how could we finely control the surface chemistry of these functional carbon cathode materials? The typical oxidation methods of carbon materials introduce several types of oxygen functional groups simultaneously, such as hydroxyl (-OH), carbonyl (-C=O), carboxylic acid (-COOH), and epoxide. But our theoretical study based on rGO have shown that only carbonyl and epoxide contribute additional capacities by reversibly reacting with Li-ions at a high redox potential (~3.0 V vs. Li). Simply increasing the oxidant concentration or time for carbon materials will increase all the oxygen species simultaneously. The excess oxygen species can only slightly increase the capacity but decrease the rate capability significantly owing to the poor conductivity. Thus, methods which can convert these inactive oxygen species (hydroxyl and carboxylic acid) into active species (carbonyl and epoxide) or which can introduce specific oxygen species (carbonyl or epoxide) on carbon materials will be highly desirable. Similarly, although we propose a high-efficiency, hydrothermal polymerization process of dopamine, hydroxyl groups are still dominant in the final polydopamine. By developing a polymerization method which can promote the formation of carbonyl-dominant polydopamine, we can expect even higher capacity (up to 364 mAh/g).

Secondly, the stability of the oxygen species should also be investigated considering both the time and temperature effect. For example, the stability of oxygen functional groups at a high operation temperature (i.e. 60 ^{o}C) should be investigated, the cycling

stability can be used as an indirect evidence for checking the stability of oxygen functional groups. In addition, the electrochemical measurements in this thesis were conducted with a high cutoff voltage of 4.5 V vs. Li which is close to the stability limit of typical EC/DMC mixture. Whether the functionalized carbon materials will catalyze the decomposition of the electrolyte should be investigated. In both cases, post-mortem analysis techniques, such as XPS, SEM, and FT-IR, will be needed. Technique challenges will be how to distinguish the oxygen and carbon from carbon-based electrodes and decomposed electrolyte.

How to increase the volumetric performance of the carbon-based cathode is another important topic should be further investigated. In specific applications, storing more energy in limited spaces is one of the critical criteria for selecting the energy storage systems. In this thesis, we were able to increase the density of graphene-based electrodes to 0.64 g/cm^3, and carbon nanotube-base electrode to 1.02 g/cm^3. However, efforts still need to be devoted to determining the optimal density of carbon-based electrodes considering the trade-off between the volumetric and gravimetric performance. In addition, we also showed the morphologies of the carbon materials have great effects on the performance of the electrodes. In this case, once the optimized morphologies of redox-active carbon materials were determined, more efforts should be devoted to investigating the thickness and the porosity of the electrodes.

The performance of the above carbon-based cathodes should also be evaluated in the full-cell configurations to evaluate their energy and power performance. For typical hybrid capacitors (Li-ion capacitors), the most widely used anodes in Li-ion capacitors are graphite or lithium titanium oxide for different requirements, while the high surface

area activated carbon serves as the cathodes. Nowadays, efforts have been devoted to introducing silicon into the anode for further increasing the energy density of the hybrid capacitors. However, the critical limitation for hybrid capacitors lies in the limited capacity from the cathode. Instead of using the typical activated carbon, we're recommending using the redox-active carbon cathodes developed in this thesis aiming higher energy density. For full-cell configuration tests, additional lithium sources are needed. Prelithiation of cathodes or anodes by either chemical or electrochemical methods are widely used in assembling full-cells. Considering the relative low first Coulombic efficiency of anode materials, prelithiation of anodes will be recommended. The lithiated anodes with high initial Coulombic efficiency are also beneficial for higher energy density by avoiding the irreversible capacity loss during the formation process of the full-cells.

Increasing the energy efficiency of these redox-active carbon cathodes is another technical challenge should be solved. Once introducing oxygen functional groups, a hysteresis up to 750 mV can be introduced between the charge and discharge profiles, resulting in a low energy efficiency of ~75%. Further improving the functionalization process which can eliminate the inactive oxygen functional species could decrease the hysteresis and improving the energy efficiency.

Other than oxygen functionalization process, heteroatoms doping, such as N, B and S, is also a promising strategy to further improve the performance of the carbon-based cathodes. Among these elements, nitrogen doping has been a widely used method to improve the performance of carbon electrode materials. Introducing nitrogen atoms in carbon frameworks can improve the conductivity and favorable for Li binding. We

believe nitrogen doping can also improve the performance of carbon-based cathodes. However, typical nitrogen doping processes are conducted under high temperatures (600-900 ^{o}C) where oxygen functional groups are no longer stable. Thus, the development of new nitrogen doping process is also highly desirable.

In terms of organic electrode materials, efforts need to be devoted to identifying new energy storage mechanisms or trying to combine the as-know mechanisms in the same electrode materials for achieving higher capacity or rate capability. Our group is currently trying to combine the n-doping and p-doping process in anthraquinone-based polymers, thus, we can change the two-electron process in anthraquinone monomers into a four-electron process in the anthraquinone-based polymers achieving higher energy. Another promising topic for organic electrode materials is the development of redox flow batteries for grid energy storage applications, but we will not discuss in this thesis.

REFERENCES

[1]. Dunn, B., H. Kamath, and J.-M. Tarascon, *Electrical Energy Storage for the Grid: A Battery of Choices.* Science, 2011. **334**(6058): p. 928-935.

[2]. Yang, Z., J. Zhang, M.C.W. Kintner-Meyer, X. Lu, D. Choi, J.P. Lemmon, and J. Liu, *Electrochemical Energy Storage for Green Grid.* Chemical Reviews, 2011. **111**(5): p. 3577-3613.

[3]. Miller, J.R. and P. Simon, *Electrochemical Capacitors for Energy Management.* Science, 2008. **321**(5889): p. 651.

[4]. Simon, P., Y. Gogotsi, and B. Dunn, *Where Do Batteries End and Supercapacitors Begin?* Science, 2014. **343**(6176): p. 1210-1211.

[5]. Chmiola, J., G. Yushin, Y. Gogotsi, C. Portet, P. Simon, and P.L. Taberna, *Anomalous Increase in Carbon Capacitance at Pore Sizes Less Than 1 Nanometer.* Science, 2006. **313**(5794): p. 1760-1763.

[6]. Simon, P. and Y. Gogotsi, *Capacitive Energy Storage in Nanostructured Carbon–Electrolyte Systems.* Accounts of Chemical Research, 2013. **46**(5): p. 1094-1103.

[7]. Merlet, C., B. Rotenberg, P.A. Madden, P.-L. Taberna, P. Simon, Y. Gogotsi, and M. Salanne, *On the molecular origin of supercapacitance in nanoporous carbon electrodes.* Nat Mater, 2012. **11**(4): p. 306-310.

[8]. Demarconnay, L., E. Raymundo-Piñero, and F. Béguin, *A symmetric carbon/carbon supercapacitor operating at 1.6V by using a neutral aqueous solution.* Electrochemistry Communications, 2010. **12**(10): p. 1275-1278.

[9]. Hulicova-Jurcakova, D., M. Seredych, G.Q. Lu, and T.J. Bandosz, *Combined Effect of Nitrogen- and Oxygen-Containing Functional Groups of Microporous Activated Carbon on its Electrochemical Performance in Supercapacitors.* Advanced Functional Materials, 2009. **19**(3): p. 438-447.

[10]. Balducci, A., R. Dugas, P.L. Taberna, P. Simon, D. Plée, M. Mastragostino, and S. Passerini, *High temperature carbon–carbon supercapacitor using ionic liquid as electrolyte.* Journal of Power Sources, 2007. **165**(2): p. 922-927.

[11]. Yu, C., C. Masarapu, J. Rong, B. Wei, and H. Jiang, *Stretchable Supercapacitors Based on Buckled Single-Walled Carbon-Nanotube Macrofilms.* Advanced Materials, 2009. **21**(47): p. 4793-4797.

[12]. An, K.H., W.S. Kim, Y.S. Park, J.M. Moon, D.J. Bae, S.C. Lim, Y.S. Lee, and Y.H. Lee, *Electrochemical Properties of High-Power Supercapacitors Using Single-Walled Carbon Nanotube Electrodes.* Advanced Functional Materials, 2001. **11**(5): p. 387-392.

[13]. Xu, Y., Z. Lin, X. Zhong, X. Huang, N.O. Weiss, Y. Huang, and X. Duan, *Holey graphene frameworks for highly efficient capacitive energy storage.* Nat Commun, 2014. **5**.

[14]. Wu, Z.S., K. Parvez, X. Feng, and K. Müllen, *Graphene-based in-plane micro-supercapacitors with high power and energy densities.* Nat Commun, 2013. **4**.

[15]. Xu, Y., Z. Lin, X. Huang, Y. Wang, Y. Huang, and X. Duan, *Functionalized Graphene Hydrogel-Based High-Performance Supercapacitors.* Adv Mater, 2013. **25**(40): p. 5779-5784.

[16]. Yang, X., C. Cheng, Y. Wang, L. Qiu, and D. Li, *Liquid-Mediated Dense Integration of Graphene Materials for Compact Capacitive Energy Storage.* Science, 2013. **341**(6145): p. 534-537.

[17]. Zhao, Y., J. Liu, Y. Hu, H. Cheng, C. Hu, C. Jiang, L. Jiang, A. Cao, and L. Qu, *Highly Compression-Tolerant Supercapacitor Based on Polypyrrole-mediated Graphene Foam Electrodes.* Advanced Materials, 2013. **25**(4): p. 591-595.

[18]. Liu, F., S. Song, D. Xue, and H. Zhang, *Folded Structured Graphene Paper for High Performance Electrode Materials.* Adv. Mater., 2012. **24**(8): p. 1089-1094.

[19]. Yu, G., L. Hu, N. Liu, H. Wang, M. Vosgueritchian, Y. Yang, Y. Cui, and Z. Bao, *Enhancing the Supercapacitor Performance of Graphene/MnO2 Nanostructured Electrodes by Conductive Wrapping.* Nano Letters, 2011. **11**(10): p. 4438-4442.

[20]. Chen, S., J. Zhu, X. Wu, Q. Han, and X. Wang, *Graphene Oxide−MnO2 Nanocomposites for Supercapacitors.* ACS Nano, 2010. **4**(5): p. 2822-2830.

[21]. Bi, R.-R., X.-L. Wu, F.-F. Cao, L.-Y. Jiang, Y.-G. Guo, and L.-J. Wan, *Highly Dispersed RuO2 Nanoparticles on Carbon Nanotubes: Facile Synthesis and Enhanced Supercapacitance Performance.* The Journal of Physical Chemistry C, 2010. **114**(6): p. 2448-2451.

[22]. Zang, J., S.-J. Bao, C.M. Li, H. Bian, X. Cui, Q. Bao, C.Q. Sun, J. Guo, and K. Lian, *Well-Aligned Cone-Shaped Nanostructure of Polypyrrole/RuO2 and Its Electrochemical Supercapacitor.* The Journal of Physical Chemistry C, 2008. **112**(38): p. 14843-14847.

[23]. Hu, C.-C., K.-H. Chang, M.-C. Lin, and Y.-T. Wu, *Design and Tailoring of the Nanotubular Arrayed Architecture of Hydrous RuO2 for Next Generation Supercapacitors.* Nano Letters, 2006. **6**(12): p. 2690-2695.

[24]. Wang, Y., X. Yang, L. Qiu, and D. Li, *Revisiting the capacitance of polyaniline by using graphene hydrogel films as a substrate: the importance of nano-architecturing.* Energy & Environmental Science, 2013. **6**(2): p. 477-481.

[25]. Wu, Q., Y. Xu, Z. Yao, A. Liu, and G. Shi, *Supercapacitors Based on Flexible Graphene/Polyaniline Nanofiber Composite Films.* ACS Nano, 2010. **4**(4): p. 1963-1970.

[26]. Zhang, K., L.L. Zhang, X.S. Zhao, and J. Wu, *Graphene/Polyaniline Nanofiber Composites as Supercapacitor Electrodes.* Chemistry of Materials, 2010. **22**(4): p. 1392-1401.

[27]. Ryu, K.S., K.M. Kim, N.-G. Park, Y.J. Park, and S.H. Chang, *Symmetric redox supercapacitor with conducting polyaniline electrodes.* Journal of Power Sources, 2002. **103**(2): p. 305-309.

[28]. Sharma, R.K., A.C. Rastogi, and S.B. Desu, *Pulse polymerized polypyrrole electrodes for high energy density electrochemical supercapacitor.* Electrochemistry Communications, 2008. **10**(2): p. 268-272.

[29]. Fan, L.-Z. and J. Maier, *High-performance polypyrrole electrode materials for redox supercapacitors.* Electrochemistry Communications, 2006. **8**(6): p. 937-940.

[30]. Zheng, S., R. Huang, Y. Makimura, Y. Ukyo, C.A.J. Fisher, T. Hirayama, and Y. Ikuhara, *Microstructural Changes in LiNi0.8Co0.15Al0.05O2 Positive Electrode Material during the First Cycle.* Journal of The Electrochemical Society, 2011. **158**(4): p. A357-A362.

[31]. Cho, Y. and J. Cho, *Significant Improvement of LiNi0.8Co0.15Al0.05O2 Cathodes at 60 °C by SiO2 Dry Coating for Li-Ion Batteries.* Journal of The Electrochemical Society, 2010. **157**(6): p. A625-A629.

[32]. Jung, S.-K., H. Gwon, J. Hong, K.-Y. Park, D.-H. Seo, H. Kim, J. Hyun, W. Yang, and K. Kang, *Understanding the Degradation Mechanisms of LiNi0.5Co0.2Mn0.3O2 Cathode Material in Lithium Ion Batteries.* Advanced Energy Materials, 2014. **4**(1): p. n/a-n/a.

[33]. Noh, M. and J. Cho, *Optimized Synthetic Conditions of LiNi0.5Co0.2Mn0.3O2 Cathode Materials for High Rate Lithium Batteries via Co-Precipitation Method.* Journal of The Electrochemical Society, 2013. **160**(1): p. A105-A111.

[34]. Chen, Z. and J.R. Dahn, *Reducing Carbon in LiFePO4 / C Composite Electrodes to Maximize Specific Energy, Volumetric Energy, and Tap Density.* Journal of The Electrochemical Society, 2002. **149**(9): p. A1184-A1189.

[35]. Yamada, A., S.C. Chung, and K. Hinokuma *Optimized LiFePO4 for Lithium Battery Cathodes.* Journal of The Electrochemical Society, 2001. **148**(3): p. A224-A229.

[36]. Park, M.-H., M.G. Kim, J. Joo, K. Kim, J. Kim, S. Ahn, Y. Cui, and J. Cho, *Silicon Nanotube Battery Anodes.* Nano Letters, 2009. **9**(11): p. 3844-3847.

[37]. Chan, C.K., H. Peng, G. Liu, K. McIlwrath, X.F. Zhang, R.A. Huggins, and Y. Cui, *High-performance lithium battery anodes using silicon nanowires.* 2007. **3**: p. 31.

[38]. Chan, C.K., X.F. Zhang, and Y. Cui, *High Capacity Li Ion Battery Anodes Using Ge Nanowires.* Nano Letters, 2008. **8**(1): p. 307-309.

[39]. Simon, P. and Y. Gogotsi, *Materials for electrochemical capacitors.* Nat Mater, 2008. **7**(11): p. 845-854.

[40]. Winter, M. and R.J. Brodd, *What Are Batteries, Fuel Cells, and Supercapacitors?* Chemical Reviews, 2004. **104**(10): p. 4245-4270.

[41]. Burke, A., *R&D considerations for the performance and application of electrochemical capacitors.* Electrochimica Acta, 2007. **53**(3): p. 1083-1091.

[42]. Gogotsi, Y. and P. Simon, *True Performance Metrics in Electrochemical Energy Storage.* Science, 2011. **334**(6058): p. 917-918.

[43]. Khomenko, V., E. Raymundo-Piñero, and F. Béguin, *A new type of high energy asymmetric capacitor with nanoporous carbon electrodes in aqueous electrolyte.* Journal of Power Sources, 2010. **195**(13): p. 4234-4241.

[44]. Chen, Y., X. Zhang, D. Zhang, P. Yu, and Y. Ma, *High performance supercapacitors based on reduced graphene oxide in aqueous and ionic liquid electrolytes.* Carbon, 2011. **49**(2): p. 573-580.

[45]. Hosono, E., T. Kudo, I. Honma, H. Matsuda, and H. Zhou, *Synthesis of Single Crystalline Spinel LiMn2O4 Nanowires for a Lithium Ion Battery with High Power Density.* Nano Letters, 2009. **9**(3): p. 1045-1051.

[46]. Kunduraci, M., J.F. Al-Sharab, and G.G. Amatucci, *High-Power Nanostructured LiMn2-xNixO4 High-Voltage Lithium-Ion Battery Electrode Materials: Electrochemical Impact of Electronic Conductivity and Morphology.* Chemistry of Materials, 2006. **18**(15): p. 3585-3592.

[47]. Li, B., F. Dai, Q. Xiao, L. Yang, J. Shen, C. Zhang, and M. Cai, *Nitrogen-doped activated carbon for a high energy hybrid supercapacitor.* Energy & Environmental Science, 2016. **9**(1): p. 102-106.

[48]. Naoi, K., W. Naoi, S. Aoyagi, J.-i. Miyamoto, and T. Kamino, *New Generation "Nanohybrid Supercapacitor".* Accounts of Chemical Research, 2013. **46**(5): p. 1075-1083.

[49]. Naoi, K., S. Ishimoto, J.-i. Miyamoto, and W. Naoi, *Second generation 'nanohybrid supercapacitor': Evolution of capacitive energy storage devices.* Energy & Environmental Science, 2012. **5**(11): p. 9363-9373.

[50]. Sivakkumar, S.R., J.Y. Nerkar, and A.G. Pandolfo, *Rate capability of graphite materials as negative electrodes in lithium-ion capacitors.* Electrochimica Acta, 2010. **55**(9): p. 3330-3335.

[51]. Sivakkumar, S.R. and A.G. Pandolfo, *Evaluation of lithium-ion capacitors assembled with pre-lithiated graphite anode and activated carbon cathode.* Electrochimica Acta, 2012. **65**: p. 280-287.

[52]. Decaux, C., G. Lota, E. Raymundo-Piñero, E. Frackowiak, and F. Béguin, *Electrochemical performance of a hybrid lithium-ion capacitor with a graphite anode preloaded from lithium bis(trifluoromethane)sulfonimide-based electrolyte.* Electrochimica Acta, 2012. **86**: p. 282-286.

[53]. Kim, J.-H., J.-S. Kim, Y.-G. Lim, J.-G. Lee, and Y.-J. Kim, *Effect of carbon types on the electrochemical properties of negative electrodes for Li-ion capacitors.* Journal of Power Sources, 2011. **196**(23): p. 10490-10495.

[54]. Dsoke, S., B. Fuchs, E. Gucciardi, and M. Wohlfahrt-Mehrens, *The importance of the electrode mass ratio in a Li-ion capacitor based on activated carbon and Li4Ti5O12.* Journal of Power Sources, 2015. **282**: p. 385-393.

[55]. Ye, L., Q. Liang, Y. Lei, X. Yu, C. Han, W. Shen, Z.-H. Huang, F. Kang, and Q.-H. Yang, *A high performance Li-ion capacitor constructed with Li4Ti5O12/C hybrid and porous graphene macroform.* Journal of Power Sources, 2015. **282**: p. 174-178.

[56]. Jung, H.-G., N. Venugopal, B. Scrosati, and Y.-K. Sun, *A high energy and power density hybrid supercapacitor based on an advanced carbon-coated Li4Ti5O12 electrode.* Journal of Power Sources, 2013. **221**: p. 266-271.

[57]. Jain, A., V. Aravindan, S. Jayaraman, P.S. Kumar, R. Balasubramanian, S. Ramakrishna, S. Madhavi, and M.P. Srinivasan, *Activated carbons derived from coconut shells as high energy density cathode material for Li-ion capacitors.* Scientific Reports, 2013. **3**: p. 3002.

[58]. Lee, S.W., N. Yabuuchi, B.M. Gallant, S. Chen, B.-S. Kim, P.T. Hammond, and Y. Shao-Horn, *High-power lithium batteries from functionalized carbon-nanotube electrodes.* Nat Nano, 2010. **5**(7): p. 531-537.

[59]. Lee, S.W., B.M. Gallant, H.R. Byon, P.T. Hammond, and Y. Shao-Horn, *Nanostructured carbon-based electrodes: bridging the gap between thin-film lithium-ion batteries and electrochemical capacitors.* Energy & Environmental Science, 2011. **4**(6): p. 1972-1985.

[60]. Byon, H.R., B.M. Gallant, S.W. Lee, and Y. Shao-Horn, *Role of Oxygen Functional Groups in Carbon Nanotube/Graphene Freestanding Electrodes for High Performance Lithium Batteries.* Adv Funct Mater, 2013. **23**(8): p. 1037-1045.

[61]. Hyder, M.N., R. Kavian, Z. Sultana, K. Saetia, P.-Y. Chen, S.W. Lee, Y. Shao-Horn, and P.T. Hammond, *Vacuum-Assisted Layer-by-Layer Nanocomposites for Self-Standing 3D Mesoporous Electrodes.* Chemistry of Materials, 2014. **26**(18): p. 5310-5318.

[62]. Kim, S.Y., J. Hong, R. Kavian, S.W. Lee, M.N. Hyder, Y. Shao-Horn, and P.T. Hammond, *Rapid fabrication of thick spray-layer-by-layer carbon nanotube electrodes for high power and energy devices.* Energy & Environmental Science, 2013. **6**(3): p. 888-897.

[63]. Lee, S.W., B.M. Gallant, Y. Lee, N. Yoshida, D.Y. Kim, Y. Yamada, S. Noda, A. Yamada, and Y. Shao-Horn, *Self-standing positive electrodes of oxidized few-walled carbon nanotubes for light-weight and high-power lithium batteries.* Energy & Environmental Science, 2012. **5**(1): p. 5437-5444.

[64]. Larcher, D. and J.M. Tarascon, *Towards greener and more sustainable batteries for electrical energy storage.* Nat Chem, 2015. **7**(1): p. 19-29.

[65]. Chen, H., M. Armand, G. Demailly, F. Dolhem, P. Poizot, and J.-M. Tarascon, *From Biomass to a Renewable LiXC6O6 Organic Electrode for Sustainable Li-Ion Batteries.* ChemSusChem, 2008. **1**(4): p. 348-355.

[66]. Tarascon, J.-M., *Towards Sustainable and Renewable Systems for Electrochemical Energy Storage.* ChemSusChem, 2008. **1**(8-9): p. 777-779.

[67]. Li, Z., L. Zhang, B.S. Amirkhiz, X. Tan, Z. Xu, H. Wang, B.C. Olsen, C.M.B. Holt, and D. Mitlin, *Carbonized Chicken Eggshell Membranes with 3D Architectures as High-Performance Electrode Materials for Supercapacitors.* Advanced Energy Materials, 2012. **2**(4): p. 431-437.

[68]. Ding, J., H. Wang, Z. Li, K. Cui, D. Karpuzov, X. Tan, A. Kohandehghan, and D. Mitlin, *Peanut shell hybrid sodium ion capacitor with extreme energy-power rivals lithium ion capacitors.* Energy & Environmental Science, 2015. **8**(3): p. 941-955.

[69]. Lotfabad, E.M., J. Ding, K. Cui, A. Kohandehghan, W.P. Kalisvaart, M. Hazelton, and D. Mitlin, *High-Density Sodium and Lithium Ion Battery Anodes from Banana Peels.* ACS Nano, 2014. **8**(7): p. 7115-7129.

[70]. Liu, T., K.C. Kim, B. Lee, Z. Chen, S. Noda, S.S. Jang, and S.W. Lee, *Self-polymerized dopamine as an organic cathode for Li- and Na-ion batteries.* Energy & Environmental Science, 2017.

[71]. Song, Z. and H. Zhou, *Towards sustainable and versatile energy storage devices: an overview of organic electrode materials.* Energy & Environmental Science, 2013. **6**(8): p. 2280-2301.

[72]. Wang, S., L. Wang, K. Zhang, Z. Zhu, Z. Tao, and J. Chen, *Organic Li4C8H2O6 Nanosheets for Lithium-Ion Batteries.* Nano Letters, 2013. **13**(9): p. 4404-4409.

[73]. Liang, Y., Z. Tao, and J. Chen, *Organic Electrode Materials for Rechargeable Lithium Batteries.* Advanced Energy Materials, 2012. **2**(7): p. 742-769.

[74]. Naoi, K., K.i. Kawase, and Y. Inoue, *A New Energy Storage Material: Organosulfur Compounds Based on Multiple Sulfur-Sulfur Bonds.* Journal of The Electrochemical Society, 1997. **144**(6): p. L170-L172.

[75]. Visco, S.J., C.C. Mailhe, L.C. De Jonghe, and M.B. Armand, *A Novel Class of Organosulfur Electrodes for Energy Storage.* Journal of The Electrochemical Society, 1989. **136**(3): p. 661-664.

[76]. Bugnon, L., C.J.H. Morton, P. Novak, J. Vetter, and P. Nesvadba, *Synthesis of Poly(4-methacryloyloxy-TEMPO) via Group-Transfer Polymerization and Its Evaluation in Organic Radical Battery.* Chemistry of Materials, 2007. **19**(11): p. 2910-2914.

[77]. Nishide, H., S. Iwasa, Y.-J. Pu, T. Suga, K. Nakahara, and M. Satoh, *Organic radical battery: nitroxide polymers as a cathode-active material.* Electrochimica Acta, 2004. **50**(2–3): p. 827-831.

[78]. Häupler, B., A. Wild, and U.S. Schubert, *Carbonyls: Powerful Organic Materials for Secondary Batteries.* Advanced Energy Materials, 2015. **5**(11): p. n/a-n/a.

[79]. Wang, H.-g., S. Yuan, Z. Si, and X.-b. Zhang, *Multi-ring aromatic carbonyl compounds enabling high capacity and stable performance of sodium-organic batteries.* Energy & Environmental Science, 2015. **8**(11): p. 3160-3165.

[80]. Wang, H.-g., S. Yuan, D.-l. Ma, X.-l. Huang, F.-l. Meng, and X.-b. Zhang, *Tailored Aromatic Carbonyl Derivative Polyimides for High-Power and Long-Cycle Sodium-Organic Batteries.* Advanced Energy Materials, 2014. **4**(7): p. n/a-n/a.

[81]. Liang, Y., P. Zhang, and J. Chen, *Function-oriented design of conjugated carbonyl compound electrodes for high energy lithium batteries.* Chemical Science, 2013. **4**(3): p. 1330-1337.

[82]. Walker, W., S. Grugeon, O. Mentre, S. Laruelle, J.-M. Tarascon, and F. Wudl, *Ethoxycarbonyl-Based Organic Electrode for Li-Batteries.* Journal of the American Chemical Society, 2010. **132**(18): p. 6517-6523.

[83]. Han, X., C. Chang, L. Yuan, T. Sun, and J. Sun, *Aromatic Carbonyl Derivative Polymers as High-Performance Li-Ion Storage Materials.* Advanced Materials, 2007. **19**(12): p. 1616-1621.

[84]. Song, Z., Y. Qian, X. Liu, T. Zhang, Y. Zhu, H. Yu, M. Otani, and H. Zhou, *A quinone-based oligomeric lithium salt for superior Li-organic batteries.* Energy & Environmental Science, 2014. **7**(12): p. 4077-4086.

[85]. Song, Z., Y. Qian, T. Zhang, M. Otani, and H. Zhou, *Poly(benzoquinonyl sulfide) as a High-Energy Organic Cathode for Rechargeable Li and Na Batteries.* Advanced Science, 2015. **2**(9): p. n/a-n/a.

[86]. Song, Z., H. Zhan, and Y. Zhou, *Anthraquinone based polymer as high performance cathode material for rechargeable lithium batteries.* Chemical Communications, 2009(4): p. 448-450.

[87]. Song, Z., Y. Qian, M.L. Gordin, D. Tang, T. Xu, M. Otani, H. Zhan, H. Zhou, and D. Wang, *Polyanthraquinone as a Reliable Organic Electrode for Stable and Fast Lithium Storage.* Angewandte Chemie, 2015. **127**(47): p. 14153-14157.

[88]. Lee, M., J. Hong, H. Kim, H.-D. Lim, S.B. Cho, K. Kang, and C.B. Park, *Organic Nanohybrids for Fast and Sustainable Energy Storage.* Advanced Materials, 2014. **26**(16): p. 2558-2565.

[89]. Song, Z., Y. Qian, M. Otani, and H. Zhou, *Stable Li–Organic Batteries with Nafion-Based Sandwich-Type Separators.* Advanced Energy Materials, 2016. **6**(7): p. n/a-n/a.

[90]. Song, Z., T. Xu, M.L. Gordin, Y.-B. Jiang, I.-T. Bae, Q. Xiao, H. Zhan, J. Liu, and D. Wang, *Polymer–Graphene Nanocomposites as Ultrafast-Charge and -Discharge Cathodes for Rechargeable Lithium Batteries.* Nano Letters, 2012. **12**(5): p. 2205-2211.

[91]. Wu, H., Q. Meng, Q. Yang, M. Zhang, K. Lu, and Z. Wei, *Large-Area Polyimide/SWCNT Nanocable Cathode for Flexible Lithium-Ion Batteries.* Advanced Materials, 2015. **27**(41): p. 6504-6510.

[92]. Wu, H., S.A. Shevlin, Q. Meng, W. Guo, Y. Meng, K. Lu, Z. Wei, and Z. Guo, *Flexible and Binder-Free Organic Cathode for High-Performance Lithium-Ion Batteries.* Advanced Materials, 2014. **26**(20): p. 3338-3343.

[93]. Armand, M. and J.M. Tarascon, *Building better batteries.* Nature, 2008. **451**(7179): p. 652-657.

[94]. Liu, C., F. Li, L.-P. Ma, and H.-M. Cheng, *Advanced Materials for Energy Storage.* Adv. Mater., 2010. **22**(8): p. E28-E62.

[95]. Byon, H.R., S.W. Lee, S. Chen, P.T. Hammond, and Y. Shao-Horn, *Thin films of carbon nanotubes and chemically reduced graphenes for electrochemical micro-capacitors.* Carbon, 2011. **49**(2): p. 457-467.

[96]. Choi, B.G., M. Yang, W.H. Hong, J.W. Choi, and Y.S. Huh, *3D Macroporous Graphene Frameworks for Supercapacitors with High Energy and Power Densities.* ACS Nano, 2012. **6**(5): p. 4020-4028.

[97]. Cui, C., W. Qian, Y. Yu, C. Kong, B. Yu, L. Xiang, and F. Wei, *Highly Electroconductive Mesoporous Graphene Nanofibers and Their Capacitance Performance at 4 V.* J. Am. Chem. Soc., 2014. **136**(6): p. 2256-2259.

[98]. El-Kady, M.F., V. Strong, S. Dubin, and R.B. Kaner, *Laser Scribing of High-Performance and Flexible Graphene-Based Electrochemical Capacitors.* Science, 2012. **335**(6074): p. 1326-1330.

[99]. Tao, Y., X. Xie, W. Lv, D.-M. Tang, D. Kong, Z. Huang, H. Nishihara, T. Ishii, B. Li, D. Golberg, F. Kang, T. Kyotani, and Q.-H. Yang, *Towards ultrahigh volumetric capacitance: graphene derived highly dense but porous carbons for supercapacitors.* Sci. Rep., 2013. **3**.

[100]. Wu, Z.-S., Y. Sun, Y.-Z. Tan, S. Yang, X. Feng, and K. Müllen, *Three-Dimensional Graphene-Based Macro- and Mesoporous Frameworks for High-Performance Electrochemical Capacitive Energy Storage.* J. Am. Chem. Soc., 2012. **134**(48): p. 19532-19535.

[101]. Yoo, E., J. Kim, E. Hosono, H.-s. Zhou, T. Kudo, and I. Honma, *Large Reversible Li Storage of Graphene Nanosheet Families for Use in Rechargeable Lithium Ion Batteries.* Nano Lett., 2008. **8**(8): p. 2277-2282.

[102]. Wang, H., L.-F. Cui, Y. Yang, H. Sanchez Casalongue, J.T. Robinson, Y. Liang, Y. Cui, and H. Dai, *Mn3O4−Graphene Hybrid as a High-Capacity Anode Material for Lithium Ion Batteries.* J. Am. Chem. Soc., 2010. **132**(40): p. 13978-13980.

[103]. Wang, G., X. Shen, J. Yao, and J. Park, *Graphene nanosheets for enhanced lithium storage in lithium ion batteries.* Carbon, 2009. **47**(8): p. 2049-2053.

[104]. Lian, P., X. Zhu, S. Liang, Z. Li, W. Yang, and H. Wang, *Large reversible capacity of high quality graphene sheets as an anode material for lithium-ion batteries.* Electrochim. Acta, 2010. **55**(12): p. 3909-3914.

[105]. Brownson, D.A.C., D.K. Kampouris, and C.E. Banks, *An overview of graphene in energy production and storage applications.* Journal of Power Sources, 2011. **196**(11): p. 4873-4885.

[106]. Dreyer, D.R., S. Park, C.W. Bielawski, and R.S. Ruoff, *The chemistry of graphene oxide.* Chem. Soc. Rev., 2010. **39**(1): p. 228-240.

[107]. Pei, S. and H.-M. Cheng, *The reduction of graphene oxide.* Carbon, 2012. **50**(9): p. 3210-3228.

[108]. Sun, Y., Q. Wu, and G. Shi, *Graphene based new energy materials.* Energy & Environmental Science, 2011. **4**(4): p. 1113-1132.

[109]. Li, D., M.B. Muller, S. Gilje, R.B. Kaner, and G.G. Wallace, *Processable aqueous dispersions of graphene nanosheets.* Nat Nano, 2008. **3**(2): p. 101-105.

[110]. Hummers, W.S. and R.E. Offeman, *Preparation of Graphitic Oxide.* J Am Chem Soc, 1958. **80**(6): p. 1339-1339.

[111]. Chen, Z., W. Ren, L. Gao, B. Liu, S. Pei, and H.-M. Cheng, *Three-dimensional flexible and conductive interconnected graphene networks grown by chemical vapour deposition.* Nat Mater, 2011. **10**(6): p. 424-428.

[112]. Chen, W., S. Li, C. Chen, and L. Yan, *Self-Assembly and Embedding of Nanoparticles by In Situ Reduced Graphene for Preparation of a 3D Graphene/Nanoparticle Aerogel.* Adv. Mater., 2011. **23**(47): p. 5679-5683.

[113]. Chen, W. and L. Yan, *In situ self-assembly of mild chemical reduction graphene for three-dimensional architectures.* Nanoscale, 2011. **3**(8): p. 3132-3137.

[114]. Qiu, L., J.Z. Liu, S.L.Y. Chang, Y. Wu, and D. Li, *Biomimetic superelastic graphene-based cellular monoliths.* Nat Commun, 2012. **3**: p. 1241.

[115]. Liu, T., R. Kavian, I. Kim, and S.W. Lee, *Self-Assembled, Redox-Active Graphene Electrodes for High-Performance Energy Storage Devices.* The Journal of Physical Chemistry Letters, 2014: p. 4324-4330.

[116]. Ha, S.H., Y.S. Jeong, and Y.J. Lee, *Free Standing Reduced Graphene Oxide Film Cathodes for Lithium Ion Batteries.* ACS Applied Materials & Interfaces, 2013. **5**(23): p. 12295-12303.

[117]. Xu, Y., K. Sheng, C. Li, and G. Shi, *Self-Assembled Graphene Hydrogel via a One-Step Hydrothermal Process.* ACS Nano, 2010. **4**(7): p. 4324-4330.

[118]. Sikha, G. and B.N. Popov, *Performance optimization of a battery–capacitor hybrid system.* J. Power Sources, 2004. **134**(1): p. 130-138.

[119]. *Jaguar, version 7.0*. 2007, Jaguar, version 7.0, Schrödinger, LLC: New York, NY.

[120]. Winget, P., C.J. Cramer, and D.G. Truhlar, *Computation of Equilibrium Oxidation and Reduction Potentials for Reversible and Dissociative Electron-Transfer Reactions.* Theor. Chem. Acc., 2004. **112**: p. 217-227.

[121]. Winget, P., E.J. Weber, C.J. Cramer, and D.G. Truhlar, *Computational Electrochemistry: Aqueous One-Electron Oxidation Potentials for Substituted Anilines.* Phys. Chem. Chem. Phys., 2000. **2**: p. 1231-1239.

[122]. Zhou, Y., Q. Bao, L.A.L. Tang, Y. Zhong, and K.P. Loh, *Hydrothermal Dehydration for the "Green" Reduction of Exfoliated Graphene Oxide to Graphene and Demonstration of Tunable Optical Limiting Properties.* Chem. Mater., 2009. **21**(13): p. 2950-2956.

[123]. Zhao, J., W. Ren, and H.-M. Cheng, *Graphene sponge for efficient and repeatable adsorption and desorption of water contaminations.* J. Mater. Chem., 2012. **22**(38): p. 20197-20202.

[124]. Worsley, M.A., P.J. Pauzauskie, T.Y. Olson, J. Biener, J.H. Satcher, and T.F. Baumann, *Synthesis of Graphene Aerogel with High Electrical Conductivity.* J. Am. Chem. Soc., 2010. **132**(40): p. 14067-14069.

[125]. Eda, G., G. Fanchini, and M. Chhowalla, *Large-area ultrathin films of reduced graphene oxide as a transparent and flexible electronic material.* Nat Nano, 2008. **3**(5): p. 270-274.

[126]. Stankovich, S., D.A. Dikin, R.D. Piner, K.A. Kohlhaas, A. Kleinhammes, Y. Jia, Y. Wu, S.T. Nguyen, and R.S. Ruoff, *Synthesis of graphene-based nanosheets via chemical reduction of exfoliated graphite oxide.* Carbon, 2007. **45**(7): p. 1558-1565.

[127]. Pei, S., J. Zhao, J. Du, W. Ren, and H.-M. Cheng, *Direct reduction of graphene oxide films into highly conductive and flexible graphene films by hydrohalic acids.* Carbon, 2010. **48**(15): p. 4466-4474.

[128]. Compton, O.C., Z. An, K.W. Putz, B.J. Hong, B.G. Hauser, L. Catherine Brinson, and S.T. Nguyen, *Additive-free hydrogelation of graphene oxide by ultrasonication.* Carbon, 2012. **50**(10): p. 3399-3406.

[129]. Yang, X., J. Zhu, L. Qiu, and D. Li, *Bioinspired Effective Prevention of Restacking in Multilayered Graphene Films: Towards the Next Generation of High-Performance Supercapacitors.* Adv. Mater., 2011. **23**(25): p. 2833-2838.

[130]. Dikin, D.A., S. Stankovich, E.J. Zimney, R.D. Piner, G.H.B. Dommett, G. Evmenenko, S.T. Nguyen, and R.S. Ruoff, *Preparation and characterization of graphene oxide paper.* Nature, 2007. **448**(7152): p. 457-460.

[131]. Gallant, B.M., S.W. Lee, T. Kawaguchi, P.T. Hammond, and Y. Shao-Horn, *Electrochemical Performance of Thin-Film Functionalized Carbon Nanotube Electrodes in Nonaqueous Cells.* Journal of The Electrochemical Society, 2014. **161**(10): p. A1625-A1633.

[132]. Senoh, H., M. Yao, H. Sakaebe, K. Yasuda, and Z. Siroma, *A two-compartment cell for using soluble benzoquinone derivatives as active materials in lithium secondary batteries.* Electrochimica Acta, 2011. **56**(27): p. 10145-10150.

[133]. Xu, W., A. Read, P.K. Koech, D. Hu, C. Wang, J. Xiao, A.B. Padmaperuma, G.L. Graff, J. Liu, and J.-G. Zhang, *Factors affecting the battery performance of*

anthraquinone-based organic cathode materials. J. Mater. Chem., 2012. **22**(9): p. 4032-4039.

[134]. Yao, M., H. Senoh, S.-i. Yamazaki, Z. Siroma, T. Sakai, and K. Yasuda, *High-Capacity Organic Positive-Electrode Material Based on a Benzoquinone Derivative for Use in Rechargeable Lithium Batteries.* J. Power Sources, 2010. **195**: p. 8336-8340.

[135]. Zhao, L., W. Wang, A. Wang, K. Yuan, S. Chen, and Y. Yang, *A novel polyquinone cathode material for rechargeable lithium batteries.* J. Power Sources, 2013. **233**(0): p. 23-27.

[136]. Nokami, T., T. Matsuo, Y. Inatomi, N. Hojo, T. Tsukagoshi, H. Yoshizawa, A. Shimizu, H. Kuramoto, K. Komae, H. Tsuyama, and J.-i. Yoshida, *Polymer-Bound Pyrene-4,5,9,10-tetraone for Fast-Charge and -Discharge Lithium-Ion Batteries with High Capacity.* J. Am. Chem Soc., 2012. **134**(19694-19700): p. 19694.

[137]. Liang, Y., P. Zhang, S. Yang, Z. Tao, and J. Chen, *Fused Heteroaromatic Organic Compounds for High-Power Electrodes of Rechargeable Lithium Batteries.* Advanced Energy Materials, 2013. **3**(5): p. 600-605.

[138]. Roberts, M., P. Johns, J. Owen, D. Brandell, K. Edstrom, G. El Enany, C. Guery, D. Golodnitsky, M. Lacey, C. Lecoeur, H. Mazor, E. Peled, E. Perre, M.M. Shaijumon, P. Simon, and P.-L. Taberna, *3D lithium ion batteries-from fundamentals to fabrication.* J. Mater. Chem., 2011. **21**(27): p. 9876-9890.

[139]. Baughman, R.H., A.A. Zakhidov, and W.A. de Heer, *Carbon Nanotubes--the Route Toward Applications.* Science, 2002. **297**(5582): p. 787-792.

[140]. Cao, Z. and B. Wei, *A perspective: carbon nanotube macro-films for energy storage.* Energy & Environmental Science, 2013. **6**(11): p. 3183-3201.

[141]. Frackowiak, E. and F. Béguin, *Electrochemical storage of energy in carbon nanotubes and nanostructured carbons.* Carbon, 2002. **40**(10): p. 1775-1787.

[142]. Pumera, M., *Graphene-based nanomaterials for energy storage.* Energy & Environmental Science, 2011. **4**(3): p. 668-674.

[143]. Liu, C., F. Li, L.P. Ma, and H.M. Cheng, *Advanced materials for energy storage.* Adv Mater, 2010. **22**(8): p. E28-E62.

[144]. Dai, H., *Carbon nanotubes: synthesis, integration, and properties.* Accounts Chem Res, 2002. **35**(12): p. 1035-1044.

[145]. Allen, M.J., V.C. Tung, and R.B. Kaner, *Honeycomb carbon: a review of graphene.* Chem Rev, 2009. **110**(1): p. 132-145.

[146]. Marcano, D.C., D.V. Kosynkin, J.M. Berlin, A. Sinitskii, Z. Sun, A. Slesarev, L.B. Alemany, W. Lu, and J.M. Tour, *Improved Synthesis of Graphene Oxide.* ACS Nano, 2010. **4**(8): p. 4806-4814.

[147]. Liu, C., Z. Yu, D. Neff, A. Zhamu, and B.Z. Jang, *Graphene-Based Supercapacitor with an Ultrahigh Energy Density.* Nano Letters, 2010. **10**(12): p. 4863-4868.

[148]. Zhang, L.L., R. Zhou, and X.S. Zhao, *Graphene-based materials as supercapacitor electrodes.* J Mater Chem, 2010. **20**(29): p. 5983-5992.

[149]. Zhu, Y., S. Murali, M.D. Stoller, K.J. Ganesh, W. Cai, P.J. Ferreira, A. Pirkle, R.M. Wallace, K.A. Cychosz, M. Thommes, D. Su, E.A. Stach, and R.S. Ruoff, *Carbon-Based Supercapacitors Produced by Activation of Graphene.* Science, 2011. **332**(6037): p. 1537-1541.

[150]. Lota, G., B. Grzyb, H. Machnikowska, J. Machnikowski, and E. Frackowiak, *Effect of nitrogen in carbon electrode on the supercapacitor performance.* Chem Phys Lett, 2005. **404**(1): p. 53-58.

[151]. Zhao, L., L.Z. Fan, M.Q. Zhou, H. Guan, S. Qiao, M. Antonietti, and M.M. Titirici, *Nitrogen-Containing Hydrothermal Carbons with Superior Performance in Supercapacitors.* Adv Mater, 2010. **22**(45): p. 5202-5206.

[152]. Hsieh, C.-T. and H. Teng, *Influence of oxygen treatment on electric double-layer capacitance of activated carbon fabrics.* Carbon, 2002. **40**(5): p. 667-674.

[153]. Hulicova-Jurcakova, D., M. Seredych, G.Q. Lu, and T.J. Bandosz, *Combined Effect of Nitrogen-and Oxygen-Containing Functional Groups of Microporous Activated Carbon on its Electrochemical Performance in Supercapacitors.* Adv Funct Mater, 2009. **19**(3): p. 438-447.

[154]. Gelormini, O. and N.E. Artz, *The Oxidation of Inosite With Nitric Acid.* J Am Chem Soc, 1930. **52**(6): p. 2483-2494.

[155]. Preisler, P.W. and L. Berger, *Preparation of Tetrahydroxyquinone and Rhodizonic Acid Salts from the Product of the Oxidation of Inositol with Nitric Acid.* J Am Chem Soc, 1942. **64**(1): p. 67-69.

[156]. Hoglan, F.A. and E. Bartow, *Preparation and Properties of Derivatives of Inositol.* J Am Chem Soc, 1940. **62**(9): p. 2397-2400.

[157]. Preisler, P.W., L. Berger, and E.S. Hill, *Oxidation—Reduction Potentials and Ionization Constants of the Reversible Series: Hexahydroxybenzene—Tetrahydroxyquinone—Rhodizonic Acid.* J Am Chem Soc, 1947. **69**(2): p. 326-329.

[158]. Preisler, P.W., L. Berger, and E.S. Hill, *Oxidation—Reduction Potentials and Ionization Constants of the Reversible Series: Hexahydroxybenzene — Tetrahydroxyquinone — Rhodizonic Acid.* J Am Chem Soc, 1948. **70**(2): p. 871-871.

[159]. Xue, T., S. Jiang, Y. Qu, Q. Su, R. Cheng, S. Dubin, C.-Y. Chiu, R. Kaner, Y. Huang, and X. Duan, *Graphene-Supported Hemin as a Highly Active Biomimetic Oxidation Catalyst.* Angewandte Chemie International Edition, 2012. **51**(16): p. 3822-3825.

[160]. Rochefort, A. and J.D. Wuest, *Interaction of Substituted Aromatic Compounds with Graphene.* Langmuir, 2008. **25**(1): p. 210-215.

[161]. Wuest, J.D. and A. Rochefort, *Strong adsorption of aminotriazines on graphene.* Chem Commun, 2010. **46**(17): p. 2923-2925.

[162]. Wang, G., J. Yang, J. Park, X. Gou, B. Wang, H. Liu, and J. Yao, *Facile Synthesis and Characterization of Graphene Nanosheets.* The Journal of Physical Chemistry C, 2008. **112**(22): p. 8192-8195.

[163]. Kortum, G.V.W.A.K., *Dissociation constants of organic acids in aqueous solution*. 1961, London: Butterworths.

[164]. Shao, Y., J. Xiao, W. Wang, M. Engelhard, X. Chen, Z. Nie, M. Gu, L.V. Saraf, G. Exarhos, J.-G. Zhang, and J. Liu, *Surface-Driven Sodium Ion Energy Storage in Nanocellular Carbon Foams.* Nano Letters, 2013. **13**(8): p. 3909-3914.

[165]. Poizot, P. and F. Dolhem, *Clean energy new deal for a sustainable world: from non-CO2 generating energy sources to greener electrochemical storage devices.* Energy & Environmental Science, 2011. **4**(6): p. 2003-2019.

[166]. Bachman, J.C., R. Kavian, D.J. Graham, D.Y. Kim, S. Noda, D.G. Nocera, Y. Shao-Horn, and S.W. Lee, *Electrochemical polymerization of pyrene derivatives on functionalized carbon nanotubes for pseudocapacitive electrodes.* Nat Commun, 2015. **6**.

[167]. Cheng, F., J. Liang, Z. Tao, and J. Chen, *Functional Materials for Rechargeable Batteries.* Advanced Materials, 2011. **23**(15): p. 1695-1715.

[168]. Yao, M., H. Senoh, S.-i. Yamazaki, Z. Siroma, T. Sakai, and K. Yasuda, *High-capacity organic positive-electrode material based on a benzoquinone derivative for use in rechargeable lithium batteries.* Journal of Power Sources, 2010. **195**(24): p. 8336-8340.

[169]. Liu, T., K.C. Kim, R. Kavian, S.S. Jang, and S.W. Lee, *High-Density Lithium-Ion Energy Storage Utilizing the Surface Redox Reactions in Folded Graphene Films.* Chemistry of Materials, 2015. **27**(9): p. 3291-3298.

[170]. Liu, T., R. Kavian, I. Kim, and S.W. Lee, *Self-Assembled, Redox-Active Graphene Electrodes for High-Performance Energy Storage Devices.* The Journal of Physical Chemistry Letters, 2014. **5**(24): p. 4324-4330.

[171]. Hu, B., K. Wang, L. Wu, S.-H. Yu, M. Antonietti, and M.-M. Titirici, *Engineering Carbon Materials from the Hydrothermal Carbonization Process of Biomass.* Advanced Materials, 2010. **22**(7): p. 813-828.

[172]. Sevilla, M. and A.B. Fuertes, *Chemical and Structural Properties of Carbonaceous Products Obtained by Hydrothermal Carbonization of Saccharides.* Chemistry – A European Journal, 2009. **15**(16): p. 4195-4203.

[173]. Wen, Z., Q. Wang, and J. Li, *Template Synthesis of Aligned Carbon Nanotube Arrays using Glucose as a Carbon Source: Pt Decoration of Inner and Outer Nanotube Surfaces for Fuel-Cell Catalysts.* Advanced Functional Materials, 2008. **18**(6): p. 959-964.

[174]. Matos, J., M. Rosales, R. Demir-Cakan, and M.M. Titirici, *Methane conversion on Pt–Ru nanoparticles alloy supported on hydrothermal carbon.* Applied Catalysis A: General, 2010. **386**(1–2): p. 140-146.

[175]. Zhao, L., L.-Z. Fan, M.-Q. Zhou, H. Guan, S. Qiao, M. Antonietti, and M.-M. Titirici, *Nitrogen-Containing Hydrothermal Carbons with Superior Performance in Supercapacitors.* Advanced Materials, 2010. **22**(45): p. 5202-5206.

[176]. Wei, L., M. Sevilla, A.B. Fuertes, R. Mokaya, and G. Yushin, *Hydrothermal Carbonization of Abundant Renewable Natural Organic Chemicals for High-Performance Supercapacitor Electrodes.* Advanced Energy Materials, 2011. **1**(3): p. 356-361.

[177]. Chen, Z., D.Y. Kim, K. Hasegawa, T. Osawa, and S. Noda, *Over 99.6 wt%-pure, sub-millimeter-long carbon nanotubes realized by fluidized-bed with careful control of the catalyst and carbon feeds.* Carbon, 2014. **80**: p. 339-350.

[178]. Kim, D.Y., H. Sugime, K. Hasegawa, T. Osawa, and S. Noda, *Sub-millimeter-long carbon nanotubes repeatedly grown on and separated from ceramic beads in a single fluidized bed reactor.* Carbon, 2011. **49**(6): p. 1972-1979.

[179]. Sun, X. and Y. Li, *Colloidal Carbon Spheres and Their Core/Shell Structures with Noble-Metal Nanoparticles.* Angewandte Chemie International Edition, 2004. **43**(5): p. 597-601.

[180]. Titirici, M.-M., M. Antonietti, and N. Baccile, *Hydrothermal carbon from biomass: a comparison of the local structure from poly- to monosaccharides and pentoses/hexoses.* Green Chemistry, 2008. **10**(11): p. 1204-1212.

[181]. Zhang, P., Z.-A. Qiao, and S. Dai, *Recent advances in carbon nanospheres: synthetic routes and applications.* Chemical Communications, 2015. **51**(45): p. 9246-9256.

[182]. Krishnan, D., K. Raidongia, J. Shao, and J. Huang, *Graphene Oxide Assisted Hydrothermal Carbonization of Carbon Hydrates.* ACS Nano, 2014. **8**(1): p. 449-457.

[183]. Stoller, M.D., S. Murali, N. Quarles, Y. Zhu, J.R. Potts, X. Zhu, H.-W. Ha, and R.S. Ruoff, *Activated graphene as a cathode material for Li-ion hybrid supercapacitors.* Physical Chemistry Chemical Physics, 2012. **14**(10): p. 3388-3391.

[184]. Higginbotham, A.L., P.G. Moloney, M.C. Waid, J.G. Duque, C. Kittrell, H.K. Schmidt, J.J. Stephenson, S. Arepalli, L.L. Yowell, and J.M. Tour, *Carbon nanotube composite curing through absorption of microwave radiation.* Composites Science and Technology, 2008. **68**(15–16): p. 3087-3092.

[185]. Imholt, T.J., C.A. Dyke, B. Hasslacher, J.M. Perez, D.W. Price, J.A. Roberts, J.B. Scott, A. Wadhawan, Z. Ye, and J.M. Tour, *Nanotubes in Microwave Fields: Light Emission, Intense Heat, Outgassing, and Reconstruction.* Chemistry of Materials, 2003. **15**(21): p. 3969-3970.

[186]. Wang, C.Y., T.H. Chen, S.C. Chang, S.Y. Cheng, and T.S. Chin, *Strong Carbon-Nanotube–Polymer Bonding by Microwave Irradiation.* Advanced Functional Materials, 2007. **17**(12): p. 1979-1983.

[187]. http://www.mccroneatlas.com/viewer/text.asp?IMAGE_ID=231417&PARTICLE_ID=71&TECHNIQUE_ID=5&MODE=RAMAN.

[188]. Cuesta, A., P. Dhamelincourt, J. Laureyns, A. Martínez-Alonso, and J.M.D. Tascón, *Raman microprobe studies on carbon materials.* Carbon, 1994. **32**(8): p. 1523-1532.

[189]. Ferrari, A.C. and J. Robertson, *Interpretation of Raman spectra of disordered and amorphous carbon.* Physical Review B, 2000. **61**(20): p. 14095-14107.

[190]. Schwan, J., S. Ulrich, V. Batori, H. Ehrhardt, and S.R.P. Silva, *Raman spectroscopy on amorphous carbon films.* Journal of Applied Physics, 1996. **80**(1): p. 440-447.

[191]. Lu, G. and G. Shi, *Electrochemical polymerization of pyrene in the electrolyte of boron trifluoride diethyl etherate containing trifluoroacetic acid and polyethylene glycol oligomer.* Journal of Electroanalytical Chemistry, 2006. **586**(2): p. 154-160.

[192]. Lu, B., J. Yan, J. Xu, S. Zhou, and X. Hu, *Novel Electroactive Proton-Doped Conducting Poly(aromatic ethers) with Good Fluorescence Properties via Electropolymerization.* Macromolecules, 2010. **43**(10): p. 4599-4608.

[193]. Lu, B., J. Xu, C. Fan, H. Miao, and L. Shen, *Electrochemical Polymerization of Benzanthrone and Characterization of its Excellent Green-light-emitting Polymer.* The Journal of Physical Chemistry B, 2009. **113**(1): p. 37-48.

[194]. Fan, B., L. Qu, and G. Shi, *Electrochemical polymerization of anthracene in boron trifluoride diethyl etherate.* Journal of Electroanalytical Chemistry, 2005. **575(**2): p. 287-292.

[195]. Jain, A., V. Aravindan, S. Jayaraman, P.S. Kumar, R. Balasubramanian, S. Ramakrishna, S. Madhavi, and M.P. Srinivasan, *Activated carbons derived from coconut shells as high energy density cathode material for Li-ion capacitors.* Sci. Rep., 2013. **3**.

[196]. Song, Z., H. Zhan, and Y. Zhou, *Polyimides: Promising Energy-Storage Materials.* Angewandte Chemie International Edition, 2010. **49**(45): p. 8444-8448.

[197]. Meng, Y., H. Wu, Y. Zhang, and Z. Wei, *A flexible electrode based on a three-dimensional graphene network-supported polyimide for lithium-ion batteries.* Journal of Materials Chemistry A, 2014. **2**(28): p. 10842-10846.

[198]. Oyama, N., T. Tatsuma, T. Sato, and T. Sotomura, *Dimercaptan-polyaniline composite electrodes for lithium batteries with high energy density.* Nature, 1995. **373**(6515): p. 598-600.

[199]. Wang, J., C.O. Too, and G.G. Wallace, *A highly flexible polymer fibre battery.* Journal of Power Sources, 2005. **150**: p. 223-228.

[200]. Sun, T., Z.-j. Li, H.-g. Wang, D. Bao, F.-l. Meng, and X.-b. Zhang, *A Biodegradable Polydopamine-Derived Electrode Material for High-Capacity and Long-Life Lithium-Ion and Sodium-Ion Batteries.* Angewandte Chemie, 2016. **128**(36): p. 10820-10824.

[201]. Lee, H., S.M. Dellatore, W.M. Miller, and P.B. Messersmith, *Mussel-Inspired Surface Chemistry for Multifunctional Coatings.* Science, 2007. **318**(5849): p. 426-430.

[202]. Lee, H., J. Rho, and P.B. Messersmith, *Facile Conjugation of Biomolecules onto Surfaces via Mussel Adhesive Protein Inspired Coatings.* Advanced Materials, 2009. **21**(4): p. 431-434.

[203]. Jiang, J., L. Zhu, L. Zhu, B. Zhu, and Y. Xu, *Surface Characteristics of a Self-Polymerized Dopamine Coating Deposited on Hydrophobic Polymer Films.* Langmuir, 2011. **27**(23): p. 14180-14187.

[204]. Xu, C., K. Xu, H. Gu, R. Zheng, H. Liu, X. Zhang, Z. Guo, and B. Xu, *Dopamine as A Robust Anchor to Immobilize Functional Molecules on the Iron Oxide Shell of Magnetic Nanoparticles.* Journal of the American Chemical Society, 2004. **126(**32): p. 9938-9939.

[205]. Liu, R., S.M. Mahurin, C. Li, R.R. Unocic, J.C. Idrobo, H. Gao, S.J. Pennycook, and S. Dai, *Dopamine as a Carbon Source: The Controlled Synthesis of Hollow Carbon Spheres and Yolk-Structured Carbon Nanocomposites.* Angewandte Chemie International Edition, 2011. **50**(30): p. 6799-6802.

[206]. Bernsmann, F., V. Ball, F. Addiego, A. Ponche, M. Michel, J.J.d.A. Gracio, V. Toniazzo, and D. Ruch, *Dopamine−Melanin Film Deposition Depends on the Used Oxidant and Buffer Solution.* Langmuir, 2011. **27**(6): p. 2819-2825.

[207]. Kim, K.C., T. Liu, S.W. Lee, and S.S. Jang, *First-Principles Density Functional Theory Modeling of Li Binding: Thermodynamics and Redox Properties of Quinone Derivatives for Lithium-Ion Batteries.* Journal of the American Chemical Society, 2016. **138**(7): p. 2374-2382.

[208]. Kim, H., J.E. Kwon, B. Lee, J. Hong, M. Lee, S.Y. Park, and K. Kang, *High Energy Organic Cathode for Sodium Rechargeable Batteries.* Chemistry of Materials, 2015. **27**(21): p. 7258-7264.

[209]. Zhu, Z., H. Li, J. Liang, Z. Tao, and J. Chen, *The disodium salt of 2,5-dihydroxy-1,4-benzoquinone as anode material for rechargeable sodium ion batteries.* Chemical Communications, 2015. **51**(8): p. 1446-1448.

[210]. Ditchfield, R., W.J. Hehre, and J.A. Pople, *Self-Consistent Molecular-Orbital Methods. IX. An Extended Gaussian-Type Basis for Molecular-Orbital Studies of Organic Molecules.* The Journal of Chemical Physics, 1971. **54**(2): p. 724-728.

[211]. *Jaguar version 7.6*. 2009, Jaguar version 7.6 Schrodinger, LLC: New York, NY.

[212]. Winget, P., J.C. Cramer, and G.D. Truhlar, *Computation of equilibrium oxidation and reduction potentials for reversible and dissociative electron-transfer reactions in solution.* Theoretical Chemistry Accounts, 2004. **112**(4): p. 217-227.

[213]. Liu, T., R. Kavian, Z. Chen, S.S. Cruz, S. Noda, and S.W. Lee, *Biomass-derived carbonaceous positive electrodes for sustainable lithium-ion storage.* Nanoscale, 2016. **8**(6): p. 3671-3677.

[214]. Zangmeister, R.A., T.A. Morris, and M.J. Tarlov, *Characterization of Polydopamine Thin Films Deposited at Short Times by Autoxidation of Dopamine.* Langmuir, 2013. **29**(27): p. 8619-8628.

[215]. Adamo, C. and V. Barone, *Toward reliable density functional methods without adjustable parameters: The PBE0 model.* J. Chem. Phys., 1999. **110**(13): p. 6158-6170.

[216]. Adamo, C., G.E. Scuseria, and V. Barone, *Accurate excitation energies from time-dependent density functional theory: Assessing the PBE0 model.* J. Chem. Phys., 1999. **111**(7): p. 2889-2899.

[217]. Wei, Q., F. Zhang, J. Li, B. Li, and C. Zhao, *Oxidant-induced dopamine polymerization for multifunctional coatings.* Polymer Chemistry, 2010. **1**(9): p. 1430-1433.

[218]. Liu, Y., K. Ai, and L. Lu, *Polydopamine and Its Derivative Materials: Synthesis and Promising Applications in Energy, Environmental, and Biomedical Fields.* Chemical Reviews, 2014. **114**(9): p. 5057-5115.

[219]. Ryou, M.-H., Y.M. Lee, J.-K. Park, and J.W. Choi, *Mussel-Inspired Polydopamine-Treated Polyethylene Separators for High-Power Li-Ion Batteries.* Advanced Materials, 2011. **23**(27): p. 3066-3070.

[220]. Karachevtsev, V.A., A.M. Plokhotnichenko, M.V. Karachevtsev, and V.S. Leontiev, *Decrease of carbon nanotube UV light absorption induced by π–π-stacking interaction with nucleotide bases.* Carbon, 2010. **48**(13): p. 3682-3691.

[221]. Clark, M.B., J.A. Gardella, T.M. Schultz, D.G. Patil, and L. Salvati, *Solid-state analysis of eumelanin biopolymers by electron spectroscopy for chemical analysis.* Analytical Chemistry, 1990. **62**(9): p. 949-956.

[222]. Hong, S., Y.S. Na, S. Choi, I.T. Song, W.Y. Kim, and H. Lee, *Non-Covalent Self-Assembly and Covalent Polymerization Co-Contribute to Polydopamine Formation.* Advanced Functional Materials, 2012. **22**(22): p. 4711-4717.

[223]. Fei, B., B. Qian, Z. Yang, R. Wang, W.C. Liu, C.L. Mak, and J.H. Xin, *Coating carbon nanotubes by spontaneous oxidative polymerization of dopamine.* Carbon, 2008. **46**(13): p. 1795-1797.

[224]. Su, Y., Y. Liu, P. Liu, D. Wu, X. Zhuang, F. Zhang, and X. Feng, *Compact Coupled Graphene and Porous Polyaryltriazine-Derived Frameworks as High Performance Cathodes for Lithium-Ion Batteries.* Angewandte Chemie International Edition, 2015. **54**(6): p. 1812-1816.

[225]. Zhang, L.L. and X.S. Zhao, *Carbon-based materials as supercapacitor electrodes.* Chemical Society Reviews, 2009. **38**(9): p. 2520-2531.

[226]. Pandolfo, A.G. and A.F. Hollenkamp, *Carbon properties and their role in supercapacitors.* Journal of Power Sources, 2006. **157**(1): p. 11-27.

[227]. Frackowiak, E. and F. Béguin, *Carbon materials for the electrochemical storage of energy in capacitors.* Carbon, 2001. **39**(6): p. 937-950.

[228]. Raccichini, R., A. Varzi, S. Passerini, and B. Scrosati, *The role of graphene for electrochemical energy storage.* Nat Mater, 2015. **14**(3): p. 271-279.

[229]. Stoller, M.D., S. Park, Y. Zhu, J. An, and R.S. Ruoff, *Graphene-Based Ultracapacitors.* Nano Letters, 2008. **8**(10): p. 3498-3502.

[230]. Wang, Y., Z. Shi, Y. Huang, Y. Ma, C. Wang, M. Chen, and Y. Chen, *Supercapacitor Devices Based on Graphene Materials.* The Journal of Physical Chemistry C, 2009. **113**(30): p. 13103-13107.

[231]. Yu, D. and L. Dai, *Self-Assembled Graphene/Carbon Nanotube Hybrid Films for Supercapacitors.* The Journal of Physical Chemistry Letters, 2010. **1**(2): p. 467-470.

[232]. Lv, W., C. Zhang, Z. Li, and Q.-H. Yang, *Self-Assembled 3D Graphene Monolith from Solution.* The Journal of Physical Chemistry Letters, 2015. **6**(4): p. 658-668.

[233]. Xu, Y., Z. Lin, X. Zhong, X. Huang, N.O. Weiss, Y. Huang, and X. Duan, *Holey graphene frameworks for highly efficient capacitive energy storage.* Nature Communications, 2014. **5**: p. 4554.

[234]. Wei, W., S. Yang, H. Zhou, I. Lieberwirth, X. Feng, and K. Müllen, *3D Graphene Foams Cross-linked with Pre-encapsulated Fe3O4 Nanospheres for Enhanced Lithium Storage.* Advanced Materials, 2013. **25**(21): p. 2909-2914.

[235]. Bai, H., K. Sheng, P. Zhang, C. Li, and G. Shi, *Graphene oxide/conducting polymer composite hydrogels.* Journal of Materials Chemistry, 2011. **21**(46): p. 18653-18658.

[236]. Yan, J., Z. Fan, W. Sun, G. Ning, T. Wei, Q. Zhang, R. Zhang, L. Zhi, and F. Wei, *Advanced Asymmetric Supercapacitors Based on Ni(OH)2/Graphene and Porous Graphene Electrodes with High Energy Density.* Advanced Functional Materials, 2012. **22**(12): p. 2632-2641.

[237]. Zhang, K., C. Guo, Q. Zhao, Z. Niu, and J. Chen, *High-Performance Organic Lithium Batteries with an Ether-Based Electrolyte and 9,10-Anthraquinone (AQ)/CMK-3 Cathode.* Advanced Science, 2015. **2**(5): p. n/a-n/a.

[238]. Kim, H., H.-D. Lim, S.-W. Kim, J. Hong, D.-H. Seo, D.-c. Kim, S. Jeon, S. Park, and K. Kang, *Scalable Functionalized Graphene Nano-platelets as Tunable Cathodes for High-performance Lithium Rechargeable Batteries.* Scientific Reports, 2013. **3**: p. 1506.

[239]. Liu, T., A.A.B. Davijani, J. Sun, S. Chen, S. Kumar, and S.W. Lee, *Hydrothermally Oxidized Single-Walled Carbon Nanotube Networks for High Volumetric Electrochemical Energy Storage.* Small, 2016. **12**(25): p. 3423-3431.

[240]. Lee, B., C. Lee, T. Liu, K. Eom, Z. Chen, S. Noda, T.F. Fuller, H.D. Jang, and S.W. Lee, *Hierarchical networks of redox-active reduced crumpled graphene oxide and functionalized few-walled carbon nanotubes for rapid electrochemical energy storage.* Nanoscale, 2016. **8**(24): p. 12330-12338.

[241]. Liu, T., K.C. Kim, B. Lee, Z. Chen, S. Noda, S.S. Jang, and S.W. Lee, *Self-polymerized dopamine as an organic cathode for Li- and Na-ion batteries.* Energy & Environmental Science, 2017. **10**(1): p. 205-215.

[242]. Kim, Y.J., W. Wu, S.-E. Chun, J.F. Whitacre, and C.J. Bettinger, *Biologically derived melanin electrodes in aqueous sodium-ion energy storage devices.* Proceedings of the National Academy of Sciences, 2013. **110**(52): p. 20912-20917.

[243]. Kim, M., C. Lee, Y.D. Seo, S. Cho, J. Kim, G. Lee, Y.K. Kim, and J. Jang, *Fabrication of Various Conducting Polymers Using Graphene Oxide as a Chemical Oxidant.* Chemistry of Materials, 2015. **27**(18): p. 6238-6248.

[244]. Yang, F., Z. Zhang, K. Du, X. Zhao, W. Chen, Y. Lai, and J. Li, *Dopamine derived nitrogen-doped carbon sheets as anode materials for high-performance sodium ion batteries.* Carbon, 2015. **91**: p. 88-95.

[245]. Xu, L.Q., W.J. Yang, K.-G. Neoh, E.-T. Kang, and G.D. Fu, *Dopamine-Induced Reduction and Functionalization of Graphene Oxide Nanosheets.* Macromolecules, 2010. **43**(20): p. 8336-8339.

[246]. Miao, J., H. Liu, W. Li, and X. Zhang, *Mussel-Inspired Polydopamine-Functionalized Graphene as a Conductive Adhesion Promoter and Protective Layer for Silver Nanowire Transparent Electrodes.* Langmuir, 2016. **32**(21): p. 5365-5372.

[247]. Li, Y., M. Liu, C. Xiang, Q. Xie, and S. Yao, *Electrochemical quartz crystal microbalance study on growth and property of the polymer deposit at gold electrodes during oxidation of dopamine in aqueous solutions.* Thin Solid Films, 2006. **497**(1–2): p. 270-278.

VITA

Tianyuan Liu

Tianyuan Liu was born in Taian, China. He received his B.S. in College of Materials Science and Engineering from Northwestern Polytechnical University in 2010, and M.S. in Materials Science and Engineering from Institute of Metal Research at University of Chinese Academy of Sciences in 2013. He then pursued a doctoral degree in Mechanical Engineering at Georgia Institute of Technology.